DISSERTATION

SIGNAL DESIGN FOR ACTIVE SENSING

Submitted by

Wenbing Dang

Department of Electrical and Computer Engineering

In partial fulfillment of the requirements

For the Degree of Doctor of Philosophy

Colorado State University

Fort Collins, Colorado

Spring 2014

Doctoral Committee:

Advisor: Ali Pezeshki
Co-Advisor: Mahmood R. Azimi-Sadjadi

Edwin K. P. Chong
Chris Peterson

ABSTRACT

SIGNAL DESIGN FOR ACTIVE SENSING

Recent advances in hardware technology across the active sensing spectra, from RF to optical, enable the construction of sophisticated excitation patterns that can be varied across time, space, frequency, wavenumber, and polarization. In the RF band, modern radars are increasingly being equipped with arbitrary waveform generators that allow the transmission of different waveforms across multiple degrees of freedoms simultaneously. The emergence of multiple-input multiple-output (MIMO) phased-array radars, with multiple degrees of freedom at transmitter and receiver, brings the promise of improved surveillance and tracking performance. In the optical band, the advent of spatial light modulators and digital light processing devices allows us to construct structured excitation patterns for illuminating objects.

These advances open up exciting possibilities for design of illumination patterns and signal processing algorithms. In this dissertation, we develop new signal design and processing methods for a subset of active sensing problems in radar and optical imaging. In addition, we exploit the Kalman filter as an efficient signal processing approach for sensing systems with dynamical state update and measurement acquisition.

Radar imaging: Broadly speaking, signal designs for radar imaging can be divided into two categories: designs for desired ambiguity functions and designs for interference rejection. The first category typically involves designing radar waveforms of a given time-bandwidth product, such that their ambiguity functions have narrow mainlobes and small sidelobes in desired regions in the range-Doppler plane. The designs in this category are typically suited for resolving point scatters in white noise. The second category typically considers the joint design of radar transmit and receive filters, to detect or estimate a point or extended target in the presence of interference and clutter.

In conventional designs in both categories, typically, the focus has been on designing a single transmit filter or a single transmit-receive pair to achieve a design goal. But recent hardware advances enable the utilization of banks of transmit-receive filters across multiple degrees of freedom, and give rise to new opportunities for radar waveform design and signal processing. In this dissertation, we take advantage of these new capabilities to develop novel signal design principles for MIMO radar in the first of the aforementioned categories. Our contributions are as follows:

Doppler resilient illuminations: In radar range detection, typically, localization in range is performed by matched filtering the received signal with the transmitted waveform. The output of the matched filter would ideally be an impulse at the desired delay. Therefore, waveforms with impulse-like autocorrelation functions are of great value in these applications. Such waveforms are typically constructed through phase coding a narrow pulse shape with appropriate unimodular codes. Unimodularity is desired due to constraints set by power amplifiers used in radar transmitters. In the absence of Doppler, the near ideal autocorrelation property of such waveforms enables separation of closely-spaced targets in range. However, all phase-coded waveforms are sensitive to Doppler effect; off the zero Doppler axis, the magnitude of range sidelobe of a phase-coded waveform's ambiguity function is typically large. These Doppler-induced range sidelobes can in turn result in masking of a weak target that is located in range near a strong reflector with a different Doppler frequency.

As part of this dissertation, we develop a general framework for designing *Doppler resilient* radar illuminations through proper waveform coordination across time, frequency, and aperture. The building blocks of our Doppler resilient illuminations are phase-coded waveforms constructed from unimodular codes such as Golay complementary codes. We first show that by properly coordinating these complementary waveforms across time, we can annihilate the range sidelobe of the corresponding pulse train's ambiguity function inside a modest Doppler around the zero-Doppler axis. This in turn enables us to extract weak targets that are situated near strong reflectors. However, this Doppler resilience comes at the expense of Doppler response. We characterize the tradeoff between the two for time-coordinated transmissions. We then extend our design to the coordination of complementary waveforms across both time and frequency. The added degrees of freedom for transmission (frequency) allow us to improve Doppler response without reducing resilience to Doppler. Finally, we extend our work to the design of Doppler resilient paraunitary waveform matrices. Construction of paraunitary illuminations has received significant attention from the MIMO radar community. However, all designs suffer from sensitivity to Doppler. Our approach provides a way to maintain the paraunitary property even in the presence of Doppler.

Optical imaging: The invention of charge-coupled devices and two-dimensional arrays revolutionize optical imaging, by shifting the measurement collection paradigm in optics from serial collection of light intensities at the detector plane to the parallel recording of light intensities. This translates to potentially several fold increase in imaging speed in many imaging systems operating in mid infrared to soft X-ray band. However, CCDs are not readily available in the Terahertz to far infrared region, and optical systems in these bands (including confocal microscopes) still rely on single pixel detectors. This has led to investigation of techniques that employ structured illumination to eliminate the need for pixel-wise scanning. A popular approach, based on compressive sensing theory, has been to use random illumination patterns along with sparse reconstruction algorithms to reconstruct the full object intensity from a small number of intensity measurements. This approach has been mostly investigate under ideal imaging conditions, with no or very little optical aberrations.

As part of this dissertation, we investigate the viability of such compressive sensing approaches for high resolution optical microscopy under more practical conditions. In particular, we analyze the sensitivity of compressive optical microscopy to misfcous effects, which are inevitable in imaging most specimens. Our analysis indicates that compressive imaging is highly sensitive to misfcous effects at high magnifications factors, which are typical in microscopy.

Kalman filtering: In the past few decades the invention of Kalman filters (KFs) and their variations has led to improved adaptive signal processing performance of various sensing systems whose state evolution and measurement acquisition can be characterized by dynamical linear model equations. valued state and measurements.

Complex-valued signals are ubiquitous in science and engineering. A random complex-valued vector $\mathbf{x}$ is said to be improper, if $\mathbf{x}$ is correlated to its complex conjugate, i.e., the complementary covariance $E\mathbf{x}\mathbf{x}^T$ is nonzero. The impropriety of complex-valued signal exists in many application including communication, smart grid, optical imaging, and acoustic imaging. Since conventional statistical signal processing essentially treats complex-valued signals as real-valued signals and ignores the complementary covariances, it becomes necessary to revisit the theory. Compared to conventional strictly linear processing, the widely linear processing is proven to be an efficient signal processing technique for resolving improper complex signals.

As part of this dissertation, we are motivated to make use of widely linear processing to develop novel complex KFs and their nonlinear versions for improper complex states. We show that complementary covariance of improper states may be used to develop widely linear complex KFs (WLCKFs) and Unscented WLCKFs. We show that, compared to the conventional complex KFs and Unscented complex KFs which ignore the complementary covariances, the WLCKFs and Unscented WLCKFs can significantly reduce the mean square error of state estimation, by utilizing full first and second order statistical information of improper complex states.

ACKNOWLEDGEMENTS

First I would like to express my deepest gratitude to my advisor, Professor Ali Pezeshki, for his continuous support and guidance throughout my PhD program. With his advise in my life and research activities, I have gradually developed a deep understanding of the nature of scientific research, the right approach to consider a problem, and how to make a statement properly. He also instructed me in forming the essential characteristics of a qualified researcher, including passion, patience, rigorousness, open mind, presentation skills, and collaboration ability, which are indeed crucial factors of my future success.

Second, my deepest gratitude is extended to my committee members: Professor Mahmood R. Azimi-Sadjadi, Professor Chris Peterson, and Professor Edwin K. P. Chong. They have contributed many insightful ideas to my research. They also helped me to broaden my perspective on both theory and application of engineering and applied mathematics.

Third, I would like to pass my sincere appreciation to Professor Randy A. Bartels. I have collaborated with him on a couple of computational optical imaging problems. Because of him I obtained my background in optics (in both theory and experiment), which has distinct flavors but shares similar principles to other sensing disciplines. He also brought to me some key components of how to conduct research and deliver research results to the public.

Fourth, I would also like to extend my sincere appreciation to Professor Louis L. Scharf. I feel grateful to work with this great mentor on problems related to statistical signal processing. He helped me to realize the importance of theory and fundamental research to the real-world applications. He helped me to realize that one should include reality in research problems, instead of crafting a over-simplified model formulation which has a beautiful mathematical solution.

Fifth, I would like to thank Dr. Sandip Bose, Dr. Bikash Sinha, Dr. Jiaqi Yang, and Dr. Pu Wang in Department of mathematics and modeling at Schlumberger-Doll Research

(SDR) Center. It is a fantastic experience for me to spend five months on a research internship in SDR, and work and study with these people. During my internship in SDR, I was impressed by their attitude of doing fundamental research, their ability of converting technical background into commercial hardwares and softwares, and their team spirits.

Finally, I would like to thank my mother Xinhui Cao, my father Yongping Dang, and my girlfriend Jing Han. They helped me a lot to face the difficulties in my life, and to be optimistic and prepared for tomorrow's opportunities/challenges. I also want to thank my college friends who are currently in US, my friends in Fort Collins, CO, and my internship friends who are doing amazing research in most prestigious universities in US. My memory is full of numerous discussions and leisure-time activities with them.

TABLE OF CONTENTS

ABSTRACT ii

ACKNOWLEDGEMENTS vi

1 INTRODUCTION 1

1.1 Active Sensing: Waveform and Receiver Design 1

1.2 Conventional Active Sensing Theory 1

1.2.1 Radar Imaging 1

1.2.2 Optical Imaging 4

1.3 Advances in Active Sensing: New Degrees of Freedom 4

1.3.1 Advances in Radar Imaging 5

1.3.2 Advances in Optical Imaging 6

1.4 Summary of Contributions 6

1.4.1 Doppler Resilient Transmit-receive Filters for Radar 6

1.4.2 Compressive Optical Imaging and Sensitivity to Misfocus 9

1.4.3 Widely Linear Complex Kalman Filters 11

1.5 Organization of the Dissertation 12

2 DOPPLER RESILIENT TRANSMIT-RECEIVE FILTERS FOR RADAR 14

2.1 $(\mathcal{P}, \mathcal{Q})$ Pulse Trains 18

2.2 Range Sidelobe Suppression 23

2.2.1 PTM vs. Binomial Design 23

2.2.2 General $(\mathcal{P}, \mathcal{Q})$ Pulse Train Design 25

2.3 Performance Analysis 29

2.3.1 Peak-to-Peak-Sidelobe Ratio 30

2.3.2 Signal-to-Noise Ratio 32

2.3.3 Doppler Estimation 35

2.3.4 Range Estimation 37
2.3.5 Tradeoff analysis for PTM and Binomial design 37
2.4 $(\mathcal{P}, \mathcal{Q})$ Pulse Train for Larger Sets of Complementary Waveforms 38
2.5 Conclusion 41
3 DOPPLER RESILIENT OFDM ILLUMINATIONS 42
3.1 Tradeoff between Range Sibelobe Suppression and Doppler Response 43
3.2 OFDM $(\mathcal{P}, \mathcal{Q})$ Pulse Trains 45
3.2.1 Spectrum Optimization 49
3.2.2 Analysis of Nonlinearity 49
3.3 Coprime OFDM $(\mathcal{P}, \mathcal{Q})$ Pulse Trains 50
3.4 $(\mathcal{P}, \mathcal{Q})$ Pulse Train Obtained by Sequence Repetition 54
3.5 SNR Analysis 57
3.5.1 OFDM $(\mathcal{P}, \mathcal{Q})$ Pulse Train 57
3.5.2 Coprime OFDM $(\mathcal{P}, \mathcal{Q})$ Pulse Train 59
3.5.3 $(\mathcal{P}, \mathcal{Q})$ Pulse Train Obtained by Sequence Repetition 61
3.6 Conclusion 62
4 DOPPLER RESILIENT PARAUNITARY ILLUMINATIONS FOR PHASED-ARRAY MIMO RADAR 63
4.1 Complementary Space-time Waveforms 65
4.1.1 Definition of Wavefrom Complimentarity 65
4.1.2 Short Pulse for Mitigating Chip-Level Doppler Effects 67
4.2 Examples of Complementary Space-time Waveforms 68
4.2.1 Paraunitary Waveform Vectors 68
4.2.2 Desired Waveform Spatial Correlation 69
4.3 Sensitivity of Complementarity to Doppler Shift in PRI 73
4.4 Doppler Resilient Waveform Matrices 74
4.5 $D = 2$ Case 76

4.6 $D > 2$ Case . . . 77
4.6.1 Principle of Residue Spectra Anihilation . . . 78
4.6.2 Number Theoretic Interpretation . . . 79
4.6.3 Spectral Interpretation . . . 80
4.7 Examples of Pulse Train Constructions . . . 81
4.7.1 First type of Pulse Train Construction: Iterative Expansion . . . 81
4.7.2 Second Type of Pulse Train Construction: Creating Band-pass Spectra 85
4.8 Noise Analysis . . . 88
4.8.1 Calculation of Signal and Noise Power . . . 88
4.8.2 Achievable Upper Bound of Noise Power . . . 90
4.8.3 Angle-invariant Noise Power . . . 91
4.9 Conclusion . . . 91
5 COMPRESSIVE OPTICAL IMAGING AND SENSITIVITY TO MISFOCUS . 92
5.1 Measurement Formation . . . 95
5.2 Compressive Imaging Approach . . . 98
5.3 Misfocus Imaging . . . 100
5.4 Numerical Results for Misfocus Imaging . . . 104
5.5 Misfocus Performance Analysis . . . 107
5.6 Other Discussions . . . 110
5.6.1 Grid Search along Optical Axis . . . 110
5.6.2 Application of Weighted and Structured Sparse Total Least-square Approach . . . 111
5.7 Conclusion . . . 113
6 WIDELY LINEAR COMPLEX KALMAN FILTERS . . . 115
6.1 Brief Review of Complex Random Vectors . . . 116
6.1.1 Cartesian and Complex Augmented Representations . . . 116
6.1.2 Dual Channel and Widely Linear Transformation . . . 117

6.1.3 Improper Complex Signal 118
6.2 Dual Channel Real and Widely Linear Complex Kalman Filter 119
6.3 Performance Comparison between WLCKF and CKF 123
6.3.1 Special Case: x_0 Is Improper, w_t and n_t Are Proper 123
6.3.2 General Case: w_t and n_t Can Be Improper 124
6.4 Discussion on Extended Widely Linear Complex Kalman Filter 126
6.5 Unscented Widely Linear Complex Kalman Filter 126
6.6 Conclusion 133
7 CONCLUSION 134
REFERENCES 136
APPENDIX A — PROOF OF THEOREM 2.3.1 144
APPENDIX B — PROOF OF THEOREM 2.3.3 145
APPENDIX C — PROOF OF THEOREM 2.4.1 147
APPENDIX D — PROOF OF LEMMA 4.6.1 148
APPENDIX E — PROOF OF THEOREM 4.6.2 149
APPENDIX F — PROOF OF THEOREM 4.7.1 151
APPENDIX G — PROOF OF THEOREM 4.7.3 152
APPENDIX H — PROOF OF THEOREM 4.7.8 154
APPENDIX I — PROOF OF THEOREM 4.8.1 155
APPENDIX J — PROOF OF THEOREM 5.5.2 157

CHAPTER 1

INTRODUCTION

1.1 Active Sensing: Waveform and Receiver Design

The task of an active sensing system is to study the environment of interest through the functionalities of its transmitter and receiver. The transmitter excites/illuminates the environment with a waveform. The receiver measures the return/reflection of targets in scene and process the measurements to form an image, estimate parameters, or detect/classify targets. For instance, a radar generates an illumination in the radio frequency band, studies the presence of targets in scene, and estimates the targets parameters (scattering coefficient, round-trip delay/range, and Doppler frequency/velocity); a sonar emits acoustic radiation to the underwater environment and detects the underwater objects; ultrasound imaging makes use of ultrasound wave propagation and diagnose subcutaneous human tissues such as vessels and organs; optical imaging utilizes optical radiation spanning from the soft X-ray regime to THz frequencies and has numerous applications such as microscopy and holography. In summary, the signal design for active sensing can boil down to two aspects: transmit waveform design and receiver design.

1.2 Conventional Active Sensing Theory

1.2.1 Radar Imaging

Broadly speaking, signal designs for radar imaging can fall in two categories: designs for desired ambiguity functions and designs for interference rejection. The first category typically involves designing radar waveforms of a given time-bandwidth product, such that their ambiguity functions have narrow mainlobes and small sidelobes in desired regions in the range-Doppler plane. The designs in this category are typically suited for resolving point scatters in white noise. The second category typically considers the joint design of radar transmit and receive filters to detect or estimate a point or extended target in the presence of interference and clutter.

- First Category: Ambiguity Function Theory

  A radar is an imaging system that forms two-dimensional delay-Doppler images of the illuminated scene. Suppose the individual scatters in scene can be viewed as point scatters, with a specific coordinate in the two-dimensional range-Doppler plane. The radar return is processed by receive filter banks outputing a map of the magnitude of scattering coefficients in the range-Doppler plane. For a point scatter with round-trip delay τ and Doppler frequency ν, its narrow-band radar return is the transmit waveform delayed by τ and modulated by frequency ν. If the receive noise process is white, then the output signal-to-noise ratio is maximized if the receive filter takes the form of the complex conjugate of the time reversed transmit waveform delayed by τ and modulated by frequency $-\nu$, or matched filter. Therefore the two-dimensional radar image for this single target is the point-spread function of the radar system centered at the target coordinate (τ, ν), which is a function of the transmit waveform, called ambiguity function of the transmit waveform, defined by Woodward [1] in early 1950's.

  Since the radar ambiguity function serves as the point-spread-function of the range-Doppler imaging system, ideally we wish it to be a thumbtack, i.e., two-dimensional Kronecker delta function. However, this is not possible, since Moyal [2] had shown that the volume under ambiguity surface equals a fixed value that is the square of the total transmit energy. In other words if we choose a specific transmit waveform whose ambiguity function can be pushed down in some region, its ambiguity function pops up in some other regions. Therefore in practice, we only hope for a desired transmit waveform whose ambiguity function has narrow mainlobe, and small sidelobes (maybe only in some regions in the range-Doppler plane). A narrow mainlobe indicates a fine image resolution, or the ability to separate closely-spaced targets. Small sidelobes mean the ability to extract weak targets nearby strong reflectors.

In the past few decades there has been a number of good designs of radar transmit waveforms. For example, many radar waveforms are generated by phase coding a narrow pulse shape with some unimodular sequences with impulse-like aperiodic autocorrelation sequences, such as the polyphase sequences by Heimiller [3], Frank codes [4], polyphase codes by Chu [5], Barker sequences [6], and generalized Barker sequences by Golomb and Scholtz [7]. However, there are still some drawbacks of the above waveform designs, such as sensitivity to Doppler. Woodward mentioned in his book that "the basic question of what to transmit remains substantially unanswered" in 1953. This is probably still true today and there exists many openings for the design of radar waveforms with better ambiguity function properties.

- Second Category: Interference Rejection

The aforementioned ambiguity function theory is suited for resolving point scatters in white noise. Now consider the case in which the targets are masked by a background of clutter returns and thermal noise. In here the targets and clutters can be extended in the range-Doppler plane. If we form a signal plus noise model for the radar return, the noise can have structured/colored spectrum due to the clutter return, as opposed to white spectrum required in the ambiguity function theory. Therefore employing matched filter banks at receiver may indicate no optimality, and more sophisticated receiver filters should be considered to reject the interference.

The signal-to-interference-noise ratio (SINR) is a major performance metric for the interference rejection category of radar signal design. Many designs of radar transmit and receive filters rely on an optimization of SINR subject to some transmit power constraint. Some fundamental works [8] consider the design of receiver with pre-selected transmit filter. Typically the design problem involves optimizing a quadratic objective function, which can be transformed to an eigenvalue/generalized eigenvalue problem. The receive filter is constructed according to the eigenvector of some semidefinite matrix associated with the biggest eigenvalue. Alternatively, other researchers consider a joint transmit-receive design for optimizing SINR [9]. This type of problems are in general hard to solve in closed form. Usually people resort to iterative optimizations. Each individual procedure either derives the optimal transmitter with fixed receiver, or derives the optimal receiver with fixed transmitter. The iterative approach can be shown to converge to a local minimum of the objective function.

1.2.2 Optical Imaging

The convectional theory of optical imaging is established on the basis of electromagnetic theory and Fourier analysis. The Fresnel diffraction approximation enables the computation of the field propagation at each position in space. In an optical system, the size of aperture controls the numerical aperture (NA) value, which determines the highest spatial frequency that can pass the system, or the bandwidth of the optical transfer function (OTF). Taking the inverse Fourier transform of the OTF yields the point-spread function, the width of which determines the transverse resolution of the imaging system. The Rayleigh limit clearly demonstrates that the imaging resolution is proportional to the light wavelength and inversely proportional to the NA. Common optical devices such as a single lens or telescope (4-f system) can be used to form images of a object with some magnification or demagnification factors.

1.3 Advances in Active Sensing: New Degrees of Freedom

Advances in sensor technology are providing active sensors that are increasingly agile both in their transmitters and receivers' capabilities [10]. The introduction of recent hardware across the active sensing spectra, from RF to optical, enables the construction of sophisticated illumination patterns that can be varied across time, space, frequency, wavenumber, and polarization. The enhanced measurement collection devices, together with novel signal processing algorithms, bring the promise to improved performance metrics.

1.3.1 Advances in Radar Imaging

Modern radars are increasingly being equipped with arbitrary waveform generators which enable generation of different wavefields across time, frequency, polarization, aperture, and wavenumber [10–12]. The transmission of these waveform patterns can be changed in a rapid succession (from pulse to pulse). The degrees of freedom in time can be exploited by separating different waveform transmissions in multiple pulse repetition intervals (PRI) [13–17]. The receiver filter bank processes radar return in each PRI, and combines the outputs across multiple PRIs to form a radar image in the range-Doppler plane. The transmission of different waveforms can also be coordinated in frequency [18–20], if proper signal processing on the measurements is employed. When the target has a polarization direction-dependent scattering property, the separation of waveform transmissions across all polarization modes brings in the additional performance gain. In this case the receiver utilizes a multi-dimensional filter bank that is carefully designed to meet the paraunitary property [14], to facilitate the extraction of the target's scattering information. Equipped with multiple transmit and receive antennas, the multiple-input multiple-output (MIMO) radars [21–24] are able to exploit the increased degrees of freedom in space, by emitting arbitrary waveforms across the transmit antenna array and processing the measurements across the receive antenna array. Proper spatial correlation of transmit waveforms across the transmit antenna array can result in a wide angle transmit beampatterns, as opposed to the narrow transmit beampattern in single antenna radar systems. In additional to the range/Doppler imaging, the MIMO radars can also integrate efficient signal processing tools to simultaneously estimate different azimuth angles for the multiple targets in scene.

1.3.2 Advances in Optical Imaging

In the past few decades, there has been a number of inventions of hardware in optical imaging systems. Many optical imaging applications make use of a spatial modulated/illumination beam which can have an arbitrary representation in space and time. This spatially illumination can be generated by the spatial light modulators (SLM) and digital light processing (DLP) devices. For instance, an SLM employs a micromirror array with the flexibility to adjust the amplitude and phase of each output spatial frequency components. Alternatives of the SLMs are the optical masks [25–30] with either transparent or blocked elements. The opens and closes on the mask correspond to the zeros and ones in some digitized space-time signals or representations. The emergence of charge-coupled devices and two-dimensional arrays revolutionize optical imaging, by shifting the measurement collection paradigm in optics from serial collection of light intensities at the detector plane to the parallel recording of light intensities. This translates to potentially several fold increase in imaging speed in many imaging systems operating in mid infrared to soft X-ray band.

1.4 Summary of Contributions

In conventional designs of active sensing systems, typically, the focus has been on designing a single illumination pattern or a single transmit-receive pair to achieve a design goal. But recent hardware advances enable the utilization of banks of transmit-receive filters across multiple degrees of freedom, and give rise to new opportunities for waveform design and receive processing. In this dissertation, we take advantage of these new capabilities to develop novel signal design principles for a subset of active sensing problems in radar and optical imaging. Our contributions are as follows:

1.4.1 Doppler Resilient Transmit-receive Filters for Radar

In this dissertation, we have developed a general framework for designing Doppler resilient illuminations through waveform coordination across time, frequency, and aperture. The issue of sensitivity to Doppler exist for all conventional phase coded waveforms designs. A radar waveform phase coded by an unimodular sequence with impulse-like aperiodic autocorrelation sequence has an impulse-like autocorrelation function. This means that the ambiguity function is impulse-like along the zero Doppler axis. However, off the zero Doppler axis the impulse-like response in range is not maintained and the ambiguity function has range sidelobe. In consequence, a weak target that is located in range near a strong reflector with a different Doppler frequency may be masked by the range sidelobe of the radar ambiguity function centered at the delay-Doppler position of the stronger reflector.

As part of this dissertation, we develop a general framework for designing *Doppler resilient* radar illuminations through properly coordinating phase-coded waveforms constructed from Golay complementary code across time, frequency, and aperture:

- We first show that by properly sequencing Golay complementary waveforms in time in constructing the transmit pulse train and the receive filter, we can essentially annihilate range sidelobes of the radar point-spread function (psf) and maintain an impulse-like point-spread function in range over a Doppler interval around the zero-Doppler axis. We construct the transmit pulse train by coordinating the transmission of Golay complementary waveforms according to zeros and ones in a binary sequence $\mathcal{P}$. We refer to this pulse train as the $\mathcal{P}$-pulse train. The pulse train used in the receive filter is constructed in a similar way, in terms of sequencing the Golay waveforms, but each waveform in the pulse train is weighted according to an element of a sequence $\mathcal{Q}$. We call this pulse train the $\mathcal{Q}$-pulse train. We show that the size of the range sidelobes of the psf is controlled by the spectrum of product of the $\mathcal{P}$ and $\mathcal{Q}$ sequences. By selecting sequences for which the spectrum of their product has a higher-order null around zero Doppler, we can annihilate the range sidelobe of the psf inside an interval around the zero-Doppler axis. For the illustration purposes we first present two specific $(\mathcal{P}, \mathcal{Q})$ designs, namely the *PTM design* and the *binomial design*. We then establish a necessary and sufficient condition for achieving an Mth-order spectral null with length-N, $N > M+1$, sequences $\mathcal{P}$ and $\mathcal{Q}$. The condition is that the product of the $\mathcal{P}$ and $\mathcal{Q}$ sequences must be in the null space of an $(M+1)\times N$ integer Vandermonde matrix. We show that the above $(\mathcal{P},\mathcal{Q})$-pulse train design can be extended to the cases when we have more than two complementary waveforms components in order to shape desired radar psf. However, with a given time-bandwidth product, the range sidelobe suppression ability, or Doppler resilience, comes at the expense of Doppler response.

- We then characterize the tradeoff between the Doppler resilience and Doppler response for time-coordinated transmissions. We show that by introducing new degrees of freedom (frequency), we are able to improve Doppler response without reducing resilience to Doppler. Thus We extend our time-coordinated waveform design to the coordination of complementary waveforms across both time and frequency. A single time-coordinated $(\mathcal{P},\mathcal{Q})$-pulse train is assigned to $2K$ orthogonal frequency-division multiplexing (OFDM) subcarriers. The $2K$ subcarriers include K subcarriers pairs with equal and opposite frequency offset relative to a common carrier frequency. The effective radar psf is a weighted summation of the squared cross ambiguity functions of the $(\mathcal{P},\mathcal{Q})$-pulse trains assigned to the total K subcarrier pairs. The Doppler response is essentially controlled by of the spectrum of the weight sequence across all subcarriers, whose zero-crossings around zero Doppler is $\mathcal{O}(1/K)$. This means that Doppler resolution for an OFDM $(\mathcal{P},\mathcal{Q})$-pulse train is $\mathcal{O}(1/K)$ and at least K/N better than a single frequency $(\mathcal{P},\mathcal{Q})$-pulse train with N pulses. But note that a fine resolution of our OFDM waveform design requires a huge frequency consumption, which may not be realistic considering the intense occupation of spectral resources nowadays. We then show that by implementing two sets of OFDM $(\mathcal{P},\mathcal{Q})$-pulse trains operating over $2K_1$ and $2K_2$ subcarriers respectively, and properly performing signal processing on the measurement, we can achieve a Doppler resolution in the order of $\mathcal{O}(1/K_1K_2)$, provided that K_1 and K_2 are coprime integers. Therefore the same Doppler response can be achieved with much less bandwidth consumption.

- Finally, we extend our work to the design of Doppler resilient illumination design for phased-array MIMO radars. Illumination design for phased-array MIMO radar, based on complementary space-time waveforms has received significant attention from the MIMO radar community. For example, the paraunitary waveform design, as one type of complementary space time waveform design, has the desired property that the autocorrelation matrices of individual waveform components sum up to the desired composite auto-correlation matrix, which is a identity matrix at zero lag, and vanishes at nonzero lags. This leads to good properties such as invariant transmit beam pattern, zero waveform coupling, and ideal pulse compression, enabling the enhanced detection and surveillance performance of MIMO radars. However, all complementary space-time waveform designs suffer from sensitivity to Doppler.

  We demonstrate a Doppler resilient design of space-time transmit/receive filter based on a paraunitary waveform set with cardinality D. The transmit filter is a length-N spatial pulse train which coordinates the transmission of waveform components in the set using a D-ary scheduling sequence $\{p[n]\}_{n=0}^{N-1}$. The receive filter is constructed in the similar way, except that the waveform component in n-th PRI is weight by the n-th element of a real weighting sequence $\{q[0]\}_{n=0}^{N-1}$. The design of binary p-sequences and real q-sequences has been ellaborated in [16, 31, 32] to coordinate the transmission of Golay complementary waveforms in time for maintaining complementarity in the presence of Doppler. We present a systematic construction of these two sequences, which enables the cross ambiguity matrix of the transceiver filter which maintains the paraunitarity inside a desired Doppler band around zero Doppler axis.

1.4.2 Compressive Optical Imaging and Sensitivity to Misfocus

The invention of charge-coupled devices and two-dimensional arrays revolutionize optical imaging, by shifting the measurement collection paradigm in optics from serial collection of light intensities at the detector plane to the parallel recording of light intensities. This translates to potentially several fold increase in imaging speed in many imaging systems operating in mid infrared to soft X-ray band. However, CCDs are not readily available in the Terahertz to far infrared region and optical systems in these bands (including confocal microscopes) still rely on single pixel detectors. This has led to investigation of techniques that employ structured illumination to eliminate the need for pixel-wise scanning. A spatial structured illumination can be generated by a spatial light modulator or digital light processing device. The single detector records inner products between the line-scans of object and the illumination pattern. Therefore the imaging speed can be much faster than that of the conventional pixel-wise scanning methods.

One class of structured illumination imaging approach, called SPatIal Frequency Imaging (SPIFI), is proposed in [29, 33]. It generates a light modulation pattern whose modulation frequency linearly increase across the spatial extent, which provides a unique modulation frequency at each spatial point in the excitation. The recovery of the object spatial information is performed via a simple Fourier transform. Note that in order to obtain high imaging resolution, a large number of temporal measurements is required to meet the Nyquist condition. Another popular approach, based on compressive sensing theory, has been to use random illumination patterns along with sparse reconstruction algorithms to reconstruct the full object intensity from a small number of intensity measurements. This approach has been mostly investigate under ideal imaging conditions, with no or very little optical aberrations.

As part of this dissertation, we investigate the viability of such compressive sensing approaches for high resolution optical microscopy under more practical conditions. In particular, we analyze the sensitivity of compressive optical microscopy to misfcous effects, which are inevitable in imaging most specimens. We formulate the measurement equations for misfocus imaging condition. The numerical analysis indicates that compressive imaging is highly sensitive to misfcous effects at high magnifications factors, which are typical in microscopy. Finally, inspired by the result of sensitivity to basis mismatch of compressive sensing in [34], we present a mathematical description for the sensitivity to misfocus effect of compressive optical imaging. The model perturbation can be characterized by the perturbation matrix, as a function of both the demagnification factor and misfocus distance. A theoretical upper bound of the compressive sensing reconstruction error at given demagnification factor and misfocus distance is developed.

1.4.3 Widely Linear Complex Kalman Filters

Complex signals are ubiquitous in science and engineering, arising as they do as complex representations of two real channels or of two-dimensional fields. A random vector $\mathbf{x}$ is said to be improper, if $\mathbf{x}$ is correlated to its complex conjugate, i.e., the complementary covariance $E\mathbf{x}\mathbf{x}^T$ is nonzero. In communication [35], smart grid [36], optical imaging [37], and acoustic imaging [38], the impropriety of complex-valued signal/measurement arises, due to unbalanced channel gains, coupled dual channels, or improper noises. In these cases a good parameter estimator may depend on both the measurement and its complex conjugate, which is intuitively a widely linear transformation from measurement space to parameter space. Thus for improper complex-valued signals it becomes necessary to revisit the conventional statistical signal processing theory and incorporate the widely linear processing treatments [39–43].

In the past few decades the invention of Kalman filters (KFs) [44] has led to improved adaptive signal processing performance in various sensing systems whose state evolution and measurement acquisition can be characterized by dynamical linear model equations. As extensions of KFs, extended KFs [45] and Unscented KFs [46] have been invented to address signal processing in systems with nonlinear models.

We are motivated to make use of widely linear processing to develop novel complex KFs and their nonlinear versions for improper complex states. We show that for improper complex states, complementary covariance matrices may be used to create widely linear complex KFs (WLCKFs) and Unscented WLCKFs. We first derive the procedures of a WLCKF, and present the duality of a WLCKF and its dual channel real KF counterpart.

We then develop the Unscented WLCKFs to address the nonlinear dynamical models of improper complex states. A systematic construction of modified complex sigma points is studied whose sample mean and covariances can preserve the full first and second order statistical information of a improper random complex vector. Our analysis and numerical results show that, compared to the conventional complex KFs and Unscented complex KFs which ignore the complementary covariances, the WLCKFs and Unscented WLCKFs can significantly reduce the mean square error of state estimation.

1.5 Organization of the Dissertation

The remainder of this dissertation is organized as follows.

In Chapter 2, we present framework for designing Doppler resilient waveform via proper coordination of complementary waveforms across time. We show that the range sidelobe of the corresponding pulse train cross ambiguity function inside a modest Doppler around the zero-Doppler axis can be annihilated. This in turn enables us to extract weak targets that are situated near strong reflectors. However, this Doppler resilience comes at the expense of Doppler response. In Chapter 3, we characterize the tradeoff between the two for time-coordinated transmissions. We then extend the design in Chapter 2 to the coordination of complementary waveforms across both time and frequency. The added degree of freedom for transmission (frequency) allows us to improve Doppler response without reducing resilience to Doppler. In Chapter 4, we extend our work to the design of Doppler resilient complementary space-time waveforms. Construction of complementary illuminations (for instance, paraunitary waveform design) has received significant attention from the MIMO radar community. However, all designs suffer from sensitivity to Doppler. Our approach provides a way to maintain the complementarity even in the presence of Doppler. In Chapter 5, we investigate the viability of such compressive sensing approaches for high resolution optical microscopy under more practical conditions. In particular, we analyze the sensitivity of compressive optical microscopy to misfcous effects, which are inevitable in imaging most specimens. Our analysis indicates that compressive imaging is highly sensitive to misfcous effects at high magnifications factors, which are typical in microscopy. In Chapter 6, we exploit Kalman filters as a powerful signal processing approach for sensing systems with dynamical state update and measurement acquisitions. We illustrate that with improper complex valued states/measurements, how we revisit the derivation of conventional Kalman filters to account for the complementary covariances of random vectors. Finally we conclude the dissertation in Chapter 7.

CHAPTER 2

DOPPLER RESILIENT TRANSMIT-RECEIVE FILTERS FOR RADAR

Modern radars are increasingly being equipped with arbitrary waveform generators which enable generation of different wavefields across space, time, frequency, polarization, and wavenumber; see, e.g., [10]– [17]. However, as the number of degrees of freedom for transmission increases so does the complexity of the waveform design problem. This motivates the assembly of full waveforms from a library with simple component waveforms. By choosing to separate waveforms across space, time, frequency, polarization, wavenumber, or a combination of these, we can modularize the design problem [50–54].

An ideal transmitted waveform should produce an impulse-like ambiguity function in the range-Doppler plane. However the Moyal's identity [55] says that there is no way to construct such a waveform. Instead due to the sidelobes of ambiguity function a weak target of interest can be possibly masked by the interference resulting from nearby strong reflectors. Since different waveforms yield various distributions of the sidelobe of ambiguity function, an attractive approach is to design a waveform library such that candidates from the library can adaptively match with the real time radar scene. Each waveform candidate in the library is selected offline according to some criterions, such that the online waveform generation through optimization can be avoided. Recently some information theoretical criterions are proposed in [56–58]. For instance, in [58] the criterion is defined as the maximum of expected mutual information between target state and measurement over all waveforms in the library. Correspondingly good waveform libraries are developed, such as the library consisting of two linear frequency modulated (LFM) waveforms [59] and fractional Fourier transform based

LFM waveforms [60].

After creating a desired waveform library, the transmit waveform design requires a waveform scheduler to coordinate the transmission of waveform candidates on the fly. In principle such a waveform scheduler takes account into previous measurement as well as the dynamic model of targets and clutters [60,61]. However, it should be noted that, the size of waveform library has to be small, so that the computational burden on the scheduler is tolerable.

In this chapter, we consider a waveform library consisting of only two component waveforms. We show that by properly sequencing these component waveforms across time we can construct transmit pulse trains and receive filters for which the radar point-spread function, given by the cross-ambiguity function of the transmit pulse train and the pulse train used in the receive filter, is essentially free of range sidelobes inside an interval around the zero-Doppler axis. This enables us to extract a weak target that is located in range near a stronger reflector at a different Doppler frequency.

The component waveforms are Golay complementary and are obtained by phase coding a narrow pulse with a pair of Golay complementary sequences (see, e.g., [62]– [64]). Golay complementary sequences have the property that the sum of their autocorrelation functions vanishes at all nonzero lags. Consequently, if the waveforms phase coded by complementary sequences are transmitted separately in time and their ambiguity functions are added together the sum of the ambiguity functions will be essentially an impulse in range along the zero-Doppler axis. This makes Golay complementary waveforms ideal for separating point targets in range when the targets have the same Doppler frequency. However, off the zero-Doppler axis the impulse-like response in range is not maintained and the sum of the ambiguity functions has range sidelobes. In consequence, a weak target that is located in range near a strong reflector with a different Doppler frequency may be masked by the range sidelobes of the radar ambiguity function centered at the delay-Doppler position of the stronger reflector.

We show in this chapter that by properly designing the way Golay complementary waveforms are assembled across time in the transmit pulse train and the receive filter, we can essentially annihilate range sidelobes of the radar point-spread function and maintain an impulse-like point-spread function in range over a Doppler interval around the zero-Doppler axis. We construct the transmit pulse train by coordinating the transmission of Golay complementary waveforms according to zeros and ones in a binary sequence $\mathcal{P}$. We refer to this pulse train as the $\mathcal{P}$-pulse train. The pulse train used in the receive filter is constructed in a similar way, in terms of sequencing the Golay waveforms, but each waveform in the pulse train is weighted according to an element of a sequence $\mathcal{Q}$. We call this pulse train the $\mathcal{Q}$-pulse train. The cross-ambiguity function of the $\mathcal{P}$- and $\mathcal{Q}$-pulse trains gives the radar point-spread function, whose shape determines our ability to detect point targets in range and Doppler. We show that the size of the range sidelobes of this cross-ambiguity function is controlled by the spectrum of the product of $\mathcal{P}$ and $\mathcal{Q}$ sequences. By selecting sequences for which the spectrum of their product has a higher-order null around zero Doppler, we can annihilate the range sidelobe of the cross ambiguity function inside an interval around the zero-Doppler axis. However, the signal-to-noise ratio (SNR) at the receiver output, defined as the ratio of the peak of the squared cross-ambiguity function to the noise power at the receiver output, depends on the choice of $\mathcal{Q}$. By jointly designing the transmit-receive sequences $(\mathcal{P}, \mathcal{Q})$, we can achieve a trade-off between the order of the spectral null and the output SNR.

We first present two specific $(\mathcal{P}, \mathcal{Q})$ designs, namely the *PTM design* and the *Binomial design*, corresponding to the two ends of the trade-off. In the former, the transmit sequence $\mathcal{P}$ is the so-called Prouhet-Thue-Morse (PTM) sequence (see, e.g., [65]) of length N and the weighting sequence $\mathcal{Q}$ at the receiver is the all one sequence. In this case, the output SNR in white noise is maximum, as the receiver filter is in fact a matched filter. However, the order of the spectral null is only logarithmic in the length N of the transmit pulse train. In the latter design, $\mathcal{P}$ is the alternating binary sequence of length N and $\mathcal{Q}$ is the sequence of binomial coefficients in the binomial expansion $(1+x)^{N-1}$. In this case, the order of the spectral null is $N-2$, which is the largest that can be achieved with a pulse train of length N. However, this comes at the expense of SNR.

We then establish a necessary and sufficient condition for achieving an Mth-order spectral null with length-N, $N > M+1$, sequences $\mathcal{P}$ and $\mathcal{Q}$. The condition is that the product of the $\mathcal{P}$ and $\mathcal{Q}$ sequences must be in the null space of an $(M+1) \times N$ integer Vandermonde matrix, whose (m,n)th element is $(n+1)^m$ for $m = 0, 1, \ldots, M$ and $n = 0, 1, \ldots, N-1$. Without additional constraints, there are infinite number of solutions to the problem. In this chapter, we constrain $\mathcal{Q}$ to be a positive integer sequence, though other designs are certainly possible. Given a pulse train of length N and a desired null of order M, we can then maximize the output SNR to determine a solution for $\mathcal{P}$ and $\mathcal{Q}$.

The PTM design was originally proposed in our earlier papers [16, 17] for constructing Doppler resilient pulse trains of Golay complementary waveforms. This chapter extends our previous work to the *joint* design of transmit pulse trains and receive filters.

In this chapter we also derive the Cramér-Rao lower bound of Doppler estimation for a general $(\mathcal{P}, \mathcal{Q})$ pulse train design. We show that the Cramér-Rao lower bound is controlled by the bandwidth of power spectrum of sequence $\mathcal{Q}$. For an arbitrary $(\mathcal{P}, \mathcal{Q})$ pulse train design, we analyze the peak-to-sidelobe ratio of its cross ambiguity function. A simulation also compares the peak-to-sidelobe ratio of cross ambiguity function for different $(\mathcal{P}, \mathcal{Q})$ designs.

We propose an systematic extension of the above $(\mathcal{P}, \mathcal{Q})$ pulse train constructions to waveform libraries with more than two complementary waveforms. From a binary sequences $\mathcal{P}_1$ coordinating the transmission of sequences in a Golay pair, and a sequence $\mathcal{Q}_1$ constructing the receive filter such that $(\mathcal{P}_1, \mathcal{Q}_1)$ can achieve up to M-th order null of range sidelobes around zero Doppler, by recursive construction we can obtain a 2^m-ary sequence $\mathcal{P}_m$ coordinating the transmission of 2^m complementary sequences, as well as a sequence $\mathcal{Q}_m$ constructing the receive filter as $\mathcal{Q}_1$ does. The design $(\mathcal{P}_m, \mathcal{Q}_m)$ maintain the property in achieving up to M-th order null of range sidelobes around zero Doppler.

2.1 $(\mathcal{P}, \mathcal{Q})$ Pulse Trains

Definition 2.1.1. (Golay Complementary Sequences [62]) Two length L unimodular sequences of complex numbers $x[\ell]$ and $y[\ell]$ are Golay complementary if for $k = -(L-1), \ldots, (L-1)$ the sum of their autocorrelation functions satisfies

$$C_x[k] + C_y[k] = 2L\delta[k], \tag{2.1}$$

where $C_x[k]$ and $C_y[k]$ are the autocorrelations of $x[\ell]$ and $y[\ell]$ at lag k respectively, and $\delta[k]$ is the Kronecker delta function. Henceforth we may drop the discrete time index ℓ from $x[\ell]$ and $y[\ell]$ and simply use x and y. Each member of the pair (x, y) is called a Golay sequence.

Consider a pair of baseband waveforms $x(t)$ and $y(t)$ that are phase coded by length-L complementary sequences x and y: that is,

$$x(t) = \sum_{\ell=0}^{L-1} x[\ell]\Omega(t - \ell T_c) \;\text{ and }\; y(t) = \sum_{\ell=0}^{L-1} y[\ell]\Omega(t - \ell T_c), \tag{2.2}$$

where $\Omega(t)$ is baseband pulse shape with duration limited to a chip interval T_c and unit energy:

$$\int_{-T_c/2}^{T_c/2} |\Omega(t)|^2 dt = 1. \tag{2.3}$$

The ambiguity function $\chi_x(\tau, \nu)$ of $x(t)$ at delay-Doppler coordinates (τ, ν) is given by

$$\begin{aligned}
\chi_x(\tau,\nu) &= \int\limits_{-\infty}^{\infty} x(t)\overline{x(t-\tau)}e^{-j\nu t}dt \\
&= \sum_{\ell=0}^{L-1} \sum_{k=-(L-1)}^{L-1} x[\ell]\overline{x([-k]} \int_{-\infty}^{\infty} \Omega(t-\ell T_c)\overline{\Omega(t-(\ell-k)T_c-\tau)}e^{-j\nu t}dt \\
&= \sum_{\ell=0}^{L-1} \sum_{k=-(L-1)}^{L-1} x[\ell]\overline{x[l-k]}e^{-j\nu\ell T_c}\chi_\Omega(\tau - kT_c, \nu) \\
&= \sum_{k=-(L-1)}^{L-1} A(k, \nu T_c)\chi_\Omega(\tau - kT_c, \nu),
\end{aligned} \tag{2.4}$$

where $\bar{\cdot}$ denotes the complex conjugate, and $A(k, \nu T_c)$ is given by

$$A(k, \nu T_c) = \sum_{\ell=0}^{L-1} x[\ell]\overline{x[l-k]}e^{-j\nu\ell T_c},\ k = -(L-1), ..., L-1, \tag{2.5}$$

and $\chi_\Omega(\tau, \nu)$ is the ambiguity function of the pulse shape $\Omega(t)$:

$$\chi_\Omega(\tau, \nu) = \int_{-T_c}^{T_c} \Omega(t)\Omega^*(t-\tau)e^{-j\nu t}dt. \tag{2.6}$$

If the complementary waveforms $x(t)$ and $y(t)$ are transmitted in time separation with a T sec time interval between the two transmissions, then the effective ambiguity function of the radar waveform $z(t) = x(t) + y(t-T)$ is [1]

$$\chi_z(\tau, \nu) = \chi_x(\tau, \nu) + e^{-j\nu T}\chi_y(\tau, \nu). \tag{2.7}$$

The duration LT_c of waveforms is typically much shorter than the PRI duration T. Thus the Doppler shift over LT_c is negligible compared to the Doppler shift over the PRI duration T, and by Eq. (2.4) and (2.7) the ambiguity function $\chi_z(\tau, \nu)$ can be approximated by

$$\chi_z(\tau, \nu) = \sum_{k=-(L-1)}^{L-1} [C_x[k] + e^{-j\nu T}C_y[k]]\chi_\Omega(\tau - kT_c, \nu). \tag{2.8}$$

Along the zero-Doppler axis ($\nu = 0$), the ambiguity function $\chi_z(\tau, \nu)$ reduces to

$$\chi_z(\tau, 0) = 2L\chi_\Omega(\tau, 0), \tag{2.9}$$

due to complementarity of the Golay sequences x and y. We notice that the ambiguity function $\chi_z(\tau, \nu)$ is "free" of range sidelobes along the zero-Doppler axis. [2] However, off the zero-Doppler axis the ambiguity function has large sidelobes in delay (range). The range sidelobe at non-zero Doppler may result the scenario that a weak moving target can be masked by the range sidelobes induced by a strong reflector which is close to the target in distance and velocity.

[1] The ambiguity function of $z(t)$ has two range aliases (cross terms) which are offset from the zero-delay axis by $\pm T$. In this chapter, we drop the range aliasing effects and refer to $\chi_z(\tau, \nu)$ as the ambiguity function of $z(t)$. Range aliasing effects can be accounted for using standard techniques devised for this purpose (e.g. see [66]) and hence will not be further discussed.

[2] The shape of the autocorrelation function depends on the autocorrelation function $\chi_\Omega(\tau, 0)$ for the pulse shape $\Omega(t)$. The Golay complementary property eliminates range sidelobes caused by replicas of $\chi_\Omega(\tau, 0)$ at nonzero integer delays.

Remark 2.1.1. The complementary property of Golay pair enables us to transmit the waveform phase coded by each sequence of one Golay pair separately in time domain, such that sum of autocorrelation functions of each waveform is free of range sidelobes. Separating Golay complementary waveforms in frequency, however, has more difficulty in theory. This is because the presence of delay-dependent phase terms impairs the complementary property of the waveforms. Recently Searle and Howard [18–20] have introduced the modified Golay pairs for OFDM channel models. The modified Golay pairs are complementary in the sense that sum of squared autocorrelation functions forms an impulse in range.

In the following we show that by properly coordinating the transmission of waveforms from the library and weighting the waveforms in the receive pulse train, we can suppress the Doppler induced range sidelobes at modest Doppler shift:

Remark 2.1.2. Throughout the dissertation, for convenience we use two representations for the length-N sequence $\{p[n]\}_{n=0}^{N-1}$ and $\{q[n]\}_{n=0}^{N-1}$. The script letters $\mathcal{P}$ and $\mathcal{Q}$ are the sequence representation of $\{p[n]\}_{n=0}^{N-1}$ and $\{q[n]\}_{n=0}^{N-1}$, whereas the bold letters $\mathbf{p}$ and $\mathbf{q}$ stands for the N-dimensional vectors generated by $\{p[n]\}_{n=0}^{N-1}$ and $\{q[n]\}_{n=0}^{N-1}$ respectively, such that $\mathbf{p} = [p[0], \ldots, p[N-1]]^T$, and $\mathbf{q} = [q[0], \ldots, q[N-1]]^T$.

Definition 2.1.2. Let $\mathcal{P} = \{p[n]\}_{n=0}^{N-1}$ be a discrete binary sequence of length N. Define the $\mathcal{P}$*-pulse train* $z_{\mathcal{P}}(t)$ as

$$z_{\mathcal{P}}(t) = \sum_{n=0}^{N-1} p[n]x(t-nT) + \overline{p}[n]y(t-nT), \tag{2.10}$$

where $\overline{p}[n] = 1 - p[n]$ is the complement of $p[n]$. The nth entry in $z_{\mathcal{P}}(t)$ is $x(t)$ if $p[n] = 1$ and is $y(t)$ if $p[n] = 0$. Consecutive entries are separated in time by a PRI T.

Definition 2.1.3. Let $\mathcal{Q} = \{q[n]\}_{n=0}^{N-1}$ be a discrete real sequence of length N, with positive entries $q[n] > 0$. Define the $\mathcal{Q}$*-pulse train* $z_{\mathcal{Q}}(t)$ as

$$z_{\mathcal{Q}}(t) = \sum_{n=0}^{N-1} q[n]\left[p[n]x(t-nT) + \overline{p}[n]y(t-nT)\right] \tag{2.11}$$

The nth element of $z_{\mathcal{Q}}(t)$ is obtained by multiplying the nth element of $z_{\mathcal{P}}(t)$ by $q[n]$.

If $z_{\mathcal{P}}(t)$ is transmitted by the radar and the return is filtered (correlated) with $z_{\mathcal{Q}}(t)$, then the receiver point-spread function in delay and Doppler will be the cross-ambiguity function between $z_{\mathcal{P}}(t)$ and $z_{\mathcal{Q}}(t)$:

$$\begin{aligned}\chi_{\mathcal{P},\mathcal{Q}}(\tau,\nu) &= \int_{-\infty}^{\infty} z_{\mathcal{P}}(t)\overline{z_{\mathcal{Q}}(t-\tau)}e^{-j\nu t}dt \\ &= \sum_{n=0}^{N-1} q[n]e^{-j\nu nT}\big[p[n]\chi_x(\tau,\nu) + \overline{p}[n]\chi_y(\tau,\nu)\big],\end{aligned} \tag{2.12}$$

where similar to (2.7), we have ignored the range aliases at offset $\pm nT$, $n = 1, 2, ..., N-1$.

Remark 2.1.3. When $q[n] = 1$ for $n = 0, ..., N-1$ the receiver is a matched filter that matches to the transmitted pulse train $z_{\mathcal{P}}(t)$ and (2.12) reduces to the ambiguity function of $z_{\mathcal{P}}(t)$. The joint design of $\mathcal{P}$ and $\mathcal{Q}$ however gives us more flexibility in tailoring the shape of the radar cross ambiguity function, as we will show in this chapter. We constrain $q[n]$ to be positive such that the peak value of the cross ambiguity function at $(0,0)$ is not reduced compared to a conventional transmission scheme.

Similar to (2.8), since the duration of a Golay waveform is much shorter than the PRI duration T, the cross ambiguity function $\chi_{\mathcal{P},\mathcal{Q}}(\tau,\nu)$ can be approximated as

$$\begin{aligned}\chi_{\mathcal{P},\mathcal{Q}}(\tau,\nu) &= \sum_{n=0}^{N-1} q[n]e^{-j\nu nT} \sum_{k=-(L-1)}^{L-1} \big[p[n]C_x[k] + \overline{p}[n]C_y[k]\big]\chi_\Omega(\tau - kT_c,\nu) \\ &= L\sum_{n=0}^{N-1} q[n]e^{-j\nu nT}\chi_\Omega(\tau,\nu) - \frac{1}{2}\sum_{n=0}^{N-1} q[n]e^{-j\nu nT}(-1)^{p[n]}\chi'_\Omega(\tau,\nu),\end{aligned} \tag{2.13}$$

where

$$\chi'_\Omega(\tau,\nu) = (C_x(k_1) - C_y(k_1))\chi_\Omega(\tau - k_1T_c,\nu) + (C_x(k_2) - C_y(k_2))\chi_\Omega(\tau - k_2T_c,\nu), \tag{2.14}$$

and integers k_1 and k_2 are defined as $k_1 = \lfloor -\frac{\tau}{T_c} \rfloor$, and $k_2 = k_1 + 1$. Along the zero Doppler axis, the ambiguity function $\chi_{\mathcal{P},\mathcal{Q}}(\tau,\nu)$ contains one copy of $\chi_\Omega(\tau,\nu)$ centered at $\tau = 0$, but no replicas as long as sequences $\mathcal{P}$ and $\mathcal{Q}$ are chosen to satisfy $\sum_{n=0}^{N-1} q[n](-1)^{p[n]} = 0$, under which $\chi_{\mathcal{P},\mathcal{Q}}(\tau,\nu)$ is range sidelobe "free" at $\nu = 0$.

After discretizing in delay (at chip intervals), and ignoring the Doppler shift over chip intervals compared to the Doppler shift across a PRI, this cross-ambiguity function is given by

$$\chi_{\mathcal{P},\mathcal{Q}}(k,\theta) = \frac{1}{2}\left[C_x[k] + C_y[k]\right]\sum_{n=0}^{N-1} q[n]e^{jn\theta} - \frac{1}{2}\left[C_x[k] - C_y[k]\right]\sum_{n=0}^{N-1}(-1)^{p[n]}q[n]e^{jn\theta} \quad (2.15)$$

where θ is the relative Doppler shift over a PRI T. Since $x(k)$ and $y(k)$ are Golay complementary, $C_x[k] + C_y[k] = 2L\delta[k]$ and the first term on the right-hand-side of (3.33) is free of range sidelobes. The second term represents the range sidelobes, as $C_x[k] - C_y[k]$ does not vanish at all $k \neq 0$. Therefore the question is: can sequences $\mathcal{P}$ and $\mathcal{Q}$ be designed such that the discretized ambiguity function (3.33) acts as a Kronecker delta in delay, at least for some modest range of Doppler frequencies.

Controlling range sidelobes. The magnitude of the range sidelobe is proportional to the magnitude of the spectrum of the sequence $(-1)^{p[n]}q[n]$, which is given by

$$S_{\mathcal{P},\mathcal{Q}}(\theta) = \sum_{n=0}^{N-1}(-1)^{p[n]}q[n]e^{jn\theta}. \quad (2.16)$$

As a result, range sidelobes inside a Doppler interval around the zero-Doppler axis can be suppressed by selecting a sequence $(-1)^{p[n]}q[n]$ whose spectrum has a higher-order null at zero Doppler.

Consider the Taylor expansion of $S_{\mathcal{P},\mathcal{Q}}(\theta)$ around $\theta = 0$, that is,

$$S_{\mathcal{P},\mathcal{Q}}(\theta) = \sum_{m=0}^{\infty} S^{(m)}_{\mathcal{P},\mathcal{Q}}(0)\frac{\theta^m}{m!}, \quad (2.17)$$

where $S^{(m)}_{\mathcal{P},\mathcal{Q}}(0)$ is the m-th order derivative of $S_{\mathcal{P},\mathcal{Q}}(\theta)$ at $\theta = 0$. To create an Mth order null, all $S^{(m)}_{\mathcal{P},\mathcal{Q}}(0)$ up to order M must vanish: that is,

$$S^{(m)}_{\mathcal{P},\mathcal{Q}}(0) = 0,\ m = 0, 1, ..., M, \quad (2.18)$$

or equivalently,

$$\sum_{n=0}^{N-1} n^m(-1)^{p[n]}q[n] = 0,\ m = 0, 1, ..., M. \quad (2.19)$$

Controlling Signal-to-Noise Ratio. Suppose the noise at the receiver input is white and has power N_0. Then, the noise power at the receiver output is

$$\eta = N_0 \int_{-\infty}^{\infty} |z_{\mathcal{Q}}(t)|^2 dt = N_0 L \|\mathbf{q}\|_2^2, \tag{2.20}$$

where $\mathbf{q} = [q[0], ..., q[N-1]]^T$. The SNR at the receiver output is given by

$$\rho = \frac{\sigma_b^2 |\chi_{\mathcal{P},\mathcal{Q}}(0,0)|^2}{\eta} = \frac{L\sigma_b^2}{N_0} \frac{\|\mathbf{q}\|_1^2}{\|\mathbf{q}\|_2^2}, \tag{2.21}$$

where σ_b^2 is the variance of the scattering coefficient of the target.

The SNR ρ is maximized when $\mathbf{q} = \alpha \mathbf{1}$ for some positive scalar α, meaning that $z_{\mathcal{Q}}(t) = \alpha z_{\mathcal{P}}(t)$ which corresponds to the usual matched filter. Any sequence $\mathcal{Q}$ other than the all one sequence results in a reduction in SNR. However, the extra degrees of freedom provided by a more general $\mathcal{Q}$ can be used to create a spectral null of higher order, through the joint design of $\mathcal{P}$ and $\mathcal{Q}$, than what is achievable by only designing $\mathcal{P}$.

Design Trade-off. The joint design of $\mathcal{P}$ and $\mathcal{Q}$ sequences enables a trade-off between the order of the spectral null for range sidelobe suppression around zero Doppler and the SNR at the receiver output. In the next section, we first present two examples of $(\mathcal{P}, \mathcal{Q})$ designs, namely the *PTM design* (see also [16, 17]) for which the order of the spectral null is logarithmic in the pulse train length N, and the *Binomial design* for which the order of the null is linear in N. The latter design maintains an impulse-like point-spread function in range over a wider Doppler interval around the zero-Doppler axis. But this added invariance comes at the expense of SNR. Later, we derive necessary and sufficient conditions for achieving an Mth order spectral null with a pulse train of length N and further investigate the trade-off.

2.2 Range Sidelobe Suppression

2.2.1 PTM vs. Binomial Design

Theorem 2.2.1. *(PTM Design [16]) Let $\mathcal{P} = \{p[n]\}_{n=0}^{N-1}$ be the length $N = 2^{M+1}$ Prouhet-Thue-Morse (PTM) sequence (see, e.g., [65]), defined recursively as $p[2k] = p[k]$ and $p[2k+$*

$1] = 1 - p[k]$ for all $k \geq 0$, with $p_0 = 0$, and let $\mathcal{Q} = \{q[n]\}_{n=0}^{N-1}$ be the all 1 sequence of length $N = 2^{M+1}$. Then, $S_{\mathcal{P},\mathcal{Q}}(\theta)$ has an Mth-order null at $\theta = 0$.

Example 2.2.1. The PTM sequence of length $N = 8$ is $\mathcal{P} = \{p[k]\}_{k=0}^{7} = 0\ 1\ 1\ 0\ 1\ 0\ 0\ 1$. The corresponding $\mathcal{P}$-pulse train of Golay complementary waveforms is given by

$$\begin{aligned} z_{\mathcal{P}}(t) &= x(t) + y(t-T) + y(t-2T) + x(t-3T) + y(t-4T) + x(t-5T) \\ &\quad + x(t-6T) + y(t-7T). \end{aligned}$$

The receive filter pulse train $z_{\mathcal{Q}}(t)$ is the same as the $\mathcal{P}$-pulse train. The order of the spectral null for range sidelobe suppression is $M = (\log_2 N) - 1 = 2$.

Remark 2.2.1. The PTM design was originally introduced in [16], [17] in the context of designing Doppler resilient waveforms. In this chapter, we further investigate this design by contrasting it against the Binomial design (to be explained next) in terms of range sidelobe suppression and SNR.

Theorem 2.2.2. *(Binomial Design.) Let $\mathcal{P} = \{p[n]\}_{n=0}^{N-1}$ be the length $N = M+2$ alternating sequence, where $p[2k] = 1$ and $p[2k+1] = 0$ for all $k \geq 0$, and let $\mathcal{Q} = \{q[n]\}_{n=0}^{N-1}$ be the length $N = M + 2$ binomial sequence $\{q[n]\}_{n=0}^{N-1} = \{\binom{N-1}{n}\}_{n=0}^{N-1}$. Then, $S_{\mathcal{P},\mathcal{Q}}(\theta)$ has an Mth order null at $\theta = 0$.*

Proof: the spectrum $S_{\mathcal{P},\mathcal{Q}}(\theta)$ for the alternating sequence $\mathcal{P}$ and binomial sequence $\mathcal{Q}$ is

$$\begin{aligned} S_{\mathcal{P},\mathcal{Q}}(\theta) &= \sum_{n=0}^{N-1} (-1)^n \binom{N-1}{n} e^{jn\theta} \\ &= (1 - e^{j\theta})^{N-1}. \end{aligned} \tag{2.22}$$

A direct evaluations of $S^{(m)}_{\mathcal{P},\mathcal{Q}}(0)$, the m-th order derivative of $S_{\mathcal{P},\mathcal{Q}}(\theta)$ at $\theta = 0$ can show that $S^{(m)}_{\mathcal{P},\mathcal{Q}}(0) = 0$ for $m = 0, 1, ..., N-2$. Interestingly, an alternative proof is as follows. By Eq.

(2.19), the m-th order derivative of $S_{\mathcal{P},\mathcal{Q}}(\theta)$ at $\theta = 0$ is

$$\begin{aligned} S^{(m)}_{\mathcal{P},\mathcal{Q}}(0) &= \sum_{n=0}^{N-1} n^m (-1)^{p[n]} q[n] \\ &= \sum_{n=0}^{N-1} n^m (-1)^n \binom{N-1}{n}. \end{aligned} \tag{2.23}$$

From the theory of finite differences, for any polynomial $P(x)$ of x with degree less than $N-1$, the following equation holds:

$$\sum_{n=0}^{N-1} (-1)^n \binom{N-1}{n} P(n) = 0. \tag{2.24}$$

Therefore $S^{(m)}_{\mathcal{P},\mathcal{Q}}(0)$ is zero for $m = 0, ..., N-2$.

Example 2.2.2. For $N = 8$, the $\mathcal{P}$-pulse train transmitted by the radar is

$$\begin{aligned} z_{\mathcal{P}}(t) &= x(t) + y(t-T) + x(t-2T) + y(t-3T) + x(t-4T) + y(t-5T) \\ &\quad + x(t-6T) + y(t-7T), \end{aligned}$$

and the $\mathcal{Q}$-pulse train (binomial) used for filtering is

$$\begin{aligned} z_{\mathcal{Q}}(t) &= q_0 x(t) + q_1 y(t-T) + q_2 x(t-2T) + q_3 y(t-3T) + q_4 x(t-4T) + q_5 y(t-5T) \\ &\quad + q_6 x(t-6T) + q_7 y(t-7T), \end{aligned}$$

where $q[n] = \binom{7}{n}$, $n = 0, 1, ..., 7$. The order of the spectral null for sidelobe suppression is $M = N - 2 = 6$.

2.2.2 General $(\mathcal{P}, \mathcal{Q})$ Pulse Train Design

We now give the general condition for achieving an Mth-order spectral null with $\mathcal{P}$ and $\mathcal{Q}$ sequences of length $N > M + 1$.

Theorem 2.2.3. *The spectrum $S_{\mathcal{P},\mathcal{Q}}(\theta)$ has an M-th order null, $M < N-1$, at $\theta = 0$ if and only if*

$$\begin{bmatrix} 1 & 1 & \cdots & 1 \\ 1 & 2 & \cdots & N \\ \vdots & \vdots & \ddots & \vdots \\ 1^M & 2^M & \cdots & N^M \end{bmatrix} \begin{bmatrix} (-1)^{p[0]} q[0] \\ (-1)^{p[1]} q[1] \\ \vdots \\ (-1)^{p[N-1]} q[N-1] \end{bmatrix} = \mathbf{0}. \tag{2.25}$$

Proof: The spectrum $S_{\mathcal{P},\mathcal{Q}}(\theta)$ has an M-th order of null at $\theta = 0$ if and only if $e^{j\theta}S_{\mathcal{P},\mathcal{Q}}(\theta)$ has an M-th order of null at $\theta = 0$. Thus the condition (2.19) is equivalent to

$$\sum_{n=0}^{N-1}(n+1)^m(-1)^{p[n]}q[n] = 0, \ m = 0, 1, ..., M, \tag{2.26}$$

which can be written in matrix form as Eq. (2.25).

Remark 2.2.2. To avoid trivial solutions, M has to be less than $N-1$. For a given pulse train length N, the Binomial design achieves the maximum order $M = N-2$ of spectral null.

Remark 2.2.3. Let $T(M')$ denote the set of product sequences $\{(-1)^{p[n]}q[n]\}_0^{N-1}$ that satisfy the null space condition (2.25) for $M = M'$. Then, clearly, we have $T(0) \supseteq T(1) \supseteq \cdots \supseteq T(N-2)$.

In the following we take a close look at the structure of feasible product sequences $\{(-1)^{p[n]}q[n]\}_0^{N-1}$ indicated as Eq. (2.25). Let $\mathbf{t}_1 = [(-1)^{p[0]}q[0], \ldots, (-1)^{p[M]}q[M]]^T$, and $\mathbf{t}_2 = [(-1)^{p[M+1]}q[M+1], \ldots, (-1)^{p[N-1]}q[N-1]]^T$. Then we have

$$\begin{bmatrix} \mathbf{V}_M & \mathbf{B} \end{bmatrix} \begin{bmatrix} \mathbf{t}_1 \\ \mathbf{t}_2 \end{bmatrix} = \mathbf{0}, \tag{2.27}$$

where

$$\mathbf{V}_M = \begin{bmatrix} 1 & 1 & \cdots & 1 \\ 1 & 2 & \cdots & M+1 \\ \vdots & \vdots & \ddots & \vdots \\ 1^M & 2^M & \cdots & (M+1)^M \end{bmatrix} \quad \text{and} \quad \mathbf{B} = \begin{bmatrix} 1 & 1 & \cdots & 1 \\ M+2 & M+3 & \cdots & N \\ \vdots & \vdots & \ddots & \vdots \\ (M+2)^M & (M+3)^M & \cdots & N^M \end{bmatrix}.$$

Note $\mathbf{t}_1 = -\mathbf{V}_M^{-1}\mathbf{B}\mathbf{t}_2$, and thus the solution $\mathbf{t}$ of Eq. (2.25) is

$$\mathbf{t} = \begin{bmatrix} \mathbf{t}_1 \\ \mathbf{t}_2 \end{bmatrix} = \begin{bmatrix} -\mathbf{V}_M^{-1}\mathbf{B} \\ \mathbf{I} \end{bmatrix} \mathbf{t}_2. \tag{2.28}$$

Therefore any solution to (2.25) is only governed by the vector $\mathbf{t}_2$ with dimension $N-M-1$.

The matrix $\mathbf{V}_M$ is a transposed $M+1$ by $M+1$ Vandermonde matrix consisting of integer entries. The element of $\mathbf{V}_M^{-1}$ can be written by [67,68]

$$(\mathbf{V}_M^{-1})_{i,j} = \sum_{l \geq i,j}^{M} \frac{(-1)^{i+j}}{l!} \begin{bmatrix} l+1 \\ j+1 \end{bmatrix} \binom{l}{i},\ 0 \leq i,j \leq M, \tag{2.29}$$

where $\begin{bmatrix} n \\ k \end{bmatrix}$ is the unsigned Stirling number of the first type [69,70], meaning the number of permutations of n elements with k disjoint cycles. By the Lagrange's polynomial interpolation formula, for each j the entries $(\mathbf{V}_M^{-1})_{j,k}$ are coefficients of following polynomial $P_j(x)$:

$$P_j(x) = \prod_{\substack{n \geq 0 \\ n \neq j}}^{M} \frac{x - x_n}{x_j - x_n} = \sum_{k=0}^{M} (\mathbf{V}_M^{-1})_{j,k} x^k,\ j = 0, ..., M, \tag{2.30}$$

where $x_n = n+1$ for $0 \leq n \leq M$. Thus it is easy to see that

$$\mathbf{V}_M^{-1}\mathbf{B} = \begin{bmatrix} P_0(M+2) & P_0(M+3) & \cdots & P_0(N) \\ P_1(M+2) & P_1(M+3) & \cdots & P_1(N) \\ \vdots & \vdots & \ddots & \vdots \\ P_M(M+2) & P_M(M+3) & \cdots & P_M(N) \end{bmatrix}. \tag{2.31}$$

The entry $P_j(M+2)$ is given by

$$\begin{aligned} P_j(M+2) &= \prod_{\substack{n \geq 0 \\ n \neq j}}^{M} \frac{M-n+1}{j-n} \\ &= \frac{(M+1)!/(M-j+1)}{j!(-1)^{M-j}(M-j)!} \\ &= (-1)^{M-j}\binom{M+1}{j},\ j = 0, ..., M. \end{aligned} \tag{2.32}$$

Thus when $M = N-2$, any solution $\mathbf{t}$ to Eq. (2.25) should be of the form $\mathbf{t} = c\big[r_0, r_1, ..., r_{N-2}, r_{N-1}\big]^T$, where $c \in \mathbb{R}$ and $r_i = (-1)^i\binom{N-1}{i}$. This means that given a fixed length of pulse train N, the Binomial design is the only choice of $(\mathcal{P}, \mathcal{Q})$ pulse train design to achieve the highest order null of range sidelobe. In general, for $k = 0, ..., N-M-2$, the entries in the k-th column of matrix $\mathbf{V}_M^{-1}\mathbf{B}$ can be computed as

$$\begin{aligned} P_j(M+k+2) &= \frac{M-j}{M-j+k}\binom{M+k}{M}P_j(M+2) \\ &= \frac{M-j}{M-j+k}(-1)^{M-j-1}\binom{M+k}{M}\binom{M}{j}, \; j=0,...,M. \end{aligned} \tag{2.33}$$

Therefore by eq. (2.28) the solution $\mathbf{t} = [t_0, t_1, ..., t_{N-1}]^T$ to Eq. (2.25) is an integer vector if $\mathbf{t}_2$ is an integer vector. Recall that $t_n = (-1)^{p[n]}q[n], n = 0, 1, ..., N-1$. Thus given an integer solution vector $\mathbf{t}$, the corresponding binary sequence $\mathcal{P}$ and positive integer sequence $\mathcal{Q}$ can recovered by vector $\mathbf{t}$:

$$p[n] = \frac{1}{2}[1 - \mathrm{sign}(t_n)], q[n] = |t_n|, \; n = 0, ..., N-1. \tag{2.34}$$

Fig. 2.1 illustrates the annihilation of range-sidelobes around the zero-Doppler axis for three different length-16 $(\mathcal{P}, \mathcal{Q})$ designs and compares their delay-Doppler responses with that of a conventional design. For the ease of observing area of cleared area, in Fig. 2.2 we present the magnified versions of plots in Fig. 2.1, whose horizontal axis covers the Doppler band $[-0.4, 0.4]$ rad. The conventional design uses an alternating transmission of Golay complementary waveforms followed by matched filtering at the receiver. The scene contains three strong reflectors of equal amplitudes at different ranges and two weak targets (each 30dB weaker) that have small Doppler frequencies relative to the stronger reflectors. Each waveform component is generated by phase coding a length-64 Golay sequence. A raised cosine is selected as the pulse shape. The chip interval is $T_c = 100$ $n$sec, and the length of PRI is $T = 50$ μsec. The horizontal axis depicts Doppler and the vertical axis illustrates delay. Color bar values are in dB.

In the conventional design, shown in Fig. 2.1(a) and Fig. 2.2(a), the weak targets are almost completely masked by the range sidelobes of the stronger reflectors. With the PTM design, shown in Fig. 2.1(b) and Fig. 2.2(b), we can clear out the range sidelobes inside a narrow Doppler interval around the zero-Doppler axis. The order of the spectral null for range sidelobe suppression in this case is $M = \log_2 16 - 1 = 3$. With this order, we can bring the range sidelobes below -80dB inside the $[-0.1, -0.1]$ rad Doppler interval and

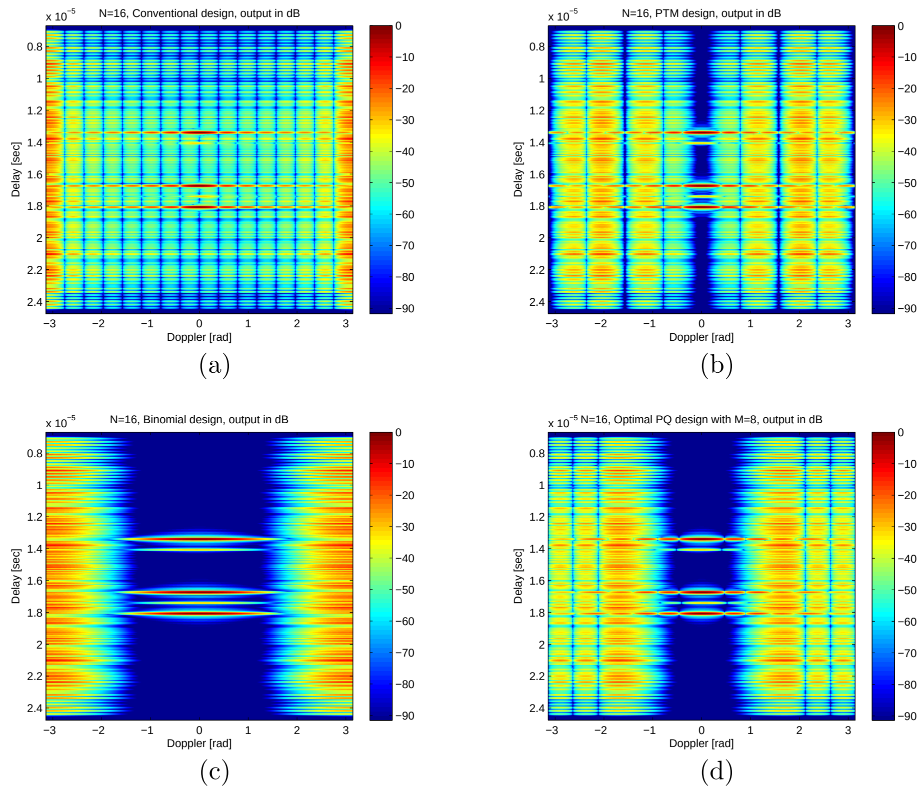

Figure 2.1: Comparison of output delay-Doppler maps for different $(\mathcal{P}, \mathcal{Q})$ designs: (a) conventional design, (b) PTM design, (c) Binomial design, and (d) max-SNR design with an 8-th order null. The scene contains three strong (equal amplitude) stationary reflectors at different ranges and two weak slow moving targets (30dB weaker).

extract the weak targets. If the difference in the Doppler frequencies of the weak and strong reflectors is larger, we need a null of higher order to annihilate the range sidelobes inside a wider Doppler band. Fig. 2.1(c) and Fig. 2.2(c) show that the Binomial design (of length $N = 16$) can expand the cleared (below -80dB) region to $[-1, -1]$ rad by creating a null of order $M = 16 - 2 = 14$ around zero Doppler. Fig. 2.1(d) and Fig. 2.2(d) shows the delay-Doppler response of a $(\mathcal{P}, \mathcal{Q})$ design that has the largest SNR among all $(\mathcal{P}, \mathcal{Q})$ designs that achieve an $(M = 8)$th order spectral null. The cleared region in this case is the $[-0.5, 0.5]$ rad Doppler interval. In summary, the three different $(\mathcal{P}, \mathcal{Q})$ designs simply redistribute the volume under the ambiguity surface in different ways to push the range sidelobes outside a Doppler interval of interest to prevent spillage of energy from a clutter mass to nearby cells.

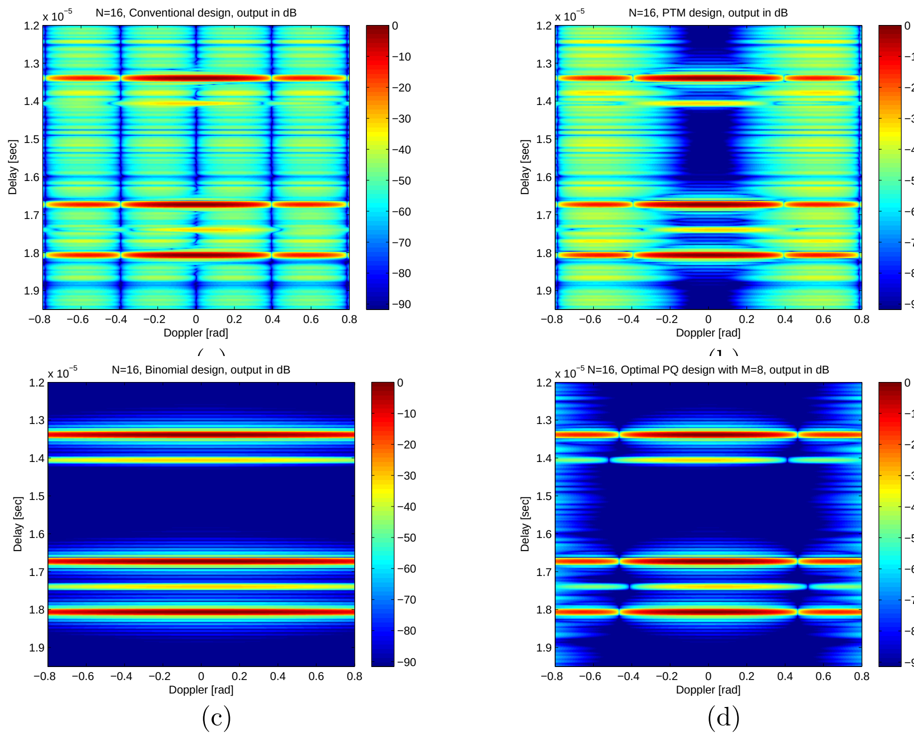

Figure 2.2: Magnified output delay-Doppler maps for different $(\mathcal{P}, \mathcal{Q})$ designs as shown in Fig. 2.1: (a) conventional design, (b) PTM design, (c) Binomial design, and (d) max-SNR design with an 8-th order null. The horizontal axis covers the ([-0.4 0.4] rad) Doppler band for easier comparison of the width of cleared area.

2.3 Performance Analysis

In last section we have shown that for a fixed pulse train length N, as the order of null M in of the spectra $S_{\mathcal{P},\mathcal{Q}}(\theta)$ increase, the range sidelobes is annihilated in a wider Doppler interval. However, it is also seen that when M increases, the cross ambiguity function along zero delay $\chi_{\mathcal{P},\mathcal{Q}}(0,\theta)$, which is proportional to the spectrum $M_{\mathcal{Q}}(\theta)$ of $\mathcal{Q}$ sequence, may become fatter in Doppler domain. In this section we will show that for a $(\mathcal{P}, \mathcal{Q})$ pulse train design, the SNR and Cramér-Rao lower bound of Doppler estimation is related to the bandwidth of power spectrum $\mathcal{M}_{\mathcal{Q}}(\theta) = |M_{\mathcal{Q}}(\theta)|^2$. The dependency of both $S_{\mathcal{P},\mathcal{Q}}(\theta)$ and $M_{\mathcal{Q}}(\theta)$ on the $\mathcal{Q}$ sequence suggests a tradeoff between performance criterions.

2.3.1 Peak-to-Peak-Sidelobe Ratio

For a general $(\mathcal{P}, \mathcal{Q})$ pulse train, define the peak-to-peak-sidelobe ratio (PPSR) of its cross ambiguity function $\chi_{\mathcal{P},\mathcal{Q}}$ at a Doppler frequency ν

$$PPSR_{\mathcal{P},\mathcal{Q}}(\nu) = \frac{|\chi_{\mathcal{P},\mathcal{Q}}(0,0)|^2}{\max_{\tau \in \mathcal{S}_d} |\chi_{\mathcal{P},\mathcal{Q}}(\tau,\nu)|^2} \tag{2.35}$$

as the ratio between the peak intensity of $\chi_{\mathcal{P},\mathcal{Q}}(\tau,\nu)$ and the peak intensity of range sidelobe of $\chi_{\mathcal{P},\mathcal{Q}}(\tau,\nu)$ along Doppler ν. It characterizes the $(\mathcal{P}, \mathcal{Q})$ pulse train's ability to suppress range sidelobes at a desired Doppler shift. The set $\mathcal{S}_d$ contains delays where the range sidelobes are located. Thus from Eq. (3.33), the discretized PPSR can be written by

$$\begin{aligned} PPSR_{\mathcal{P},\mathcal{Q}}(\theta) &= \frac{\left|2L \sum_{n=0}^{N-1} q_n\right|^2}{\max_{k\neq 0} \left|[C_x[k] - C_y[k]] \sum_{n=0}^{N-1} (-1)^{p_n} q_n e^{jn\theta}\right|^2} \\ &= \left(\frac{L}{m_c}\right)^2 \frac{||\mathbf{q}||_1^2}{\left|S_{\mathcal{P},\mathcal{Q}}(\theta)\right|^2}, \end{aligned} \tag{2.36}$$

where $m_c = \max_{k\neq 0} |C_x[k]| = \max_{k\neq 0} |C_y[k]|$. Suppose the spectrum $S_{\mathcal{P},\mathcal{Q}}(\theta) = \sum_{n=0}^{N-1} (-1)^{p_n} q_n e^{jn\theta}$ has up to an M-th order null around $\theta = 0$. Then for sufficiently small θ, $S_{\mathcal{P},\mathcal{Q}}(\theta)$ can be dominated by the $(M+1)$-th order term in its Taylor expansion. We can derive the following lower bound of $PPSR_{\mathcal{P},\mathcal{Q}}(\theta)$:

Theorem 2.3.1. *Suppose a $(\mathcal{P}, \mathcal{Q})$ pulse train design achieves up to an M-th order null of range sidelobe of its cross ambiguity function. At sufficiently small Doppler shift θ, the $PPSR_{\mathcal{P},\mathcal{Q}}(\theta)$ of the cross ambiguity function $\chi_{\mathcal{P},\mathcal{Q}}(k,\theta)$ can be approximately*[3] *lower bounded by*

$$PPSR_{\mathcal{P},\mathcal{Q}}(\theta) \geq L^{0.2} \frac{[(M+1)!]^2 (2M+3)}{N^{2M+3}} \theta^{-2(M+1)}. \tag{2.37}$$

Proof: See appendix A.

[3] *by approximately we mean that the powers of θ at orders higher then $M+1$ in the Taylor expansion of $S_{\mathcal{P},\mathcal{Q}}(\theta)$ are neglected.*

For a fixed choice of $\mathcal{P}$ and $\mathcal{Q}$ sequences, the lower bound of $PPSR_{\mathcal{P},\mathcal{Q}}(\theta)$ increases as the length of Golay sequences L increases. However, it can be shown that the function

$$f(M) = \frac{[(M+1)!]^2(2M+3)}{N^{2M+3}} \tag{2.38}$$

is monotonically decreasing for $M \in [0, N-2]$. This suggests that given a fixed L, a $(\mathcal{P}, \mathcal{Q})$ achieving higher order null of range sidelobes does not necessarily have higher PPSR at small Doppler shift θ.

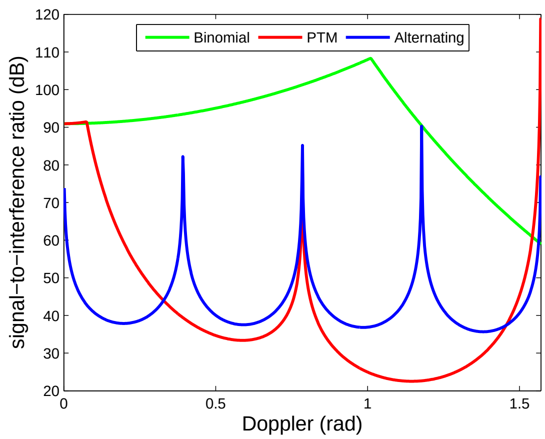

Figure 2.3: Comparison of PPSR for different $(\mathcal{P}, \mathcal{Q})$ pulse train designs.

Fig. 2.3 compares the PPSR for PTM, Binomial, and conventional pulse train designs with length 16. Within the Doppler interval ($[0, 1]$ rad), the PPSR for Binomial design is at most 65dB higher than alternating pulse train. Inside the Doppler interval ($[0, 0.3]$ rad) the PTM design outperforms the alternating pulse train with at most 50dB performance gain. When the Doppler shift is less than 0.1 rad, PTM and Binomial designs have almost the same performance. However, as Doppler shift increases from 0.1 rad the PPSR of PTM design dramatically falls down, while the PPSR of Binomial design shows the invariance inside the Doppler interval ($[0, 1.2]$ rad). Therefore compared to the PTM design, the Binomial design has a much wider *PPSR-invariant* Doppler band. For Binomial design the PPSR is maximized at around $\theta = 1$ rad instead zero Doppler. This is because the raised cosine pulse shape results in an imperfect ambiguity function which is not completely confined in $[-T_c, T_c]$ along zero Doppler.

2.3.2 Signal-to-Noise Ratio

Assume the transmit waveform illuminates a point target. Without loss of generality, assume that the target is located at the origin of range-Doppler plane. In the presence of noise, the radar return is

$$r(t) = bz_{\mathcal{P}}(t) + n(t), \tag{2.39}$$

where b is the target's random scattering coefficient with variance σ_b^2 which is assumed to be constant within a PRI, and the noise $n(t)$ is a random process which is independent with $z_{\mathcal{P}}(t)$ and satisfies $E[n(t)\overline{n(t')}] = N_0\delta(t-t')$ for all t and t'. Thus the output of matched filter is

$$\begin{aligned} \xi_{\mathcal{P},\mathcal{Q}}(\tau,\nu) &= \int_{-\infty}^{\infty} r(t)\overline{w_{\mathcal{Q}}(t-\tau)}e^{-j\nu t}dt \\ &= b\int_{-\infty}^{\infty} z_{\mathcal{P}}(t)\overline{w_{\mathcal{Q}}(t-\tau)}e^{-j\nu t}dt + \int_{-\infty}^{\infty} n(t)\overline{w_{\mathcal{Q}}(t-\tau)}e^{-j\nu t}dt \\ &= b\chi_{\mathcal{P},\mathcal{Q}}(\tau,\nu) + \chi_{\mathcal{N},\mathcal{Q}}(\tau,\nu), \end{aligned} \tag{2.40}$$

and from independence the expected value of $|\xi_{\mathcal{P},\mathcal{Q}}(\tau,\nu)|^2$ is

$$\begin{aligned} E[|\xi_{\mathcal{P},\mathcal{Q}}(\tau,\nu)|^2] &= \sigma_b^2|\chi_{\mathcal{P},\mathcal{Q}}(\tau,\nu)|^2 + E\left[\int_{-\infty}^{\infty} n(t)\overline{w_{\mathcal{Q}}(t-\tau)}e^{-j\nu t}dt \int_{-\infty}^{\infty} \overline{n(t')}w_{\mathcal{Q}}(t'-\tau)e^{j\nu t'}dt'\right] \\ &= \sigma_b^2|\chi_{\mathcal{P},\mathcal{Q}}(\tau,\nu)|^2 + N_0\int_{-\infty}^{\infty} |w_{\mathcal{Q}}(t-\tau)|^2 dt \\ &= \sigma_b^2|\chi_{\mathcal{P},\mathcal{Q}}(\tau,\nu)|^2 + N_0 L||\mathbf{q}||_2^2. \end{aligned} \tag{2.41}$$

Note $\chi_{\mathcal{P},\mathcal{Q}}(0,0) = L\mathbf{q}^T\mathbf{1}$, thus the signal-to-noise ratio after matched filtering is

$$\rho = \frac{\sigma_b^2|\chi_{\mathcal{P},\mathcal{Q}}(0,0)|^2}{\eta} = \frac{L||\mathbf{q}||_1^2}{N_0||\mathbf{q}||_2^2} = \frac{L\sigma_b^2}{N_0\beta_{\mathcal{Q}}}, \tag{2.42}$$

where $\beta_{\mathcal{Q}}$ is the *effective bandwidth* of power spectrum $\mathcal{M}_{\mathcal{Q}}(\theta) = |M_{\mathcal{Q}}(\theta)|^2$ of sequence $\mathcal{Q}$ [71]:

$$\beta_{\mathcal{Q}} = \frac{\frac{1}{2\pi}\int_{-\pi}^{\pi}\mathcal{M}_{\mathcal{Q}}(\theta)d\theta}{\mathcal{M}_{\mathcal{Q}}(0)} = \frac{\sum_{n=0}^{N-1} q[n]^2}{\left(\sum_{n=0}^{N-1} q[n]\right)^2} = \frac{||\mathbf{q}||_2^2}{||\mathbf{q}||_1^2}. \tag{2.43}$$

In general smaller value of $\beta_{\mathcal{Q}}$ means narrower mainlobe as well as lower sidelobes of $\mathcal{M}_{\mathcal{Q}}(\theta)$. Thus narrower spectrum $\mathcal{M}_{\mathcal{Q}}(\theta)$ implies higher SNR. It is clear that ρ is maximized if and only if $\mathbf{q} = \alpha \mathbf{1}$ for some positive scalar α, meaning $w_{\mathcal{Q}}(t) = \alpha z_{\mathcal{P}}(t)$ which corresponds to the usual matched filtering. Therefore by introducing non-trivial $\mathcal{Q}$ sequence we have to lose some SNR. In other words, the increase in the order of null of range sidelobes comes at the expense of SNR.

Table 2.1 compares the three designs in terms of the null order and the output SNR, and shows that by jointly designing the $\mathcal{P}$ and $\mathcal{Q}$ sequences we can achieve a null of relatively high order without considerable reduction in SNR compared to a matched filter design.

Table 2.1: Null order and SNR for different designs

$(\mathcal{P}, \mathcal{Q})$ design	Null order	SNR ($\|\mathbf{q}\|_1^2/\|\mathbf{q}\|_2^2$)
Conventional	0	16
PTM	3	16
Max-SNR with $M = 8$	8	13.76
Binomial	14	6.92

With a noisy radar return, bringing out the targets is interfered by the spillage of energy coming from nearby cells as well as noises. Consider a two point targets case in which the two targets are $\theta = \nu T$ away in Doppler shift. The ratio

$$\begin{aligned} r_{\mathcal{P},\mathcal{Q}}(\theta) &= \frac{|\chi_{\mathcal{P},\mathcal{Q}}(0,0)|^2}{\max\limits_{k\neq 0} |\chi_{\mathcal{P},\mathcal{Q}}(k,\theta)|^2 + \eta} \\ &= \left(PPSR(\theta)_{\mathcal{P},\mathcal{Q}}^{-1} + \frac{N_0 \beta}{L} \right)^{-1} \end{aligned} \tag{2.44}$$

characterizes the separability of two targets in the noisy environment. Note for a certain $(\mathcal{P}, \mathcal{Q})$ pulse train design, $r_{\mathcal{P},\mathcal{Q}}(\theta)$ is controlled by both the PPSR at Doppler shift θ and the SNR.

Fig. 2.4 compares the ratio $r_{\mathcal{P},\mathcal{Q}}(\theta)$ for different length-16 pulse train schemes, at different noise levels. Fig. 2.4(a)-(c) shows the comparison of $r_{\mathcal{P},\mathcal{Q}}(\theta)$ at noise power N_0= -40dB, -20dB, and 0dB respectively. When N_0 = -40dB, inside the Doppler interval ($[0, 0.2]$ rad)

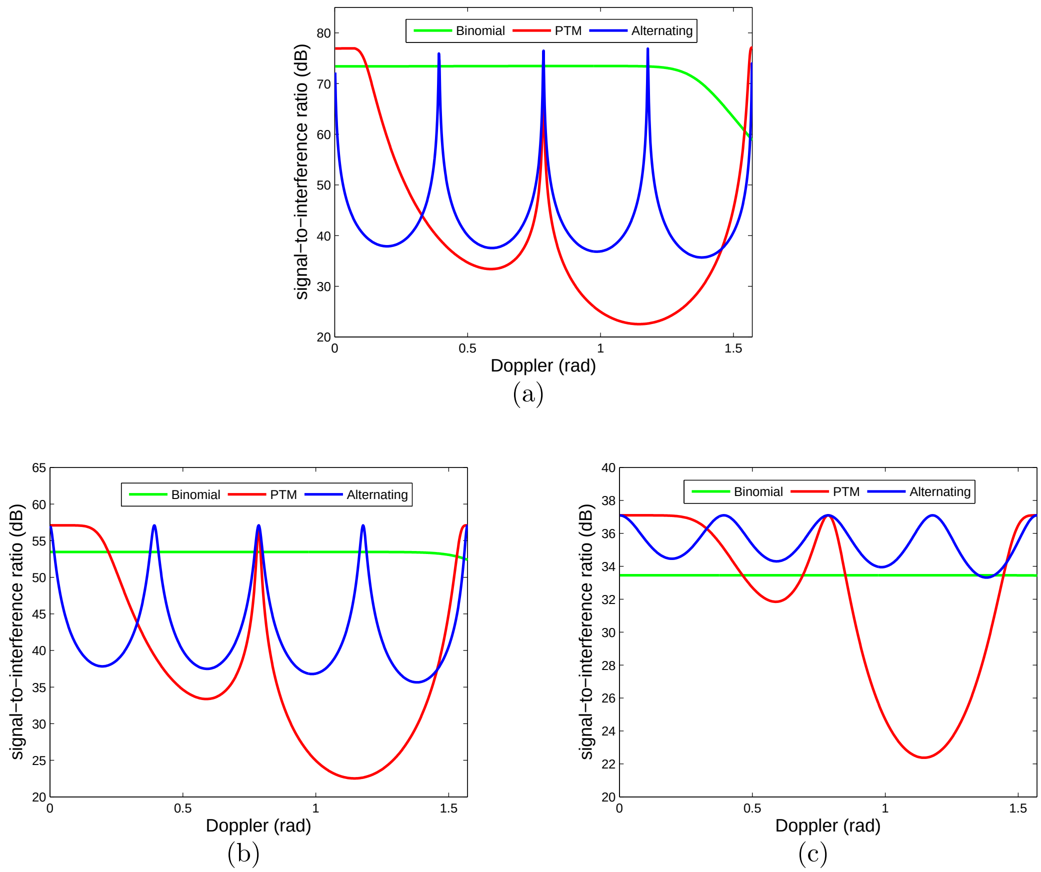

Figure 2.4: Comparison of signal-to-interference ratio for different $(\mathcal{P}, \mathcal{Q})$ pulse train designs: (a) noise power N_0 = -40dB, (b) N_0 = -20dB, (c) N_0 = 0dB.

PTM design bits Binomial design by 4dB at most. This is because the noise power dominates range sidelobe and Binomial design has lower SNR after matched filtering. However, inside ($[0.2, 0.5\pi]$ rad) Binomial design still outperforms PTM design. When N_0 = -20dB, Binomial design remains to have much higher $r(\theta)$ then PTM design at almost each Doppler shift in ($[0.3, 0.5\pi]$ rad). When N_0 = 0dB, Binomial design is worse then PTM design at most Doppler shifts. PTM design still behaves slightly better then alternating pulse train inside ($[0, 0.3]$ rad). Note the fairly high noise level case might not be interested for the $(\mathcal{P}, \mathcal{Q})$ pulse train design since all weak targets are possibly to be hidden by noises.

2.3.3 Doppler Estimation

Assume that the receiver is implemented by a square law detector. It is shown in [72] that the likelihood function of parameters $\boldsymbol{\theta} = [\tau, \nu]^T$ is

$$\ln \Lambda(\boldsymbol{\theta}) = c|L(\tau, \nu)|^2 \tag{2.45}$$

where the coefficient $c = \frac{E_r}{N_0}\frac{E_r}{E_r+N_0}$, E_r is the energy of received waveform, and N_0 is the power of white noise assumed here, and the function $L(\tau, \nu)$ is

$$L(\tau, \nu) = \int_{-\infty}^{\infty} \widetilde{r}(t)\overline{\widetilde{w}_{\mathcal{Q}}(t-\tau)}e^{-j\nu t}dt \tag{2.46}$$

The integrants $\widetilde{r}(t)$ and $\widetilde{w}_{\mathcal{Q}}(t)$ are the normalized radar return and $\mathcal{Q}$-pulse train respectively. For the parameter vector $\boldsymbol{\theta} = [\tau, \nu]^T$, the corresponding Fisher information matrix is

$$\mathbf{J} = \begin{bmatrix} J_{1,1} & J_{1,2} \\ J_{1,2} & J_{2,2} \end{bmatrix} \tag{2.47}$$

where the elements of $\mathbf{J}$ is defined as

$$J_{i,j} = -E\left[\frac{\partial^2 \ln \Lambda(\boldsymbol{\theta})}{\partial\theta_i \partial\theta_j}\right], \; 1 \leq i, j \leq 2. \tag{2.48}$$

The Fisher information for Doppler frequency can be found as [72, 73]

$$J_{2,2} = -c\frac{\partial^2 \phi(\tau, \nu)}{\partial \nu^2}\bigg|_{\tau,\nu=0}, \tag{2.49}$$

where $\phi(\tau, \nu) = |\chi_{\mathcal{P},\mathcal{Q}}(\tau, \nu)|^2/|\chi_{\mathcal{P},\mathcal{Q}}(0, 0)|^2$ is the normalized modular square of cross ambiguity function $\chi_{\mathcal{P},\mathcal{Q}}(\tau, \nu)$. Thus we have

$$\phi(0, \nu) = \frac{\mathcal{M}_{\mathcal{Q}}(\nu T)}{\mathcal{M}_{\mathcal{Q}}(0)} \tag{2.50}$$

and the Fisher information of Doppler frequency is

$$J_{2,2} = -cT^2\frac{\mathcal{M}_{\mathcal{Q}}^{(2)}(0)}{\mathcal{M}_{\mathcal{Q}}(0)} = \frac{4cT^2}{\gamma_{\mathcal{Q}}^2} \tag{2.51}$$

Therefore the Cramér-Rao lower bound of Doppler estimation error is right proportional to square of the 3-dB bandwidth $\gamma_{\mathcal{Q}}$ [71]:

$$\gamma_{\mathcal{Q}} \approx 2\sqrt{\left|\frac{\mathcal{M}_{\mathcal{Q}}(0)}{\mathcal{M}_{\mathcal{Q}}^{(2)}(0)}\right|} = \frac{2\sum_{n=1}^{N-1} q[n]}{\sqrt{\sum_{i\neq j}(i-j)^2 q[i]q[j]}} \tag{2.52}$$

2.3.4 Range Estimation

The Fisher information of range estimation is

$$J_{1,1} = -c\frac{\partial^2\phi(\tau,\nu)}{\partial\tau^2}\bigg|_{\tau,\nu=0}, \tag{2.53}$$

and it's each to check that $\phi(\tau, 0) = |\chi_\Omega(\tau, 0)^2|$, which is invariant to the choice of $\mathcal{P}$ and $\mathcal{Q}$ sequences. Therefore achieving a desirable Cramér-Rao lower bound of range estimation for $(\mathcal{P}, \mathcal{Q})$ pulse trains is only an issue of choosing proper pulse shapes, including choosing the function $\Omega(t)$ and chip interval T_c.

2.3.5 Tradeoff analysis for PTM and Binomial design

For general $(\mathcal{P}, \mathcal{Q})$ pulse trains following the null space condition (2.18), it might be not straightforward to derive the quantitative tradeoff relations. However, such a relation can be easily analyzed for some special cases such as PTM and Binomial design.

Notation: For any $(\mathcal{P}, \mathcal{Q})$ pulse train with length N, let $M_{\mathcal{P},\mathcal{Q}}$ be the highest order of null of the range sidelobes at $\theta = 0$. For the envelop of the power spectrum $\mathcal{M}_{\mathcal{Q}}(\theta)$, define its normalized slope at the 3-dB point $\theta = \gamma_{\mathcal{Q}}/2$ as

$$SL_{\mathcal{Q}} = \frac{1}{\mathcal{M}_{\mathcal{Q}}(0)}\frac{d}{d\theta}\left[\text{envolope}(\mathcal{M}_{\mathcal{Q}}(\theta))\right]\bigg|_{\theta=\gamma_{\mathcal{P},\mathcal{Q}}/2}. \tag{2.54}$$

The following results give a analytical tradeoff analysis for PTM and Binomial designs:

Theorem 2.3.2. *(Range Sidelobe Suppression Ability) For a length-N $(\mathcal{P}, \mathcal{Q})$ pulse train design,*

1. *If $\mathcal{P}$ is a PTM sequence, and $\mathcal{Q}$ is an all 1 sequence, then $M_{\mathcal{P},\mathcal{Q}} = \mathcal{O}(\log_2 N)$. For sufficiently small Doppler θ, $PPSR_{\mathcal{P},\mathcal{Q}}(\theta) = \mathcal{O}(\theta^{-2\log_2 N})$.*

2. *If $\mathcal{P}$ is an alternating sequence, and $\mathcal{Q}$ is a binomial sequence, then $M_{\mathcal{P},\mathcal{Q}} = \mathcal{O}(N)$. For sufficiently small Doppler θ, $PPSR_{\mathcal{P},\mathcal{Q}}(\theta) = \mathcal{O}(\theta^{-2N})$.*

Proof: (1) is proved in [16, 17], and (2) has been shown in section 2.2

Theorem 2.3.3. *(SNR and Doppler Estimation) For a $(\mathcal{P}, \mathcal{Q})$ pulse train design with length N,*

1. *If $\mathcal{P}$ is a PTM sequence, and $\mathcal{Q}$ is an all 1 sequence, then $\beta_{\mathcal{P},\mathcal{Q}} = \mathcal{O}(N^{-1})$, $\gamma_{\mathcal{P},\mathcal{Q}} = \mathcal{O}(N^{-1})$, and $-SL_{\mathcal{P},\mathcal{Q}} = \mathcal{O}(N)$.*

2. *If $\mathcal{P}$ is an alternating sequence, and $\mathcal{Q}$ is a binomial sequence, then $\beta_{\mathcal{P},\mathcal{Q}} = \mathcal{O}(N^{-1/2})$, $\gamma_{\mathcal{P},\mathcal{Q}}(N^{-1/2})$, and $-SL_{\mathcal{P},\mathcal{Q}} = \mathcal{O}(N^{1/2})$.*

Proof: See appendix B.

2.4 $(\mathcal{P}, \mathcal{Q})$ Pulse Train for Larger Sets of Complementary Waveforms

So far, we have studied the design of $(\mathcal{P}, \mathcal{Q})$ pulse trains for a library consisting of only two complementary waveforms. We now extend our constructions to larger waveform libraries. Suppose we have a set of D-*complementary* length-L sequences $\mathcal{Z} = \{z_0, z_1, ..., z_{D-1}\}$, meaning that the autocorrelations $C_{z_d}[k]$ of the z_d sequences satisfy

$$\sum_{d=0}^{D-1} C_{z_d}[k] = DL\delta[k]. \tag{2.55}$$

We take the size D of the set $\mathcal{Z}$ to be a power of 2, but its elements are not necessarily pairwise complementary. For example, for $D = 4$, we can choose z_0, z_1, z_2, and z_3 to form a Golay complementary quad, satisfying Eq. (2.55), without making z_i, z_j, $i \neq j$ Golay complementary pairs. The reader is referred to [74] for construction of Golay quads. Larger complementary sets are also possible.

Let $\mathcal{P} = \{p[n]\}_{n=0}^{N-1}$ and $\mathcal{Q} = \{q[n]\}_{n=0}^{N-1}$ be the sequences used for waveform coordination on transmit and receive respectively. To allow for coordination of D different waveforms z_d, $d = 0, 1, ..., D-1$, we take $\mathcal{P}$ to be a D-ary sequence defined over the alphabet $\mathcal{D} = \{0, 1, ..., D-1\}$. That is the element of $\mathcal{P}$ take their values from $\mathcal{D}$. At the n-th PRI of the $\mathcal{P}$ pulse train the waveform $s_{z_d}(t)$, phase coded by z_d, is transmitted if $p[n] = d$. The ordering of the waveforms in the $\mathcal{Q}$ pulse train is the same as that in the $\mathcal{P}$ pulse train, but the n-th waveform is weighted by $q[n]$ as before. In this case, the cross ambiguity function $\chi_{\mathcal{P},\mathcal{Q}}(k, \theta)$ can be written as

$$\chi_{\mathcal{P},\mathcal{Q}}(k,\theta) = \sum_{d=0}^{D-1}\Bigg(\sum_{\substack{n=0\\p[n]=d}}^{N-1} q[n]e^{jn\theta}\Bigg)C_{z_d}(k). \tag{2.56}$$

Denote $\omega = e^{j\frac{2\pi}{D}}$, Note that for each d from 0 to $D-1$, we have

$$\sum_{r=0}^{D-1}\omega^{r(p[n]-d)} = \begin{cases} D, & p_n = d \\ 0, & p_n \neq d \end{cases}. \tag{2.57}$$

Thus the cross ambiguity function can be written by

$$\begin{aligned}\chi_{\mathcal{P},\mathcal{Q}}(k,\theta) &= \frac{1}{D}\sum_{d=0}^{D-1}C_{z_d}(k)\sum_{n=0}^{N-1}q[n]e^{jn\theta}\sum_{r=0}^{D-1}\omega^{r(p[n]-d)} \\ &= \frac{1}{D}\sum_{r=0}^{D-1}\Bigg(\sum_{n=0}^{N-1}\omega^{rp[n]}q[n]e^{jn\theta}\Bigg)\Bigg(\sum_{d=0}^{D-1}\omega^{-rd}C_{z_d}(k)\Bigg) \\ &= \frac{1}{D}\sum_{r=0}^{D-1}S_{\mathcal{P},\mathcal{Q},r}(\theta)\Delta_r,\end{aligned} \tag{2.58}$$

where

$$S_{\mathcal{P},\mathcal{Q},r}(\theta) = \sum_{n=0}^{N-1}\omega^{rp[n]}q[n]e^{jn\theta}, \tag{2.59}$$

$$\Delta_r = \sum_{d=1}^{D-1}\omega^{-rd}C_{z_d}[k]. \tag{2.60}$$

From (2.55) we know that Δ_0 is a impulse being free of Doppler effect. However $\Delta_1, ..., \Delta_{D-1}$ cause the range sidelobes of cross ambiguity function $\chi_{\mathcal{P},\mathcal{Q}}(k, \theta)$. Rewrite $\chi_{\mathcal{P},\mathcal{Q}}(k, \theta)$ as

$$\chi_{\mathcal{P},\mathcal{Q}}(k,\theta) = \frac{1}{D}\Bigg(DL\delta[k]\sum_{n=0}^{N-1}q[n]e^{jn\theta} + \sum_{r=1}^{D-1}S_{\mathcal{P},\mathcal{Q},r}(\theta)\Delta_r\Bigg). \tag{2.61}$$

Recall that when $D = 2$, the term $S_{\mathcal{P},\mathcal{Q},1}(\theta)$ is the spectrum $S_{\mathcal{P},\mathcal{Q}}(\theta)$ which has been analyzed in sections 2.2 and 2.3. Therefore to suppress the range sidelobes in Eq. (2.61), it is sufficient to suppress the spectrum $S_{\mathcal{P},\mathcal{Q},1}(\theta), ..., S_{\mathcal{P},\mathcal{Q},D-1}(\theta)$. The following Theorem presents a construction of $\mathcal{P}$ and $\mathcal{Q}$ sequences that render a high order of null for each of $S_{\mathcal{P},\mathcal{Q},1}(\theta), ..., S_{\mathcal{P},\mathcal{Q},D-1}(\theta)$:

Theorem 2.4.1. *For a set of $D = 2^m$ complementary sequences, from a pair of length-N sequences $\mathcal{P}' = \{p'[0], \ldots, p'[N-1]\}$ and $\mathcal{Q}' = \{q'[0], \ldots, q'[N-1]\}$ satisfying the null space equation (2.18) with the order of null M, if the length-N^m sequences $\mathcal{P}$ and $\mathcal{Q}$ are constructed by following recursions:*

1. *At $1 < t \leq m$, if $t = 2$, let sequence $\widetilde{\mathcal{P}}_0 = \mathcal{P}'$, otherwise set $\widetilde{\mathcal{P}}_0$ to be the length-N^{t-1} sequence $\mathcal{P}$ generated at last iteration. Let $\widetilde{\mathcal{P}}_1$ be the sequence obtained by adding each element in $\widetilde{\mathcal{P}}_0$ with 2^{t-1}. Generate the length-N^t sequence $\mathcal{P}$ by concatenating $\widetilde{\mathcal{P}}_0$ and $\widetilde{\mathcal{P}}_1$ according to the positions of 0's and 1's in the length-N sequence $\mathcal{P}'$. That is, for $k = 0, ..., N-1$, the k-th block of $\mathcal{P}$ is $\widetilde{\mathcal{P}}_0$ if $p'[k] = 0$ or $\widetilde{\mathcal{P}}_1$ if $p'[k] = 1$.*

2. *At $1 < t \leq m$, if $t = 2$, let sequence $\widetilde{\mathcal{Q}} = \mathcal{Q}'$, otherwise set $\widetilde{\mathcal{Q}}$ to be the length-N^{t-1} sequence $\mathcal{Q}$ generated at last iteration. Generate the length N^t sequence $\mathcal{Q}$ by concatenation: $\mathcal{Q} = \{q'[0]\widetilde{\mathcal{Q}}, q'[1]\widetilde{\mathcal{Q}}, \ldots, q'[N-1]\widetilde{\mathcal{Q}}\}$. After all iterations, it can be seen that for each n from 0 to $N^m - 1$, the n-th element of the length-N^m desired sequence $\mathcal{Q}$ is $q[n] = \prod_{k=0}^{m-1} q'[n_k]$, where $n_{m-1}...n_1 n_0$ is the N-ary expression for n, i.e., $n = n_0 + N n_1 + \cdots + N^{m-1} n_{m-1}$.*

Then for $r = 1, ..., D-1$, each spectrum $S_{\mathcal{P},\mathcal{Q},r}(\theta)$ has a M-th order null at $\theta = 0$.

Proof: See appendix C.

Example 2.4.1. Suppose a set of $D = 4$ complementary sequence is $\{z_0, z_1, z_2, z_3\}$ (Golay complementary quad). If the length-4 sequences $\mathcal{P}'$ and $\mathcal{Q}'$ are selected as $\mathcal{P}' = 0\ 1\ 0\ 1$ and $\mathcal{Q}' = 1\ 3\ 3\ 1$ (Binomial Design), we have known that $\mathcal{P}'$ and $\mathcal{Q}'$ together creates a second-order null of range sidelobes at $\theta = 0$. If we generate the length-16 sequence $\mathcal{P}$ as

$$\mathcal{P} = \{p[n]\}_{n=0}^{15} = 0\ 1\ 0\ 1\ 2\ 3\ 2\ 3\ 0\ 1\ 0\ 1\ 2\ 3\ 2\ 3,$$

hence the transmitted waveform can be vectorized by

$$\mathbf{s} = [z_0\ z_1\ z_0\ z_1\ z_2\ z_3\ z_2\ z_3\ z_0\ z_1\ z_0\ z_1\ z_2\ z_3\ z_2\ z_3].$$

Also construct the length-16 sequence $\mathcal{Q}$ as

$$\mathcal{Q} = \{q[n]\}_{n=0}^{15} = 1\ 3\ 3\ 1\ 3\ 9\ 9\ 3\ 3\ 9\ 9\ 3\ 1\ 3\ 3\ 1,$$

and the receiver waveform can be vectorized by

$$\mathbf{w} = [z_0\ 3z_1\ 3z_0\ z_1\ 3z_2\ 9z_3\ 9z_2\ 3z_3\ 3z_0\ 9z_1\ 9z_0\ 3z_1\ z_2\ 3z_3\ 3z_2\ z_3].$$

It can be shown that the spectrum is

$$\begin{aligned}
S_{\mathcal{P},\mathcal{Q},1}(\theta) &= (1 + je^{j\theta})^3(1 - e^{j4\theta})^3,\\
S_{\mathcal{P},\mathcal{Q},2}(\theta) &= (1 + e^{j4\theta})^3(1 - e^{j\theta})^3,\\
S_{\mathcal{P},\mathcal{Q},3}(\theta) &= (1 - je^{j\theta})^3(1 - e^{j4\theta})^3,
\end{aligned}$$

Thus each of $S_{\mathcal{P},\mathcal{Q},1}(\theta)$, $S_{\mathcal{P},\mathcal{Q},2}(\theta)$, and $S_{\mathcal{P},\mathcal{Q},3}(\theta)$ has a second-order null at $\theta = 0$.

Remark 2.4.1. It can be readily shown that by oversampling the sequences $\mathcal{P}$ and $\mathcal{Q}$, the spectrum $S_{\mathcal{P},\mathcal{Q},1}(\theta)$, ..., $S_{\mathcal{P},\mathcal{Q},,D-1}(\theta)$ can be also suppressed around higher Doppler shifts.

2.5 Conclusion

In this chapter we have presented a general approach for constructing radar transmit-receive pulse trains whose cross-ambiguity functions are free of range sidelobe inside a desired Doppler interval. The transit pulse train is constructed by a binary sequence $\mathcal{P}$ which coordinates the transmission of a pair of Golay complementary waveforms across time. For the receiver pulse train each waveform is weighted by an entry in sequence $\mathcal{Q}$. The range sidelobe of the cross-ambiguity function is shaped by a spectra which is jointly determined by $\mathcal{P}$ and $\mathcal{Q}$. By properly choosing $\mathcal{P}$ and $\mathcal{Q}$ sequences the range sidelobe can be annihilated inside a desired Doppler interval. A detailed comparison of two special cases of $(\mathcal{P}, \mathcal{Q})$ pulse train design: PTM and Binomial design is demonstrated. This comparison shows that the joint design of $\mathcal{P}$ and $\mathcal{Q}$ sequences also enables the tradeoff of Doppler resilience and output signal-to-noise ratio.

CHAPTER 3

DOPPLER RESILIENT OFDM ILLUMINATIONS

In Chapter 2 we constructed the transmit pulse train by coordinating the transmission of Golay complementary waveforms according to zeros and ones in a binary sequence $\mathcal{P}$. The pulse train used in the receive filter is constructed in a similar way, in terms of sequencing the Golay waveforms, but each waveform in the pulse train is weighted according to an element of a sequence $\mathcal{Q}$. The cross-ambiguity function of the $(\mathcal{P}, \mathcal{Q})$ pulse trains is essentially the radar point-spread function, describing the blurring of the radar image of a point targets on range-Doppler plane. We show that the magnitude of the range sidelobe of this cross-ambiguity function is controlled by the magnitude of spectrum of the product of $\mathcal{P}$ and $\mathcal{Q}$ sequences. By selecting sequences for which the spectrum of their product has a higher-order null around zero Doppler, we can annihilate the range sidelobe of the cross ambiguity function inside a Doppler band around the zero-Doppler axis. This enables us to extract a weak target that is located in range near a stronger reflector at a different Doppler frequency.

However, in Chapter 2 we also showed that with a fixed available time-bandwidth product, the range sidelobe suppression ability, or Doppler resilience, comes at the expense of Doppler response. This motivates an improvement of the Doppler response. In this Chapter, we consider the exploration of the degrees of freedom in time and frequency for radar imaging. We show that the Doppler response can be improved by waveform coordination across frequency, without impacting Doppler resilience. The time-coordinated $(\mathcal{P}, \mathcal{Q})$-pulse trains are assigned to $2K$ orthogonal frequency-division multiplexing (OFDM) subcarriers. The $2K$ subcarriers include K subcarriers pairs with equal and opposite frequency offset relative to a common carrier frequency. The effective radar psf is a weighted summation of the squared cross ambiguity functions of the $(\mathcal{P}, \mathcal{Q})$-pulse trains assigned to the total K

subcarrier pairs. The Doppler response is essentially controlled by of the spectrum of the weight sequence across all subcarriers, whose zero-crossings around zero Doppler is $\mathcal{O}(1/K)$. This means that Doppler resolution for an OFDM $(\mathcal{P}, \mathcal{Q})$-pulse train is $\mathcal{O}(1/K)$ and at least K/N better than a single frequency $(\mathcal{P}, \mathcal{Q})$-pulse train with N pulses. But note that a fine resolution of our OFDM waveform design requires a huge frequency consumption, which may not be realistic considering the intense occupation of spectral resources nowadays. We then show that by implementing two sets of OFDM $(\mathcal{P}, \mathcal{Q})$-pulse trains operating over $2K_1$ and $2K_2$ subcarriers respectively, and properly performing signal processing on the measurement, we can achieve a Doppler resolution in the order of $\mathcal{O}(1/K_1K_2)$, provided that K_1 and K_2 are coprime integers. Therefore the same Doppler response can be achieved with much less bandwidth consumption.

3.1 Tradeoff between Range Sibelobe Suppression and Doppler Response

Controlling Range Sidelobes. The magnitude of the range sidelobes is proportional to the magnitude of the spectrum of the sequence $(-1)^{p[n]}q[n]$, given by

$$S_{\mathcal{P},\mathcal{Q}}(\theta) = \sum_{n=0}^{N-1}(-1)^{p[n]}q[n]e^{jn\theta}. \tag{3.1}$$

As a result, range sidelobes inside a Doppler interval around the zero-Doppler axis can be suppressed by selecting a sequence $(-1)^{p[n]}q[n]$ whose spectrum has a higher-order null at zero Doppler. Suppose $S^{(m)}_{\mathcal{P},\mathcal{Q}}(0)$ is the m-th order derivative of $S_{\mathcal{P},\mathcal{Q}}(\theta)$ at $\theta = 0$. To create an Mth order null, all $S^{(m)}_{\mathcal{P},\mathcal{Q}}(0)$ up to order M must be zero-forced.

Doppler Response. The cross ambiguity function $\chi_{\mathcal{P},\mathcal{Q}}(k, \theta)$ across zero delay is proportional to the spectrum

$$S_{\mathcal{Q}}(\theta) = \sum_{n=0}^{N-1} q[n]e^{jn\theta}, \tag{3.2}$$

which is the spectrum of the $\mathcal{Q}$ sequence. The width $\Delta\theta$ of the mainlobe of the magnitude spectrum $|S_{\mathcal{Q}}(\theta)|$ defined as the location of the first zero crossing of $S_{\mathcal{Q}}(\theta)$, determine the Doppler resolution of the $(\mathcal{P}, \mathcal{Q})$ pulse train, which can be controlled by designing the sequence $\mathcal{Q}$.

However, there exists a tradeoff between the order of the null at $\theta = 0$ in $S_{\mathcal{P},\mathcal{Q}}(\theta)$ and the width of the mainlobe of $S_{\mathcal{Q}}(\theta)$. A high-order null comes at the expense of Doppler resolution, and vice versa. We now present two specific design that highlight the two extremes of this tradeoff.

The following two theorems together illustrate the tradeoff between range sidelobe suppression and Doppler resolution of a $(\mathcal{P}, \mathcal{Q})$ pulse train design:

Theorem 3.1.1. *(PTM Design) Let* $\mathcal{P} = \{p[n]\}_{n=0}^{N-1}$ *be the length* N *Prouhet-Thue-Morse (PTM) sequence [65], defined recursively as* $p[2k] = p[k]$ *and* $p[2k+1] = 1-p[k]$ *for all* $k \geq 0$, *with* $p_0 = 0$, *and let* $\mathcal{Q} = \{q[n]\}_{n=0}^{N-1}$ *be the all 1 sequence of length* N. *Then, (1) the spectrum* $S_{\mathcal{P},\mathcal{Q}}(\theta)$ *has a* $(\log_2(N)-1)$*th-order null at* $\theta = 0$, *(2) the spectrum* $S_{\mathcal{Q}}(\theta) = \sin(\frac{N\theta}{2})/\sin(\frac{N\theta}{2})$ *has zero crossings at* $\theta = \pm\frac{2\pi}{N}$, *and the Doppler resolution is* $\Delta\theta = \frac{4\pi}{N}$.

Theorem 3.1.2. *(Binomial Design) Let* $\mathcal{P} = \{p[n]\}_{n=0}^{N-1}$ *be the length* N *alternating sequence, where* $p_{2k} = 1$ *and* $p_{2k+1} = 0$ *for all* $k \geq 0$, *and let* $\mathcal{Q} = \{q[n]\}_{n=0}^{N-1}$ *be the length* N *binomial sequence* $\{q[n]\}_{n=0}^{N-1} = \{\binom{N-1}{n}\}_{n=0}^{N-1}$. *Then, (1) the spectrum* $S_{\mathcal{P},\mathcal{Q}}(\theta)$ *has a* $(N-2)$*th-order null at* $\theta = 0$, *(2) the spectrum* $S_{\mathcal{Q}}(\theta) = (1 + e^{j\theta})^{N-1}$ *has zero crossings at* $\theta = \pm\frac{\pi}{2}$, *and the Doppler resolution is* $\Delta\theta = \pi$.

A revisit of Fig. 2.1 can help better understand the above tradeoff between Doppler resilience and Doppler response. The conventional design depicted by Fig. 2.1(a) uses an alternating transmission of Golay complementary waveforms followed by matched filtering at the receiver. In Fig. 2.1(a), the weak targets are almost completely masked by the range sidelobes of the stronger reflectors. The PTM design shown in Fig. 2.1(b) has an $M = \log_2(N) - 1 = 3$ order of the spectral null for range sidelobe suppression. With this order, we can bring the range sidelobes below -80dB inside the $[-0.1, -0.1]$ rad Doppler interval and extract the weak targets. The spectrum $S_{\mathcal{Q}}(\theta)$ has zero-crossings at $\theta = \pm\frac{2\pi}{N} = \pm\frac{\pi}{8}$,

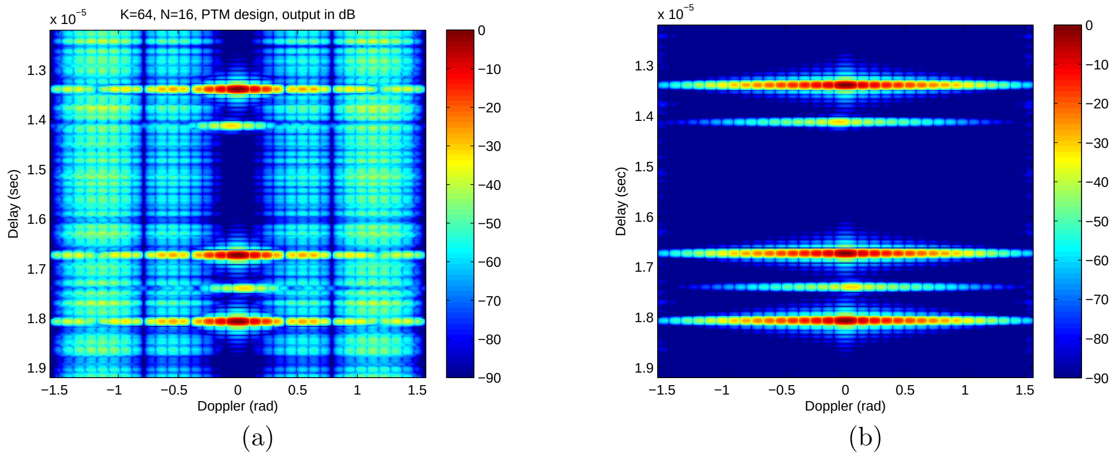

Figure 3.1: Illustration of Doppler resolution improvement by using OFDM $(\mathcal{P},\mathcal{Q})$ pulse train. $K = 64$. (a) PTM design, (b) Binomial design.

meaning Doppler resolution is roughly $\Delta\theta = \frac{\pi}{4}$ rad. Fig. 2.1(c) shows that the Binomial design can expand the cleared (below -80dB) region to $[-1, -1]$ rad by creating a null of order $M = N - 2 = 14$ around zero Doppler. However, this increase in the order of the range sidelobe null comes at the expense of Doppler resolution. The spectrum $S_{\mathcal{Q}}(\theta)$ has zero-crossings at $\theta = \pm\frac{\pi}{2}$, meaning Doppler resolution is roughly $\Delta\theta = \pi$ rad.

3.2 OFDM $(\mathcal{P},\mathcal{Q})$ Pulse Trains

Suppose the radar can transmit a set of $\mathcal{P}$-pulse trains $\{z_{\mathcal{P}_1}(t), ..., z_{\mathcal{P}_K}(t)\}$ across K subcarriers. Over the k-th subcarrier, $k = 0, 1, ..., K-1$, the receiver correlates the radar return with a $\mathcal{Q}$-pulse train $z_{\mathcal{Q}_k}(t)$. Denote $\omega_c + \omega_k$ as the central carrier frequency of the k-th subcarrier, where where ω_c is the some carrier frequency which is common for all k, and ω_k is the k-th frequency offset ($\omega_0 = 0$).

Suppose there is a target in scene with range τ_0 and radial velocity v. Over the k-th subcarrier, the down-converted radar return should be

$$r_k(t) = z_{\mathcal{P}_k}(t - \tau_0)e^{j\frac{2v}{c}(\omega_c+\omega_k)t}e^{-j(\omega_c+\omega_k)\tau_0}, \tag{3.3}$$

Denote $\nu_k = \frac{2v}{c}(\omega_c+\omega_k)$ as the target's Doppler frequency with respect to the k-th subcarrier.

In reality we have that $v \ll c$, and $\omega_k \ll \omega_c$, and we can reasonably assume that each Doppler frequency $\nu_k \approx \nu_0 = \frac{2v}{c}\omega_c$ for all k. Then it follows that the output of the matched filter over the k-th subcarrier is

$$\begin{aligned} z_k(\tau,\nu) &= \int_{-\infty}^{\infty} r_k(t)\overline{z_{\mathcal{Q}_k}(t-\tau)}e^{-j\nu t}dt \\ &= e^{-j(\omega_c+\omega_k)\tau_0}e^{j(\nu_0-\nu)\tau_0}\chi_{\mathcal{P}_k,\mathcal{Q}_k}(\tau-\tau_0,\nu-\nu_0), \end{aligned} \tag{3.4}$$

where $\chi_{\mathcal{P}_k,\mathcal{Q}_k}(\tau,\nu)$ is the cross ambiguity functions with respect to the pulse trains $z_{\mathcal{P}_k}(t)$ and $z_{\mathcal{Q}_k}(t)$. The phase of $z_k(\tau,\nu)$ includes the range-dependent term $(\omega_c+\omega_k)\tau_0$ which is unknown. Moreover, the unknown phases $(\omega_c+\omega_k)\tau_0$ are not identical for all k. Later on we will show that for the purpose of improving Doppler resolution, it is important to coherently combine the cross ambiguity functions $\chi_{\mathcal{P}_k,\mathcal{Q}_k}$, $k=0,1,...,K-1$. To avoid the above phase difference we refer to the approach in [20]. Suppose we are given additional $K-1$ subcarriers frequency $\omega_c-\omega_k$, $k=1,...,K-1$. Over the subcarrier at central frequency $\omega_c-\omega_k$, if the radar transmits the waveform $z_{\mathcal{P}_k}(t)$, and the receiver correlates the down-converted radar return

$$r'_k(t) = z_{\mathcal{P}_k}(t-\tau_0)e^{j\frac{2v}{c}(\omega_c-\omega_k)t}e^{-j(\omega_c-\omega_k)\tau_0}, \tag{3.5}$$

with $z_{\mathcal{Q}_k}(t)$, then the output of matched filter is

$$z'_k(\tau,\nu) = e^{-j(\omega_c-\omega_k)\tau_0}e^{j(\nu_0-\nu)\tau_0}\chi_{\mathcal{P}_k,\mathcal{Q}_k}(\tau-\tau_0,\nu-\nu_0). \tag{3.6}$$

Let $z'_0(\tau,\nu) = z_0(\tau,\nu)$. Then for each $k=0,1,...,K-1$, the product of $z_k(\tau,\nu)$ and $z'_k(\tau,\nu)$ is

$$\begin{aligned} \xi_k(\tau,\nu) &= z_k(\tau,\nu)z'_k(\tau,\nu) \\ &= e^{-2j\omega_c\tau_0}e^{2j(\nu_0-\nu)\tau_0}\chi^2_{\mathcal{P}_k,\mathcal{Q}_k}(\tau-\tau_0,\nu-\nu_0). \end{aligned} \tag{3.7}$$

So far the complex factor $e^{-2j\omega_c\tau_0}e^{2j(\nu_0-\nu)\tau_0}$ is common for all k. Ignoring the common factor and we can write

$$\sum_{k=0}^{K-1}\xi_k(\tau,\nu) = \sum_{k=0}^{K-1}\chi^2_{\mathcal{P}_k,\mathcal{Q}_k}(\tau-\tau_0,\nu-\nu_0). \tag{3.8}$$

Eq. (3.8) shows that the function $\sum_{k=0}^{K-1} \chi^2_{\mathcal{P}_k,\mathcal{Q}_k}(\tau,\nu)$, which is the composite square of cross ambiguity function, can be viewed as the point-spread-function of the new radar system, where the inputs of the system are the square of targets's scattering functions. Hence, the remaining problem is to find candidates for pulse trains $\{z_{\mathcal{P}_k}(t)\}_{k=0}^{K-1}$ and $\{z_{\mathcal{Q}_k}(t)\}_{k=0}^{K-1}$, such that the function $\sum_{k=0}^{K-1} \chi^2_{\mathcal{P}_k,\mathcal{Q}_k}(\tau,\nu)$ owns a desired Doppler resolution and meanwhile keeps a satisfactory range sidelobe suppression. To achieve the goal, we present one way to building the pulse trains $\{z_{\mathcal{P}_k}(t)\}_{k=0}^{K-1}$ and $\{z_{\mathcal{Q}_k}(t)\}_{k=0}^{K-1}$ in the following. If we select $\{z_{\mathcal{P}_k}(t)\}_{k=0}^{K-1}$ and $\{z_{\mathcal{Q}_k}(t)\}_{k=0}^{K-1}$ as

$$\begin{cases} z_{\mathcal{P}_k}(t) = z_{\mathcal{P}}(t - kT/2) \\ z_{\mathcal{Q}_k}(t) = r_k z_{\mathcal{Q}}(t - kT/2) \end{cases} , k = 0, ..., K-1, \tag{3.9}$$

where r_k is some complex scaler, and the pulse trains $z_{\mathcal{P}}(t)$ and $_{\mathcal{Q}}(t)$ are generated by a pair of sequences $(\mathcal{P},\mathcal{Q})$ corresponding to an M-th order range sidelobe as in section 3.1. This implies that

$$\chi_{\mathcal{P}_k,\mathcal{Q}_k}(\tau,\nu) = r_k e^{-j\nu kT/2} \chi_{\mathcal{P},\mathcal{Q}}(\tau,\nu). \tag{3.10}$$

Let $\theta = \nu T$, then we have

$$\sum_{i=0}^{K-1} \chi^2_{\mathcal{P}_k,\mathcal{Q}_k}(\tau,\nu) = \mathcal{R}(\theta)\chi^2_{\mathcal{P},\mathcal{Q}}(\tau,\nu), \tag{3.11}$$

where $\mathcal{R}(\theta) = \sum_{k=0}^{K-1} r_k^2 e^{-jk\theta}$ is the spectrum of the sequence $\{r_k^2\}_{k=0}^{K-1}$.

By choosing proper sequence $\{r_k^2\}_{k=0}^{K-1}$, the spectrum $R(\theta)$ can have desirably lowpass, and thus the Doppler resolution can be controlled by $R(\theta)$. For example, if $r_k = 1$ for all k, then $R(\theta)$ is the well-known Dirichlet kernel whose closest zero crossings around zero Doppler are $\theta = \pm\frac{2\pi}{K}$. Therefore the Doppler resolution of the point-spread-function $\sum_{i=0}^{K-1} \chi^2_{\mathcal{P}_k,\mathcal{Q}_k}(\tau,\nu)$ is $\mathcal{O}(\frac{1}{K})$, which is at least $\frac{N}{K}$ time better than that of a single frequency $(\mathcal{P},\mathcal{Q})$ pulse train of length N.

Remark 3.2.1. Eq. (3.9) shows that each pulse train $z_{\mathcal{P}_k}(t)$ is the pulse train $z_{\mathcal{P}_k}(t)$ delayed by $k\frac{T}{2}$. But this does not mean that over subcarriers with central frequencies $\omega_c \pm \omega_k$, $z_{\mathcal{P}}(t)$ needs to be transmitted $k\frac{T}{2}$ later than over the subcarrier with central frequency ω_c. This

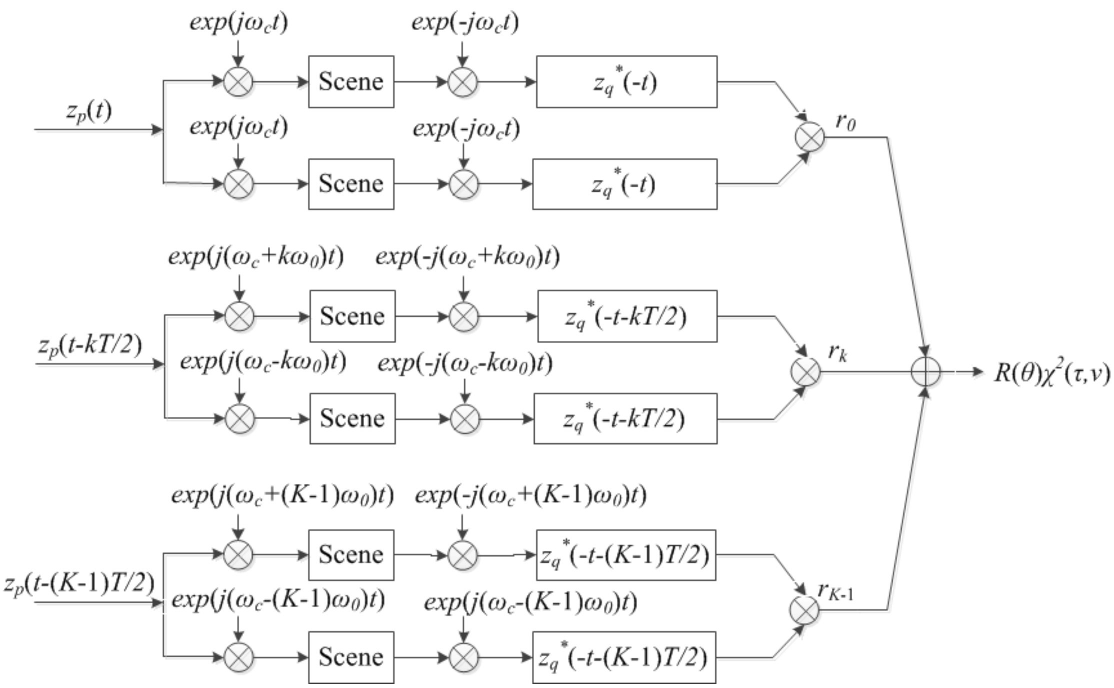

Figure 3.2: Implementation of OFDM radar using Golay complementary waveforms.

is because that for each k, the absolute time t does not affect the measurements $z_k(\tau,\nu)$ and $z'_k(\tau,\nu)$ in eq. (3.4) and (3.6). Thus to let the transmission of waveforms across all the subcarriers share the same time interval NT, one can "tune the clock" for the subcarriers with central frequencies $\omega_c \pm \omega_k$ with $k\frac{T}{2}$ seconds ahead of the clock for the subcarrier with central frequency ω_c.

Fig. 3.1 shows the delay-Doppler maps for a OFDM radar with $2K-1 = 127$ subcarriers, and $(z_{\mathcal{P}}(t), z_{\mathcal{Q}}(t))$ corresponding to the PTM (Fig. 2.1(b)) and Binomial (Fig. 2.1(c)) designs. The sequence $\{r_k^2\}_{k=0}^{K-1}$ is chosen to be the all 1 sequence in both cases. The OFDM point-spread-functions have the same cleared region of range sidelobes as shown in Fig. 2.1, but their Doppler resolution is roughly $\Delta\theta = \frac{4\pi}{K} = \frac{\pi}{16}$. The implementation of the OFDM radar is illustrated in Fig. 3.2.

3.2.1 Spectrum Optimization

The Doppler response of the OFDM $(\mathcal{P}, \mathcal{Q})$ pulse train is controlled by the spectrum $\mathcal{R}(\theta)S_{\mathcal{Q}}^2(\theta)$. Define the sequence $a(n) = (\gamma * \mathcal{Q} * \mathcal{Q})(n)$. From the Parseval's theorem we have

$$\sum_{n=0}^{2N+K-3} |a(n)|^2 = \int_{-\pi}^{\pi} |\mathcal{R}(\theta)S_{\mathcal{Q}}^2(\theta)|^2 d\theta. \tag{3.12}$$

And we can also show that

$$\sum_{n=0}^{2N+K-3} |a(n)|^2 = \boldsymbol{\gamma}^H \mathbf{Q}_K^H \mathbf{Q}_{N+K-1}^H \mathbf{Q}_{N+K-1} \mathbf{Q}_K \boldsymbol{\gamma}, \tag{3.13}$$

where $\mathbf{Q}_K$ and $\mathbf{Q}_{N+K-1}$ are the convolution matrices represented by $\mathcal{Q}$, for length-K and length-$N+K-1$ vectors. Note that $\mathcal{R}(0)S_{\mathcal{Q}}^2(0) = \sum_{k=0}^{K-1} \gamma_k (\sum_{n=0}^{N-1} q[n])^2$. Thus to minimize the sidelobe to peak ratio

$$\frac{1}{|\mathcal{R}(0)S_{\mathcal{Q}}^2(0)|^2} \int_{-\pi}^{\pi} |\mathcal{R}(\theta)S_{\mathcal{Q}}^2(\theta)|^2 d\theta, \tag{3.14}$$

it suffices to solve the optimization problem

$$\begin{aligned} \min_{\boldsymbol{\gamma}} \ & \boldsymbol{\gamma}^H \mathbf{Q}_K^H \mathbf{Q}_{N+K-1}^H \mathbf{Q}_{N+K-1} \mathbf{Q}_K \boldsymbol{\gamma} \\ \text{s.t. } & |\sum_{k=0}^{K-1} \gamma_k|^2 = 1. \end{aligned} \tag{3.15}$$

3.2.2 Analysis of Nonlinearity

Suppose there are two targets in scene with coordinates (τ_0, ν_0) and (τ_1, ν_1) respectively. From eq. (3.4) and (3.6) we know that the corresponding matched filter outputs are

$$\begin{cases} z_k(\tau,\nu) = \sum_{\ell=0}^{1} e^{-j(\omega_c+\omega_k)\tau_\ell} e^{j(\nu_\ell-\nu)\tau_\ell} e^{-j(\nu-\nu_\ell)kT/2} \chi_{\mathcal{P},\mathcal{Q}}(\tau-\tau_\ell, \nu-\nu_\ell) \\ z'_k(\tau,\nu) = \sum_{\ell=0}^{1} e^{-j(\omega_c-\omega_k)\tau_\ell} e^{j(\nu_\ell-\nu)\tau_\ell} e^{-j(\nu-\nu_\ell)kT/2} \chi_{\mathcal{P},\mathcal{Q}}(\tau-\tau_\ell, \nu-\nu_\ell) \end{cases} , k = 0, 1, ..., K_1 - 1. \tag{3.16}$$

Therefore the product of $z_k(\tau,\nu)$ and $z'_k(\tau,\nu)$ is

$$\xi_k(\tau,\nu) = \sum_{\ell=0}^{1} e^{-j2\omega_c\tau_\ell} e^{j2(\nu_\ell-\nu)\tau_\ell} e^{-j(\nu-\nu_\ell)kT} \chi^2_{\mathcal{P},\mathcal{Q}}(\tau-\tau_\ell,\nu-\nu_\ell) + 2e^{-j\omega_c(\tau_0+\tau_1)}\cos(\omega_k(\tau_0-\tau_1)) \\ \cdot e^{j[(\nu_0-\nu)\tau_0+(\nu_1-\nu)\tau_1]} e^{j(2\nu-\nu_0-\nu_1)kT/2} \chi_{\mathcal{P},\mathcal{Q}}(\tau-\tau_0,\nu-\nu_0)\chi_{\mathcal{P},\mathcal{Q}}(\tau-\tau_1,\nu-\nu_1), \tag{3.17}$$

and thus

$$\sum_{k=0}^{K-1} \xi_k(\tau,\nu) = \sum_{\ell=0}^{1} e^{-j2\omega_c\tau_\ell} e^{j2(\nu_\ell-\nu)\tau_\ell} \mathcal{R}((\nu-\nu_\ell)T)\chi^2_{\mathcal{P},\mathcal{Q}}(\tau-\tau_\ell,\nu-\nu_\ell) + \sum_{k=0}^{K-1}\cos(\omega_k(\tau_0-\tau_1)) \\ \cdot 2e^{j(2\nu-\nu_0-\nu_1)kT/2} e^{-j\omega_c(\tau_0+\tau_1)} e^{j[(\nu_0-\nu)\tau_0+(\nu_1-\nu)\tau_1]} \chi_{\mathcal{P},\mathcal{Q}}(\tau-\tau_0,\nu-\nu_0)\chi_{\mathcal{P},\mathcal{Q}}(\tau-\tau_1,\nu-\nu_1) \tag{3.18}$$

If $|\tau_0-\tau_1|$ is greater than T_c, which is the range resolution of $\chi_{\mathcal{P},\mathcal{Q}}(\tau,\nu)$, the cross term is close to zero due to the range sidelobe suppression ability of the $(\mathcal{P},\mathcal{Q})$ pulse train. If $|\tau_0-\tau_1| \le T_c$, the cross term cannot be neglected when τ is near τ_0 and τ_1. Suppose $\omega_k = k\omega_1$, $k=0,1,...,K-1$, then by omitting the bulk phases in eq. (3.18), we have

$$\sum_{k=0}^{K-1} \xi_k(\tau,\nu) = \sum_{\ell=0}^{1} \mathcal{R}((\nu-\nu_\ell)T)\chi^2_{\mathcal{P},\mathcal{Q}}(\tau-\tau_\ell,\nu-\nu_\ell) + [\mathcal{R}((\nu-\frac{\nu_1+\nu_2}{2})T-\omega_1(\tau_0-\tau_1)) \\ + \mathcal{R}((\nu-\frac{\nu_1+\nu_2}{2})T+\omega_1(\tau_0-\tau_1))]\chi_{\mathcal{P},\mathcal{Q}}(\tau-\tau_0,\nu-\nu_0)\chi_{\mathcal{P},\mathcal{Q}}(\tau-\tau_1,\nu-\nu_1). \tag{3.19}$$

Thus the above two cross terms are centered at

$$\nu_{cr} = \frac{\nu_0+\nu_1}{2} \pm \frac{\omega_1(\tau_0-\tau_1)}{T} \tag{3.20}$$

in Doppler.

3.3 Coprime OFDM $(\mathcal{P},\mathcal{Q})$ Pulse Trains

Suppose the radar system can utilize two frequency bands $\mathcal{B}_1$ and $\mathcal{B}_2$. The frequency band $\mathcal{B}_1$ consists of $2K_1-1$ subcarriers with the central frequencies $\omega_{c,1}-\omega_{K_1-1,1},...,\omega_{c,1},...,\omega_{c,1}+\omega_{K_1-1,1}$ respectively. The frequency band $\mathcal{B}_2$ consists of $2K_2-1$ subcarriers with the central frequencies $\omega_{c,2} - \omega_{K_2-1,2}, ..., \omega_{c,2}, ..., \omega_{c,2} + \omega_{K_2-1,2}$ respectively. As in section 3.2, over each subcarrier the radar transmits a time delayed $\mathcal{P}$-pulse train $z_{\mathcal{P}}(t)$, and the receiver correlates the radar return with a $\mathcal{Q}$-pulse train $z_{\mathcal{Q}}(t)$. In specific, over the subcarriers in $\mathcal{B}_1$ with central frequencies $\omega_{c,1} \pm \omega_{k,1}$, the transmit and receive pulse trains are

$$\begin{cases} z_{\mathcal{P}_{1,k}}(t) = z_{\mathcal{P}}(t - kK_2T/2) \\ z_{\mathcal{Q}_{1,k}}(t) = h_k z_{\mathcal{Q}}(t - kK_2T/2) \end{cases}, k = 0, ..., K_1 - 1. \tag{3.21}$$

Over the subcarriers in $\mathcal{B}_2$ with central frequencies $\omega_{c,2} \pm \omega_{k,2}$, the transmit and receive pulse trains are

$$\begin{cases} z_{\mathcal{P}_{2,k}}(t) = z_{\mathcal{P}}(t - kK_1T/2) \\ z_{\mathcal{Q}_{2,k}}(t) = g_k z_{\mathcal{Q}}(t - kK_1T/2) \end{cases}, k = 0, ..., K_2 - 1. \tag{3.22}$$

Accordingly, we have the following expressions of the cross ambiguity functions:

$$\chi_{\mathcal{P}_{1,k},\mathcal{Q}_{1,k}}(\tau, \nu) = h_k e^{-j\nu k K_2 T/2} \chi_{\mathcal{P},\mathcal{Q}}(\tau, \nu), \ k = 0, ..., K_1 - 1, \tag{3.23}$$

$$\chi_{\mathcal{P}_{2,k},\mathcal{Q}_{2,k}}(\tau, \nu) = g_k e^{-j\nu k K_1 T/2} \chi_{\mathcal{P},\mathcal{Q}}(\tau, \nu), \ k = 0, ..., K_2 - 1. \tag{3.24}$$

Denote $\xi_{1,k}$ as the product of two matched filters' output over the subcarriers in $\mathcal{B}_1$ with central frequencies $\omega_{c,1} \pm \omega_{k,1}$. By ignoring the common bulk phase term we have

$$\begin{aligned} \sum_{k=0}^{K_1-1} \xi_{1,k}(\tau, \nu) &= \sum_{k=0}^{K_1-1} \chi^2_{\mathcal{P}_{1,k},\mathcal{Q}_{1,k}}(\tau - \tau_0, \nu - \nu_0) \\ &\triangleq \eta_1(\tau - \tau_0, \nu - \nu_0), \end{aligned} \tag{3.25}$$

where the function $\eta_1(\tau, \nu)$ can be written by

$$\begin{aligned} \eta_1(\tau, \nu) &= \sum_{k=0}^{K_1-1} h_k^2 e^{-j\nu k K_2 T} \chi^2_{\mathcal{P},\mathcal{Q}}(\tau, \nu) \\ &= H(K_2\theta) \chi^2_{\mathcal{P},\mathcal{Q}}(\tau, \nu), \end{aligned} \tag{3.26}$$

and $H(\theta) = \sum_{k=0}^{K_1-1} h_k^2 e^{-jk\theta}$ is the spectrum of the length-K_1 sequence $\{h_k^2\}_{k=0}^{K_1-1}$. Similarly, by combining the measurements from frequency band $\mathcal{B}_2$, we can have

$$\begin{aligned} \sum_{k=0}^{K_2-1} \xi_{2,k}(\tau, \nu) &= \sum_{k=0}^{K_2-1} \chi^2_{\mathcal{P}_{2,k},\mathcal{Q}_{2,k}}(\tau - \tau_0, \nu - \nu_0) \\ &\triangleq \eta_2(\tau - \tau_0, \nu - \nu_0), \end{aligned} \tag{3.27}$$

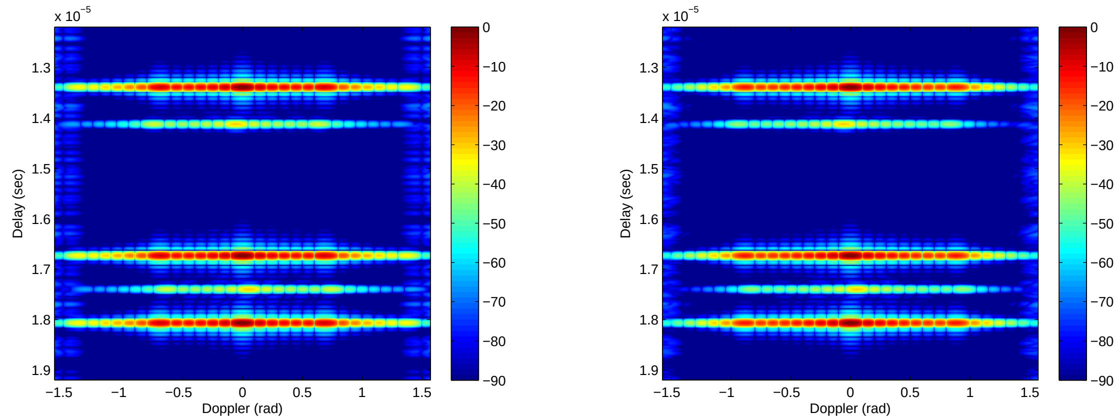

(a) (b)

Figure 3.3: Range and Doppler map for the measurements collected over frequency bands $\mathcal{B}_1$ and $\mathcal{B}_2$, $K_1 = 7$ and $K_2 = 9$. (a) $\sum_{k=0}^{K_1-1} \xi_{1,k}(\tau, \nu)$, (b) $\sum_{k=0}^{K_2-1} \xi_{2,k}(\tau, \nu)$.

where

$$\begin{aligned} \eta_2(\tau, \nu) &= \sum_{k=0}^{K_2-1} g_k^2 e^{-j\nu k K_1 T} \chi_{\mathcal{P},\mathcal{Q}}^2(\tau, \nu) \\ &= G(K_1\theta)\chi_{\mathcal{P},\mathcal{Q}}^2(\tau, \nu). \end{aligned} \tag{3.28}$$

and $G(\theta) = \sum_{k=0}^{K_2-1} g_k^2 e^{-jk\theta}$ is the spectrum of the length-K_2 sequence $\{g_k^2\}_{k=0}^{K_2-1}$. Therefore, the functions $\eta_1(\tau, \nu)$ and $\eta_2(\tau, \nu)$ are obtained by modulating the square of cross ambiguity function $\chi_{\mathcal{P},\mathcal{Q}}^2(\tau, \nu)$ with the spectrum $H(K_2\theta)$ and $G(K_1\theta)$ respectively. The spectrums $H(K_2\theta)$ and $G(K_1\theta)$ have periodicity $\frac{2\pi}{K_2}$ and $\frac{2\pi}{K_1}$, and their mainlobe width are both $\mathcal{O}(\frac{1}{K_1 K_2})$. Fig. 3.3 shows the range and Doppler map for the measurements $\sum_{k=0}^{K_1-1} \xi_{1,k}(\tau, \nu)$ and $\sum_{k=0}^{K_2-1} \xi_{2,k}(\tau, \nu)$ in eq. (3.25) and (3.27). We set $K_1 = 7$ and $K_2 = 9$. The sequences $\{h_k\}_{k=0}^{K_1-1}$ and $\{g_k\}_{k=0}^{K_2-1}$ are set to be all 1 sequences. The Doppler resolution $\Delta\theta = \frac{4\pi}{K_1 K_2} = \frac{4\pi}{63}$. However, since the periodic pattern of $H(K_2\theta)$ and $G(K_1\theta)$, some "artificial targets" appear in the screen. The following theorem demonstrates how to eliminate the artifact issue:

Theorem 3.3.1. *Suppose the spectrum $H(\theta)$ and $G(\theta)$ are ideally lowpass such that $H(\theta)$ is nonzero only within $|\theta| \leq \frac{\pi}{K_1}$, and $G(\theta)$ is nonzero only within $|\theta| \leq \frac{\pi}{K_2}$. If the integers K_1 and K_2 are coprime, then for $\theta \in [-\pi, \pi]$, the product spectrum $H(K_2\theta)G(K_1\theta)$ is nonzero*

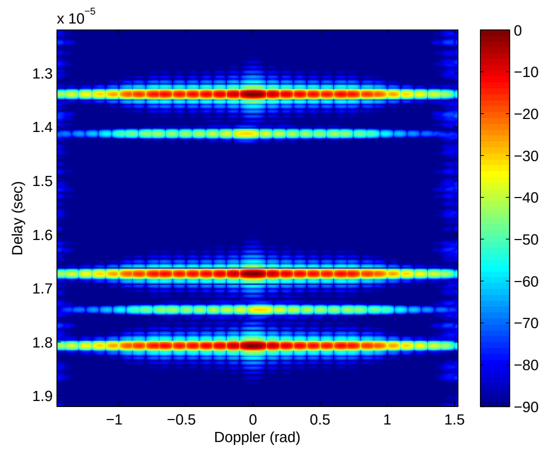

Figure 3.4: Product of measurements $\sum_{k=0}^{K_1-1} \xi_{1,k}(\tau,\nu)$ and $\sum_{k=0}^{K_2-1} \xi_{2,k}(\tau,\nu)$. Artificial targets are removed.

only within $|\theta| \leq \frac{\pi}{K_1K_2}$. *In other words,* $H(K_2\theta)G(K_1\theta)$ *is ideally lowpass with bandwidth* $\frac{2\pi}{K_1K_2}$.

Proof: The original proof is given in [75]. For illustration purpose, here we simply recap the proof. The spectrum $H(K_2\theta)$ has K_2 passbands with width $\frac{2\pi}{K_1K_2}$ each. The K_2 passbands are centered at $\frac{2\pi k_2}{K_2} = \frac{2\pi K_1 k_2}{K_1K_2}$, $k_2 = 0, ..., K_2 - 1$. Similarly, the spectrum $G(K_1\theta)$ has K_1 passbands with width $\frac{2\pi}{K_1K_2}$ each. The K_1 passbands are centered at $\frac{2\pi k_1}{K_1} = \frac{2\pi K_2 k_1}{K_1K_2}$, $k_1 = 0, ..., K_1 - 1$. Since K_1 and K_2 are coprime, $K_1k_2 \neq K_2k_1$ except for $k_1 = k_2 = 0$.

Theorem 3.3.1 guarantees that product of $\eta_1(\tau,\nu)$ and $\eta_2(\tau,\nu)$

$$\eta_1(\tau,\nu)\eta_2(\tau,\nu) = H(K_2\theta)G(K_1\theta)\chi^4_{\mathcal{P},\mathcal{Q}}(\tau,\nu). \tag{3.29}$$

has a unique peak at $(0,0)$ if the spectrums $H(\theta)$ and $\mathrm{G}(\theta)$ both have lowpass behavior. Hence the the function $H(K_2\theta)G(K_1\theta)\chi^4_{\mathcal{P},\mathcal{Q}}(\tau,\nu)$ can serve as the point-spread-function of the new radar system, where the inputs of the system are the fourth power of targets's scattering functions. It is clear that the Doppler resolution of the point-spread-function $H(K_2\theta)G(K_1\theta)\chi^4_{\mathcal{P},\mathcal{Q}}(\tau,\nu)$ is $\mathcal{O}(\frac{1}{K_1K_2})$.

Fig. 3.4 shows that product of measurements Product of measurements $\sum_{k=0}^{K_1-1} \xi_{1,k}(\tau,\nu)$ and $\sum_{k=0}^{K_2-1} \xi_{2,k}(\tau,\nu)$. Due to the coprimality between K_1 and K_2, The artifacts in Fig. 3.3

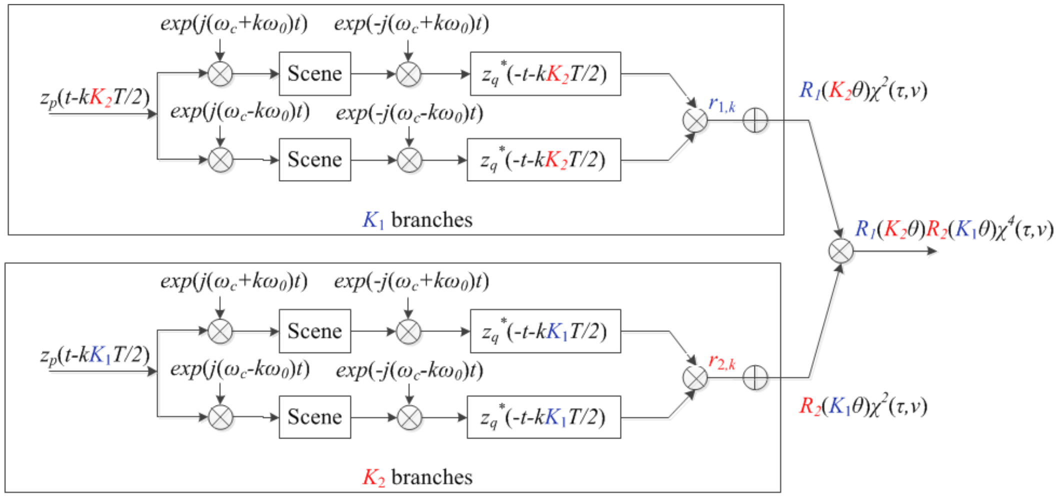

Figure 3.5: Implementation of coprime OFDM radar using Golay complementary waveforms.

are removed, whereas the desired Doppler resolution is maintained.

Remark 3.3.1. Compared to the OFDM $(\mathcal{P},\mathcal{Q})$ pulse trains derived in section 3.2, the coprime OFDM $(\mathcal{P},\mathcal{Q})$ pulse trains can significant compress the required frequency bandwidth. If the desired Doppler resolution is $\mathcal{O}(\frac{1}{K_1K_2})$, where K_1 and K_2 are coprime integers, the number of required subcarriers for a OFDM $(\mathcal{P},\mathcal{Q})$ pulse train is $\mathcal{O}(K_1K_2)$, whereas the number of required subcarriers for a coprime OFDM $(\mathcal{P},\mathcal{Q})$ pulse train is only $\mathcal{O}(K_1+K_2)$. We will see the price paid for this bandwidth compression in section 3.5. Readers can refer to Fig. 3.5 for the implementation of coprime OFDM radar.

3.4 $(\mathcal{P},\mathcal{Q})$ Pulse Train Obtained by Sequence Repetition

Suppose a length-N_1 $(\mathcal{P}_1,\mathcal{Q}_1)$ pulse train design has an M_1-th order-null range sidelobe of cross ambiguity function at $\theta=0$. From the sequences $\mathcal{P}_1=\{p_1[r]\}_{r=0}^{N_1-1}$ and $\mathcal{Q}_1=\{q_1[r]\}_{r=0}^{N_1-1}$ we construct the length-N_1N_2 sequences $\widetilde{\mathcal{P}}_1=\{\widetilde{p}_1[r]\}_{r=0}^{N_1N_2-1}$ and $\widetilde{\mathcal{Q}}_1=\{\widetilde{q}_1[r]\}_{r=0}^{N_1N_2-1}$ as follows. Let $\widetilde{p}_1[bN_1+r]=p_1[r]$ and $\widetilde{q}_1[bN_1+r]=h_bq_1[r]$ for $r=0,1,...,N_1-1$ and $b=0,1,...,N_2-1$. In other words, the sequences $\widetilde{\mathcal{P}}_1$ and $\widetilde{\mathcal{Q}}_1$

are generated by repeating sequences $\mathcal{P}_1$ and $\mathcal{Q}_1$ for N_2 times. From this, the new $\mathcal{P}$ and $\mathcal{Q}$ pulse trains are

$$z_{\widetilde{\mathcal{P}}_1}(t) = \sum_{b=0}^{N_2-1} z_{\mathcal{P}_1}(t - bN_1T), \tag{3.30}$$

and

$$z_{\widetilde{\mathcal{Q}}_1}(t) = \sum_{b=0}^{N_2-1} h_b z_{\mathcal{Q}_1}(t - bN_1T). \tag{3.31}$$

The cross ambiguity function of $z_{\widetilde{\mathcal{P}}_1}(t)$ and $z_{\widetilde{\mathcal{Q}}_1}(t)$ is

$$\begin{aligned}
&\chi_{\widetilde{\mathcal{P}}_1,\widetilde{\mathcal{Q}}_1}(\tau,\nu)\\
&= \sum_{b=0}^{N_2-1}\sum_{r=0}^{N_1-1} \widetilde{q}_1[bN+r]e^{j(bN+r)\nu T} \sum_{k=-(L-1)}^{L-1} [\widetilde{p}_1[bN+r]C_x[k] + \overline{\widetilde{p}}_1[bN+r]C_y[k]]\chi_\Omega(\tau - kT_c,\nu)\\
&= \sum_{b=0}^{N_2-1} e^{jbN\theta} \sum_{r=0}^{N_1-1} \widetilde{q}_1[bN+r]e^{jr\theta} \sum_{k=-(L-1)}^{L-1} [\widetilde{p}_1[bN+r]C_x[k] + \overline{\widetilde{p}}_1[bN+r]C_y[k]]\chi_\Omega(\tau - kT_c,\nu)\\
&= \sum_{b=0}^{N_2-1} h_b e^{jbN\theta} \sum_{r=0}^{N_1-1} q_1[r]e^{jr\theta} \sum_{k=-(L-1)}^{L-1} [p_1[r]C_y[k] + \overline{p}_1[r]C_y[k]]\chi_\Omega(\tau - kT_c,\nu)\\
&= H(-N_2\theta)\chi_{\mathcal{P}_1,\mathcal{Q}_1}(\tau,\nu),
\end{aligned} \tag{3.32}$$

where $H(\theta) = \sum_{b=0}^{N_2-1} h_b e^{-jb\theta}$ is the spectrum of the length-N_2 sequence $\{h_b\}_{b=0}^{N_2-1}$.

Suppose a length-N_2 $(\mathcal{P}_2, \mathcal{Q}_2)$ pulse train design has an M_2-th order-null range sidelobe of cross ambiguity function at $\theta = 0$. From the sequences $\mathcal{P}_2 = \{p_2[r]\}_{r=0}^{N_2-1}$ and $\mathcal{Q}_2 = \{q_2[r]\}_{r=0}^{N_2-1}$ we construct the length-N_1N_2 sequences $\widetilde{\mathcal{P}}_2 = \{\widetilde{p}_2[r]\}_{r=0}^{N_1N_2-1}$ and $\widetilde{\mathcal{Q}}_2 = \{\widetilde{q}_2[r]\}_{r=0}^{N_1N_2-1}$ as follows. Let $\widetilde{p}_2[bN_2+r] = p_2[r]$ and $\widetilde{q}_2[bN_2+r] = g_b q_2[r]$ for $r = 0,1,...,N_2-1$ and $b = 0,1,...,N_1-1$. Similarly, the cross ambiguity function of $z_{\widetilde{\mathcal{P}}_2}(t)$ and $z_{\widetilde{\mathcal{Q}}_2}(t)$ is

$$\chi_{\widetilde{\mathcal{P}}_2,\widetilde{\mathcal{Q}}_2}(\tau,\nu) = G(-N_1\theta)\chi_{\mathcal{P}_2,\mathcal{Q}_2}(\tau,\nu), \tag{3.33}$$

where $G(\theta) = \sum_{b=0}^{N_1-1} g_b e^{-jb\theta}$ is the spectrum of the length-N_1 sequence $\{g_b\}_{b=0}^{N_1-1}$.

Now let the radar transmit the $\mathcal{P}$ pulse trains $z_{\widetilde{\mathcal{P}}_1}(t)$ and $z_{\widetilde{\mathcal{P}}_2}(t)$. The transmission of $z_{\widetilde{\mathcal{P}}_1}(t)$ and $z_{\widetilde{\mathcal{P}}_2}(t)$ can be separated in frequency or time. The receiver correlates the radar

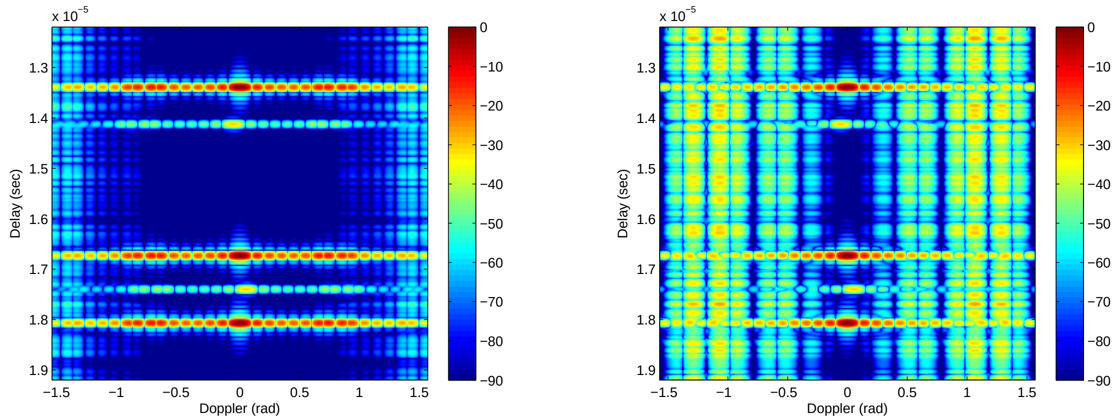

(a) (b)

Figure 3.6: (a) Range and Doppler map of the product $\xi(\tau,\nu) = z_1(\tau,\nu)$ and $z_2(\tau,\nu)$, $N_1 = 7$ and $N_2 = 9$, (b) length-64 PTM design.

returns of $z_{\widetilde{\mathcal{P}}_1}(t)$ and $z_{\widetilde{\mathcal{P}}_2}(t)$ with $z_{\widetilde{\mathcal{Q}}_1}(t)$ and $z_{\widetilde{\mathcal{Q}}_2}(t)$ respectively. If the radar scene contains a target with coordinate (τ_0, ν_0), by omitting the bulk phases the outputs of two matched filters are

$$z_1(\tau,\nu) = H(-N_2(\nu-\nu_0)T)\chi_{\mathcal{P}_1,\mathcal{Q}_1}(\tau-\tau_0,\nu-\nu_0), \tag{3.34}$$

and

$$z_2(\tau,\nu) = G(-N_1(\nu-\nu_0)T)\chi_{\mathcal{P}_2,\mathcal{Q}_2}(\tau-\tau_0,\nu-\nu_0). \tag{3.35}$$

The product of $z_1(\tau,\nu)$ and $z_2(\tau,\nu)$ is

$$\xi(\tau,\nu) = H(-N_2(\nu-\nu_0)T)G(-N_1(\nu-\nu_0)T)\chi_{\widetilde{\mathcal{P}}_1,\widetilde{\mathcal{Q}}_1}(\tau-\tau_0,\nu-\nu_0)\chi_{\widetilde{\mathcal{P}}_2,\widetilde{\mathcal{Q}}_2}(\tau-\tau_0,\nu-\nu_0). \tag{3.36}$$

Therefore the function $H(-N_2\theta)G(-N_1\theta)\chi_{\widetilde{\mathcal{P}}_1,\widetilde{\mathcal{Q}}_1}(\tau,\nu)\chi_{\widetilde{\mathcal{P}}_2,\widetilde{\mathcal{Q}}_2}(\tau,\nu)$ can be viewed as the point-spread-function of the new radar system. If integers N_1 and N_2 are coprime, from theorem 3 we know that the Doppler resolution of the point-spread function is $\mathcal{O}(\frac{1}{N_1N_2})$. And the point spread function should have desired range sidelobe suppression ability since $(\mathcal{P}_1,\mathcal{Q}_1)$ and $(\mathcal{P}_2,\mathcal{Q}_2)$ pulse train designs have good range sidelobe suppressions.

Fig. 3.6(a) illustrates the range and Doppler map of the product $\xi(\tau,\nu) = z_1(\tau,\nu)$ and $z_2(\tau,\nu)$. We set $N_1 = 7$ and $N_2 = 9$. The sequences $\{h_b\}_{b=0}^{N_2-1}$ and $\{g_b\}_{b=0}^{N_1-1}$ are selected as all 1 sequences. The pulse train design $(\mathcal{P}_1, \mathcal{Q}_1)$ is a length-N_1 Binomial design, and the pulse train design $(\mathcal{P}_2, \mathcal{Q}_2)$ is a length-N_2 Binomial design. Therefore, the lengths of pulse train designs $(\widetilde{\mathcal{P}}_1, \widetilde{\mathcal{Q}}_1,)$ and $(\widetilde{\mathcal{P}}_1, \widetilde{\mathcal{Q}}_1,)$ are both $N_1N_2 = 63$, and the Doppler resolution of the function $H(-N_2\theta)\cdot G(-N_1\theta)\chi_{\widetilde{\mathcal{P}}_1,\widetilde{\mathcal{Q}}_1}(\tau,\nu)$ is $\Delta\theta = \frac{4\pi}{N_1N_2} = \frac{4\pi}{63}$. As a benchmark, the range and Doppler map for the length-64 PTM design is plotted in Fig. 3.6(b). Although the length-64 PTM design presents comparable Doppler resolution, its point-spread-function has a much narrower Doppler band. This is because for the length-64 PTM design, its range sidelobe only has a $(\log_2(64) - 1 = 5)$th order of null at $\theta = 0$. But for the design depicted in Fig. 3.6(a), the null order of its range sidelobe is $\frac{N_1+N_2}{2} = 8$.

3.5 SNR Analysis

3.5.1 OFDM $(\mathcal{P}, \mathcal{Q})$ Pulse Train

For simplicity, here we assume that the target's scattering coefficients over all subcarrier are identical (unity). The matched filter outputs are

$$\begin{cases} z_k = r_k\left[e^{-j(\omega_c+\omega_k)\tau_0}e^{j(\nu_0-\nu)\tau_0}\alpha_k\chi_{\mathcal{P},\mathcal{Q}}(0,0) + \chi_{\mathcal{N}_k,\mathcal{Q}}(\tau_0,\nu_0)\right] \\ z'_k = r'_k\left[e^{-j(\omega_c-\omega_k)\tau_0}e^{j(\nu_0-\nu)\tau_0}\alpha'_k\chi_{\mathcal{P},\mathcal{Q}}(0,0) + \chi_{\mathcal{N}'_k,\mathcal{Q}}(\tau_0,\nu_0)\right] \end{cases}, k = 0, 1, ..., K-1. \tag{3.37}$$

thus the product of z_k and z'_k is

$$\xi_k = \gamma_k[e^{-j2\omega_c\tau_0}e^{j2(\nu_0-\nu)\tau_0}\alpha_k\alpha'_k\chi^2_{\mathcal{P},\mathcal{Q}}(0,0) + \phi_k], \tag{3.38}$$

where $\gamma_k = r_kr'_k$, and ϕ_k is the noise component in ξ_k:

$$\begin{aligned} \phi_k &= e^{-j(\omega_c-\omega_k)\tau_0}e^{j(\nu_0-\nu)\tau_0}\alpha'_k\chi_{\mathcal{P},\mathcal{Q}}(0,0)\chi_{\mathcal{N}_k,\mathcal{Q}}(\tau_0,\nu_0) \\ &\quad + e^{-j(\omega_c+\omega_k)\tau_0}e^{j(\nu_0-\nu)\tau_0}\alpha_k\chi_{\mathcal{P},\mathcal{Q}}(0,0)\chi_{\mathcal{N}'_k,\mathcal{Q}}(\tau_0,\nu_0) + \chi_{\mathcal{N}_k,\mathcal{Q}}(\tau_0,\nu_0)\chi_{\mathcal{N}'_k,\mathcal{Q}}(\tau_0,\nu_0). \end{aligned} \tag{3.39}$$

Then the signal power of the composite measurement $\sum_{k=0}^{K-1}\xi_k$ is

$$\begin{aligned} P_s &= |\sum_{k=0}^{K-1}\gamma_ke^{-j2\omega_c\tau_0}e^{j2(\nu_0-\nu)\tau_0}\alpha_k\alpha'_k\chi^2_{\mathcal{P},\mathcal{Q}}(0,0)|^2 \\ &= |\sum_{k=0}^{K-1}\gamma_k\alpha_k\alpha'_k|^2\chi^4_{\mathcal{P},\mathcal{Q}}(0,0). \end{aligned} \tag{3.40}$$

The noise power of $\sum_{k=0}^{K-1} \xi_k$ is

$$
\begin{aligned}
P_n &= E\big\{\big|\sum_{k=0}^{K-1} \gamma_k \phi_k\big|^2\big\} \\
&= \sum_{k=0}^{K-1} |\gamma_k|^2 E\big\{|\phi_k|^2\big\}.
\end{aligned}
\tag{3.41}
$$

The second equation of (3.41) is due to the noise independence. For each k, it is also easy to show that

$$
\begin{aligned}
E\big\{\chi_{\mathcal{N}_k,\mathcal{Q}}(\tau_0,\nu_0)\overline{\chi_{\mathcal{N}'_k,\mathcal{Q}}(\tau_0,\nu_0)}\big\} &= 0, \\
E\big\{\chi_{\mathcal{N}_k,\mathcal{Q}}(\tau_0,\nu_0)\overline{\chi_{\mathcal{N}_k,\mathcal{Q}}(\tau_0,\nu_0)\chi_{\mathcal{N}'_k,\mathcal{Q}}(\tau_0,\nu_0)}\big\} &= 0, \\
E\big\{\chi_{\mathcal{N}'_k,\mathcal{Q}}(\tau_0,\nu_0)\overline{\chi_{\mathcal{N}_k,\mathcal{Q}}(\tau_0,\nu_0)\chi_{\mathcal{N}'_k,\mathcal{Q}}(\tau_0,\nu_0)}\big\} &= 0.
\end{aligned}
\tag{3.42}
$$

Therefore we have

$$
P_n = \sum_{k=0}^{K-1} |\gamma_k|^2 \big[|\alpha'_k|^2 \chi_{\mathcal{P},\mathcal{Q}}(0,0)^2 \eta_k + |\alpha_k|^2 \chi_{\mathcal{P},\mathcal{Q}}(0,0)^2 \eta'_k + \eta_k \eta'_k\big], \tag{3.43}
$$

where $\eta_k = E\{|\chi_{\mathcal{N}_k,\mathcal{Q}}(\tau_0,\nu_0)|^2\}$ and $\eta'_k = E\{|\chi_{\mathcal{N}'_k,\mathcal{Q}}(\tau_0,\nu_0)|^2\}$. Define the ratios $\rho_k = \chi_{\mathcal{P},\mathcal{Q}}(0,0)^2/\eta_k$ and $\rho'_k = \chi_{\mathcal{P},\mathcal{Q}}(0,0)^2/\eta'_k$. Therefore the signal to noise ratio is

$$
\begin{aligned}
\mathrm{SNR} &= \frac{P_s}{P_n} \\
&= \frac{|\sum_{k=0}^{K-1} \gamma_k \alpha_k \alpha'_k|^2}{\sum_{k=0}^{K-1} |\gamma_k|^2 \big[|\alpha'_k|^2 \rho_k^{-1} + |\alpha_k|^2 \rho_k'^{-1} + \rho_k^{-1}\rho_k'^{-1}\big]}
\end{aligned}
\tag{3.44}
$$

Denote $\mathrm{SNR}_k = |\alpha_k|^2 \rho_k$ and $\mathrm{SNR}'_k = |\alpha'_k|^2 \rho'_k$ as the SNRs over the subcarriers at central frequencies $\omega_c \pm \omega_k$ respectively. Since $\rho_k^{-1}\rho_k'^{-1} = (|\alpha'_k|^2\rho'_k)^{-1}|\alpha'_k|^2\rho_k^{-1} = (|\alpha_k|^2\rho_k)^{-1}|\alpha_k|^2\rho_k'^{-1}$, at high SNR regime we may drop the term $\rho_k^{-1}\rho_k'^{-1}$ from denominator of eq (3.44). Therefore the SNR can be approximated by

$$
\mathrm{SNR} = \frac{|\sum_{k=0}^{K-1} \gamma_k \alpha_k \alpha'_k|^2}{\sum_{k=0}^{K-1} |\gamma_k|^2 \big[|\alpha'_k|^2 \rho_k^{-1} + |\alpha_k|^2 \rho_k'^{-1}\big]}. \tag{3.45}
$$

Using Cauchy-Schwarz inequality, we have

$$
\begin{aligned}
|\sum_{k=0}^{K-1} \gamma_k \alpha_k \alpha'_k|^2 &= \frac{1}{4}\big|\sum_{k=0}^{K-1} (\gamma_k \alpha'_k \sqrt{\rho_k^{-1}})(\alpha_k \sqrt{\rho_k}) + (\gamma_k \alpha_k \sqrt{\rho_k'^{-1}})(\alpha_k \sqrt{\rho'_k})\big|^2 \\
&\le \frac{1}{4}\big(\sum_{k=0}^{K-1} |\gamma_k|^2 \big[|\alpha'_k|^2 \rho_k^{-1} + |\alpha_k|^2 \rho_k'^{-1}\big]\big)\big(\sum_{k=0}^{K-1} |\alpha_k|^2 \rho_k + |\alpha'_k|^2 \rho'_k\big).
\end{aligned}
\tag{3.46}
$$

This shows that

$$\text{SNR} \leq \frac{1}{4}\sum_{k=0}^{K-1}(\text{SNR}_k + \text{SNR}'_k). \tag{3.47}$$

This means that the signal to noise ratio is attenuated at least by a factor of 4 due to the non-linear processing.

If assume that $\alpha_k = \alpha'_k = \alpha$, and $\rho_k = \rho'_k = \rho$ for all k, then the SNR becomes

$$\text{SNR} = \frac{|\alpha|^2\rho}{2}\frac{|\sum_{k=0}^{K-1}\gamma_k|^2}{\sum_{k=0}^{K-1}|\gamma_k|^2}. \tag{3.48}$$

Clearly, the SNR is maximized when the sequence $\{\gamma_k\}_{k=0}^{K-1}$ is collinear to an all 1 sequence, and the maximum SNR is $\text{SNR}_{max} = \frac{K}{2}|\alpha|^2\rho$.

3.5.2 Coprime OFDM $(\mathcal{P}, \mathcal{Q})$ Pulse Train

The k-th product of matched filter outputs in first and second filter-bank are

$$\begin{cases} \xi_{k,1} = \gamma_{k,1}[c_1\alpha_{k,1}\alpha'_{k,1}\chi^2_{\mathcal{P},\mathcal{Q}}(0,0) + \phi_{k,1}], k = 0, ..., K_1 - 1, \\ \xi_{k,2} = \gamma_{k,2}[c_2\alpha_{k,2}\alpha'_{k,2}\chi^2_{\mathcal{P},\mathcal{Q}}(0,0) + \phi_{k,2}], k = 0, ..., K_2 - 1, \end{cases} \tag{3.49}$$

where the complex constants c_1 and c_2 are $c_1 = e^{-j2\omega_{c,1}\tau_0}e^{j2(\nu_0-\nu)\tau_0}$, $c_2 = e^{-j2\omega_{c,2}\tau_0}e^{j2(\nu_0-\nu)\tau_0}$. The noise terms over $\phi_{k,1}$ and $\phi_{k,2}$ over OFDM blocks $\mathcal{B}_1$ and $\mathcal{B}_2$ are defined similarly as eq. (3.39). Thus for the measurement $\sum_{k=0}^{K_1-1}\xi_{k,1}\sum_{k=0}^{K_2-1}\xi_{k,2}$, its signal power is

$$\begin{aligned} P_s &= \Big|c_1\sum_{k=0}^{K_1-1}\gamma_{k,1}\alpha_{k,1}\alpha'_{k,1}\chi^2_{\mathcal{P},\mathcal{Q}}(0,0)c_2\sum_{k=0}^{K_2-1}\gamma_{k,2}\alpha_{k,2}\alpha'_{k,2}\chi^2_{\mathcal{P},\mathcal{Q}}(0,0)\Big|^2 \\ &= \Big|\sum_{k=0}^{K_1-1}\gamma_{k,1}\alpha_{k,1}\alpha'_{k,1}\Big|^2\Big|\sum_{k=0}^{K_2-1}\gamma_{k,2}\alpha_{k,2}\alpha'_{k,2}\Big|^2\chi^8_{\mathcal{P},\mathcal{Q}}(0,0). \end{aligned} \tag{3.50}$$

The noise power for $\sum_{k=0}^{K_1-1}\xi_{k,1}\sum_{k=0}^{K_2-1}\xi_{k,2}$ is

$$\begin{aligned} p[n] = E\Big\{\Big|\sum_{k=0}^{K_1-1}\gamma_{k,1}\phi_{k,1}\Big|^2\Big\}\Big|\sum_{k=0}^{K_2-1}\gamma_{k,2}\alpha_{k,2}\alpha'_{k,2}\Big|^2\chi^4_{\mathcal{P},\mathcal{Q}}(0,0) \\ + E\Big\{\Big|\sum_{k=0}^{K_2-1}\gamma_{k,2}\phi_{k,2}\Big|^2\Big\}\Big|\sum_{k=0}^{K_2-1}\gamma_{k,1}\alpha_{k,1}\alpha'_{k,1}\Big|^2\chi^4_{\mathcal{P},\mathcal{Q}}(0,0) + E\Big\{\Big|\sum_{k=0}^{K_1-1}\gamma_{k,1}\phi_{k,1}\Big|^2\Big\}E\Big\{\Big|\sum_{k=0}^{K_2-1}\gamma_{k,2}\phi_{k,2}\Big|^2\Big\}. \end{aligned} \tag{3.51}$$

Note that

$$\frac{E\{|\sum_{k=0}^{K_1-1}\gamma_{k,1}\phi_{k,1}|^2\}|\sum_{k=0}^{K_2-1}\gamma_{k,2}\alpha_{k,2}\alpha'_{k,2}|^2\chi^4_{\mathcal{P},\mathcal{Q}}(0,0)}{E\{|\sum_{k=0}^{K_1-1}\gamma_{k,1}\phi_{k,1}|^2\}E\{|\sum_{k=0}^{K_2-1}\gamma_{k,2}\phi_{k,2}|^2\}} = \frac{|\sum_{k=0}^{K_2-1}\gamma_{k,2}\alpha_{k,2}\alpha'_{k,2}|^2\chi^4_{\mathcal{P},\mathcal{Q}}(0,0)}{E\{|\sum_{k=0}^{K_2-1}\gamma_{k,2}\phi_{k,2}|^2\}} \triangleq \mathrm{SNR}_2,$$
$$\frac{E\{|\sum_{k=0}^{K_2-1}\gamma_{k,2}\phi_{k,2}|^2\}|\sum_{k=0}^{K_1-1}\gamma_{k,1}\alpha_{k,1}\alpha'_{k,1}|^2\chi^4_{\mathcal{P},\mathcal{Q}}(0,0)}{E\{|\sum_{k=0}^{K_1-1}\gamma_{k,1}\phi_{k,1}|^2\}E\{|\sum_{k=0}^{K_2-1}\gamma_{k,2}\phi_{k,2}|^2\}} = \frac{|\sum_{k=0}^{K_1-1}\gamma_{k,1}\alpha_{k,1}\alpha'_{k,1}|^2\chi^4_{\mathcal{P},\mathcal{Q}}(0,0)}{E\{|\sum_{k=0}^{K_1-1}\gamma_{k,1}\phi_{k,1}|^2\}} \triangleq \mathrm{SNR}_1, \tag{3.52}$$

where SNR_1 and SNR_2 are the SNRs for $\sum_{k=0}^{K_1-1}\xi_{k,1}$ and $\sum_{k=0}^{K_2-1}\xi_{k,2}$ respectively. Thus for large SNR_1 and SNR_2, we may drop the third term on the right hand side of eq. (3.51). Therefore the SNR of $\sum_{k=0}^{K_1-1}\xi_{k,1}\sum_{k=0}^{K_2-1}\xi_{k,2}$ can be approximated by

$$\begin{aligned}\mathrm{SNR} &= \frac{|\sum_{k=0}^{K_1-1}\gamma_{k,1}\alpha_{k,1}\alpha'_{k,1}|^2|\sum_{k=0}^{K_2-1}\gamma_{k,2}\alpha_{k,2}\alpha'_{k,2}|^2\chi^4_{\mathcal{P},\mathcal{Q}}(0,0)}{E\{|\sum_{k=0}^{K_1-1}\gamma_{k,1}\phi_{k,1}|^2\}|\sum_{k=0}^{K_2-1}\gamma_{k,2}\alpha_{k,2}\alpha'_{k,2}|^2+E\{|\sum_{k=0}^{K_2-1}\gamma_{k,2}\phi_{k,2}|^2\}|\sum_{k=0}^{K_1-1}\gamma_{k,1}\alpha_{k,1}\alpha'_{k,1}|^2}\\ &= \left(\frac{1}{\mathrm{SNR}_1}+\frac{1}{\mathrm{SNR}_2}\right)^{-1}\\ &\le \frac{1}{4}(\mathrm{SNR}_1+\mathrm{SNR}_2).\end{aligned} \tag{3.53}$$

Using eq. (3.47), we have

$$\mathrm{SNR} \le \frac{1}{16}\Big[\sum_{k=0}^{K_1-1}(\mathrm{SNR}_{k,1}+\mathrm{SNR}'_{k,1})+\sum_{k=0}^{K_2-1}(\mathrm{SNR}_{k,2}+\mathrm{SNR}'_{k,2})\Big], \tag{3.54}$$

where $\mathrm{SNR}_{k,1}$ and $\mathrm{SNR}'_{k,1}$ are the SNRs over the subcarriers at central frequencies $\omega_{c,1}\pm\omega_{k,1}$ in $\mathcal{B}_1$ respectively. And $\mathrm{SNR}_{k,2}$ and $\mathrm{SNR}'_{k,2}$ are the SNRs over the subcarriers at central frequencies $\omega_{c,2}\pm\omega_{k,2}$ in $\mathcal{B}_2$ respectively.

As a special case, when the coefficients $\{\alpha_{k,1},\alpha'_{k,1}\}_{k=0}^{K_1-1}$ and $\{\alpha_{k,2},\alpha'_{k,2}\}_{k=0}^{K_2-1}$ all equal to α, and the noise power over all subcarriers are identical, the maximum SNR is

$$\begin{aligned}\mathrm{SNR}_{max} &= \frac{|\alpha|^2\rho}{2}\left(\frac{1}{K_1}+\frac{1}{K_2}\right)^{-1}\\ &= \frac{|\alpha|^2\rho}{2}\frac{K_1K_2}{K_1+K_2}.\end{aligned} \tag{3.55}$$

The condition to achieve SNR_{max} is that the both $\{\gamma_{k,1}\}_{k=0}^{K_1-1}$ and $\{\gamma_{k,2}\}_{k=0}^{K_2-1}$ are collinear to some all 1 sequence. Let $K=K_1K_2$ be the integer which is inverse proportional to the

Doppler resolution. Then since K_1 and K_2 are coprime (not equal), we know that

$$\mathrm{SNR}_{max} < \frac{|\alpha|^2 \rho}{4} \sqrt{K}, \tag{3.56}$$

which implies that K_1 and K_2 should be close in value for large SNR_{max}.

3.5.3 $(\mathcal{P}, \mathcal{Q})$ Pulse Train Obtained by Sequence Repetition

The first matched filter output is

$$z_1 = \alpha_1 \chi_{\widetilde{\mathcal{P}}_1, \widetilde{\mathcal{Q}}_1}(0,0) + \chi_{N_1, \widetilde{\mathcal{Q}}_1}(\tau_0, \nu_0). \tag{3.57}$$

Let $n_{1,\ell}(t) = n_1(t - \ell N_2 T)$ for $\ell N_1 T + \tau_0 \leq t < (\ell+1) N_1 T + \tau_0$. Then by the construction of $\mathcal{Q}$-pulse train $z_{\widetilde{\mathcal{Q}}_1}(t)$ we know that

$$\begin{aligned} \chi_{N_1, \widetilde{\mathcal{Q}}_1}(\tau_0, \nu_0) &= \int_{-\infty}^{\infty} n_1(t) \overline{z_{\widetilde{\mathcal{Q}}_1}(t - \tau_0)} e^{-j\nu_0 t} dt \\ &= \sum_{\ell=0}^{N_2 - 1} \int_{\tau_0}^{N_1 T + \tau_0} n_{1,\ell}(t) \overline{h_\ell z_{\mathcal{Q}_1}(t - \tau_0)} e^{-j\nu_0 (t + \ell N_1 T)} dt \\ &= \sum_{\ell=0}^{N_2 - 1} e^{-j\nu_0 \ell N_1 T} \overline{h_\ell} \chi_{N_{1,\ell}, \mathcal{Q}_1}(\tau_0, \nu_0). \end{aligned} \tag{3.58}$$

Thus z_1 can be written by

$$z_1 = \alpha_1 \chi_{\mathcal{P}_1, \mathcal{Q}_1}(0,0) \sum_{\ell=0}^{N_2-1} h_{1,\ell} + \sum_{\ell=0}^{N_2-1} e^{-j\nu_0 \ell N_1 T} h_{1,\ell}^* \chi_{N_{1,\ell}, \mathcal{Q}_1}(\tau_0, \nu_0), \tag{3.59}$$

and similarly, the second matched filter output is

$$z_2 = \alpha_2 \chi_{\mathcal{P}_2, \mathcal{Q}_2}(0,0) \sum_{\ell=0}^{N_1-1} h_{2,\ell} + \sum_{\ell=0}^{N_1-1} e^{-j\nu_0 \ell N_2 T} h_{2,\ell}^* \chi_{N_{2,\ell}, \mathcal{Q}_2}(\tau_0, \nu_0). \tag{3.60}$$

Therefore the signal power for $z_1 z_2$ is

$$P_s = |\alpha_1 \alpha_2|^2 \chi^2_{\mathcal{P}_1, \mathcal{Q}_1}(0,0) \chi^2_{\mathcal{P}_2, \mathcal{Q}_2}(0,0) \Big| \sum_{\ell=0}^{N_2-1} h_{1,\ell} \Big|^2 \Big| \sum_{\ell=0}^{N_1-1} h_{2,\ell} \Big|^2 \tag{3.61}$$

Denote $\eta_1 = E\{|\chi_{N_{1,\ell}, \mathcal{Q}_1}(\tau_0, \nu_0)|^2\}$ for $\ell = 0, ..., N_2 - 1$ and $\eta_2 = E\{|\chi_{N_{2,\ell}, \mathcal{Q}_2}(\tau_0, \nu_0)|^2\}$ for $\ell = 0, ..., N_1 - 1$. Ignoring the product of noises in z_1 and z_2, the noise power for $z_1 z_2$ is

$$p[n] = |\alpha_1|^2 \eta_2 \Big| \sum_{\ell=0}^{N_2-1} h_{1,\ell} \Big|^2 \sum_{\ell=0}^{N_1-1} |h_{2,\ell}|^2 \chi^2_{\mathcal{P}_1, \mathcal{Q}_1}(0,0) + |\alpha_2|^2 \eta_1 \Big| \sum_{\ell=0}^{N_1-1} h_{2,\ell} \Big|^2 \sum_{\ell=0}^{N_2-1} |h_{1,\ell}|^2 \chi^2_{\mathcal{P}_2, \mathcal{Q}_2}(0,0). \tag{3.62}$$

The signal to noise ratio of $z_1 z_2$ is

$$\begin{aligned}
\mathrm{SNR} &= \left(\Big(\frac{|\sum_{\ell=0}^{N_2-1} h_{1,\ell}|^2}{\sum_{\ell=0}^{N_2-1} |h_{1,\ell}|^2} |\alpha_1|^2 \rho_1 \Big)^{-1} + \Big(\frac{|\sum_{\ell=0}^{N_1-1} h_{2,\ell}|^2}{\sum_{\ell=0}^{N_1-1} |h_{2,\ell}|^2} |\alpha_2|^2 \rho_2 \Big)^{-1} \right)^{-1} \\
&\leq \left(\frac{1}{N_2 |\alpha_1|^2 \rho_1} + \frac{1}{N_1 |\alpha_2|^2 \rho_2} \right)^{-1},
\end{aligned} \tag{3.63}$$

where $\rho_1 = \chi^2_{\mathcal{P}_1,\mathcal{Q}_1}(0,0)/\eta_1$, and $\rho_2 = \chi^2_{\mathcal{P}_2,\mathcal{Q}_2}(0,0)/\eta_2$. If $\alpha_1 = \alpha_2 = \alpha$, the maximum SNR is

$$\mathrm{SNR}_{max} = |\alpha|^2 \left(\frac{1}{N_2 \rho_1} + \frac{1}{N_1 \rho_2} \right)^{-1}. \tag{3.64}$$

3.6 Conclusion

In this chapter, we have developed the sequencing of time-coordinated ($\mathcal{P}$, $\mathcal{Q}$) pulse trains in frequency. Through utilizing added degree of freedoms in frequency domain, we are able to craft a point spread function of OFDM radar which owns a narrow Doppler response, whereas the Doppler response of a single frequency radar, as the price of improved Doppler resilience, is typically flat.

CHAPTER 4

DOPPLER RESILIENT PARAUNITARY ILLUMINATIONS FOR PHASED-ARRAY MIMO RADAR

In chapters 2 and 3, we studied the design of Doppler resilient waveforms for single-input single-output (SISO) radars. The proposed transmit-receive pulse trains are simply generated by separating a small number of waveform components in a pre-determined waveform library across across multiple degrees of freedom. We showed that by properly coordinating the transmission of waveform components in time, the point spread function of a SISO radar system can be essentially free of range sidelobe inside a desired Doppler band around zero Doppler axis. This in turn improves the performance of range detection of weak targets that are surrounded by strong reflectors moving at different velocities. We further demonstrated that through carefully sequencing the transmission of waveform components in both time and frequency, we are able to create a point spread function with a narrow Doppler response. Therefore the Doppler response, which has been traded for Doppler resilience in a single-frequency SISO radar, can be compensated by using an OFDM SISO radar along with proper signaling strategy.

We mentioned earlier that modern radars are increasingly being equipped with arbitrary waveform generators which enable generation of different wavefields across aperture, time, frequency, polarization, and wavenumber. Recently, the advent of multiple-input multiple-output (MIMO) radar brings the promise of increased performance for target detection and tracking. A phased-array MIMO radar is equipped with multiple transmit and receive apertures that enable the transmission of independent waveforms across the transmit array and parallel signal processing across the receive array. Therefore the spatial waveform diversity brings in the promise of several performance improvements, such as enhanced target detection capability [14], and desired transmit beampattern due to the general spatial waveform correlation [21].

Recent advances of space-time waveform design for phased-array MIMO radar essentially fall into two categories. Works in the first category aim for seeking transmit space-time waveform with desired ambiguity matrix. Designs of orthogonal [21] and nonorthogonal [76, 77] zero-lag ambiguity matrix (waveform spatial correlation) are carried out for addressing transmit beamforming. Attention has been also paid to the ambiguity matrix at non-zero lags [14, 78, 79] to reduce range sidelobe. The second category involves the optimization-based waveform design, which is defined by [80] through joint design of transceiver filters to optimize metrics like mean square error of target estimation or signal-to-interference-noise ratio, to account for the statistics of clutter and noise.

In this chapter, we focus on the utilization of paraunitary waveforms [14,64,81] for phased-array MIMO radar. A set of paraunitary waveform matrices has the property that the sum of autocorrelation matrices of waveform components is diagonal at zero delay and vanishes at nonzero delays. This leads to many good properties such as invariant transmit beam pattern, zero inter-channel interference, and ideal pulse compression. However, a major challenge of implementing the paraunitary waveforms is the sensitivity of paraunitarity to Doppler effect. In the presence of Doppler, the combination of matched filtered returns of multiple waveform components separated in pulse-repetition intervals (PRIs), is characterized by the ambiguity matrix of transmit pulse train. This ambiguity matrix fails to maintain the paraunitarity off the zero-Doppler axis, which in turn deteriorates the radar imaging capability. For instance, a weak target can potentially be masked by the range sidelobe generated by a nearby strong reflector moving at different velocity. Such a Doppler sensitivity needs to be mitigated for preserving the waveform integrity for phased-array MIMO radar [82–84].

We develop a Doppler resilient design of space-time transmit/receive filter based on a paraunitary waveform set with cardinality D. The transmit filter is a length-N spatial pulse train which coordinates the transmission of waveform components in the set using a D-ary scheduling sequence $\{p[n]\}_{n=0}^{N-1}$. The receive filter is constructed in the similar way, except that the waveform component in n-th PRI is weight by the n-th element of a real weighting sequence $\{q[n]\}_{n=0}^{N-1}$. The design of binary p-sequences and real q-sequences has been elaborated in [16, 31, 32] to coordinate the transmission of Golay complementary waveforms in time for maintaining complementarity in the presence of Doppler. We present a systematic construction of these two sequences, which enables the cross ambiguity matrix of the transceiver filter which maintains the paraunitarity inside a desired Doppler band around zero Doppler axis.

4.1 Complementary Space-time Waveforms

In this section we illustrate the notion of a set of complementary space-time waveform components. For such a waveform set, the auto-correlation matrices of individual waveform components can sum up to some composite auto-correlation matrix which carries desired illumination property for a phased-array MIMO radar. We then emphasize the practical concerns of implementing the complementary space-time signals, which serves as a guidance of designing implementable and mathematically sound complementary waveforms.

4.1.1 Definition of Wavefrom Complimentarity

Consider a MIMO radar system with M colocated transmit and M colocated receive antennas. Suppose the space-time waveform of the MIMO radar is constructed through scheduling the components in a waveform library with cardinality D. Each component $\mathbf{s}_{D,d}(t) = [s_{1,d}(t), \ldots, s_{M,d}(t)]^T \in (L^2(\mathbb{R}))^M$ is a candidate of spatial illumination across the transmit array, $d = 0, \ldots, D-1$. The auto-correlation of $\mathbf{s}_{D,d}(t)$ is

$$\mathbf{C}_{D,d}(\tau) = \int_{-\infty}^{\infty} \mathbf{s}_{D,d}(t)\mathbf{s}_{D,d}(t-\tau)^H dt. \tag{4.1}$$

We say that the waveform components $\mathbf{s}_1(t), \ldots, \mathbf{s}_D(t)$ are *complementary* if the sum of their auto-correlations

$$\mathbf{C}_D(\tau) = \sum_{d=1}^{D} \mathbf{C}_{D,d}(\tau)$$

has some desired structure.

Suppose each component $\mathbf{s}_{D,d}(t)$ of space-time waveform is modulated by some length-L sequence of spatial amplitude vectors

$$\mathbf{s}_{D,d}(t) = \sum_{\ell=0}^{L-1} \mathbf{s}_{D,d}[\ell]\Omega(t - \ell T_c), \tag{4.2}$$

where $\Omega(t)$ is the pulse shape with unit energy and T_c is the transmitter's chip interval. Each spatial amplitude vector $\mathbf{s}_{D,d}[\ell] = [s_{D,d,1}[\ell], \ldots, s_{D,d,M}[\ell]]^T$ consists of amplitudes emitted across transmit array in the ℓ-th chip interval associated to the d-th waveform component $\mathbf{s}_d(t)$. Therefore the analog waveform auto-correlation matrix can be further written by

$$\begin{aligned}\mathbf{C}_{D,d}(\tau) &= \sum_{k=-(L-1)}^{L-1} \mathbf{C}_{D,d}[k] C_\Omega(\tau - kT_c) \\ &= C_\Omega(\tau - k_1 T_c)\mathbf{C}_{D,d}[k_1] + C_\Omega(\tau - k_1 T_c)\mathbf{C}_{D,d}[k_1],\end{aligned} \tag{4.3}$$

where $C_\Omega(\tau)$ is the auto-correlation of pulse shape $\Omega(t)$, $k_1 = \lfloor -\frac{\tau}{T_c} \rfloor$, and $k_2 = k_1 + 1$, and $\mathbf{C}_{D,d}[k]$ is the aperiodic auto-correlation matrix $\mathbf{C}_{D,d}[k]$ of sequence $\mathbf{s}_{D,d}[0], \ldots, \mathbf{s}_{D,d}[L-1]$:

$$\mathbf{C}_{D,d}[k] = \sum_{\ell=0}^{L-1} \mathbf{s}_{D,d}[\ell]\mathbf{s}_{D,d}[\ell - k]^H. \; k = -(L-1), \ldots, L-1. \tag{4.4}$$

Note that in deriving the second equality in eq (4.3), we presumed that $C_\Omega(\tau)$ vanishes outside $[-T_c, T_c]$. Therefore the composite waveform auto-correlation matrix becomes

$$\mathbf{C}_D(\tau) = C_\Omega(\tau - k_1 T_c) \sum_{d=1}^{D} \mathbf{C}_{D,d}[k_1] + C_\Omega(\tau - k_2 T_c) \sum_{d=1}^{D} \mathbf{C}_{D,d}[k_2]. \tag{4.5}$$

The auto-correlation matrix $\mathbf{C}_D(\tau)$ sampled at discrete time $\tau = kT_c$ is

$$\begin{aligned}\mathbf{C}_D[k] &= \sum_{d=1}^{D} \mathbf{C}_{D,d}[k] \\ &= \sum_{\ell=0}^{L-1} \mathbf{S}_D[\ell]\mathbf{S}_D[\ell - k]^H,\end{aligned} \tag{4.6}$$

where

$$\mathbf{S}_D[\ell] = \Big[\mathbf{s}_{D,0}[\ell] \ldots, \mathbf{s}_{D,D-1}[\ell]\Big]$$

is the amplitude matrix whose vectors corresponds to the spatial amplitude distribution of a certain waveform component at ℓ-th chip interval. This indicates that in order to design proper analog component waveform vectors $\mathbf{s}_d(t)$'s with desired sum of auto-correlations $\mathbf{C}_{D,d}(\tau)$, it is equivalent to design proper discrete amplitude component vectors $\mathbf{s}_d[\ell]$'s with desired sum of aperiodic auto-correlations $\mathbf{C}_{D,d}[k]$. Later we will demonstrate the validity of this statement for $\mathbf{C}_D(\tau)$ with τ off the sampling grid.

4.1.2 Short Pulse for Mitigating Chip-Level Doppler Effects

In the presence of Doppler shift, each auto-correlation matrix $\mathbf{C}_{D,d}(\tau)$ cannot directly represent the point target response by using $\mathbf{s}_{D,d}(t)$ as the transmit and receive waveform. Instead it is the auto-ambiguity matrix $\mathbf{A}_{D,d}(\tau,\nu)$ of $\mathbf{s}_{D,d}(t)$ which actually captures the time-frequency distribution of target:

$$\begin{aligned}\mathbf{A}_{D,d}(\tau,\nu) &= \int_{-\infty}^{\infty} \mathbf{s}_{D,d}(t)\mathbf{s}_{D,d}(t-\tau)^H e^{-j\nu t} dt \\ &= \chi_\Omega(\tau - k_1 T_c, \nu)\mathbf{A}_{D,d,\nu}[k_1] + \chi_\Omega(\tau - k_2 T_c, \nu)\mathbf{A}_{D,d,\nu}[k_2],\end{aligned} \tag{4.7}$$

where matrix $\mathbf{A}_{D,d,\nu}[k]$ is the aperiodic cross-correlation matrix of $\mathbf{s}_{D,d}[\ell]$ and Doppler modulated $\mathbf{s}_{D,d}[\ell]$:

$$\mathbf{A}_{D,d,\nu}[k] = \sum_{\ell=0}^{L-1} \mathbf{s}_{D,d}[\ell]\mathbf{s}_{D,d}[\ell-k]^H e^{-j\nu\ell T_c}, \tag{4.8}$$

and $\chi_\Omega(\tau,\nu)$ is the scaler auto-ambiguity function of pulse shape $\Omega(t)$:

$$\chi_\Omega(\tau,\nu) = \int_{-\infty}^{\infty} \Omega(t)\Omega^*(t-\tau)e^{-j\nu t} dt. \tag{4.9}$$

However, in general, to design the sequences $\mathbf{s}_{D,d}[0], \ldots, \mathbf{s}_{D,d}[L-1]$ such that $\mathbf{A}_{D,d,\nu}[k]$'s sum up to some desired structure at arbitrary Doppler frequency ν is not an easy problem. And we shall not ask $\mathbf{s}_{D,d}[0], \ldots, \mathbf{s}_{D,d}[L-1]$ for extra functionality to accomplish this goal. Instead, a typical treatment to reduce the sensitivity of $\mathbf{A}_{D,d}(\tau,\nu)$ to chip level Doppler shift is to use short pulses, i.e., L shall be a small positive integer and hence the Doppler shift $L\nu T_c$ over the pulse duration is negligible fo ν inside Doppler band $\mathcal{B}$ of interest. From this we have $\mathbf{A}_{D,d}[k] \approx \mathbf{C}_{D,d}[k]$, $\forall d$, and $\chi_\Omega(\tau,\nu) \approx C_\Omega(\tau)$, which in turn yields the approximation

$$\mathbf{A}_{D,d}(\tau,\nu) \approx \mathbf{C}_{D,d}(\tau),\ \nu \in \mathcal{B}, d = 1, \ldots, D, \tag{4.10}$$

Therefore, to maintain complementarity of space-time waveform components $\mathbf{s}_{D,d}(t)$ in the presence of chip-level Doppler effect, each of $\mathbf{s}_{D,d}(t)$ needs to have a short time duration.

4.2 Examples of Complementary Space-time Waveforms

In above section, we introduced the concept of complementary space-time waveforms. We demonstrated that in order to construct a set of base-D complementary sequence-modulated waveform components $\{\mathbf{s}_{D,d}(t)\}_{d=1}^{D}$, it is sufficient to seek D vector sequences $\mathbf{s}_{D,d}[0], \ldots, \mathbf{s}_{D,d}[L-1]$, $d = 1, \ldots, D$, whose composite aperiodic auto-correlation matrix $\mathbf{C}_D[k]$ has desired property. In the following we illustrate two designs of above vector sequences.

4.2.1 Paraunitary Waveform Vectors

Start with the notion of Golay complementary sequences. Two length L unimodular sequences of complex numbers $x[\ell]$ and $y[\ell]$ are Golay complementary if the sum of their auto-correlation functions satisfies

$$C_x[k] + C_y[k] = 2L\delta[k],\ k = -(L-1), \ldots, (L-1), \tag{4.11}$$

where $C_x[k]$ and $C_y[k]$ are the aperiodic auto-correlations of $x[\ell]$ and $y[\ell]$ at lag k respectively, and $\delta[k]$ is the Kronecker delta function.

In [14, 64] a sequence of 2×2 matrices

$$\begin{aligned}\mathbf{S}_2[\ell] &= \begin{bmatrix}\mathbf{s}_{2,1}[\ell] & \mathbf{s}_{2,2}[\ell]\end{bmatrix} \\ &= \begin{bmatrix} x[\ell] & -y^*[L-1-\ell] \\ y[\ell] & x^*[L-1-\ell]\end{bmatrix},\ \ell = 0, ..., L-1.\end{aligned} \tag{4.12}$$

is developed with the paraunitary property

$$\mathbf{C}_2[k] = \sum_{\ell=0}^{L-1} \mathbf{S}_2[\ell]\mathbf{S}_2^H[\ell-k] = 2\delta[k]\mathbf{I}_2. \tag{4.13}$$

Similarly we can derive the sequence of $2^K \times 2^K$ matrices

$$\begin{aligned}\mathbf{S}_{2^K}[\ell] &= \begin{bmatrix}\mathbf{s}_{2^K,1}[\ell], \dots, \mathbf{s}_{2^K,2^K}[\ell]\end{bmatrix} \\ &= \begin{bmatrix}\mathbf{S}_{2^{K-1}}[\ell] & \mathbf{S}_{2^{K-1}}[\ell] \\ \mathbf{S}_{2^{K-1}}[\ell] & -\mathbf{S}_{2^{K-1}}[\ell]\end{bmatrix} \\ &= \underbrace{\mathbf{H}_2 \otimes \cdots \otimes \mathbf{H}_2}_{K-1} \otimes \mathbf{S}_2[\ell],\ \ell = 0, ..., L-1,\end{aligned} \tag{4.14}$$

where $\mathbf{H}_2$ is the 2×2 Hadamard matrix. Thus the auto-correlation matrix of sequence $\mathbf{S}_{2^K}[\ell]$ is the identity matrix at zero lag and vanishes at nonzero lags:

$$\mathbf{C}_{2^K}[k] = \sum_{\ell=0}^{L-1} \mathbf{S}_{2^K}[\ell]\mathbf{S}_{2^K}^H[\ell-k] = 2^K\delta[k]\mathbf{I}_{2^K}. \tag{4.15}$$

4.2.2 Desired Waveform Spatial Correlation

The spatial correlation of radar space-time waveform has been exploited in [76, 77]. In these works, it is demonstrated that the spatial correlation matrix, or the zero-lag waveform auto-correlation matrix, is essential for building the desired waveform diversity as well as detection/surveillance performance. In these works, the space-time waveform is typically modulated by an $M_t \times N_c$ amplitude matrix $\mathbf{S}$, where $\mathbf{M}_t$ is the number of transmit antennas, and N_c is the total number of chip intervals included in the transmit waveform associated to each transmit antenna. Thus spatial correlation matrix can be written by the Grammian matrix

$$\mathbf{G}_{\mathbf{S}} = \mathbf{S}\mathbf{S}^H. \tag{4.16}$$

In the presence of Doppler frequency ν, $\mathbf{G}_{\mathbf{S}}$ becomes the Doppler induced-spatial correlation

$$\mathbf{A}_{\mathbf{S}}(\nu) = \mathbf{S}\mathbf{D}(-\nu)\mathbf{S}^H, \tag{4.17}$$

where $\mathbf{D}(\nu) = diag([1, e^{j\nu T_c}, \ldots, e^{j\nu(N_c-1)T_c}])$ is the diagonal Doppler modulation matrix. It can be seen that $\mathbf{A}_{\mathbf{S}}(\nu)$ equals the cross-correlation $\mathbf{A}_{D,d,\nu}[k]$ defined in eq (4.8), evaluated at $k = 0$, with $L = N_c$ and $D = d = 1$, meaning that the waveform library has only one component.

From the analysis in section 4.1.2, we know that $\mathbf{A}_{\mathbf{S}}(\nu)$ is approximately $\mathbf{G}_{\mathbf{S}}$ for $\nu \in \mathcal{B}$, provided that the cumulative Doppler shift $N_c\nu T_c$ is negligible. However, it turns out that some designs in above reference actually suffers from the chip-level Doppler effect.

Fig. 4.1 illustrates the sensitivity to chip-level Doppler shifts for the spatial correlation matrix of a space-time waveform with long time duration. In here the matrix $\mathbf{S}$ has dimension 128 by 128, and is constructed following [77] with $\alpha = 0.125$. Fig. 4.1(a) and Fig. 4.1(d) depict the magnitude and phase information of the 128 by 128 spatial correlation matrix in the absence of Doppler. Set the carrier frequency as 17GHz. Fig. 4.1(b) and Fig. 4.1(e) depict the magnitude and phase discrepancy of spatial correlation, at the Doppler frequency corresponding to the 5m/s velocity. The amplitude discrepancy is defined as the difference of dB magnitude of spatial correlation with Doppler effect and without Doppler effect. It can be seen that the magnitude discrepancy on the entries in the zero-Doppler spatial correlation matrix with low magnitude (-25dB) can be as large as 32dB. Large Doppler-induced phase discrepancy can be also found on those entries. At the Doppler frequency corresponding to the 10m/s velocity, the magnitude and phase mismatch of spatial correlation matrix, as shown in Fig. 4.1(c) and Fig. 4.1(f), can be more severe.

To reduce the Doppler sensitivity as shown in the experiment, one can truncate the space time waveform in time into several segments. This is because the cumulative Doppler

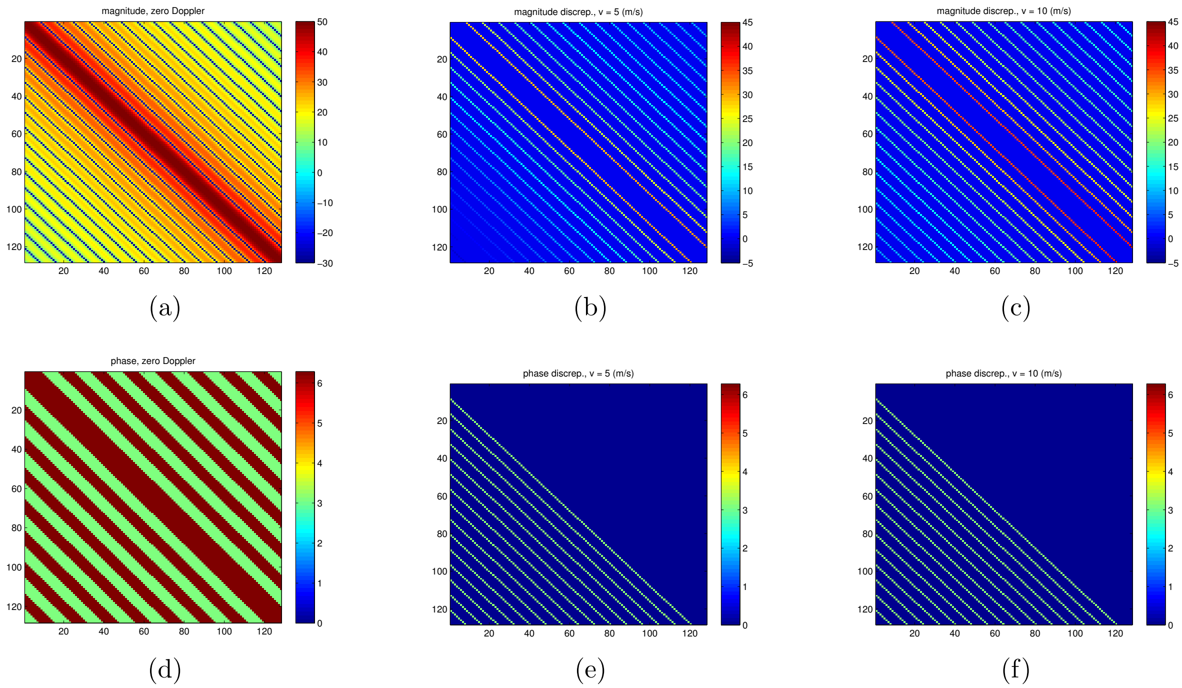

Figure 4.1: Discussion of sensitivity to chip-level Doppler shifts of the spatial correlation matrix of a space-time waveform with long time duration. Each individual waveform for a 128 by 128 phased-array MIMO radar is phase coded by a length-128 matrix sequence. (a) and (d) depict the magnitude and phase of entries in spatial correlation matrix at zero Doppler. Colorbars are in dB and radian respectively. (b) and (e) depict the magnitude and phase discrepancies of spatial correlation at Doppler frequency associated to velocity 5m/s. (c) and (f) characterize the magnitude and phase discrepancies at Doppler frequency associated to velocity 10m/s.

shift inside each waveform component is much smaller than the Doppler shift we had before waveform truncation. Mathematically, if we group the columns of matrix $\mathbf{S}$ by

$$\mathbf{S} = \Big[[\mathbf{s}_{D,1}[0], \ldots, \mathbf{s}_{D,1}[L-1]], \ldots, [\mathbf{s}_{D,D}[0], \ldots, \mathbf{s}_{D,D}[L-1]] \Big], \tag{4.18}$$

then the original spatial correlation matrix now becomes the composite spatial correlation, or composite zero-lag auto-correlation of waveform components generated by waveform truncation:

$$\begin{aligned} \mathbf{G}_{\mathbf{S}} &= \sum_{\ell=0}^{L-1} \sum_{d=1}^{D} \mathbf{s}_{D,d}[\ell] \mathbf{s}_{D,d}[\ell]^H \\ &= \mathbf{C}_D[0]. \end{aligned} \tag{4.19}$$

Consequently, the cumulative Doppler shift for each waveform component is $L\nu T_c = N_c \nu T_c / D$, which can be mitigated by choosing a large value of D.

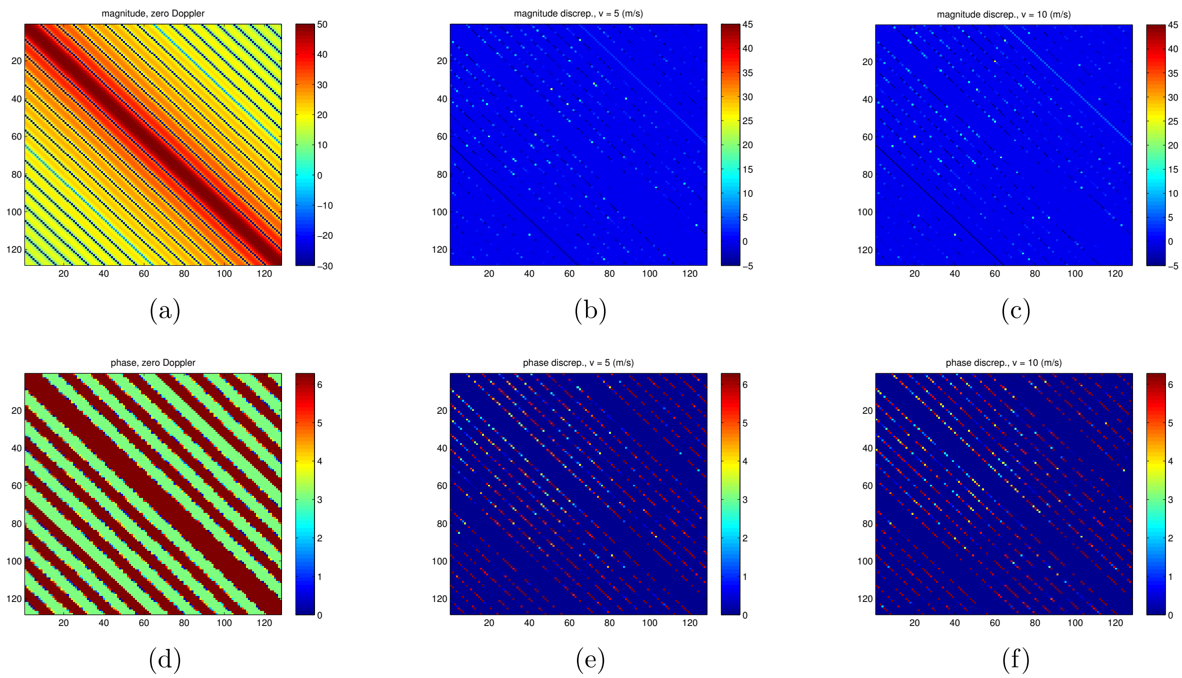

Figure 4.2: Reduction of sensitivity of spatial correlation to chip-level Doppler shift, through waveform truncating in time by a factor of 8, and separating 8 waveform components in time by PRI. (a) and (d) depict the amplitude and phase of entries in the composite spatial correlation matrix. Colorbars are in dB and radian respectively. (b) and (e) depict the amplitude and phase discrepancies of composite spatial correlations at Doppler frequency associated to velocity 5m/s, where the carrier fequency is 17GHz. (c) and (f) characterize the amplitude and phase discrepancies at Doppler frequency associated to velocity 10m/s.

Fig. 4.2 shows how the magnitude and phase of spatial correlation pattern is sensitive to chip-level Doppler shift can be mitigated, by truncating the 128 by 128 amplitude matrix $\mathbf{S}$ to 8 blocks in time. Through waveform truncation, the Doppler-induced magnitude discrepancy is significantly annihilated. The phase discrepancy is negligible, except along a few off-diagonal lines in the spatial correlation matrix. However, the entries on these off-diagonal lines are of very low magnitude.

To summarize, the complementary space-time waveform components, generated by truncating the existing space-time waveform designs [76, 77] in time by a factor of D, have the property that the sum of their spatial correlation has desired structure. Note that the larger library size D, the more robust each waveform component is to Doppler, but the smaller the duty cycle of pulse train becomes. Therefore in practice D shall be chosen properly for tradeoff.

4.3 Sensitivity of Complementarity to Doppler Shift in PRI

The above analysis shows that by separating the transmission of complementary waveform components in time, one can obtain the desired composite auto-correlation matrix, which determines the point target response in the absence of Doppler. However, the complementarity shows significant sensitivity to nonzero Doppler frequency. To illustrate such a Doppler-induced sensitivity, suppose the transmit waveform is generated by separating $\mathbf{s}_{2^K,0}(t)$ through $\mathbf{s}_{D,D-1}(t)$ in time by a PRI:

$$\mathbf{z}(t) = \sum_{d=0}^{D-1} \mathbf{s}_{D,d}(t - dT). \tag{4.20}$$

The ambiguity matrix of $\mathbf{z}(t)$ is

$$\boldsymbol{\chi}_{\mathbf{z}}(\tau, \nu) = \int_{-\infty}^{\infty} \mathbf{z}(t)\mathbf{z}(t-\tau)^H e^{-j\nu t} dt, \tag{4.21}$$

which discrete samples at $\tau = kT_c$ are

$$\boldsymbol{\chi}_{\mathbf{z}}(k, \theta) = \sum_{d=0}^{D-1} e^{jd\theta} \mathbf{C}_{D,d}[k], \tag{4.22}$$

where $\theta = \nu T$ is the Doppler shift in one PRI. In eq (4.22) we had ignored the chip-level Doppler shifts. In general the ambiguity matrix $\boldsymbol{\chi}_{\mathbf{z}}(k, \theta)$ is not equal the composite auto-correlation $\mathbf{C}_D[k]$ due to different phase modulation on each PRI.

Fig. 4.3 illustrates the severe sensitivity to Doppler of a 2 by 2 ambiguity matrix $\boldsymbol{\chi}_{\mathbf{z}}(\tau, \nu)$. The transmit pulse train is constructed following the paraunitary design. The horizontal axis depicts Doppler and the vertical axis illustrates delay. Color bar values are in dB. Slightly off the zero-Doppler axis, the diagonal entry $[\boldsymbol{\chi}_{\mathbf{z}}(\tau, \nu)]_{1,1}$ has significant range sidelobe, and the

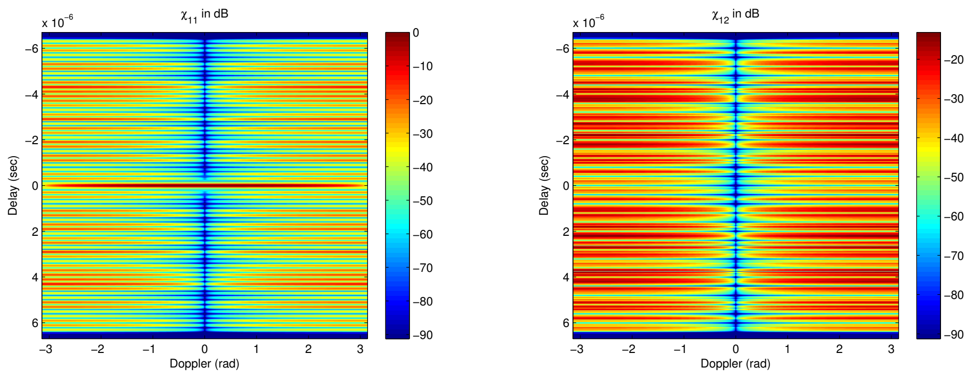

(a) (b)

Figure 4.3: Magnitude of 2 by 2 ambiguity matrix $\boldsymbol{\chi}_{\mathbf{z}}(\tau,\nu)$ corresponding to the paraunitary design. The length-2 pulse train is phase coded by the matrix sequence in eq (4.12). Horizontal and vertical axis stand for Doppler shift $\theta = \nu T$ (in radian) and delay τ (in sec). Color-bar uses dB scale. (a): $[\boldsymbol{\chi}_{\mathbf{z}}(\tau,\nu)]_{1,1}$, (b): $[\boldsymbol{\chi}_{\mathbf{z}}(\tau,\nu)]_{1,2}$

magnitude of off-diagonal entry $[\boldsymbol{\chi}_{\mathbf{z}}(\tau,\nu)]_{1,2}$ rapidly grows. The Doppler induced performance deterioration can result in miss detection of weak targets masked by range sidelobes generated by nearby strong reflectors moving at different velocity, or degraded signal-to-noise ratio due to fluctuating transmit beampattern.

4.4 Doppler Resilient Waveform Matrices

In above sections we present the complementary space-time waveform components whose auto-correlation matrices sum up to some desired composite auto-correlation matrix. Each space-time waveform components is restricted to consist of a small number of chip intervals, such that the chip-level Doppler shift is negligible. In practice, the transmission of these waveform components is separate in time by pulse-repetition interval (PRI) T, which is typically much longer than the

Definition 4.4.1. ($\mathbf{p}$-transmit space-time waveform): Let $\mathbf{p} = [p[0], \ldots, p[N-1]]^T \in (\mathbb{Z}/D\mathbb{Z})^N$. Define the $\mathbf{p}$-transmit space-time waveform as

$$\mathbf{z}_{\mathbf{p}}(t) = \sum_{n=0}^{N-1} \mathbf{s}_{D,p[n]}(t - nT). \tag{4.23}$$

The nth temporal component in $\mathbf{z_p}(t)$ is $\mathbf{s}_{D,d}(t)$ if $p[n] = d$, $d = 0, ..., D-1$. Consecutive entries are separated in time by a PRI T sec.

Definition 4.4.2. ($\mathbf{q}$-receive filter bank): Let $\mathbf{q} = [q[0], \ldots, q[N-1]] \in \mathbb{C}^N$ be an N-dimensional vector. Define the $\mathbf{q}$-receive filter bank as

$$\mathbf{z_q}(t) = \sum_{n=0}^{N-1} q[n]\mathbf{s}_{D,p[n]}(t - nT). \tag{4.24}$$

Thus nth entry in $\mathbf{z_q}(t)$ is obtained by multiplying the n-th temporal component of $\mathbf{z_p}(t)$ by $q[n]$.

The MIMO radar cross-ambiguity matrix is

$$\begin{aligned} \boldsymbol{\chi}_{\mathbf{p},\mathbf{q}}(\tau, \nu) &= \int_{-\infty}^{\infty} \mathbf{z_p}(t)\mathbf{z_q}(t-\tau)^H e^{-j\nu t} dt \\ &= \sum_{n=0}^{N-1} q[n] e^{j\nu nT} \boldsymbol{\chi}_{\mathbf{s}_{D,p[n]}}(\tau, \nu), \end{aligned} \tag{4.25}$$

where $\boldsymbol{\chi}_{\mathbf{s}_{D,d}}(\tau, \nu)$ is the auto-ambiguity matrix of d-th waveform component $s_{D,d}(t)$. Note that in the second equality of eq (4.25), we had ignored the range aliases centered at $\pm T, \pm 2T, \ldots, \pm(N-1)T$. After discretizing in delay (at chip intervals), and ignoring the Doppler shift over chip intervals compared to the Doppler shift across a PRI, the cross ambiguity matrix can be written

$$\boldsymbol{\chi}_{\mathbf{p},\mathbf{q}}(k, \theta) = \sum_{n=0}^{N-1} q[n] e^{jn\theta} \mathbf{C}_{D,p[n]}[k]. \tag{4.26}$$

where k is the discrete delay index, and $\theta = \nu T$ is the Doppler shift in one PRI.

Clearly, the cross-ambiguity matrix at zero Doppler $\boldsymbol{\chi}_{\mathbf{p},\mathbf{q}}(k, 0)$ is simply a weighted sum of the individual auto-correlation matrices $\mathbf{C}_d[k]$'s. With balanced weights, i.e.,

$$\sum_{\substack{n=0 \\ p[n]=d}} q[n] = \sum_{\substack{n=0 \\ p[n]=d'}} q[n], \ \forall 1 \le d, d' \le D, \tag{4.27}$$

$\boldsymbol{\chi}_{\mathbf{p},\mathbf{q}}(k, 0)$ is proportional to the desired composite auto-correlation $\mathbf{C}_D[k]$. The goal of designing the MIMO radar transceiver pair $(\mathbf{z_p}(t), \mathbf{z_q}(t))$, or specifically the vectors $\mathbf{p} \in (\mathbb{Z}/D\mathbb{Z})^N$ and $\mathbf{q} \in \mathbb{C}^N$, is the Doppler resilience of $\boldsymbol{\chi}_{\mathbf{p},\mathbf{q}}(k, \theta)$, which is $\boldsymbol{\chi}_{\mathbf{p},\mathbf{q}}(k, \theta) \approx \boldsymbol{\chi}_{\mathbf{p},\mathbf{q}}(k, 0)$ for arbitrary Doppler frequency $\nu = \theta/T$ inside the desired Doppler band $\mathcal{B}$.

4.5 $D = 2$ Case

For the 2×2 MIMO radar ($K = 1$), the cross ambiguity matrix $\boldsymbol{\chi}_{\mathbf{p},\mathbf{q}}(k, \theta)$ is written by

$$\begin{aligned}
\boldsymbol{\chi}_{\mathbf{p},\mathbf{q}}(k,\theta) &= \sum_{n=0}^{N-1} q[n]e^{jn\theta}\left(\sum_{p[n]=0}\mathbf{C}_{2,0}[k] + \sum_{p[n]=1}\mathbf{C}_{2,1}[k]\right) \\
&= \frac{1}{2}\sum_{n=0}^{N-1} q[n]e^{jn\theta}\left(\mathbf{C}_{2,0}[k] + \mathbf{C}_{2,1}[k]\right) + \frac{1}{2}\sum_{n=0}^{N-1} q[n](-1)^{p[n]}e^{jn\theta}\left(\mathbf{C}_{2,0}[k] - \mathbf{C}_{2,1}[k]\right) \\
&\triangleq \sum_{n=0}^{N-1} q[n]e^{jn\theta}\mathbf{C}_2[k] + \boldsymbol{\Delta}_2(k,\theta),
\end{aligned} \tag{4.28}$$

where the residue matrix

$$\boldsymbol{\Delta}_2(k,\theta) = \frac{1}{2}\sum_{n=0}^{N-1} q[n](-1)^{p[n]}e^{jn\theta}\left(\mathbf{C}_{2,0}[k] - \mathbf{C}_{2,1}[k]\right) \tag{4.29}$$

represents the cross-diagonal interference and range-sidelobe in the presence of Doppler. Therefore, to maintain the waveform paraunitary property and the perfect range response, we need to annihilate the residue matrix inside some Doppler band.

Theorem 4.5.1. *The necessary and sufficient condition of zero forcing the first M Taylor moments of all entries in $\boldsymbol{\Delta}_2(k,\theta)$ around $\theta = 0$ is that the spectra*

$$S_{\mathbf{p},\mathbf{q}}(\theta) = \sum_{n=0}^{N-1}(-1)^{p[n]}q[n]e^{jn\theta} \tag{4.30}$$

has zero first M Taylor moments around $\theta = 0$, or equivalently the vector pair $(\mathbf{p}, \mathbf{q})$ belong to

$$\mathcal{N}_2(N,M) = \left\{ \begin{array}{c} (\mathbf{p},\mathbf{q}), \\ \mathbf{p}=[p_0,\ldots,p_{N-1}]^T, \\ \mathbf{q}=[q_0,\ldots,q_{N-1}]^T, \\ \mathbf{p}\in(\mathbb{Z}/2\mathbb{Z})^N, \mathbf{q}\in\mathbb{C}^N \end{array} \middle| \begin{bmatrix} 1 & 1 & \cdots & 1 \\ 1 & 2 & \cdots & N \\ \vdots & \vdots & \ddots & \vdots \\ 1^M & 2^M & \cdots & N^M \end{bmatrix} \begin{bmatrix} (-1)^{p_0}q_0 \\ (-1)^{p_1}q_1 \\ \vdots \\ (-1)^{p_{N-1}}q_{N-1} \end{bmatrix} = \mathbf{0} \right\}. \tag{4.31}$$

Proof: See theorem 2.2.3.

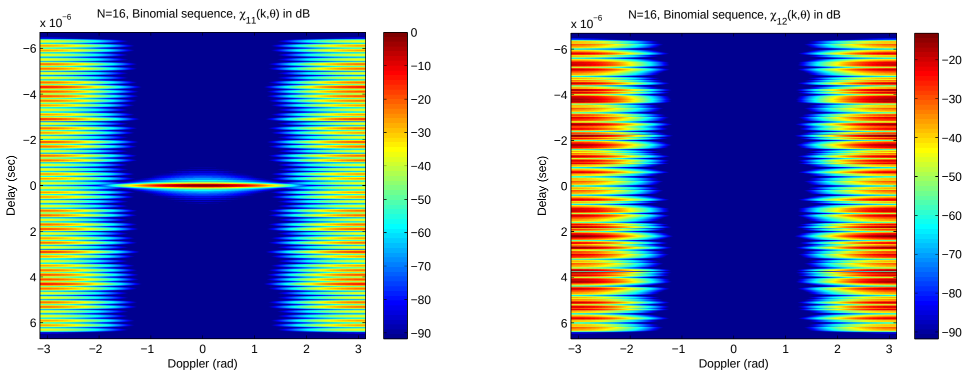

(a) (b)

Figure 4.4: Magnitude of entries (a) $[\boldsymbol{\chi}_{\mathbf{p},\mathbf{q}}(\tau,\nu)]_{1,1}$, and (b) $[\boldsymbol{\chi}_{\mathbf{p},\mathbf{q}}(\tau,\nu)]_{1,2}$ in a 2×2 cross ambiguity matrix $\boldsymbol{\chi}_{\mathbf{p},\mathbf{q}}(\tau,\nu)$ corresponding to the Binomial design $(\mathbf{p},\mathbf{q}) \in \mathcal{N}_2(16,14)$.

Fig. 4.4 illustrates the annihilation of the 2 by 2 residue matrix corresponding to paraunitary waveforms, by using the length-16 Binomial design, which zero-forces the first 14 Taylor moments of each entry in $\boldsymbol{\Delta}(k,\theta)$ around $\theta = 0$. Fig. 4.4(a) depicts the magnitude of the northwest entry $[\boldsymbol{\chi}_{\mathbf{p},\mathbf{q}}(\tau,\nu)]_{1,1}$ of the 2 by 2 cross ambiguity matrix $\boldsymbol{\chi}_{\mathbf{p},\mathbf{q}}(\tau,\nu)$. Inside the Doppler band $[-1,1]$ rad range sidelobe of $[\boldsymbol{\chi}_{\mathbf{p},\mathbf{q}}(\tau,\nu)]_{1,1}$ is 80 dB below to the mainlobe in magnitude. The northeast entry $[\boldsymbol{\chi}_{\mathbf{p},\mathbf{q}}(\tau,\nu)]_{1,2}$, shown in Fig. 4.4(b), is 80 dB below the peak of $[\boldsymbol{\chi}_{\mathbf{p},\mathbf{q}}(\tau,\nu)]_{1,1}$ at each delay inside the Doppler band $[-1,1]$ rad. Therefore the paraunitarity of transceiver filters is well preserved.

4.6 $D > 2$ Case

At $D > 2$, denote $\omega_D = e^{j\frac{2\pi}{D}}$ as the root of unity with order D. Note that for each $0 \le d \le D-1$, we have

$$\frac{1}{D}\sum_{r=0}^{D-1} \omega_D^{r(p[n]-d)} = \delta[p[n]-d]. \tag{4.32}$$

Therefore the cross ambiguity function for a $D \times D$ MIMO radar can be written by

$$\begin{aligned}\boldsymbol{\chi}_{\mathbf{p},\mathbf{q}}(k,\theta) &= \frac{1}{D}\sum_{n=0}^{N-1} q[n]e^{jn\theta}\sum_{d=0}^{D-1}\mathbf{C}_{D,d}[k]\sum_{r=0}^{D-1}\omega_D^{r(p[n]-d)} \\ &= \frac{1}{D}\sum_{r=0}^{D-1}\left(\sum_{n=0}^{N-1}\omega_D^{rp[n]}q[n]e^{jn\theta}\right)\left(\sum_{d=0}^{D-1}\omega_D^{-rd}\mathbf{C}_{D,d}[k]\right) \\ &= \sum_{n=0}^{N-1} q[n]e^{jn\theta}\delta[k]\mathbf{I}_D + \frac{1}{D}\sum_{r=1}^{D-1} S_{\mathbf{p},\mathbf{q},r}(\theta)\boldsymbol{\Delta}_{D,r}[k] \\ &= S_{\mathbf{q}}(\theta)\delta[k]\mathbf{I}_D + \boldsymbol{\Delta}_D(k,\theta),\end{aligned} \tag{4.33}$$

where the residue matrix is

$$\boldsymbol{\Delta}_D(k,\theta) = \frac{1}{D}\sum_{r=1}^{D-1} S_{\mathbf{p},\mathbf{q},r}(\theta)\boldsymbol{\Delta}_{D,r}[k], \tag{4.34}$$

and $S_{\mathbf{p},\mathbf{q},r}(\theta)$ and $S_{\mathbf{q}}(\theta)$ are the spectra of $\omega_D^{rp[0]}q[0],\ldots,\omega_D^{rp[N-1]}q[N-1]$ and $q[0],\ldots,q[N-1]$:

$$S_{\mathbf{p},\mathbf{q},r}(\theta) = \sum_{n=0}^{N-1}\omega_D^{rp[n]}q[n]e^{jn\theta},\ r = 1,...,2^K-1, \tag{4.35}$$

$$S_{\mathbf{q}}(\theta) = \sum_{n=0}^{N-1} q[n]e^{jn\theta}, \tag{4.36}$$

and the rth component of residue matrix

$$\boldsymbol{\Delta}_{D,r}[k] = \sum_{d=0}^{D-1}\omega_D^{-rd}\mathbf{C}_{D,d}[k] \tag{4.37}$$

does not vanish at nonzero delay in general. In the following we show the approach of annihilating $\boldsymbol{\Delta}_D(k,\theta)$ by creating nulls of each $S_{\mathbf{p},\mathbf{q},r}(\theta)$ around zero Doppler, $r = 1,\ldots,D-1$.

4.6.1 Principle of Residue Spectra Anihilation

Definition 4.6.1. A sequence of amplitude vectors $\mathbf{s}_{D,0}[\ell],\ldots,\mathbf{s}_{D,D-1}[\ell]$ is said to have linear independent auto-correlation matrices if

$$\sum_{d=0}^{D-1} a_d\mathbf{C}_{D,d}[k] = \mathbf{0},\ \forall 1-L \le k \le L-1 \tag{4.38}$$

only when $a_d = 0$ for all $0 \le d \le D-1$.

Lemma 4.6.1. *Thee paraunitary design established in eq. (4.14) has linear independent auto-correlation matrices* $\mathbf{C}_{2^K,d}[k]$.

Proof: See appendix D.

Theorem 4.6.2. *The necessary and sufficient condition of zero forcing the first M Taylor moments of all entries in $\mathbf{\Delta}_D(k,\theta)$ around $\theta = 0$, $\forall k$ is that the spectra*

$$S_{\mathbf{p},\mathbf{q},r}(\theta) = \sum_{n=0}^{N-1} \omega_D^{rp[n]} q[n] e^{jn\theta} \tag{4.39}$$

has zero first M Taylor moments around $\theta = 0$ for $r = 1, ..., D-1$, or equivalently $(\mathbf{p}, \mathbf{q})$ belongs to

$$\mathcal{N}_D(N,M) = \left\{ \begin{array}{c} (\mathbf{p},\mathbf{q}), \\ \mathbf{p}{=}[p[0],...,p[N-1]]^T, \\ \mathbf{q}{=}[q[0],...,q[N-1]]^T, \\ \mathbf{p}{\in}(\mathbb{Z}/D\mathbb{Z})^N,\ \mathbf{q}{\in}\mathbb{C}^N. \end{array} \middle| \begin{bmatrix} 1 & 1 & \cdots & 1 \\ 1 & 2 & \cdots & N \\ \vdots & \vdots & \ddots & \vdots \\ 1^M & 2^M & \cdots & N^M \end{bmatrix} \begin{bmatrix} \omega_D^{rp[0]} q[0] \\ \omega_D^{rp[1]} q[1] \\ \vdots \\ \omega_D^{rp[N-1]} q[N-1] \end{bmatrix} = \mathbf{0}, r{=}1,...,D{-}1 \right\}. \tag{4.40}$$

Proof: See appendix E. In the proof we had used the result of Lemma 4.6.1.

4.6.2 Number Theoretic Interpretation

Theorem 4.6.3. *The necessary and sufficient condition of zero forcing the first M Taylor moments in $S_{\mathbf{p},\mathbf{q},r}(\theta)$ around $\theta = 0$, $\forall r$, is that the pair $(\mathbf{p}, \mathbf{q})$ satisfies*

$$\sum_{\substack{n=0 \\ p[n]=d}}^{N-1} q[n] n^m = \sum_{\substack{n=0 \\ p[n]=d'}}^{N-1} q[n] n^m,\ 0 \le d, d' \le D-1, 0 \le m \le M. \tag{4.41}$$

Proof: By rearranging the constraints in equation (4.40), we have

$$\begin{bmatrix} 1 & \omega_D & \dots & \omega_D^{D-1} \\ 1 & \omega_D^2 & \dots & \omega_D^{2(D-1)} \\ \vdots & \vdots & \ddots & \vdots \\ 1 & \omega_D^{D-1} & \dots & \omega_D^{(D-1)^2} \end{bmatrix} \begin{bmatrix} \rho_{0,m} \\ \rho_{1,m} \\ \vdots \\ \rho_{2^K-1,m} \end{bmatrix} = \mathbf{0},\ m = 0, \dots, M. \tag{4.42}$$

where $\rho_{d,m} = \sum_{\substack{n=0 \\ p[n]=d}}^{N-1} q[n]n^m$, $d = 0, \ldots, D-1$, $m = 0, \ldots, M$. It can be easily shown that for each m, the vector $[\rho_{0,m}, \ldots, \rho_{D-1,m}]^T$ is of the form $c \cdot [1, \ldots, 1]^T$, where c is some constant.

When $\mathbf{q}$ is chosen as $q[n] = 1, n = 0, \ldots, N-1$, problem (4.41) is referred to the *generalized Tarry-Escott (GTE) problem.* The solution of GTE at $D = 2^K$ can be the following:

Result 4.6.4. *For each integer n between 0 and $2^{K(M+1)}-1$, write its 2^K-ary representation as $n = \sum_{\ell=0}^{M} a_{\ell,n} 2^{K\ell}$, where $0 \leq a_{n,\ell} \leq 2^K - 1$, $\forall \ell$. Construct the vector $\mathbf{p} \in (\mathbb{Z}/2^K\mathbb{Z})^{2^{K(M+1)}}$ as $p[n] = (\sum_{\ell=0}^{M} a_{n,\ell})$ mod 2^K. Let $\mathbf{q}$ be the all-1 vector. Then $(\mathbf{p}, \mathbf{q}) \in \mathcal{N}_{2^K}(2^{K(M+1)}, M)$.*

Note that our dictionary of $(\mathbf{p}, \mathbf{q})$ shall be much richer than the dictionary dictated by the solutions of GTE, since the choice of $\mathbf{q}$ can be very general.

Definition 4.6.2. Let $\pi_D : \mathbb{Z}/D\mathbb{Z} \to \mathbb{Z}/D\mathbb{Z}$ be a permutation on $\mathbb{Z}/D\mathbb{Z}$. Define $\mathcal{A}(\pi_D) : (\mathbb{Z}/D\mathbb{Z})^N \to (\mathbb{Z}/D\mathbb{Z})^N$ as the permutation operator generated from π_D such that $\mathcal{A}(\pi_D)\mathbf{p} = [\pi_D(p[0]), \ldots, \pi_D(p[N-1])]^T$.

Corollary 4.6.5. *If $(\mathbf{p}, \mathbf{q}) \in \mathcal{N}_D(N, M)$, then for an arbitrary permutation π_D, we have $(\mathcal{A}(\pi_D)\mathbf{p}, \mathbf{q}) \in \mathcal{N}_D(N, M)$.*

Proof: This can be directly shown using the result of corollary 4.6.3.

Corollary 4.6.5 indicates that the set $\mathcal{N}_D(N, M)$ is closed under permutation of vector $\mathbf{p}$ by $\mathcal{A}(\pi_D)$. Later we will show a PQ-pulse train based on $(\mathbf{p}, \mathbf{q})$ is equivalent to the PQ-pulse trains based on $(\mathcal{A}(\pi_D)\mathbf{p}, \mathbf{q})$ in noise performance.

4.6.3 Spectral Interpretation

Theorem 4.6.6. *The necessary and sufficient condition of zero forcing the first M Taylor moments in $S_{\mathbf{p},\mathbf{q},r}(\theta)$ around $\theta = 0$, $\forall r$, is that each spectra $S_{\mathbf{p},\mathbf{q},r}(\theta)$ can be factorized as*

$$S_{\mathbf{p},\mathbf{q},r}(\theta) = (1 - e^{j\theta})^{M+1} S_r(\theta), \; r = 1, \ldots, D-1, \tag{4.43}$$

in other words, $e^{j\theta} = 1$ is at least a $(M+1)$-order zero of $S_{\mathbf{p},\mathbf{q},r}(\theta)$, $\forall r$.

Proof: This can be shown by writing the Taylor expansion of each $S_{\mathbf{p},\mathbf{q},r}(\theta)$ around $\theta = 0$.

Theorem 4.6.6 suggests that, as the spectra of the sequence $\omega_D^{rp[0]}, \ldots, \omega_D^{rp[N-1]}$, each $S_{\mathbf{p},\mathbf{q},r}(\theta)$ has a high-order zero at $e^{j\theta} = 1$ and is nonzero at high frequency, $r = 1, \ldots, D-1$. Therefore, each sequence $\omega_D^{rp[0]}, \ldots, \omega_D^{rp[N-1]}$ can be used to construct an FIR band-pass filter with a high-order zero at zero frequency. Later on we will use this insight to develop sequence pairs $(\mathbf{p}, \mathbf{q})$.

4.7 Examples of Pulse Train Constructions

4.7.1 First type of Pulse Train Construction: Iterative Expansion

In this section, we present a systematic generation of sequence pairs $(\mathbf{p}, \mathbf{q})$ satisfying the number-theoretic constraint eq (4.41). The key idea is to use sequence pairs $(\mathbf{p}, \mathbf{q})$ for base waveform libraries to construct a $(\mathbf{p}, \mathbf{q})$ for a larger waveform library, such that the cardinality of the larger library can factorized into product of cardinalities of base library.

4.7.1.1 General Results

Let us first consider to generate a new sequence pair based on two arbitrary existing pairs $(\mathbf{p}_1, \mathbf{q}_1) \in \mathcal{N}_{D_1}(N_1, M)$ and $(\mathbf{p}_2, \mathbf{q}_2) \in \mathcal{N}_{D_2}(N_2, M)$.

Theorem 4.7.1. *Suppose* $(\mathbf{p}_1, \mathbf{q}_1) \in \mathcal{N}_{D_1}(N_1, M)$, *and* $(\mathbf{p}_2, \mathbf{q}_2) \in \mathcal{N}_{D_2}(N_2, M)$. *Let* R_1, R_2 *are two integers such that for an arbitrary integer* $0 \le n \le (N_1 - 1)R_1 + (N_2 - 1)R_2$, n *can be uniquely written as the form* $n_1R_1 + n_2R_2$, $0 \le n_1 \le N_1 - 1$, $0 \le n_2 \le N_2 - 1$. *Construct* $\mathbf{p}_3 \in (\mathbb{Z}/D_1D_2\mathbb{Z})^{(N_1-1)R_1+(N_2-1)R_2+1}$ *as* $p_3[n_1R_1 + n_2R_2] = D_2p_1[n_1] + p_2[n_2]$, *and* $\mathbf{q}_3 \in \mathbb{C}^{(N_1-1)R_1+(N_2-1)R_2+1}$ *as* $q_3[n_1R_1 + n_2R_2] = q_1[n_1]q_2[n_2]$, $0 \le n_1 \le N_1 - 1$, $0 \le n_2 \le N_2 - 1$. *Then we have* $(\mathbf{p}_3, \mathbf{q}_3) \in \mathcal{N}_{D_1D_2}((N_1 - 1)R_1 + (N_2 - 1)R_2 + 1, M)$.

Proof: See appendix F.

Remark 4.7.1. The construction in theorem 4.7.1 picks N_1N_2 integers inside $[0, (N_1-1)R_1 + (N_2-1)R_2]$ as the indices of "active" PRIs in which a pulse is transmitted, received, and processed. Therefore for an arbitrary $n \in [0, (N_1 - 1)R_1 + (N_2 - 1)R_2]$ which cannot be written as $n_1 R_1 + n_2 R_2$, the MIMO radar is silent during the n-th PRI. To achieve highest time efficiency, The pulse train length $(N_1 - 1)R_1 + (N_2 - 1)R_2 + 1$ shall equal to $N_1 N_2$, which occurs if and only if $R_1 = 1, R_2 = N_1$, or $R_1 = N_2, R_2 = 1$. In this chapter, our analysis is focused on the case with the above choice of R_1 and R_2.

Theorem 4.7.2. *From the sequence pairs* $(\mathbf{p}_1^1, \mathbf{q}_1^1) \in \mathcal{N}_{D_1}(N_1, M), \ldots, (\mathbf{p}_1^t, \mathbf{q}_1^t) \in \mathcal{N}_{D_t}(N_t, M), t > 1$, *we can obtain* $(\mathbf{p}, \mathbf{q}) \in \mathcal{N}_D(N, M)$, *where* $D = \prod_{i=1}^t D_i$ *and* $N = \prod_{i=1}^t N_t$, *based on iterative Kronecker product-construction algorithm as shown in Table 4.1.*

Proof: This is a consequence of theorem 4.7.1.

Note that in above algorithm the addition and multiplication in computing the entries in $\mathbf{p}'_\ell$ is done in field $(\mathbb{R}/D'_\ell\mathbb{R})$.

Table 4.1: First construction of $(\mathbf{p}, \mathbf{q}) \in \mathcal{N}_D(N, M)$

Iterative Kronecker product construction of $(\mathbf{p}, \mathbf{q}) \in \mathcal{N}_D(N, M)$
Begin with $\mathbf{p}'_1 = \mathbf{p}_1^1$, $\mathbf{q}'_1 = \mathbf{q}_1^1$, $D'_1 = D_1$, and $N'_1 = N_1$; for $\ell = 2 : t + 1$ Denote $D'_{\ell-1} = \prod_{i=1}^{k-1} D_i$ and $N'_{k-1} = \prod_{i=1}^{\ell-1} N_i$, and construct $\mathbf{p}'_\ell$ and $\mathbf{q}'_\ell$ as $\mathbf{p}'_\ell = \mathbf{1}_{N_\ell} \otimes \mathbf{p}'_{\ell-1} + D'_{\ell-1} \cdot \mathbf{p}_1^{\ell-1} \otimes \mathbf{1}_{N'_{\ell-1}}$; $\mathbf{q}'_\ell = \mathbf{q}_\ell \otimes \mathbf{q}'_{\ell-1}$; end Assign $\mathbf{p} = \mathbf{p}'_{t+1}$, $\mathbf{q} = \mathbf{q}'_{t+1}$, $D = \prod_{i=1}^t D_i$, and $N = \prod_{i=1}^t N_i$. Exit.

4.7.1.2 Results for Paraunitary Waveforms

For the paraunitary waveforms presented in eq (4.14), the waveform library is of size 2^K. The constructions of sequence pairs $(\mathbf{p}, \mathbf{q})$ in $\mathcal{N}_2(N, M)$ is well-established. Such construction, combined with the algorithm in Table 4.1, enables the construction of elements in $\mathcal{N}_{2^K}(N', M)$. In specific, given K sequence pairs $(\mathbf{p}_1^1, \mathbf{q}_1^1) \in \mathcal{N}_2(N_1, M), \ldots, (\mathbf{p}_1^K, \mathbf{q}_1^K) \in \mathcal{N}_2(N_K, M)$, from the first ℓ terms of them we can obtain an element $(\mathbf{p}_\ell, \mathbf{q}_\ell)$ in

$\mathcal{N}_{2^\ell}(\prod_{i=1}^{\ell} N_i, M)$, $\ell = 2, \ldots, K$. By doing so we have the following recurrence relation of residue matrices of $(\mathbf{p}_\ell, \mathbf{q}_\ell)$:

Theorem 4.7.3. *Let $(\mathbf{p}_\ell, \mathbf{p}_\ell) \in \mathcal{N}_{2^\ell}(\prod_{i=1}^{\ell} N_i, M)$ be the sequence pair generated by the first ℓ terms of $(\mathbf{p}_1^1, \mathbf{q}_1^1) \in \mathcal{N}_2(N_1, M), \ldots, (\mathbf{p}_1^K, \mathbf{q}_1^K) \in \mathcal{N}_2(N_K, M)$, for $\ell = 2, \ldots, K$. Denote $\boldsymbol{\Delta}_{2^\ell}(k,\theta)$ as the residue matrix of $(\mathbf{p}_\ell, \mathbf{q}_\ell)$ defined in eq (4.34). The recurrence relation of $\boldsymbol{\Delta}_{2^\ell}(k,\theta)$ is*

$$\boldsymbol{\Delta}_{2^\ell}(k,\theta) = \mathbf{A}_{\ell-1}(\theta) \otimes \boldsymbol{\Delta}_{2^{\ell-1}}(k,\theta) + b_{\ell-1}(\theta)\delta[k]\mathbf{J}_2 \otimes \mathbf{I}_{2^{\ell-1}}, \;\; \ell \geq 2, \tag{4.44}$$

where

$$\mathbf{A}_\ell(\theta) = S_{\mathbf{q}_1^\ell}\left(\prod_{i=1}^{\ell} N_i\theta\right)\mathbf{I}_2 + S_{\mathbf{p}_1^\ell,\mathbf{q}_1^\ell}\left(\prod_{i=1}^{\ell} N_i\theta\right)\mathbf{J}_2, \tag{4.45}$$

and $\mathbf{J}_2$ is the 2×2 anti-diagonal matrix whose anti-diagonal entries are all 1, and

$$b_\ell(\theta) = S_{\mathbf{p}_1^\ell,\mathbf{q}_1^\ell}\left(\prod_{i=1}^{\ell} N_i\theta\right) S_{\mathbf{q}_\ell}(\theta). \tag{4.46}$$

Proof: See appendix G.

Corollary 4.7.4. *The residue matrix $\boldsymbol{\Delta}_{2^K}(k,\theta)$ can be written as*

$$\boldsymbol{\Delta}_{2^K}(k,\theta) = \boldsymbol{\Psi}_{2^K}(\theta)\delta[k] + \boldsymbol{\Phi}_{2^K}(k,\theta), \tag{4.47}$$

where matrix $\boldsymbol{\Psi}_{2^K}(\theta)$ produces the zero-lag inter-channel interference, and $\boldsymbol{\Phi}_{2^K}(k,\theta)$ controls the range sidelobe at nonzero Doppler shift θ, which can be described as

$$\begin{aligned}\boldsymbol{\Psi}_{2^K}(\theta) &= \sum_{t=1}^{K-2} \mathbf{A}_{K-1}(\theta) \otimes \cdots \otimes \mathbf{A}_{t+1}(\theta) \otimes b_t(\theta)\mathbf{J}_2 \otimes \mathbf{I}_{2^t} + b_{K-1}(\theta)\mathbf{J}_2 \otimes \mathbf{I}_{2^{K-1}}, \\ \boldsymbol{\Phi}_{2^K}(k,\theta) &= S_{\mathbf{p}_1,\mathbf{q}_1}(\theta)\mathbf{A}_{K-1}(\theta) \otimes \cdots \otimes \mathbf{A}_1(\theta) \otimes \left(\mathbf{C}_{2,0}[k] - \mathbf{C}_{2,1}[k]\right).\end{aligned} \tag{4.48}$$

Proof: This can be shown by using the result of theorem 4.7.3.

Remark 4.7.2. The structure of $\boldsymbol{\Psi}_{2^K}(\theta)$ satisfies that $\boldsymbol{\Psi}_{2^K}(\theta)[i,j] \neq 0$ only if $i+j$ is even and $i \neq j$, $1 \neq i, j, 2^K$. The magnitude of entries in the northeast and southwest corners of $\boldsymbol{\Psi}_{2^K}(\theta)$ are controlled by that of the spectra $S_{\mathbf{p}_1,\mathbf{q}_1}(N_1^{K-1}\theta)$, whereas the magnitude of entries in the northwest and southeast corners of $\boldsymbol{\Psi}_{2^K}(\theta)$ are controlled by that of the spectra $S_{\mathbf{p}_1,\mathbf{q}_1}(N_1^{K-2}\theta), \cdots, S_{\mathbf{p}_1,\mathbf{q}_1}(N_1\theta)$. The magnitude of entries in $\boldsymbol{\Phi}_{2^K}(k,\theta)$ are controlled by that of the spectra $S_{\mathbf{p}_1,\mathbf{q}_1}(\theta)$. Therefore, compared to the $(\mathbf{p}_1,\mathbf{q}_1)$ design for a 2×2 MIMO radar, the Doppler resilience of range sidelobe suppression of the $(\mathbf{p}_K,\mathbf{q}_K)$ design of a $2^K \times 2^K$ MIMO radar is maintained, whereas the Doppler resilience of waveform unitarity of the $(\mathbf{p}_K,\mathbf{q}_K)$ design is reduced by a factor of N_1^{K-1}.

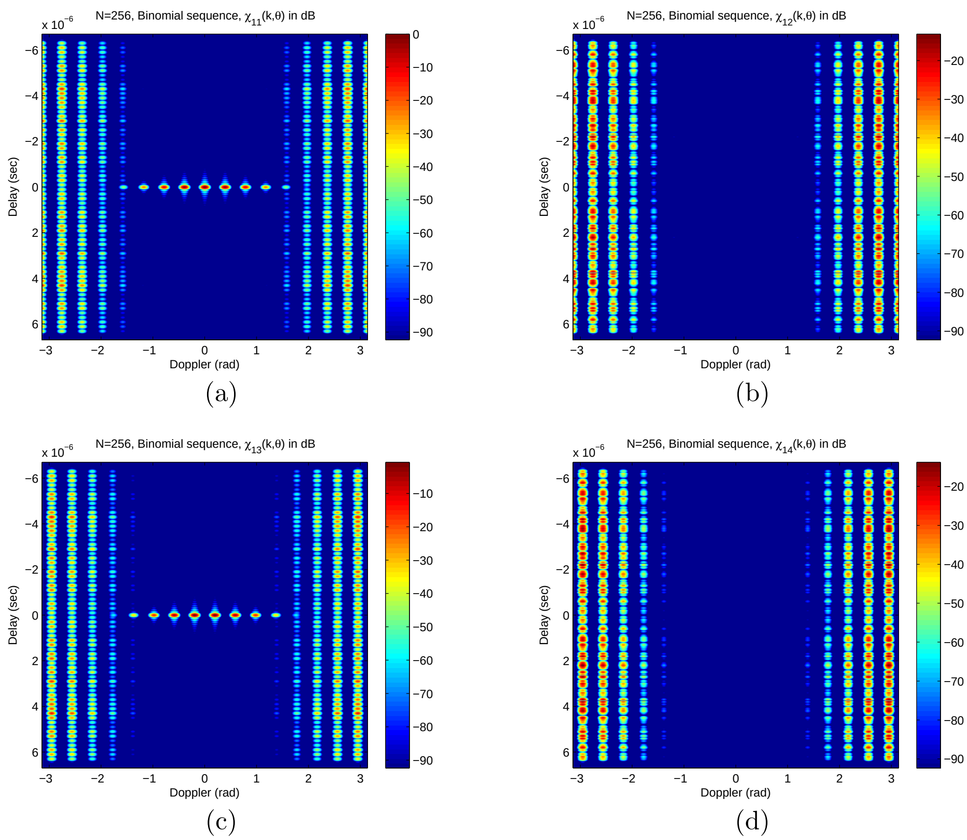

Figure 4.5: Magnitude of entries (a) $[\boldsymbol{\chi}_{\mathbf{p},\mathbf{q}}(\tau,\nu)]_{1,1}$, (b) $[\boldsymbol{\chi}_{\mathbf{p},\mathbf{q}}(\tau,\nu)]_{1,2}$, (c) $[\boldsymbol{\chi}_{\mathbf{p},\mathbf{q}}(\tau,\nu)]_{1,3}$, and (d) $[\boldsymbol{\chi}_{\mathbf{p},\mathbf{q}}(\tau,\nu)]_{1,4}$ in a 4×4 cross ambiguity matrix $\boldsymbol{\chi}_{\mathbf{p},\mathbf{q}}(\tau,\nu)$ corresponding to $(\mathbf{p},\mathbf{q}) \in \mathcal{N}_{2^2}(256,14)$, which is generated from Binomial design $(\mathbf{p}_1,\mathbf{q}_1) \in \mathcal{N}_2(16,14)$ using first type of construction.

Fig. 4.5 illustrates the representative entries of the 4×4 ($K = 2$) cross ambiguity matrix. The vectors $(\mathbf{p},\mathbf{q}) \in \mathcal{N}_2(256,14)$ is generated from the Binomial design $(\mathbf{p}_1,\mathbf{q}_1) \in \mathcal{N}_2(16,14)$, meaning that the first 14-th Taylor moments each entry in the residue matrix $\boldsymbol{\Delta}_4(k,\theta)$ around $\theta = 0$ are annihilated. Along Fig. 4.5(a) to Fig. 4.5(d) we plot the magnitude of entries $[\boldsymbol{\chi}_{\mathbf{p},\mathbf{q}}(\tau,\nu)]_{1,1}$, $[\boldsymbol{\chi}_{\mathbf{p},\mathbf{q}}(\tau,\nu)]_{1,2}$, $[\boldsymbol{\chi}_{\mathbf{p},\mathbf{q}}(\tau,\nu)]_{1,3}$, and $[\boldsymbol{\chi}_{\mathbf{p},\mathbf{q}}(\tau,\nu)]_{1,4}$ of the cross ambiguity matrix $\boldsymbol{\chi}_{\mathbf{p},\mathbf{q}}(\tau,\nu)$. It can been seen that the range sidelobe in each entry of $\boldsymbol{\chi}_{\mathbf{p},\mathbf{q}}(\tau,\nu)$, whose magnitude is proportional to that of spectra $S_{\mathbf{p}_1,\mathbf{q}_1}(\theta)$, is suppressed inside the Doppler band $[-1,1]$ rad. However, the zero-delay response of the off-diagonal entry $[\boldsymbol{\chi}_{\mathbf{p},\mathbf{q}}(\tau,\nu)]_{1,3}$ is only suppressed inside the Doppler intervals of width $1/8$ rad centered at $\theta = 0, \pm 2\pi/16, \ldots, 14\pi/16$, and has significant peaks at $\theta = \pm 1\pi/16, \pm 3\pi/16, \ldots, \pm 15\pi/16$. Because this inter-channel interference is governed by the spectra $S_{\mathbf{p}_1,\mathbf{q}_1}(16\theta)$.

4.7.2 Second Type of Pulse Train Construction: Creating Band-pass Spectra

The cross-ambiguity matrix described in eq (4.33) indicates that a sequence $q[0], \ldots, q[N-1]$ whose spectra $S_{\mathbf{q}}(\theta)$ is energy-concentrated around the zero Doppler is desired. Intuitively, suppose $S_{\mathbf{q}}(\theta)$ is ideally low-pass. If each sequences $\omega_D^{rp[0]}, \ldots, \omega_D^{rp[N-1]}$, $r = 1, \ldots, D-1$ is picked from the unit circle with linearly-increasing phase, then each spectra $S_{\mathbf{p},\mathbf{q},r}(\theta)$, as a circularly-shifted $S_{\mathbf{q}}(\theta)$ in frequency, would be ideally band-pass, provided that the frequency translation is larger than the bandwidth of $S_{\mathbf{q}}(\theta)$. Therefore each spectra $S_{\mathbf{p},\mathbf{q},r}(\theta)$ satisfies the band-pass condition eq (4.43). In the following we give more rigorous constraint of $(\mathbf{p},\mathbf{q})$ to achieve the band-pass patterns $S_{\mathbf{p},\mathbf{q},r}(\theta)$.

Theorem 4.7.5. *Let $p[0], \ldots, p[N-1]$ be the D-ary alternating sequence, such that $p[n] = n \bmod D$, $n = 0, \ldots, N-1$. Then $(\mathbf{p},\mathbf{q}) \in \mathcal{N}_D(N,M)$ if and only if $S_{\mathbf{q}}(\theta)$ has up to M order of nulls at $\theta = -r2\pi/D$, $r = 1, \ldots, D-1$.*

Proof: Each spectra $S_{\mathbf{p},\mathbf{q},r}(\theta)$ can be written by

$$\begin{aligned} S_{\mathbf{p},\mathbf{q},r}(\theta) &= \sum_{n=0}^{N-1} \omega_D^{rp[n]} q[n] e^{jn\theta} \\ &= \sum_{n=0}^{N-1} \omega_D^{rn} q[n] e^{jn\theta} \\ &= S_{\mathbf{q}}(\theta + \frac{r2\pi}{D}),\ r = 1, \ldots, D-1. \end{aligned} \tag{4.49}$$

.

Corollary 4.7.6. *Given* $(\mathbf{p}_1, \mathbf{q}_1) \in \mathcal{N}_2(N_1, M)$. *Let* $p[0], \ldots, p[(N_1-1)(D-1)]$ *be the* D*-ary alternating sequence. If the product*

$$S_{\mathbf{q}}(\theta) = \prod_{r=1}^{D-1} S_{\mathbf{p}_1,\mathbf{q}_1}(\theta + \frac{r2\pi}{D}). \tag{4.50}$$

is the spectra of $q[0], \ldots, q[(N_1-1)(D-1)]$*, then we have* $(\mathbf{p}, \mathbf{q}) \in \mathcal{N}_D((N_1-1)(D-1)+1, M)$.

Proof: This is a direct consequence of theorem 4.7.5.

From this, a closed-form of $(\mathbf{p}, \mathbf{q}) \in \mathcal{N}_2((N_1-1)(D-1)+1, M)$ generated by $(\mathbf{p}_1, \mathbf{q}_1) \in \mathcal{N}_2(N_1, M)$ can be summarized in Table 4.2.

Table 4.2: Second construction of $(\mathbf{p}, \mathbf{q}) \in \mathcal{N}_D(N, M)$

Sequence convolution construction of $(\mathbf{p}, \mathbf{q}) \in \mathcal{N}_D(N, M)$
Set $p[n] = n \bmod D$, $n = 0, \ldots, (N_1-1)(D-1)$; Denote $h_r[n] = (-1)^{p_1[n]} q_1[n] \omega_D^{-rn}$, $n_1 = 0, \ldots, N_1-1$, $r = 1, \ldots, D-1$; Set $q[n] = (h_1 * \cdots * h_{D-1})[n]$.

Corollary 4.7.7. *Suppose* $(\mathbf{p}, \mathbf{q}) \in \mathcal{N}_D(N, M)$*, where* $p[0], \ldots, p[N-1]$ *is the* D*-ary alternating sequence. For a fixed* M*,* N *is minimized if and only if* $q[0], \ldots, q[N-1]$ *has the spectra*

$$S_{\mathbf{q}}(\theta) = c \cdot \prod_{r=1}^{D-1} \left(1 - \omega_D^r e^{j\theta}\right)^{M+1}, \tag{4.51}$$

where c *is some nonzero scaler. Therefore, in this case the base sequence pair* $(\mathbf{p}_1, \mathbf{q}_1) \in \mathcal{N}_2(M+2, M)$ *corresponds to the binomial design, and the minimum* N *at* M *is* $(M+1)(D-1)+1$.

Proof: This can be shown using results in theorem 4.6.6 and 4.7.5.

Theorem 4.7.8. *The residue matrix* $\mathbf{\Delta}_D(k, \theta)$ *can be written by*

$$\mathbf{\Delta}_D(k, \theta) = \mathbf{J}_2 \otimes \mathbf{B}_{K,1}(k, \theta) + \mathbf{I}_2 \otimes \mathbf{B}_{K,2}(k, \theta), \tag{4.52}$$

where

$$\mathbf{B}_{K,1}(k, \theta) = \frac{1}{2^{K-1}} \sum_{\substack{r=1 \\ r \text{ is odd}}}^{2^K-1} S_{\mathbf{q}}(\theta + \frac{r2\pi}{2^K}) \sum_{d=0}^{2^{K-1}-1} \omega_{2^K}^{-rd} \mathbf{C}_{2^{K-1},d}[k], \tag{4.53}$$

and

$$\mathbf{B}_{K,2}(k,\theta) = \frac{1}{2^{K-1}} \sum_{\substack{r=1 \\ r \;\; is\ even}}^{2^K-1} S_{\mathbf{q}}(\theta + \frac{r2\pi}{2^K})\mathbf{\Delta}_{2^{K-1},\frac{r}{2}}[k]. \tag{4.54}$$

Proof: See appendix H.

Remark 4.7.3. As aforementioned, to ensure large diagonal values in cross-ambiguity matrix $\boldsymbol{\chi}_{\mathbf{p},\mathbf{q}}(0,0)$, we require $S_{\mathbf{q}}(\theta)$ to be low-pass around zero Doppler. As a consequence of using the D-ary alternating sequence as the transmit waveform scheduler, each spectra $S_{\mathbf{p},\mathbf{q},r}(\theta)$ of the resulted $(\mathbf{p},\mathbf{q}) \in \mathcal{N}_D(N,M)$ is band-pass around Doppler shift $\theta = -\frac{2\pi}{D}$. Therefore the "cleared Doppler band" inside which every $S_{\mathbf{p},\mathbf{q},r}(\theta)$ is "well annihilated" is no broader than $\frac{4\pi}{D}$.

Fig. 4.6 illustrates the representative entries of the 4×4 ($K = 2$) cross ambiguity matrix. The vectors $(\mathbf{p},\mathbf{q}) \in \mathcal{N}_2(3 * 15 + 1, 14)$ is generated from the Binomial design $(\mathbf{p}_1,\mathbf{q}_1) \in \mathcal{N}_2(16,14)$, indicating up to the 14-th order of nulls of the residue matrix $\mathbf{\Delta}_4(k,\theta)$ around $\theta = 0$. Fig. 4.6(a)-(d) depict the magnitude of entries $[\boldsymbol{\chi}_{\mathbf{p},\mathbf{q}}(\tau,\nu)]_{1,1}$, $[\boldsymbol{\chi}_{\mathbf{p},\mathbf{q}}(\tau,\nu)]_{1,2}$, $[\boldsymbol{\chi}_{\mathbf{p},\mathbf{q}}(\tau,\nu)]_{1,3}$, and $[\boldsymbol{\chi}_{\mathbf{p},\mathbf{q}}(\tau,\nu)]_{1,4}$ of the cross ambiguity matrix $\boldsymbol{\chi}_{\mathbf{p},\mathbf{q}}(\tau,\nu)$. Inside $[-\pi,\pi]$ rad, the spectra $S_{\mathbf{p},\mathbf{q},r}(\theta) = S_{\mathbf{q}}(\theta + \frac{r2\pi}{4})$ is nonzero at $\theta = -\frac{r2\pi}{4}$ (wrapped) and has up to 14-th order of nulls when θ is rest multiples of $\frac{2\pi}{4}$, $r = 1,2,3$. As a result, the residues in $[\boldsymbol{\chi}_{\mathbf{p},\mathbf{q}}(\tau,\nu)]_{1,1}$ and $[\boldsymbol{\chi}_{\mathbf{p},\mathbf{q}}(\tau,\nu)]_{1,2}$ are controlled by $S_{\mathbf{p},\mathbf{q},2}(\theta)$, and thus annihilated inside the Doppler band $[-\frac{3\pi}{4}, -\frac{3\pi}{4}]$ rad. The residues in $[\boldsymbol{\chi}_{\mathbf{p},\mathbf{q}}(\tau,\nu)]_{1,3}$ and $[\boldsymbol{\chi}_{\mathbf{p},\mathbf{q}}(\tau,\nu)]_{1,4}$ are controlled by $S_{\mathbf{p},\mathbf{q},1}(\theta)$ and $S_{\mathbf{p},\mathbf{q},3}(\theta)$, and thus annihilated inside the Doppler bands of width $\frac{\pi}{2}$ rad centered at $\theta = 0, \pi$. In summary, the waveform paraunitary property is maintained inside the Doppler band $[-\frac{\pi}{4}, \frac{\pi}{4}]$.

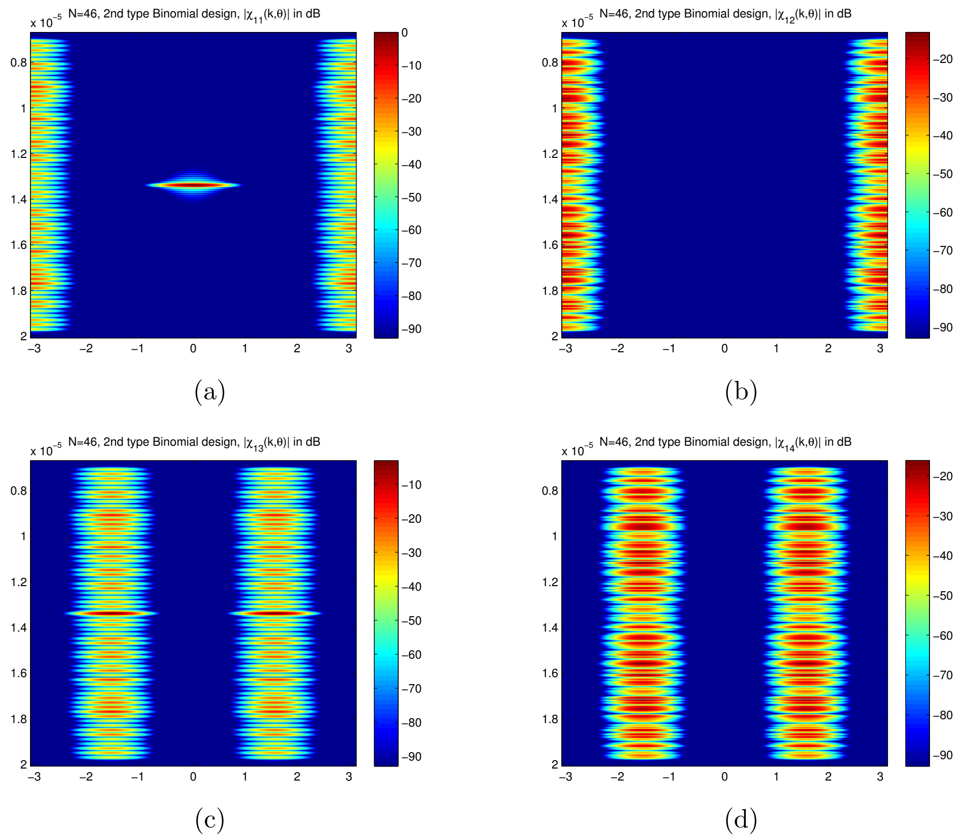

Figure 4.6: Magnitude of entries (a) $[\boldsymbol{\chi}_{\mathbf{p},\mathbf{q}}(\tau,\nu)]_{1,1}$, (b) $[\boldsymbol{\chi}_{\mathbf{p},\mathbf{q}}(\tau,\nu)]_{1,2}$, (c) $[\boldsymbol{\chi}_{\mathbf{p},\mathbf{q}}(\tau,\nu)]_{1,3}$, and (d) $[\boldsymbol{\chi}_{\mathbf{p},\mathbf{q}}(\tau,\nu)]_{1,4}$ in a 4×4 cross ambiguity matrix $\boldsymbol{\chi}_{\mathbf{p},\mathbf{q}}(\tau,\nu)$ corresponding to $(\mathbf{p},\mathbf{q}) \in \mathcal{N}_{2^2}(46,14)$, which is generated from Binomial design $(\mathbf{p}_1,\mathbf{q}_1) \in \mathcal{N}_2(16,14)$ using second type of construction.

4.8 Noise Analysis

4.8.1 Calculation of Signal and Noise Power

With a point scatter at electrical angle ϕ, delay τ, and Doppler frequency ν, the radar return is

$$\mathbf{r}(t) = e^{-j\nu t}\mathbf{a}(\phi)\mathbf{a}(\phi)^T\mathbf{z}_p(t-\tau) + \mathbf{n}(t), \tag{4.55}$$

where $\mathbf{a}(\phi) = [1, e^{j\phi}, \ldots, e^{j(D-1)\phi}]^T$ is the array manifold steered to angle ϕ. In eq (4.55) we had ignored the target scattering coefficient. When the receive filter matches the angle ϕ

and delay τ, it outputs

$$\begin{aligned} y &= \int_{-\infty}^{\infty} \mathbf{z}_q(t-\tau)^H \mathbf{a}(\phi)^* \mathbf{a}(\phi)^H e^{j\nu_0 t} \mathbf{r}(t) dt \\ &= D\mathbf{a}(\phi)^T \boldsymbol{\chi}_{\mathbf{p},\mathbf{q}}(0, \nu - \nu_0) \mathbf{a}(\phi)^* + D\mathbf{a}(\phi)^H \boldsymbol{\chi}_{\mathbf{n},\mathbf{q}}(\tau, -\nu_0) \mathbf{a}(\phi)^*, \end{aligned} \tag{4.56}$$

where ν_0 stands for the Doppler frequency estimate, and $\boldsymbol{\chi}_{\mathbf{n},\mathbf{q}}(\tau, \nu)$ denotes the colored noise matrix

$$\boldsymbol{\chi}_{\mathbf{nq}}(\tau, \nu) = \int_{-\infty}^{\infty} \mathbf{n}(t) \mathbf{z}_{\mathbf{q}}(t-\tau)^H e^{-j\nu t} dt. \tag{4.57}$$

The detection problem can be expressed as

$$\begin{cases} \mathcal{H}_0 : y = y_n \\ \mathcal{H}_1 : y = y_s + y_n \end{cases}. \tag{4.58}$$

With sufficiently small Doppler mismatch $(\nu - \nu_0)T$, the cross ambiguity matrix $\chi_{\mathbf{p},\mathbf{q}}(\tau, \nu)$ approximately equals $S_{\mathbf{q}}(e^{j\theta})|_{\theta=0} \mathbf{C}_D[0]$. Thus the signal power can be approximated by

$$P_s(\mathbf{p}, \mathbf{q}, \phi) = D^2 \cdot \left| S_{\mathbf{q}}(e^{j\theta}) \right|_{\theta=0}^2 \cdot \left| \mathbf{a}(\phi)^T \mathbf{C}_D[0] \mathbf{a}(\phi)^* \right|^2. \tag{4.59}$$

The noise power is

$$\begin{aligned} & P_n(\mathbf{p}, \mathbf{q}, \phi) \\ &= D^2 E\left\{ \mathbf{a}(\phi)^H \boldsymbol{\chi}_{\mathbf{nq}}(\tau, -\nu_0) \mathbf{a}(\phi)^* \mathbf{a}(\phi)^T \boldsymbol{\chi}_{\mathbf{nq}}(\tau, -\nu_0)^* \mathbf{a}(\phi) \right\} \\ &= D^2 E\left\{ \mathbf{a}(\phi)^H \int_{-\infty}^{\infty} \int_{-\infty}^{\infty} \mathbf{n}(t) \mathbf{z}_{\mathbf{q}}(t-\tau)^H e^{j\nu_0 t} \mathbf{a}(\phi)^* \mathbf{a}(\phi)^T \mathbf{n}(t')^* \mathbf{z}_q(t'-\tau)^T e^{-j\nu_0 t'} dt dt' \mathbf{a}(\phi) \right\} \\ &= D^2 \int_{-\infty}^{\infty} E\left\{ |\mathbf{a}(\phi)^H \mathbf{n}(t)|^2 \right\} \mathbf{z}_{\mathbf{q}}(t-\tau)^H \mathbf{a}(\phi)^* \mathbf{z}_{\mathbf{q}}(t-\tau)^T \mathbf{a}(\phi) dt \\ &= 8^K \sigma_n^2 \mathbf{a}(\phi)^T \int \mathbf{z}_{\mathbf{q}}(t) \mathbf{z}_{\mathbf{q}}(t)^H dt \mathbf{a}(\phi)^* \\ &= D^3 \sigma_n^2 \mathbf{a}(\phi)^T \left(\sum_{n=0}^{N-1} |q[n]|^2 \sum_{\substack{d=0 \\ p_n = d}}^{2^K-1} \mathbf{C}_{2^K, d}[0] \right) \mathbf{a}(\phi)^*. \end{aligned} \tag{4.60}$$

In the rest of this section, we restrict the analysis to the paraunitary waveform case.

4.8.2 Achievable Upper Bound of Noise Power

Theorem 4.8.1. *Suppose* $(\mathbf{p},\mathbf{q}) \in \mathcal{N}_{2^K}(N,M)$. *Then the noise power* $P_n(\mathcal{A}(\pi_{2^K})\mathbf{p},\mathbf{q},\phi)$ *for all possible pairs* $(\mathcal{A}(\pi_{2^K})\mathbf{p},\mathbf{q}) \in \mathcal{N}_{2^K}(N,M)$ *satisfies*

$$\max_{\pi_{2^K},\phi} P_n(\mathcal{A}(\pi_{2^K})\mathbf{p},\mathbf{q},\phi)$$
$$= 2^{5K-1}\sigma_n^2\left(\sum_{\substack{n=0\\p[n]=d_0}}^{N-1}|q[n]|^2+\sum_{\substack{n=0\\p[n]=d_1}}^{N-1}|q[n]|^2+|C_{xy}[0]|\cdot\left(\sum_{\substack{n=0\\p[n]=d_0}}^{N-1}|q[n]|^2-\sum_{\substack{n=0\\p[n]=d_1}}^{N-1}|q[n]|^2\right)\right), \tag{4.61}$$

where

$$d_0 = \arg\max_{0\le d\le 2^K-1}\sum_{\substack{n=0\\p[n]=d}}^{N-1}|q[n]|^2,\ \ d_1 = \arg\max_{\substack{0\le d\le 2^K-1\\d\ne d_0}}\sum_{\substack{n=0\\p[n]=d}}^{N-1}|q[n]|^2. \tag{4.62}$$

A sufficient condition to achieve the equality in eq (4.61) is:

(1) π_{2^K} *satisfies that for* $1\le k\le K-1$, *we have*

$$\sum_{\substack{n=0\\p[n]=\pi_{2^K}(i)}}^{N-1}|q[n]|^2 \ge \sum_{\substack{n=0\\p[n]=\pi_{2^K}(i)+2^k}}^{N-1}|q[n]|^2,\ \ 0\le i\le 2^k-1; \tag{4.63}$$

(2) $\pi_{2^K}(0)=d_0$ *if* $C_{xy}[0]\ge 0$ *or* $\pi_{2^K}(0)=d_1$ *if* $C_{xy}[0]<0$;

(3) $\phi=0$.

Proof: See appendix I.

Corollary 4.8.2. *Suppose* $(\mathbf{p},\mathbf{q}) \in \mathcal{N}_{2^K}(N,M)$. *Then the noise power* $P_n(\mathcal{A}(\pi_{2^K})\mathbf{p},\mathbf{q},\phi)$ *for all possible pairs* $(\mathcal{A}(\pi_{2^K})\mathbf{p},\mathbf{q}) \in \mathcal{N}_{2^K}(N,M)$ *is upper-bounded as*

$$\max_{\pi_{2^K},\phi} P_n(\mathcal{A}(\pi_{2^K})\mathbf{p},\mathbf{q},\phi) \le 2^{5K}\sigma_n^2\max_{0\le d\le 2^K-1}\sum_{\substack{n=0\\p[n]=d}}^{N-1}|q[n]|^2. \tag{4.64}$$

Proof: This can be directly shown by using the result of theorem 4.4.13.

Remark 4.8.1. Eq. (4.64) yield an insightful interpretation: Low variation of $P_n(\mathbf{p},\mathbf{q},\phi)$ in angle is possible the sum of $|q[n]|^2$ over distinct index sets specified by $p[n]=d$, $d=0,\dots,2^K-1$ are close in value. In other words, higher value of worst-case SNR requires a sequence $q[0],\dots,q[N]$ which is alphabet-wise energy-balanced conditioned on $\mathbf{p}$. Naturally we have the following result:

4.8.3 Angle-invariant Noise Power

Theorem 4.8.3. *The noise power* $P_n(\mathbf{p}, \mathbf{q}, \phi)$ *for* $(\mathbf{p}, \mathbf{q}) \in \mathcal{N}_{2^K}(N, M)$ *is a constant at all* ϕ *if and only if* $\sum_{p[n]=d} |q[n]|^2 = \sum_{p[n]=d'} |q[n]|^2$ *for* $0 \leq d, d' \leq 2^K - 1$*. Consequently, if* $P_n(\mathbf{p}, \mathbf{q}, \phi)$ *is a constant at all* ϕ*, then* $P_n(\mathcal{A}(\pi_{2^K})\mathbf{p}, \mathbf{q}, \phi)$ *equals the same constant at all* ϕ *for all permutations* π_{2^K}*.*

Proof: This is the direct consequence of theorem 4.8.1 and corollary 4.8.2.

4.9 Conclusion

We presented a framework for designing Doppler resilient paraunitary illumination for MIMO radar. By properly coordinating the transmission of waveform components in time across aperture, we can maintain the paraunitary property by annihilating the Doppler-induced sensitivity of the cross-ambiguity matrix inside a Doppler interval around zero axis.

CHAPTER 5

COMPRESSIVE OPTICAL IMAGING AND SENSITIVITY TO MISFOCUS

Optical imaging is ubiquitous in science and engineering [85,86]. Recently novel imaging methods which make use of spatial beam modulation of have been intensively studied [30, 87–89]. These techniques can spatially structure the excitation beam by using proper mask patterns. A single pixel detector records a series of inner products between the object and mask representations. Compared to the other imaging methods, the spatial beam modulated imaging with a single detector has the following benefits: (1) the 2-D detectors, such as charge-coupled semiconductor devices (CCD) and CMOS detectors, are only available in visible and near-infrared, less common in mid-infrared and far-infrared, and almost non-existent in Terahertz regions, whereas the single detectors can operate in most frequency regions. (2) to acquire a high resolution image, many current imaging methods use the point-by-point object scanning with a single-element detector [90, 91]. The drawback of these approaches is that a long time is needed to acquire the whole image.

The image acquisition of a single-pixel detector based imaging system can be increased by employing spatial beam modulation [29,30,33,88,89]. For instance, one unique imaging approach among imaging methods based on spatial beam modulation is the spatial frequency modulation for imaging (SPIFI) [29,33]. It generates a spatially modulated excitation onto the object, using a spinning linearly-chirped optical mask across its spatial extent. Such a structured illumination provides a unique modulation frequency at each spatial point in the beam. The detector temporally collects the spatial integral of incoming intensity, which for each time sample, is seen as an inner product of a pure spatial frequency and the line sample of the object. The recovery of the object spatial information is performed via a simple Fourier transform. Note that in order to obtain high imaging resolution, a large number of temporal measurements is required to meet the Nyquist condition. However, other imaging approaches based on structured illumination, such as compressive [30, 88], can effectively improve the image acquisition speed by recording a small number of measurements.

In this chapter, we investigate compressive sensing as a principle for line-scanned imaging with a single pixel detector. The optical setup is illustrated in Fig. 5.1. The object is scanned in a line by line fashion. We spin a mask disc which spatially modulate the excitation beam, and the detector temporally collects the spatial integral of incoming intensity, which for each time sample, is seen as an inner product of the mask representation and the line sample of the object. The compressive sensing method enables us to reconstruct the sparse line-scans of the object with small number of measurements. The classical theory of compressive sensing is developed by early literature [92–95]. Suppose the object of interest has a sparse or compressible representation in a certain basis. If the measurement matrix satisfies the *Restricted Isometry Property* (RIP), then the object can be precisely reconstructed by using Basis Pursuit algorithm. This reconstruction algorithm also shows some robustness to the measurement noises. Although the compressive sensing is theoretically sound, in practice we have the following physical challenges to utilize it for optical imaging:

- *Poisson Statistics.* The detector spatially integrates the intensity by counting incoming photons. Each temporal measurement is a discrete variable and follows Poisson distribution [96, 97].

- *Model Perturbation.* The actual measurement model may differ with presumed model due to various aberrations, which can be resulted in misfocus, spherical wave, mask wobbling, etc. This means that the actual measurement matrix may be different with the presumed measurement matrix.

The first issue has been discussed in the papers of Raginsky, et. al [96, 97]. To improve the performance of compressive sensing under Poisson noise, an algorithm which optimizes the penalized likelihood objective function is proposed for object recovery. Much attention has been payed on the second issue [34, 98–100]. The reconstruction error of Basis Pursuit with model mismatch has been studied in [98]. The sensitivity of basis mismatch in compressive sensing is analyzed in [34, 99]. It turns out that even at small mismatch between the actual and presumed basis in which the image sparse coefficients, the image inversion error can be large. In [100] a sparse-total least square (S-TLS) algorithm that incorporates the total least square and LASSO is developed to address the modal mismatch. It is numerically shown that for some specific problems the S-TLS reduces reconstruction error compared to traditional sparse recovery methods.

In this chapter, we investigate the sensitivity of compressive sensing to the model perturbation due to misfocus error in the imaging system. To the best of our knowledge, such an analysis has not yet been presented. We first formulate general measurement equations which can apply to both in-focus and misfocus imaging cases. We show that when a sparse object is located at in-focus position, its reconstruction via compressive sensing approach is precise.

We then numerically test the performance of compressive sensing versus the misfocus effect. The simulation results show that the robustness of CS reconstruction depends on the demagnification factor. At low to medium demagnification factors, the CS reconstruction is robust to misfocus, when the misfocus distance is within the depth of field. However, at high demagnification factors, the model mismatch caused by misfocus effect becomes significant, and hence the CS algorithm fails to extract the object information from the perturbed measurements.

We give a mathematical description of model perturbation caused by misfocus effect. The model perturbation can be characterized by the perturbation matrix, as a function of both the demagnification factor and misfocus distance. A theoretical upper bound of the compressive sensing reconstruction error at given demagnification factor and misfocus

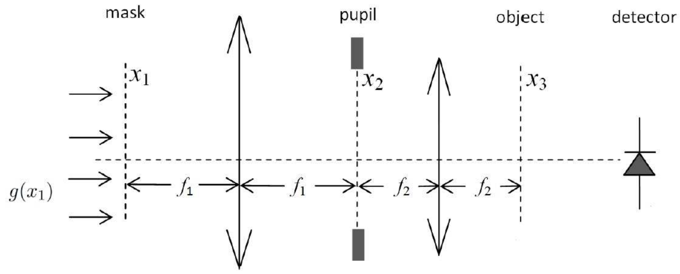

Figure 5.1: Spatial positions of mask and object planes.

distance is developed. Compared to the theoretical performance bound proposed in [98] that is expressed by the spectrum norm of the perturbation matrix, our performance bound has a closed form and is easy to compute. The performance bound indicates that the reconstruction error increases in both demagnification factor and misfocus distance.

5.1 Measurement Formation

Consider the Abbe system (4-f system) shown in Fig. 5.1. The front and back lenses are labeled as L_1 and L_2. The focal lengths of L_1 and L_2 are f_1 and f_2, respectively. An optical mask shown in Fig. 5.1 is placed in the front focal plane of L_1. We assume that the mask is composed of a set of discrete, identical binary $\{0, 1\}$ (0 for close, and 1 for open) field transmission elements (rectangular functions of width Δ) that are positioned at discrete positions along the lateral line focus. A field $g(x_1)$ illuminates the mask and then modulates the object representation. The object comes to focus at the back focal plane of lens L_2. The demagnification factor of the Abbe system is

$$M = \frac{f_1}{f_2}. \tag{5.1}$$

In the imaging process, the optical mask is continually spun. Each time a certain radial section of the mask modulates the excitation beam. With a sampling interval t_0, the optical detector temporally samples the spatial integration of the intensity of the object illuminated by the excitation beam. At $t = mt_0$, the excitation beam is modulated by m-th radial section of the mask, whose field transmittance is:

$$t_{mask}(x_1; m) = \sum_{\ell=0}^{N-1} a_{m,\ell} w(x_1 - (\ell - \frac{N}{2})\Delta), \tag{5.2}$$

where the binary coefficients $a_{m,0}$, ... ,$a_{m,N-1}$ indicates the open and close status of elements along the m-th radial section of the mask. The function $w(x)$ is a rectangular function with support $[0, \Delta)$. We introduce the spatial offset $\frac{N}{2}\Delta$ to keep the function $t_{mask}(x_1; m)$ centered at $x_1 = 0$. Denote $g(x_1)$ as the field that incident on the mask plane and spans all N modulation elements. The field passing through $t_{mask}(x_1; m)$ is

$$u_{mask}(x_1; m) = g(x_1) t_{mask}(x_1; m), \tag{5.3}$$

At the back focal plane of the lens L_2, the excitation field is

$$u_{exc}(x_3; m) = u_0 \int_{-\infty}^{\infty} u_{mask}(x_1; m) h(x_1 + Mx_3) dx_1, \tag{5.4}$$

where the complex-valued scaler u_0 is $u_0 = \frac{M e^{ikf_1(1+M)} e^{i\frac{kM}{2f_1}x_3^2(1+M)}}{f_1^2\lambda^2}$, and $h(x)$ is the *in-focus* psf of the Abbe system:

$$h(x) = \int_{-\infty}^{\infty} P(x_2) e^{-i\frac{k}{f_1}x_2 x} dx_2. \tag{5.5}$$

In the limit where we can treat the psf $h(x)$ a delta function, then clearly we have that $u_{exc}(x_3; m) = u_{mask}(-Mx_3; m)$, meaning that the excitation field illuminating the object is a reversed, demagnified version of $u_{mask}(x_1; m)$. However, the finite width of the psf in eq. (5.5) broadens the excitation field to

$$\begin{aligned} u_{exc}(x_3; m) &= u_0 \sum_{\ell=0}^{N-1} a_{m,\ell} \int_{(\ell-N/2)\Delta}^{(\ell-N/2+1)\Delta} g(x_1) h(x_1 + Mx_3) dx_1 \\ &= u_0 \sum_{\ell=0}^{N-1} a_{m,\ell} \mathcal{G}_\ell(x_3), \end{aligned} \tag{5.6}$$

where the blurred window function $\mathcal{G}_\ell(x_3)$ is

$$\mathcal{G}_\ell(x_3) = \int_{(\ell-N/2)\Delta}^{(\ell-N/2+1)\Delta} g(x_1) h(x_1 + Mx_3) dx_1, \tag{5.7}$$

whose major part lies in the interval $[(\frac{N}{2}-\ell-1)\frac{\Delta}{M},(\frac{N}{2}-\ell)\frac{\Delta}{M}]$ with a narrow $h(x)$.

The optical detector spatially integrates the intensity right behind the object:

$$y_m=\int_{-\infty}^{\infty}|u_{exc}(x_3;m)t_{obj}(x_3)|^2dx_3 \tag{5.8}$$

Assume that the support of object in x_3 axis is $[-\frac{N\Delta}{2M},\frac{N\Delta}{2M}]$. Here we require that inside each spatial bin $[(\ell-\frac{N}{2})\frac{\Delta}{M},(\ell-\frac{N}{2}+1)\frac{\Delta}{M}]$, $\ell=0,1,...N-1$, the variation of object intensity $|t_{obj}(x_3)|^2$ is negligible, and $|t_{obj}(x_3)|^2$ approximately equals a constant θ_ℓ. This physically requires that the spatial frequency components of the object are confined in $|f_{x_3}|\le\frac{M}{\Delta}$. From this, the m-th temporal measurement y_m can be expressed as

$$\begin{aligned} y_m&=\sum_{\ell=0}^{N-1}\theta_\ell\int_{(\ell-N/2)\Delta/M}^{(\ell-N/2+1)\Delta/M}|u_{exc}(x_3;m)|^2dx_3\\ &=|u_0|^2\sum_{\ell=0}^{N-1}\theta_\ell\int_{(\ell-N/2)\Delta/M}^{(\ell-N/2+1)\Delta/M}\Big|\sum_{\ell'=0}^{N-1}a_{m,\ell'}\mathcal{G}_{\ell'}(x_3)\Big|^2dx_3. \end{aligned} \tag{5.9}$$

After rewriting $\theta_\ell=\theta_{N-1-\ell}$ for $\ell=0,1,...,N-1$, y_m can be expressed by

$$y_m=|u_0|^2\sum_{\ell=0}^{N-1}\theta_\ell\int_{(N/2-\ell-1)\Delta/M}^{(N/2-\ell)\Delta/M}\Big|\sum_{\ell'=0}^{N-1}a_{m,\ell'}\mathcal{G}_{\ell'}(x_3)\Big|^2dx_3. \tag{5.10}$$

Our goal is that by modulating the object with a certain row of the mask, the measurement y_m can be formed as a scaled inner product between the intensity of mask and object. However, it can be seen that over each spatial interval $[(\frac{N}{2}-\ell-1)\frac{\Delta}{M},(\frac{N}{2}-\ell)\frac{\Delta}{M}]$, the intensity integration contains the contribution from the ℓ-th mask element $a_{m,\ell}$, as well as other mask elements, due to the leakage of functions $\mathcal{G}_{\ell'}(x_3)$ with $\ell'\neq\ell$ as a result of the finite psf width. We will see that this leakage increases with increased misfocus error of the imaging system. Therefore the measurement y_m is a distorted inner product between the mask and object representations. Denote $d_\ell=(\frac{N}{2}-\ell)\frac{\Delta}{M}$, $\ell=0,1,...,N-1$, then using that fact that $|a_{m,\ell}|^2=a_{m,\ell}$ for all m and ℓ, we can further write y_m as

$$\begin{aligned} y_m=&|u_0|^2\sum_{\ell=0}^{N-1}a_{m,\ell}\theta_\ell\int_{d_{\ell+1}}^{d_\ell}|\mathcal{G}_\ell(x_3)|^2dx_3+|u_0|^2\sum_{\ell=0}^{N-1}\theta_\ell\int_{d_{\ell+1}}^{d_\ell}|\sum_{\ell'\neq\ell}a_{m,\ell'}\mathcal{G}_{\ell'}(x_3)|^2dx_3\\ &+|u_0|^2\sum_{\ell=0}^{N-1}\theta_\ell\int_{d_{\ell+1}}^{d_\ell}\sum_{\ell'\neq\ell}2\mathrm{Re}\Big\{a_{m,\ell}a_{m,\ell'}\mathcal{G}_\ell(x_3)\mathcal{G}_{\ell'}(x_3)\Big\}dx_3. \end{aligned} \tag{5.11}$$

Denote $\widetilde{\theta}_\ell = \theta_\ell \int_{d_{\ell+1}}^{d_\ell} |\mathcal{G}_\ell(x_3)|^2 dx_3$ for $\ell = 0, 1, ..., N-1$. Then by dropping the constant intensity $|u_0|^2$ we can write y_m by

$$y_m = \sum_{\ell=0}^{N-1} a_{m,\ell} \widetilde{\theta}_\ell + p_m. \tag{5.12}$$

The first term of y_m is a scaled inner product between the vectors $\mathbf{a}_m = [a_{m,0}, ..., a_{m,N-1}]^T$ and $\widetilde{\boldsymbol{\theta}} = [\widetilde{\theta}_0, ..., \widetilde{\theta}_{N-1}]^T$. The second term p_m is the measurement perturbation due to the finite psf width:

$$\begin{aligned} p_m = &\sum_{\ell=0}^{N-1} \theta_\ell \int_{d_{\ell+1}}^{d_\ell} |\sum_{\ell' \neq \ell} a_{m,\ell'} \mathcal{G}_{\ell'}(x_3)|^2 dx_3 \\ &+ \sum_{\ell=0}^{N-1} \theta_\ell \int_{d_{\ell+1}}^{d_\ell} \sum_{\ell' \neq \ell} 2\mathrm{Re}\big\{a_{m,\ell} a_{m,\ell'} \mathcal{G}_\ell(x_3) \mathcal{G}_{\ell'}(x_3)\big\} dx_3. \end{aligned} \tag{5.13}$$

Note that eq. (5.11)-(5.13) are general enough for a arbitrary psf $h(x)$.

For the in-focus psf given in eq. (5.5), with appropriate pupil size, it should be sufficiently narrow in space, such that with respect to each function $\mathcal{G}_\ell(x_3)$, $\ell = 0, ..., N-1$, its portion outside the interval $[d_{\ell+1}, d_\ell]$ can be negligible. This means that the amplitude of perturbations p_m's are desirably small compared to that of the signals. Hence, the vectorized temporal measurement $\mathbf{y} = [y_0, ..., y_{M-1}]^T$ is approximately

$$\mathbf{y} = \mathbf{A}\widetilde{\boldsymbol{\theta}}, \tag{5.14}$$

where the matrix $\mathbf{A} = [a_{m,\ell}] = [\mathbf{a}_0, ..., \mathbf{a}_{M-1}]^T$ is the *intensity measurement matrix*.

5.2 Compressive Imaging Approach

For the optical system whose measurement is well approximated characterized by eq. (5.14), we are concerned with the following two primary questions: (1) how to design a good matrix $\mathbf{A}$, and (2) how to process the measurement $\mathbf{y}$ to invert the object $\boldsymbol{\theta}$. In the following we answer above questions by introducing the rudiments of compressive sensing theory.

The key assumption of compressive sensing is that the object of interest $\widetilde{\boldsymbol{\theta}}$ has a sparse or compressible representation. Suppose the N-dimensional vector $\widetilde{\boldsymbol{\theta}}$ is k-sparse or compressible, where $k \ll N$. Our goal is to reconstruct the object $\widetilde{\boldsymbol{\theta}}$ from M measurements such that $M \ll N$:

$$\mathbf{y} = \mathbf{A}\widetilde{\boldsymbol{\theta}} + \mathbf{n}. \tag{5.15}$$

where the matrix $\mathbf{A}$ is an M by N underdetermined measurement matrix, and $\mathbf{n}$ stands for any potential measurement perturbation. This sparse reconstruction is possible if the matrix $\mathbf{A}$ satisfies the $2k$-restricted isometry property (RIP), that is, for any $2k$-sparse vector $\mathbf{u}$,

$$(1 - \delta_{2k}\mathbf{A})\|\mathbf{u}\|_2^2 \leq \|\mathbf{A}\mathbf{u}\|_2^2 \leq (1 + \delta_{2k}^{\mathbf{A}})\|\mathbf{u}\|_2^2, \tag{5.16}$$

where $\delta_{2k}^{\mathbf{A}}$ is called the restricted isometry constant. If $\delta_{2k}^{\mathbf{A}} < \sqrt{2} - 1$, then $\widetilde{\boldsymbol{\theta}}$ can be reconstructed by the ℓ_1 minimization (Basis Pursuit)

$$\begin{aligned} \widetilde{\boldsymbol{\theta}}^* &= \arg\min_{\widetilde{\boldsymbol{\theta}}} \|\widetilde{\boldsymbol{\theta}}\|_1 \\ \text{s.t. } &\|\mathbf{y} - \mathbf{A}\widetilde{\boldsymbol{\theta}}\|_2 \leq \epsilon, \end{aligned} \tag{5.17}$$

where ϵ is an upper bound of $\|\mathbf{n}\|_2$. In this case the number of measurements M is $\mathcal{O}(k \log \frac{N}{k})$, and the reconstruction error satisfies

$$\|\widetilde{\boldsymbol{\theta}} - \widetilde{\boldsymbol{\theta}}^*\|_2 \leq C_0 k^{-\frac{1}{2}} \|\widetilde{\boldsymbol{\theta}} - \widetilde{\boldsymbol{\theta}}_k\|_1 + C_1\epsilon, \tag{5.18}$$

where $\widetilde{\boldsymbol{\theta}}_k$ is the best k-term approximation of $\widetilde{\boldsymbol{\theta}}$, and C_0 and C_1 are some constants determined by $\delta_{2k}^{\mathbf{A}}$. One candidate of binary RIP matrix is the Bernoulli random matrix, in which each entry is drawn from an identical and independent Bernoulli distribution.

Here we validate the in-focus object reconstruction of compressive imaging method. We set the pupil radius W as 10mm. The focal lens of L_1 is $f_1 = 40$mm. The magnification factor is $M = 100$, and thus the focal length of L_2 is $f_2 = f_1/100$. The width of a mask element is $\Delta = 0.05$mm.

The original feather object is depicted in Fig. 5.2, which has 157 rows and 256 columns. The colorbar shows that the amplitude of each object element ranges from 0 to 255. In the simulation, we perform a row scan of the feather object. The intensity of each row of the

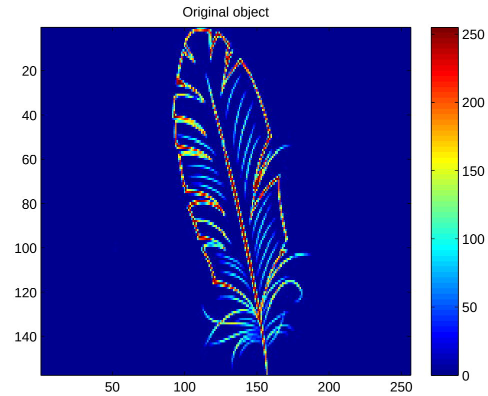

Figure 5.2: Original 2-dimensional feather object, with 157 rows and 256 columns. Source: shutterstock.com, image ID: 4847238.

object is treated as a length-256 sparse or compressible vector $\boldsymbol{\theta}$, with sparsity k less than 30. The object is placed at the back focal plane of lens L_2.

The compressive sensing mask is represented by a 96×256 Bernoulli matrix. Thus for each row scan of the feather object, the number of temporal measurements required for object inversion is only $\frac{3}{8}$ of the object size.

Fig. 5.3 shows the reconstruction results for CS and SPIFI masks, with the 2-D object placed at in-focus postion. The compressive sensing approach provides a faithful reconstruction of the object. The SPIFI approach also precisely recover the object, apart from little background-noise like error. This may be resulted in the mask quantization error.

5.3 Misfocus Imaging

Now suppose the object is misplaced with distance z_3 away from the back focal plane of L_2 along the optical axis. The *misfocus* psf of Abbe system under such condition is [101]:

$$h(x, z_3) = \int_{-\infty}^{\infty} P(x_2) e^{i\frac{k}{2f_1^2}M^2 z_3 x_2^2} e^{-i\frac{k}{f_1}x_2 x} dx_2, \tag{5.19}$$

and the excitation field onto object is

$$u_{exc}(x_3; m) = u_0 \int_{-\infty}^{\infty} u_{mask}(x_1; m) h(x_1 + Mx_3, z_3) dx_1. \tag{5.20}$$

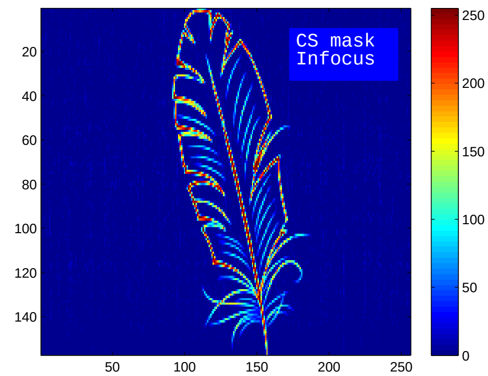

Figure 5.3: In-focus object reconstruction of compressive imaging approach.

Note that unlike the in-focus case, in eq (5.19) the psf is the Fourier transform of the pupil function modulated by a spatial chirp pattern, whose chirp rate is proportional to $M^2 z_3$. Thus the higher demagnification factor M and misfocus distance z_3, the wider the psf becomes and the mask becomes more distorted. Intuitively a wide psf implies a low imaging resolution. It will be shown that under the misfocus condition, the temporal measurements of the detector are

$$\mathbf{y} = (\mathbf{A} + \mathbf{E})\widetilde{\boldsymbol{\theta}}, \tag{5.21}$$

where the matrix $\mathbf{E}$ is an *unknown* perturbation matrix depending on the parameters M and z_3. We will elaborate on the breakdown of matrix $\mathbf{E}$ shortly after this.

The excitation field in eq (5.20) can be also approximated as

$$u_{exc}(x_3; m) = \{u_{mask}(-Mx; m) *_x \widetilde{h}(x, z_3)\}(x_3), \tag{5.22}$$

where $*_x$ denotes the convolution for variable x, and assuming that $\widetilde{h}(x, z_3)$ can be adequately approximated by a Gaussian beam to allow for an analytic result in what follows [102]:

$$h_g(x, z_3) = \frac{h_0 e^{ikz_3}}{1 + 2i\frac{z_3}{kw_0^2}} \exp\left(-\frac{x^2}{w_0^2(1 + 2i\frac{z_3}{kw_0^2})}\right), \tag{5.23}$$

Define the parameter $z_R = \frac{kw_0^2}{2}$. Then the Gaussian beam can be rewritten as

$$\begin{aligned} h_g(x, z_3) &= h_0 \frac{w_0}{w(z_3)} e^{-(\frac{x_0}{w(z_3)})^2} e^{i[kz_3 - \eta(z_3) + \frac{kx_0^2}{2R(z_3)}]} \\ &\triangleq h_g(z_3) \widetilde{h}_g(x, z_3), \end{aligned} \tag{5.24}$$

where the function

$$h_g(z_3) = h_0 \frac{w_0}{w(z_3)} e^{i[kz_3 - \eta(z_3)]} \tag{5.25}$$

is independent of x, and the function $\widetilde{h}_g(x, z_3)$ is

$$\widetilde{h}_g(x, z_3) = e^{-(\frac{x_0}{w(z_3)})^2} e^{i \frac{kx_0^2}{2R(z_3)}}. \tag{5.26}$$

The misfocus beam size $w(z)$ is given by the classic quadratic propagation law:

$$w(z) = w_0 \sqrt{1 + (\frac{z}{z_R})^2}. \tag{5.27}$$

where w_0 is the spot size of a focused Gaussian beam. With a pupil radius W, the width of a focused Guassian beam w_0 is

$$w_0 = \frac{\lambda f_1}{\pi M W}. \tag{5.28}$$

The curvature radius $R(z)$ is defined by $R(z) = z[1 + (\frac{z_R}{z})^2]$, and the Gouy phase is $\eta(z) = \tan^{-1}(\frac{z}{z_R})$. By substituting (5.24) into (5.22), we can write the excitation field $u_{exc}(x_3; m)$ as

$$\begin{aligned} u_{exc}(x_3; m) &= \int_{-\infty}^{\infty} u_{mask}(-Mx; m) h_g(x_3 - x, z_3) dx \\ &= h_g(z_3) \int_{-\infty}^{\infty} u_{mask}(x; m) \widetilde{h}_g(x_3 + \frac{x}{M}, z_3) \frac{1}{M} dx. \end{aligned} \tag{5.29}$$

By checking eq. (5.20), if we ignore the term $h_g(z_3)$ which is independent of x, we can relate the function $\widetilde{h}_g(x, z_3)$ with the misfocus psf $h(x, z_3)$ of the Abbe system as

$$h(x, z_3) = \frac{1}{M} \widetilde{h}_g(\frac{x}{M}, z_3) \tag{5.30}$$

The misfocus temporal measurements are

$$y_m = \sum_{\ell=0}^{N-1} a_{m,\ell} \widetilde{\theta}_\ell + p_m, m = 0, 1, ..., M-1.$$

where $\widetilde{\theta}_\ell = \theta_\ell \int_{d_\ell}^{d_{\ell+1}} |\mathcal{G}_\ell(x_3)|^2 dx_3$, and the perturbation terms p_m are

$$\begin{aligned} p_m = &\sum_{\ell=0}^{N-1} \theta_\ell \int_{d_{\ell+1}}^{d_\ell} |\sum_{\ell' \neq \ell} a_{m,\ell'} \mathcal{G}_{\ell'}(x_3)|^2 dx_3 \\ &+ \sum_{\ell=0}^{N-1} \theta_\ell \int_{d_{\ell+1}}^{d_\ell} \sum_{\ell' \neq \ell} 2\mathrm{Re}\big\{a_{m,\ell} a_{m,\ell'} \mathcal{G}_\ell(x_3) \mathcal{G}_{\ell'}(x_3)\big\} dx_3. \end{aligned}$$

To simplify the future analysis, we set the $g(x) \equiv 1$, meaning an uniform illumination on the mask plane. In this case, the function $\mathcal{G}_\ell(x_3)$ becomes

$$\begin{aligned} \mathcal{G}_\ell(x_3) &= \int_{(\ell-N/2)\Delta}^{(\ell-N/2+1)\Delta} h(x_1 + Mx_3) dx_1 \\ &= \frac{1}{M} \int_{(\ell-N/2)\Delta}^{(\ell-N/2+1)\Delta} \exp\left(-(\frac{\frac{x_1}{M} + x_3}{w(z_3)})^2\right) \exp\left(ik \frac{(\frac{x_1}{M} + x_3)^2}{2R(z_3)}\right) dx_1 \\ &= \int_{(\ell-N/2)\Delta/M}^{(\ell-N/2+1)\Delta/M} \exp\big(-(\frac{x + x_3}{w(z_3)})^2\big) \exp\big(ik \frac{(x + x_3)^2}{2R(z_3)}\big) dx \\ &= \int_{(\ell-N/2)\Delta/M + x_3}^{(\ell-N/2+1)\Delta/M + x_3} e^{-(\frac{x}{w(z_3)})^2} e^{ik \frac{x^2}{2R(z_3)}} dx \\ &\triangleq \mathcal{G}\big(x_3 + (\ell - N/2)\Delta/M, z_3\big), \end{aligned} \tag{5.31}$$

where the function $\mathcal{G}(x_3, z_3)$ is defined as

$$\mathcal{G}(x_3, z_3) = \int_{x_3}^{x_3 + \Delta/M} e^{-(\frac{x}{w(z_3)})^2} e^{ik \frac{x^2}{2R(z_3)}} dx, \tag{5.32}$$

which basically becomes wider as the misfocus distance z_3 grows. Define

$$I(z_3) = \int_{-\Delta/M}^{0} \mathcal{G}(x_3, z_3) dx_3. \tag{5.33}$$

It is clear that $\int_{d_{\ell+1}}^{d_\ell} \mathcal{G}_\ell(x_3) dx_3 = I(z_3)$ for all ℓ. Letting $p = \ell' - \ell$, and we can write each perturbation term p_m as

$$\begin{aligned} p_m = &\sum_{\ell=0}^{N-1} \theta_\ell \int_{-\Delta/M}^{0} |\sum_{p \neq 0} a_{m,\ell+p} \mathcal{G}(x_3 + p\Delta/M, z_3)|^2 dx_3 \\ &+ \sum_{\ell=0}^{N-1} \theta_\ell \int_{-\Delta/M}^{0} \sum_{p \neq 0} 2\mathrm{Re}\big\{a_{m,\ell} a_{m,\ell+p} \mathcal{G}(x_3, z_3) \mathcal{G}(x_3 + p\Delta/M, z_3)\big\} dx_3. \end{aligned} \tag{5.34}$$

Therefore we can write each temporal measurement y_m as

$$y_m = \sum_{\ell=0}^{N-1} (a_{m,\ell} + e_{m,\ell}(z_3)) \widetilde{\theta}_\ell, \tag{5.35}$$

where each perturbation coefficient $e_{m,\ell}(z_3)$ can be expressed as a function of misfocus distance z_3:

$$e_{m,\ell}(z_3) = \frac{1}{I(z_3)}\Big\{\int_{-\Delta/M}^{0} |\sum_{p\neq 0} a_{m,\ell+p}\mathcal{G}(x_3 + p\Delta/M, z_3)|^2 dx_3 \\ + \int_{-\Delta/M}^{0} \sum_{p\neq 0} 2\mathrm{Re}\big\{a_{m,\ell}a_{m,\ell+p}\mathcal{G}(x_3, z_3)\mathcal{G}(x_3 + p\Delta/M, z_3)\big\}dx_3\Big\}. \tag{5.36}$$

The matrix form of eq. (5.37) is

$$\mathbf{y} = (\mathbf{A} + \mathbf{E}(z_3))\widetilde{\boldsymbol{\theta}}, \tag{5.37}$$

where the perturbation matrix $\mathbf{E}(z_3) = [e_{m,\ell}(z_3)]$.

The amplitude of elements from matrix $\mathbf{E}(z_3)$ characterizes the extent of modal perturbation due to misfocus. Eq. (5.36) shows that $|e_{m,\ell}|$ equals the interference from the mask elements other than $a_{m,\ell}$ to the ℓ-th bin of object, divided by the illumination intensity $I(z_3)$. Therefore the perturbation matrix $\mathbf{E}(z_3)$ is determined by both the misfocus distance z_3 and the demagnification factor M.

5.4 Numerical Results for Misfocus Imaging

In this section we test the reconstruction performances versus misfocus distant z_3 as well as demagnification factor M, for all mask designs. In simulation we fix the focal length f_1, and vary f_2 according to different M. We use the depth of field to be a unit of misfocus distance. Given a demagnification factor M, the system's depth of field is [103]

$$\mathrm{DOF} = \frac{\lambda_0 n}{\mathrm{NA}^2} + \frac{n}{M - \mathrm{NA}}e, \tag{5.38}$$

where n is the refractive index of medium (we let it be 1.5). The numerical aperture is $\mathrm{NA} = n\sin\theta = nW/\sqrt{W^2 + f_2^2}$. The variable e is the smallest distance (between a value of 4 and 24 microns) that can be resolved by a detector that is placed in the image plane of the microscope objective. We choose it to be 10μm.

In Fig. 5.4, the magnification factor is set to $M = 100$. From (a) to (d), we plot the feather reconstruction of compressive imaging method, at misfocus distance $z_3 = \mathrm{DOF}$,

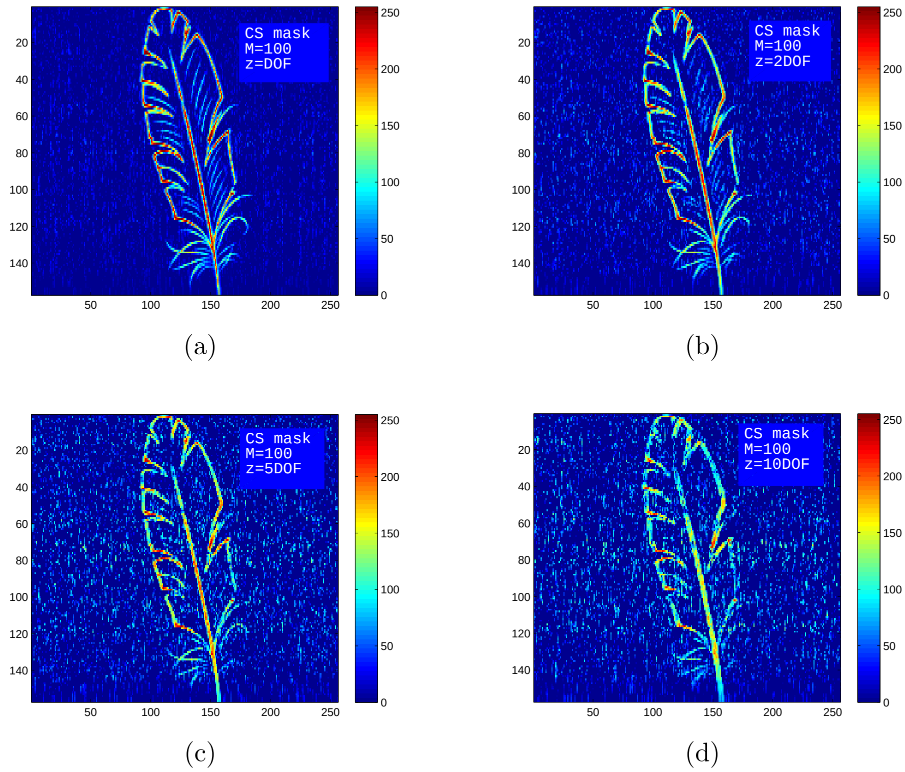

Figure 5.4: Reconstruction of misfocus object of compressive imaging method. Magnification factor is $M = 100$. From (a) to (d) the misfocus distance z_3 is $z_3 = \text{DOF}$, $z_3 = 2\text{DOF}$, $z_3 = 5\text{DOF}$, and $z_3 = 10\text{DOF}$ respectively, where DOF denotes the depth of field of the imaging system. Colorbar is in linear scale.

$z_3 = 2\text{DOF}$, $z_3 = 5\text{DOF}$, and $z_3 = 10\text{DOF}$ respectively. For ease of observation, each reconstruction has been scaled such that the largest amplitude of its elements is 255. At $z_3 = \text{DOF}$, the reconstruction is robust to misfocus effect. As z_3 goes above the DOF and increases, the object contour is becoming blurred, meaning a degradation of imaging resolution. At $z_3 \geq 5\text{DOF}$, significant background-noise like error appear in reconstructed object, in which the feather texture is completely lost.

Fig. 5.5 illustrate the sensitivity of compressive imaging to misfocus effect at a high magnification factor $M = 1000$. From (a) to (d), we plot the feather reconstruction of compressive imaging method, at misfocus distance $z_3 = 0.1\text{DOF}$, $z_3 = 0.5\text{DOF}$, $z_3 = \text{DOF}$, and $z_3 = 2\text{DOF}$ respectively. It can be seen that even at $z_3 \leq \text{DOF}$, the object reconstruction does not possess robustness to misfocus effect. At $z_3 = 2\text{DOF}$, compressive imaging fails to invert the object information from the misfocus measurements.

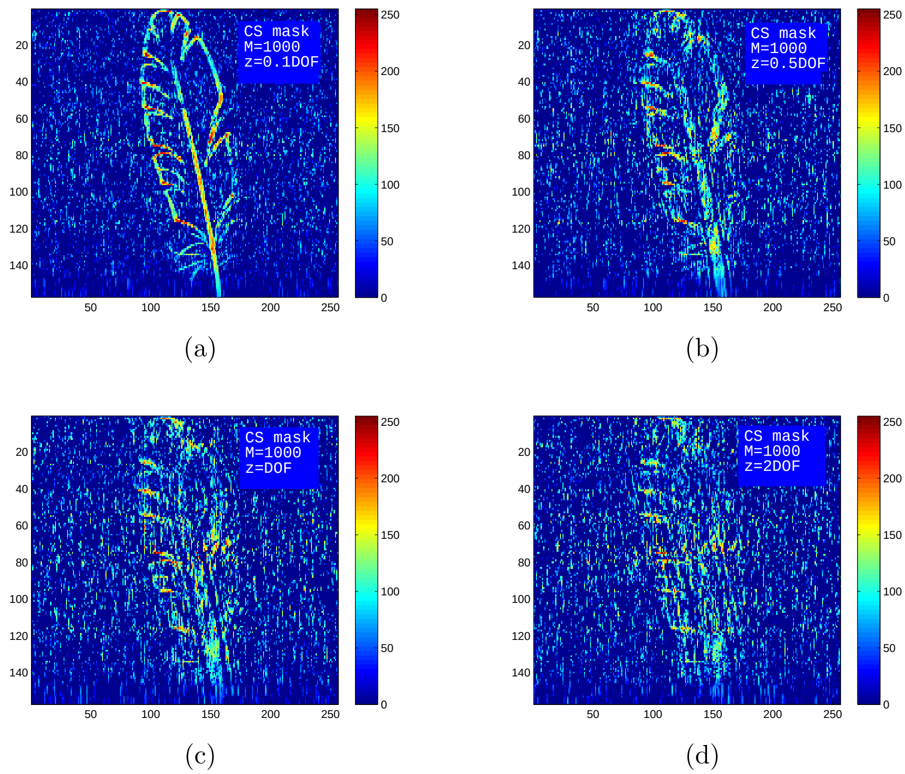

Figure 5.5: Reconstruction of misfocus object of compressive imaging method. Magnification factor is $M = 1000$. From (a) to (d) the misfocus distance z_3 is $z_3 = 0.1\text{DOF}$, $z_3 = 0.5\text{DOF}$, $z_3 = \text{DOF}$, and $z_3 = 2\text{DOF}$ respectively, where DOF denotes the depth of field of the imaging system. Colorbar is in linear scale.

Fig. 5.6 plots the numerical normalized reconstruction error $\|\boldsymbol{\theta} - \boldsymbol{\theta}^*(z_3)\|_2/\|\boldsymbol{\theta}\|_2$ of the CS approach. At $M = 100$ and $M = 1000$, the normalized reconstruction error both linearly increases with respect to z_3. In the presence of large misfocus, the model perturbation is such significant that the reconstruction error $\|\boldsymbol{\theta} - \boldsymbol{\theta}^*(z_3)\|_2$ can be much bigger than the power of object $\|\boldsymbol{\theta}\|_2$.

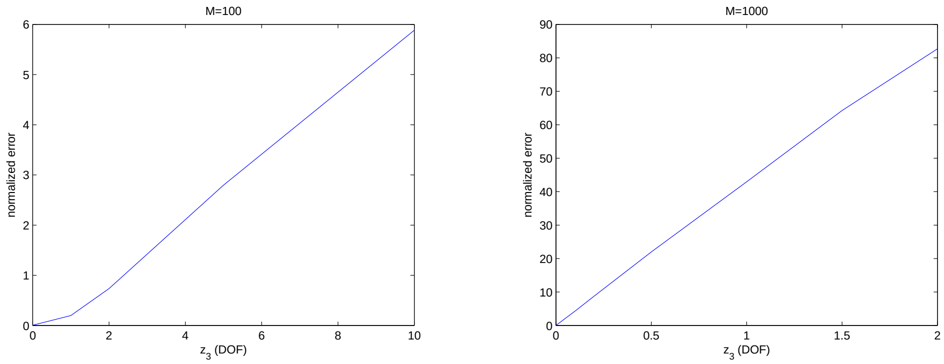

(a) (b)

Figure 5.6: Numerical normalized reconstruction error $\|\boldsymbol{\theta} - \boldsymbol{\theta}^*(z_3)\|_2/\|\boldsymbol{\theta}\|_2$ of compressive sensing versus misfocus distance, (a) M=100, (b) M=1000.

5.5 Misfocus Performance Analysis

Despite of the actual physical model as shown in eq (5.21), for the object inversion, people usually resort to the mathematical model

$$\mathbf{y} = \mathbf{A}\widetilde{\boldsymbol{\theta}} + \mathbf{n}, \tag{5.39}$$

where $\mathbf{n}$ accounts for certain unknown measurement perturbations. Suppose we use Basis Pursuit to reconstruct the vector $\widetilde{\boldsymbol{\theta}}$, with solution $\widetilde{\boldsymbol{\theta}}^*(z_3)$. Then the estimate of object $\boldsymbol{\theta}$ is $\boldsymbol{\theta}^*(z_3) = \frac{1}{I(z_3)}\widetilde{\boldsymbol{\theta}}^*(z_3)$. If we were told by the prophecy that $\|\mathbf{E}(z_3)\widetilde{\boldsymbol{\theta}}\| \leq \epsilon(z_3)$, then the object reconstruction error follows

$$\|\boldsymbol{\theta} - \boldsymbol{\theta}^*(z_3)\|_2 \leq C_0 k^{-\frac{1}{2}}\|\boldsymbol{\theta} - \boldsymbol{\theta}_k\|_1 + C_1\frac{\epsilon(z_3)}{I(z_3)}. \tag{5.40}$$

In this section we derive a upper bound of noise energy $\epsilon(z)$ at the misfocus position z. Then from eq. (5.40) we present a theoretical bound of reconstruction error.

Lemma 5.5.1. *Let $1 \leq p, q \leq \infty$ and $1/p + 1/q = 1$. If the rows $\mathbf{e}_m^T(z_3) \in \mathbb{R}^{1\times N}$ of $\mathbf{E}(z_3)$ are bounded as $\|\mathbf{e}_m(z_3)\|_p \leq \alpha(z_3)$, $\forall m$, then*

$$\|\mathbf{n}(z_3)\|_2 = \|\mathbf{E}(z_3)\widetilde{\boldsymbol{\theta}}\|_2 \leq M^{1/2} I(z_3)\alpha(z_3)\|\boldsymbol{\theta}\|_q. \tag{5.41}$$

If $\boldsymbol{\theta}$ is k-sparse with support $\mathcal{S} \subseteq \{1, 2, \ldots, N\}$, then

$$\|\mathbf{n}(z_3)\|_2 \leq M^{1/2} I(z_3) \alpha_{\mathcal{S}}(z_3) \|\boldsymbol{\theta}\|_q, \tag{5.42}$$

where $\alpha_{\mathcal{S}}(z_3)$ is an upper bound of $\|\mathbf{e}_{\mathcal{S},m}(z_3)\|_p\ \forall m$, and $\mathbf{e}_{\mathcal{S},m}(z_3)$ is the m-th row of the partition of $\mathbf{E}(z_3)$ with column support $\mathcal{S}$. *Proof:* $\mathbf{n}(z_3)$ can be written by

$$\mathbf{n}(z) = \begin{bmatrix} n_1(z_3) \\ n_2(z_3) \\ \vdots \\ n_M(z_3) \end{bmatrix} = \begin{bmatrix} \mathbf{e}_1^T(z_3)\boldsymbol{\theta} \\ \mathbf{e}_2^T(z_3)\boldsymbol{\theta} \\ \vdots \\ \mathbf{e}_M^T(z_3)\boldsymbol{\theta} \end{bmatrix}. \tag{5.43}$$

By Hölder's inequality, for each m we have

$$|n_m(z_3)| = |\mathbf{e}_m^T(z_3)\widetilde{\boldsymbol{\theta}}| \leq I(z_3)\|\mathbf{e}_m(z_3)\|_p \|\boldsymbol{\theta}\|_q \leq I(z_3)\alpha(z_3)\|\boldsymbol{\theta}\|_q. \tag{5.44}$$

This yields $\|\mathbf{n}(z_3)\|_2 \leq M^{1/2} I(z_3)\alpha(z_3)\|\boldsymbol{\theta}\|_q$. The second inequality can be similarly proved.

The following theorem derives an analytical upper bound of $\|\mathbf{e}_m(z_3)\|_p$:

Theorem 5.5.2. *The max norm $\|\mathbf{E}(z_3)\|_{max} = \max_{m,\ell} |e_{m,\ell}(z_3)|$ of $\mathbf{E}(z_3)$ can be upper bounded by $\beta(z_3)$, where*

$$\begin{aligned} \beta(z) =& \frac{4}{I(z_3)}(\Delta/M)^2 w(z)\Bigg[\sqrt{2}\bigg(1 + \frac{\sqrt{\pi}}{2} r(z)\, erf\big((N-1)r(z)\big)\bigg) erf\big(r(z)\big) e^{r^2(z)} \\ &+ \bigg(1 + \frac{\sqrt{\pi}}{2} r(z)\, erf\big((N-1)r(z)\big)\bigg)^2 erf\big(\sqrt{2} r(z)\big) e^{2r^2(z)}\Bigg], \end{aligned} \tag{5.45}$$

and the factor $r(z)$ is defined as $r(z) = \frac{\Delta}{\sqrt{2}Mw(z)}$. Therefore the p-norm of each row vector $e_m^T(z_3)$ is bounded by $\|\mathbf{e}_m(z_3)\|_p \leq N^{1/p}\beta(z_3)$

Proof: see appendix J.

Corollary 5.5.3. *The reconstruction error $\|\boldsymbol{\theta} - \boldsymbol{\theta}^*(z_3)\|_2$ of Basis Pursuit satisfies*

$$\|\boldsymbol{\theta} - \boldsymbol{\theta}^*(z_3)\|_2 \leq C_0 k^{-\frac{1}{2}} \|\boldsymbol{\theta} - \boldsymbol{\theta}_k\|_1 + C_1 M^{1/2} N^{1/p} \beta(z_3) \|\boldsymbol{\theta}\|_q, \tag{5.46}$$

where $\beta(z_3)$ is given in eq. (5.45). If $\boldsymbol{\theta}$ is k-sparse, we have

$$\|\boldsymbol{\theta} - \boldsymbol{\theta}^*(z_3)\|_2 \leq C_1 M^{1/2} k^{1/p} \beta(z_3) \|\boldsymbol{\theta}\|_q, \tag{5.47}$$

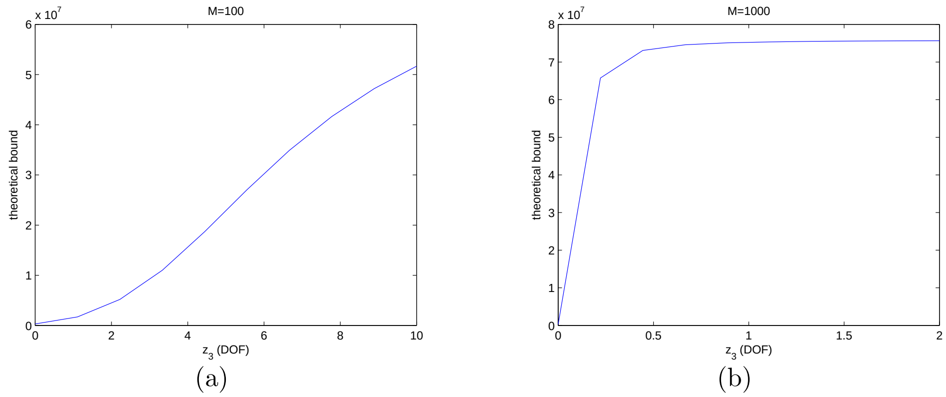

Figure 5.7: Theoretical bound of normalized reconstruction error $\|\boldsymbol{\theta} - \boldsymbol{\theta}^*(z_3)\|_2 / \|\boldsymbol{\theta}\|_2$. (a) M =100, (b) M =1000.

Proof: the corollary can be simply proved by combining lemma 1, theorem 2, and the basis pursuit result in eq. (5.40).

With a k-sparse object $\boldsymbol{\theta}$, by letting $p = q = 2$, the normalized reconstruction error can be bounded by

$$\frac{\|\boldsymbol{\theta} - \boldsymbol{\theta}^*(z_3)\|_2}{\|\boldsymbol{\theta}\|_2} \leq C_1 \sqrt{Mk} \beta(z_3). \tag{5.48}$$

Eq. (5.48) means that, the upper bound of the normalized reconstruction increases with increased number of measurement M and sparsity k, and linearly increases with increased $\beta(z_3)$, which is an upper bound of $\|\mathbf{E}(z_3)\|_{max}$.

Fig. 5.7 shows the theoretical bound of the normalized reconstruction error as indicated by eq. (5.48). We set $N = 256$ and $k = 30$. It can be observed that the the value of theoretical bounds will be much higher than that of the numerical results, because to derive the upper bound in theorem 2 we have ignored the phasing of excitation field, and using Cauchy-Schwartz inequality may introduce large gaps. However, at $M = 100$, the linear increment of the theoretical bound with respect to z_3 well matches the trend of numerical result. At $M = 1000$, the upper bound converges as z_3 increases. Intuitively, this is since that with large M the parameters $w(z_3)$ and $R(z_3)$ are sufficiently large, such that the function $\mathcal{G}(x_3, z_3)$ in eq. (5.32) is close to a constant function.

5.6 Other Discussions

5.6.1 Grid Search along Optical Axis

The intensity measurement vector is assumed to be

$$\begin{aligned}\mathbf{y} &= I(z)[\mathbf{A} + \mathbf{E}(z)]\boldsymbol{\theta} \\ &= \begin{bmatrix}\mathbf{A}(z_0) & \mathbf{A}(z_1) & \dots & \mathbf{A}(z_{G-1})\end{bmatrix} \cdot \begin{bmatrix}\boldsymbol{\theta}_0 \\ \boldsymbol{\theta}_1 \\ \vdots \\ \boldsymbol{\theta}_{G-1}\end{bmatrix},\end{aligned} \tag{5.49}$$

which is a block-sparse signal with sparsity one:

$$\|[\boldsymbol{\theta}_0^T, \boldsymbol{\theta}_1^T, \dots, \boldsymbol{\theta}_{G-1}^T]^T\|_{2,0} = \sum_{g=0}^{G-1} \mathcal{I}(\|\boldsymbol{\theta}_g\|_2 > 0) = 1. \tag{5.50}$$

where each block model matrix $\mathbf{A}(z_g)$ is

$$\mathbf{A}(z_g) = I(z_g) \cdot [\mathbf{A} + \mathbf{E}(z_g)], \tag{5.51}$$

and $\mathcal{I}(\cdot)$ is the indicator function.

The following simulation studies the effect of grid mismatch in recovery of sparse object $\boldsymbol{\theta}$, from the block-sparse measurement written as eq. (5.50). Assume a misfocus object near the grid point z_0 on optical axis. The misfocus mismatch Δz is the distance between the actual object misfocus position and z_0. Fig. 5.8(a)-(b) show the recovered feather object using Basis Pursuit algorithm, with misfocus mismatch $\Delta z = 0.05$DOF and $\Delta z = 0.1$DOF at $M = 100$. It can be seen that at low-mid magnification factor, compressive imaging of misfocus object is robust to grid mismatch. Fig. 5.9(a)-(b) illustrate the recovered feather object with misfocus mismatch $\Delta z = 0.05$DOF and $\Delta z = 0.1$DOF at $M = 1000$. With a misfocus $\Delta z = 0.1$DOF, the object recovery is significantly degraded. The misfocus mismatch can be annihilated by using a fine grid along optical axis, which comes with the expense of model coherence loss [104, 105].

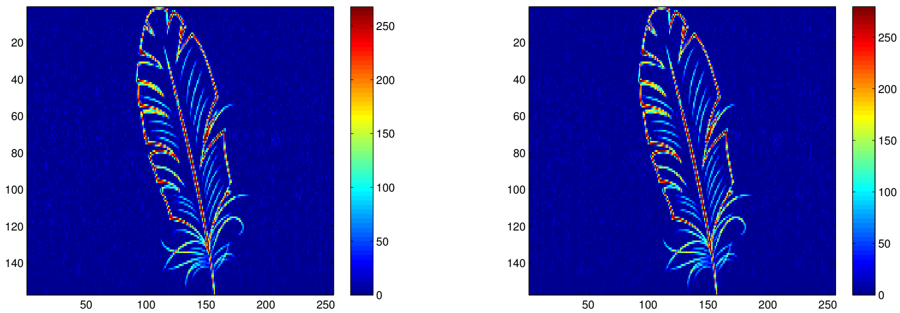

(a) (b)

Figure 5.8: Effect of grid mismatch in Basis-Pursuit recovery of a misfocus object. Magnification factor $M = 1000$. Grid point on optical axsis is $z_0 = 0.5$DOF. (a) Misfocus mismatch is 0.05DOF, and (b) Δz is 0.1DOF.

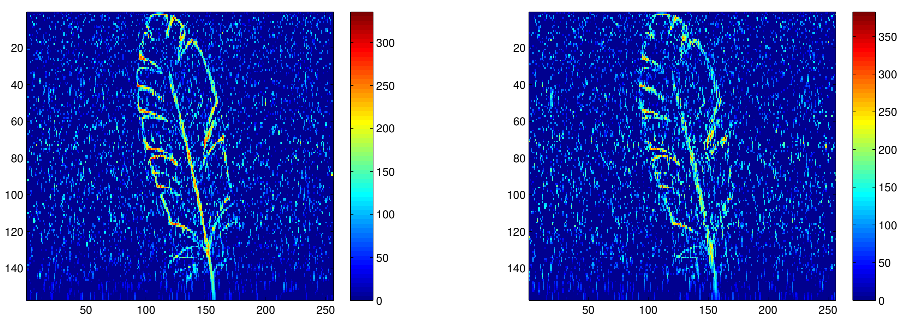

(a) (b)

Figure 5.9: Effect of grid mismatch in Basis Pursuit recovery of a misfocus object. Magnification factor $M = 100$. Grid point on optical axsis is $z_0 = 0.5$DOF. (a) Misfocus mismatch Δz is 0.05DOF, and (b) Δz is 0.1DOF.

5.6.2 Application of Weighted and Structured Sparse Total Least-square Approach

The weighted and structured sparse total least-square (WSSTLS) approach proposed by [100] is to address the model mismatch in compressive sensing problems. The key assumption in [100] is to exploit the parameterization of model perturbation matrix.

Suppose with a set of grid points $z_0, z_1, \ldots, z_{G-1}$, for a misfocus distance $z \in [z_g, z_{g+1}]$, we can approximate the model matrix $\mathbf{A}(z)$ as

$$\mathbf{A}(z) \approx \mathbf{A}(z_g) + \Delta z_g \Delta\mathbf{A}(z_g), \tag{5.52}$$

where $\Delta z_g = z - z_g$, and $\Delta\mathbf{A}(z)$

$$\Delta\mathbf{A}(z) = \Delta I(z)\mathbf{A} + \Delta I(z)\mathbf{E}(z) + I(z)\Delta\mathbf{E}(z) \tag{5.53}$$

is the first order derivative of $\mathbf{A}(z)$ with respect to z. With above approximation, the measurement $\mathbf{y}$ approximately equals

$$\begin{aligned} \mathbf{y} &= \mathbf{A}(z)\boldsymbol{\theta} \\ &\approx \left[\sum_{g=0}^{G-1} e_g \mathbf{A}(z_g) + \sum_{g=0}^{G-1} e_g \Delta z_g \Delta\mathbf{A}(z_g)\right]\boldsymbol{\theta}. \end{aligned} \tag{5.54}$$

where each coefficient $e_g = 1$ if the z_g is grid point closest to true misfocus distance, and $e_g = 0$ otherwise, and Δz_g is the misfocus offset presuming $e_g = 1$. Eq. (5.54) describes the parameterization of model matrix $\mathbf{A}(z)$.

Suppose it is known that the actual misfocus distance z is inside $[z_g, z_{g+1}]$. The above parameterized measurement model is

$$\mathbf{y} = [\mathbf{A}(z_g) + \Delta z_g \Delta\mathbf{A}(z_g)]\,\boldsymbol{\theta}. \tag{5.55}$$

It remains to solve the misfocus mismatch Δz_g and sparse object $\boldsymbol{\theta}$ from $\mathbf{y}$. The WSSTLS approach seeks Δz_g and $\boldsymbol{\theta}$ by solving the following optimization:

$$\begin{aligned} &\min_{\boldsymbol{\theta},\Delta z_g,\boldsymbol{\epsilon}_y} \begin{bmatrix}\Delta z_g & \boldsymbol{\epsilon}_y^T\end{bmatrix} \begin{bmatrix} w_{AA} & \mathbf{0}^T \\ \mathbf{0} & \mathbf{W}_{yy}\end{bmatrix} \begin{bmatrix}\Delta z_g \\ \boldsymbol{\epsilon}_y\end{bmatrix} + \lambda\|\boldsymbol{\theta}\|_1 \\ &\text{s.t. } \Delta z_g \Delta\mathbf{A}(z_g) - \boldsymbol{\epsilon}_y = \mathbf{y} - \mathbf{A}(z_g)\boldsymbol{\theta}. \end{aligned} \tag{5.56}$$

The vector $\boldsymbol{\epsilon}_y$ captures additional measurement noise.

As shown in the end of this chapter, Fig. 5.10 compares the performance of misfocus object recovery with a grid mismatch, based on WSSTLS and Basis Pursuit (BP) methods. Magnification factor is $M = 1000$. Grid point on optical axis is $z_0 = 0.5$DOF. Along (a), (c) and (e) we plot WSSTLS recovery with misfocus mismatch $\Delta z = 0.002$DOF, $\Delta z = 0.01$DOF, and $\Delta z = 0.05$DOF respectively. Along (b), (d), and (f) we plot BP recovery with misfocus mismatch $\Delta z = 0.002$DOF, $\Delta z = 0.01$DOF, and $\Delta z = 0.05$DOF respectively. It can be seen that only with minimal misfocus mismatch, WSSTLS outperforms BP in reducing background noise in recovered image.

5.7 Conclusion

In this chapter, we investigated compressive sensing as a principle for line-scanning imaging with a single pixel detector. We first show that for a in-focus sparse object, the compressive sensing can precisely reconstruct the object with a fewer number of measurements. This opens the possibility of increased imaging speed than other imaging methods based on spatially structured illumination. We then considered the sensitivity of compressive imaging to misfocus effect. Numerical results show that the compressive imaging is robust to misfocus at low and medium demagnification factor. At high demagnification factor, which is typical in microscopy, however, compressive imaging fail to invert the object information from the misfocus measurements. We also mathematically formulated the model perturbation as a function of both demagnification factor and misfocus distance. The theoretical performances bounds explains how the reconstruction error increases with both increased demagnification and misfocus distance.

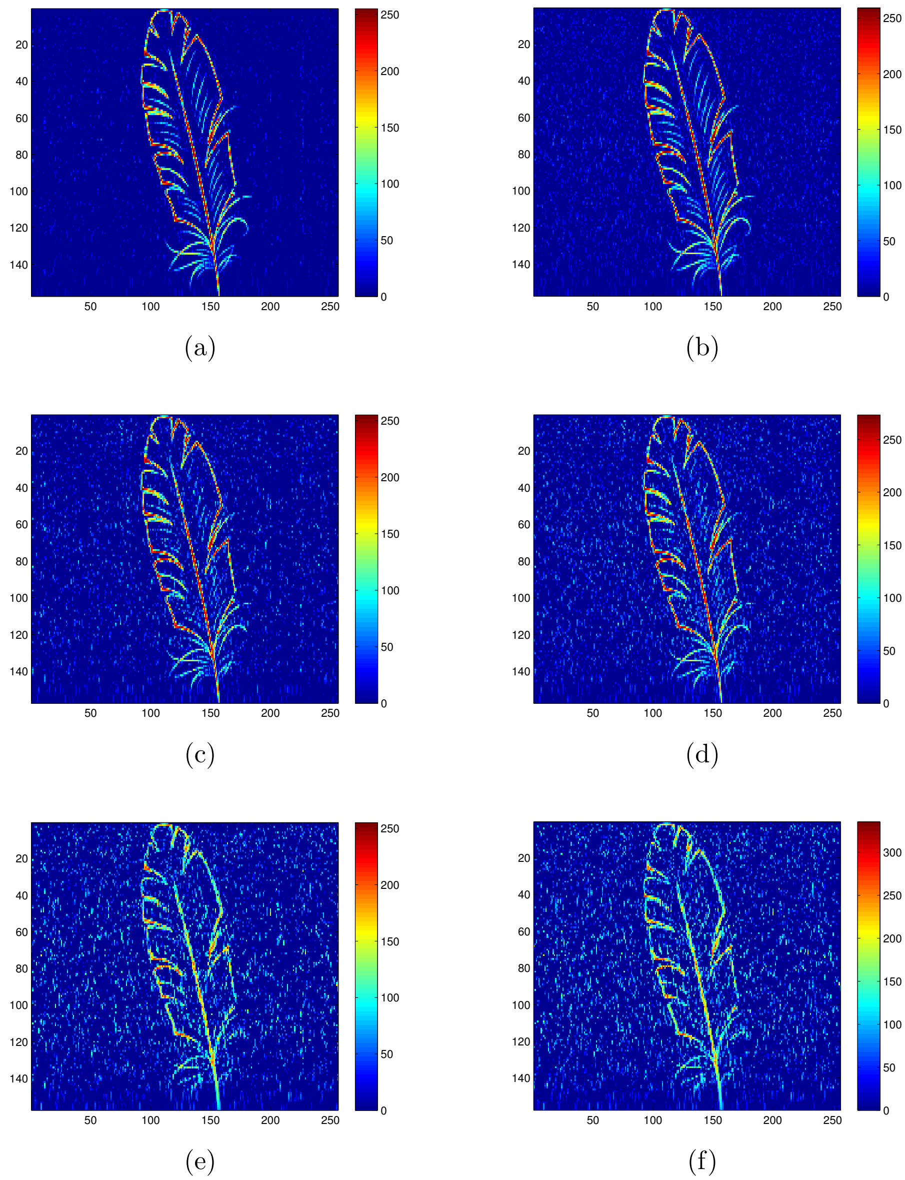

Figure 5.10: Comparison of misfocus object recovery with a grid mismatch, based on Weighted and Structured Sparse Total Least-squares (WSSTLS) and Basis Pursuit (BP) methods. Magnification factor is $M = 1000$. Grid point on optical axis is $z_0 = 0.5$DOF. Along (a), (c) and (e) we plot WSSTLS recovery with misfocus mismatch $\Delta z = 0.002$DOF, $\Delta z = 0.01$DOF, and $\Delta z = 0.05$DOF respectively. Along (b), (d), and (f) we plot BP recovery with misfocus mismatch $\Delta z = 0.002$DOF, $\Delta z = 0.01$DOF, and $\Delta z = 0.05$DOF respectively.

CHAPTER 6

WIDELY LINEAR COMPLEX KALMAN FILTERS

Complex signals are ubiquitous in science and engineering, arising as they do as complex representations of two real channels or of two-dimensional fields. Consider a zero mean complex random vector $\mathbf{x}$. The usual covariance matrix defined as $E\mathbf{x}\mathbf{x}^H$ describes its Hermitian second order covariance. But when $\mathbf{x}$ and its complex conjugate $\mathbf{x}^*$ are correlated, the complementary covariance matrix $E\mathbf{x}\mathbf{x}^T$ does not vanish, so it carries useful second order information about the complex random vector $\mathbf{x}$. We call a complex random vector proper as long as its complementary covariance matrix vanishes and improper otherwise. Proper complex vectors have a statistical description similar to real vectors, but improper random vectors do not. A comprehensive second order analysis of improper random vectors and processes is considered in [39–43].

For any improper random vector $\mathbf{x}$, for which $\mathbf{x}$ is correlated with its complex conjugate $\mathbf{x}^*$, intuition suggests that a good estimator of $\mathbf{x}$ should depend on $\mathbf{x}^*$. This requires a methodology of *widely linear processing* instead of strictly linear processing [39]. For random complex signals, the merit of widely linear processing has been exploited in various papers on estimation [41, 43], filtering [40, 41, 106], detection [107, 108], and equalization [109]. It turns out that widely linear processing brings improvement in performance over strictly linear processing [41, 110] when there is complementary covariance to be exploited.

In the past few decades the reasoning of the Kalman filter [44] has been modified to apply to nonlinear problems, producing Extended Kalman filters [45] and Unscented Kalman filters [46]. The motivation of this chapter is to make use of widely linear processing to develop novel complex Kalman filters and their nonlinear versions for improper complex states. We show that for improper complex states, complementary covariance matrices may be used to create widely linear complex KFs (denoted WLCKFs) and Unscented WLCKFs. The key contributions of this chapter are as follows:

- From a *linear* real dual channel dynamical model we derive an equivalent *widely linear* complex single channel dynamical model, where the updates of random states and measurements depend on both states and noises and their conjugates. For the complex model we derive a WLCKF which is equivalent to the conventional KF for the dual channel model. The WLCKFs proposed in [106] consider special dual channel problems and their corresponding complex dynamical models. In these complex models the updates of complex random states and measurements do not depend on the conjugates of states and noises.

- We compare the performance between the WLCKFs and conventional KFs. Our analytical and numerical results show that for some special distributions of states and noises, the mean squared error (MSE) of the WLCKF is significantly smaller than the MSE of a CKF that does not exploit non-zero complementary covariance.

- For dynamical models with complex nonlinear state and measurement equations, we develop an Unscented WLCKF for which a systematic paradigm to construct *modified* complex sigma points is studied. The property of modified sigma points is that they preserve the complete first and second order statistical information of complex random vectors. The UWLCKF of [106] uses sigma points that only preserve the mean and Hermitian covariance, but not the complementary covariance of states.

6.1 Brief Review of Complex Random Vectors

6.1.1 Cartesian and Complex Augmented Representations

Let Ω be the sample space of a random experiment that generates two channels of real signals $\mathbf{u}, \mathbf{v} \in \mathbb{R}^n$ defined on Ω. From this we construct the *real composite* random vector $\mathbf{z} \in \mathbb{R}^{2n}$ as $\mathbf{z}^T = [\mathbf{u}^T, \mathbf{v}^T]$, and the *complex* random vector $\mathbf{x} \in \mathbb{C}^n$, obtained by composing $\mathbf{u}$

and $\mathbf{v}$ into its real and imaginary parts:

$$\mathbf{x} = \mathbf{u} + j\mathbf{v}. \tag{6.1}$$

The *complex augmented* random vector $\underline{\mathbf{x}}$ corresponding to $\mathbf{x}$ is defined as

$$\underline{\mathbf{x}}^T = [\mathbf{x}^T\ \mathbf{x}^H]. \tag{6.2}$$

From here the complex augmented random vector will always be underlined. It's easy to check that the real composite vector $\mathbf{z}$ and the complex augmented vector $\underline{\mathbf{x}}$ are related as

$$\underline{\mathbf{x}} = \mathbf{T}_n\mathbf{z}. \tag{6.3}$$

The real-to-complex transformation $\mathbf{T}_n$ is

$$\mathbf{T}_n = \begin{bmatrix} \mathbf{I} & j\mathbf{I} \\ \mathbf{I} & -j\mathbf{I} \end{bmatrix}, \tag{6.4}$$

which is unitary within a factor of 2:

$$\mathbf{T}_n\mathbf{T}_n^H = \mathbf{T}_n^H\mathbf{T}_n = 2\mathbf{I}. \tag{6.5}$$

In fact, it is equation (6.3) that governs the equivalence between dual channel filtering for $\mathbf{z}$ and complex filtering for $\mathbf{x}$.

6.1.2 Dual Channel and Widely Linear Transformation

Given a real linear transformation $\mathbf{M} \in \mathbb{R}^{2m\times 2n}$ and a composite real vector $\mathbf{z} \in \mathbb{R}^{2n}$, then the most general linear transformation of the real channels $\mathbf{u}$ and $\mathbf{v}$ into the real channels $\mathbf{a}$, $\mathbf{b}$ is

$$\begin{bmatrix} \mathbf{a} \\ \mathbf{b} \end{bmatrix} = \begin{bmatrix} \mathbf{M}_{11} & \mathbf{M}_{12} \\ \mathbf{M}_{21} & \mathbf{M}_{22} \end{bmatrix} \begin{bmatrix} \mathbf{u} \\ \mathbf{v} \end{bmatrix}, \tag{6.6}$$

Call $\mathbf{y} = \mathbf{a} + j\mathbf{b}$. Then the corresponding complex augmented vector $\underline{\mathbf{y}}$ is

$$\underline{\mathbf{y}} = \begin{bmatrix} \mathbf{y} \\ \mathbf{y}^* \end{bmatrix} = \mathbf{T}_m \begin{bmatrix} \mathbf{a} \\ \mathbf{b} \end{bmatrix} = \left(\frac{1}{2}\mathbf{T}_m\mathbf{M}\mathbf{T}_n^H\right)\left(\mathbf{T}_n \begin{bmatrix} \mathbf{u} \\ \mathbf{v} \end{bmatrix}\right) = \underline{\mathbf{H}}\underline{\mathbf{x}}, \tag{6.7}$$

The matrix $\underline{\mathbf{H}} = \frac{1}{2}\mathbf{T}_m\mathbf{M}\mathbf{T}_n^H$ is called an augmented matrix with the property that its southeast block is the conjugate of its northwest block, and its southwest block is the conjugate of the northeast block:

$$\underline{\mathbf{H}} = \begin{bmatrix} \mathbf{H}_1 & \mathbf{H}_2 \\ \mathbf{H}_2^* & \mathbf{H}_1^* \end{bmatrix}, \tag{6.8}$$

where

$$\mathbf{H}_1 = \frac{1}{2}\left[\mathbf{M}_{11} + \mathbf{M}_{22} + j\left(\mathbf{M}_{21} - \mathbf{M}_{12}\right)\right], \tag{6.9}$$

$$\mathbf{H}_2 = \frac{1}{2}\left[\mathbf{M}_{11} - \mathbf{M}_{22} + j\left(\mathbf{M}_{21} + \mathbf{M}_{12}\right)\right]. \tag{6.10}$$

Therefore the augmented matrix $\underline{\mathbf{H}}$ rules the widely linear transformation

$$\begin{aligned} \mathbf{y} = \mathbf{H}_1\mathbf{x} + \mathbf{H}_2\mathbf{x}^* \iff \mathbf{a} + j\mathbf{b} =& \mathbf{H}_1(\mathbf{u} + j\mathbf{v}) + \mathbf{H}_2(\mathbf{u} - j\mathbf{v}) \\ =& (\mathbf{H}_1 + \mathbf{H}_2)\mathbf{u} + j(\mathbf{H}_1 - \mathbf{H}_2)\mathbf{v} \end{aligned} \tag{6.11}$$

We see that if and only if $\mathbf{H}_2 = \mathbf{0}$, the widely linear transformation is a strictly linear transformation. This corresponds to the special case $\mathbf{M}_{11} = \mathbf{M}_{22}$ and $\mathbf{M}_{12} = -\mathbf{M}_{21}$ in the linear transformation of $\mathbf{u}$, $\mathbf{v}$ into $\mathbf{a}$, $\mathbf{b}$.

6.1.3 Improper Complex Signal

The augmented mean vector of the complex random vector $\mathbf{x}$ is

$$\underline{\boldsymbol{\mu}}_{\mathbf{x}} = E\underline{\mathbf{x}} = [\boldsymbol{\mu}_x^T \ \boldsymbol{\mu}_x^H]^T = [\boldsymbol{\mu}_u^T + j\boldsymbol{\mu}_v^T \quad \boldsymbol{\mu}_u^T - j\boldsymbol{\mu}_v^T]^T = \mathbf{T}\boldsymbol{\mu}_z, \tag{6.12}$$

and the augmented covariance matrix of $\mathbf{x}$ is

$$\underline{\mathbf{R}}_{xx} = E(\underline{\mathbf{x}} - \underline{\boldsymbol{\mu}}_x)(\underline{\mathbf{x}} - \underline{\boldsymbol{\mu}}_x)^H = \begin{bmatrix} \mathbf{R}_{xx} & \widetilde{\mathbf{R}}_{xx} \\ \widetilde{\mathbf{R}}_{xx}^* & \mathbf{R}_{xx}^* \end{bmatrix} = \mathbf{T}\mathbf{R}_{zz}\mathbf{T}^H, \tag{6.13}$$

where the matrix $\mathbf{R}_{xx} = E(\mathbf{x} - \boldsymbol{\mu}_x)(\mathbf{x} - \boldsymbol{\mu}_x)^H$ is the conventional *Hermitian* covariance matrix, and the matrix $\widetilde{\mathbf{R}}_{xx} = E(\mathbf{x} - \boldsymbol{\mu}_x)(\mathbf{x} - \boldsymbol{\mu}_x)^T$ is the *complementary* covariance matrix.

Definition 6.1.1. If the complementary covariance matrix $\widetilde{\mathbf{R}}_{xx}$ is zero, then $\mathbf{x}$ is called proper; otherwise $\mathbf{x}$ is improper.

The random vector $\mathbf{x} = \mathbf{u} + j\mathbf{v}$ is proper if and only if $\mathbf{R}_{uu} = \mathbf{R}_{vv}$ and $\mathbf{R}_{uv} = -\mathbf{R}_{uv}^T$, where $\mathbf{u}$ and $\mathbf{v}$ are the real and imaginary parts of $\mathbf{x}$ respectively.

6.2 Dual Channel Real and Widely Linear Complex Kalman Filter

Start with two *real* channels worth of random states $\mathbf{u}_t, \mathbf{v}_t \in \mathbb{R}^n$. Denote $\mathbf{z}_t^T = [\mathbf{u}_t^T \ \mathbf{v}_t^T]$ as the corresponding real *composite* state. Suppose the composite state and measurement equations are

$$\mathbf{z}_t = \begin{bmatrix} \mathbf{u}_t \\ \mathbf{v}_t \end{bmatrix} = \mathbf{E}\mathbf{z}_{t-1} + \mathbf{F}\boldsymbol{\omega}_{t-1} = \begin{bmatrix} \mathbf{E}_{11} & \mathbf{E}_{12} \\ \mathbf{E}_{21} & \mathbf{E}_{22} \end{bmatrix} \begin{bmatrix} \mathbf{u}_{t-1} \\ \mathbf{v}_{t-1} \end{bmatrix} + \begin{bmatrix} \mathbf{F}_{11} & \mathbf{F}_{12} \\ \mathbf{F}_{21} & \mathbf{F}_{22} \end{bmatrix} \begin{bmatrix} \boldsymbol{\mu}_{t-1} \\ \boldsymbol{\sigma}_{t-1} \end{bmatrix}, \ t = 1, 2, ..., \tag{6.14}$$

and

$$\boldsymbol{\psi}_t = \begin{bmatrix} \boldsymbol{\xi}_t \\ \boldsymbol{\kappa}_t \end{bmatrix} = \mathbf{G}\mathbf{z}_t + \boldsymbol{\eta}_t = \begin{bmatrix} \mathbf{G}_{11} & \mathbf{G}_{12} \\ \mathbf{G}_{21} & \mathbf{G}_{22} \end{bmatrix} \begin{bmatrix} \mathbf{u}_t \\ \mathbf{v}_t \end{bmatrix} + \begin{bmatrix} \boldsymbol{\rho}_t \\ \boldsymbol{\phi}_t \end{bmatrix}, \ t = 0, 1, ..., \tag{6.15}$$

where $\boldsymbol{\omega}_t^T = [\boldsymbol{\mu}_t^T \ \boldsymbol{\sigma}_t^T]$ and $\boldsymbol{\eta}_t^T = [\boldsymbol{\rho}_t^T \ \boldsymbol{\phi}_t^T]$ are the composite real driving and measurement noises, and $\boldsymbol{\psi}_t^T = [\boldsymbol{\xi}_t^T \ \boldsymbol{\kappa}_t^T]$ is the composite measurement. This dynamical model allows the states and measurements on the respective real channels to be arbitrarily coupled. For the real composite vectors $\mathbf{z}_t$, $\boldsymbol{\omega}_t$, $\boldsymbol{\eta}_t$, and $\boldsymbol{\psi}_t$, establish their complex augmented representations as $\underline{\mathbf{x}}_t = [\mathbf{x}_t^T \ \mathbf{x}_t^H]^T = \mathbf{T}\mathbf{z}_t$, $\underline{\mathbf{w}}_t = [\mathbf{w}_t^T \ \mathbf{w}_t^H]^T = \mathbf{T}\boldsymbol{\omega}_t$, $\underline{\mathbf{y}}_t = [\mathbf{y}_t^T \ \mathbf{y}_t^H]^T = \mathbf{T}\boldsymbol{\psi}_t$, and $\underline{\mathbf{n}}_t = [\mathbf{n}_t^T \ \mathbf{n}_t^H]^T = \mathbf{T}\boldsymbol{\eta}_t$. Then the resulting augmented complex state and measurement equations are

$$\underline{\mathbf{x}}_t = \underline{\mathbf{A}}\underline{\mathbf{x}}_{t-1} + \underline{\mathbf{B}}\underline{\mathbf{w}}_{t-1}, \ t = 1, 2, ..., \tag{6.16}$$

and

$$\underline{\mathbf{y}}_t = \underline{\mathbf{C}}\underline{\mathbf{x}}_t + \underline{\mathbf{n}}_t, \ t = 0, 1, ..., \tag{6.17}$$

where the augmented matrices $\underline{\mathbf{A}}$, $\underline{\mathbf{B}}$, and $\underline{\mathbf{C}}$ are

$$\underline{\mathbf{A}} = \frac{1}{2}\mathbf{T}\mathbf{E}\mathbf{T}^H = \begin{bmatrix} \mathbf{A}_1 & \mathbf{A}_2 \\ \mathbf{A}_2^* & \mathbf{A}_1^* \end{bmatrix}, \underline{\mathbf{B}} = \frac{1}{2}\mathbf{T}\mathbf{F}\mathbf{T}^H = \begin{bmatrix} \mathbf{B}_1 & \mathbf{B}_2 \\ \mathbf{B}_2^* & \mathbf{B}_1^* \end{bmatrix}, \underline{\mathbf{C}} = \frac{1}{2}\mathbf{T}\mathbf{G}\mathbf{T}^H = \begin{bmatrix} \mathbf{C}_1 & \mathbf{C}_2 \\ \mathbf{C}_2^* & \mathbf{C}_1^* \end{bmatrix}. \tag{6.18}$$

More straightforwardly, a widely linear complex Kalman filter's dynamical model is characterized by

$$\mathbf{x}_t = \mathbf{A}_1\mathbf{x}_{t-1} + \mathbf{A}_2\mathbf{x}_{t-1}^* + \mathbf{B}_1\mathbf{w}_{t-1} + \mathbf{B}_2\mathbf{w}_{t-1}^*,\ t = 1, 2, ..., \tag{6.19}$$

and

$$\mathbf{y}_t = \mathbf{C}_1\mathbf{x}_t + \mathbf{C}_2\mathbf{x}_t^* + \mathbf{n}_t,\ t = 0, 1, ..., \tag{6.20}$$

Suppose the initial state has mean $E\underline{\mathbf{x}}_0 = \mathbf{0}$, and augmented covariance

$$E\underline{\mathbf{x}}_0\underline{\mathbf{x}}_0^H = \begin{bmatrix} E\mathbf{x}_0\mathbf{x}_0^H & E\mathbf{x}_0\mathbf{x}_0^T \\ E\mathbf{x}_0^*\mathbf{x}_0^H & E\mathbf{x}_0^*\mathbf{x}_0^T \end{bmatrix} = \begin{bmatrix} \mathbf{\Pi}_0 & \widetilde{\mathbf{\Pi}}_0 \\ \widetilde{\mathbf{\Pi}}_0^* & \mathbf{\Pi}_0^* \end{bmatrix} = \underline{\mathbf{\Pi}}_0. \tag{6.21}$$

Assume that $E\underline{\mathbf{u}}_t = \mathbf{0}$ and $E\underline{\mathbf{n}}_t = \mathbf{0}$ for all t. Further assume the real and imaginary parts of $\mathbf{x}_0$ are uncorrelated with the real and imaginary parts of $\mathbf{u}_t$ and $\mathbf{n}_t$, meaning $E\underline{\mathbf{x}}_0\underline{\mathbf{u}}_t^H = \mathbf{0}$ and $E\underline{\mathbf{x}}_0\underline{\mathbf{n}}_t^H = \mathbf{0}$ for $t \geq 0$. Using the representation advocated in [111], the augmented second-order characterization of $(\underline{\mathbf{x}}_0, \underline{\mathbf{u}}_t, \underline{\mathbf{n}}_t)$ is given by

$$E\begin{bmatrix} \underline{\mathbf{x}}_0 \\ \underline{\mathbf{w}}_n \\ \underline{\mathbf{n}}_n \end{bmatrix} \begin{bmatrix} \underline{\mathbf{x}}_0^H & \underline{\mathbf{w}}_m^H & \underline{\mathbf{n}}_m^H & \underline{\mathbf{1}}^H \end{bmatrix} = \begin{bmatrix} \underline{\mathbf{\Pi}}_0 & \mathbf{0} & \mathbf{0} & \mathbf{0} \\ \mathbf{0} & \delta_{nm}\underline{\mathbf{Q}} & \delta_{nm}\underline{\mathbf{S}} & \mathbf{0} \\ \mathbf{0} & \delta_{nm}\underline{\mathbf{S}}^H & \delta_{nm}\underline{\mathbf{R}} & \mathbf{0} \end{bmatrix}, m, n \geq 0. \tag{6.22}$$

We further assume that for $n \geq m$, $E\underline{\mathbf{w}}_n\underline{\mathbf{x}}_m^H = \mathbf{0}$ and $E\underline{\mathbf{n}}_n\underline{\mathbf{x}}_m^H = \mathbf{0}$, and for $n > m$, $E\underline{\mathbf{w}}_n\underline{\mathbf{y}}_m^H = \mathbf{0}$ and $E\underline{\mathbf{n}}_n\underline{\mathbf{y}}_m^H = \mathbf{0}$. This is the same setup as that of the usual Kalman filter, but with covariances augmented to account for non-zero complementary covariance.

Suppose the linear minimum mean squared error (LMMSE) estimator of $\underline{\mathbf{x}}_{t-1}$ from measurements $\underline{\mathbf{Y}}_{t-1}^T = (\underline{\mathbf{y}}_1^T, \ldots, \underline{\mathbf{y}}_{t-1})^T$ is $\hat{\underline{\mathbf{x}}}_{t-1|t-1}$. Then the LMMSE prediction of $\underline{\mathbf{x}}_t$ from $\underline{\mathbf{Y}}_{t-1}^T$ is

$$\hat{\underline{\mathbf{x}}}_{t|t-1} = \underline{\mathbf{A}}\hat{\underline{\mathbf{x}}}_{t-1|t-1}, \tag{6.23}$$

and the prediction of $\underline{\mathbf{y}}_t$ from $\underline{\mathbf{Y}}_{t-1}^T$ is

$$\hat{\underline{\mathbf{y}}}_{t|t-1} = \underline{\mathbf{C}}\hat{\underline{\mathbf{x}}}_{t|t-1}. \tag{6.24}$$

Given the error covariance matrix $\underline{\mathbf{P}}_{t-1|t-1}$ for $\hat{\underline{\mathbf{e}}}_{t-1|t-1} = \hat{\underline{\mathbf{x}}}_{t-1|t-1} - \underline{\mathbf{x}}_{t-1}$, the error covariance matrix $\underline{\mathbf{P}}_{t|t-1}$ for $\hat{\underline{\mathbf{e}}}_{t|t-1} = \hat{\underline{\mathbf{x}}}_{t|t-1} - \underline{\mathbf{x}}_t$ is

$$\underline{\mathbf{P}}_{t|t-1} = \underline{\mathbf{A}}\underline{\mathbf{P}}_{t-1|t-1}\underline{\mathbf{A}}^H + \underline{\mathbf{B}}\underline{\mathbf{Q}}\underline{\mathbf{B}}^H \triangleq \begin{bmatrix} \mathbf{P}_{t|t-1} & \widetilde{\mathbf{P}}_{t|t-1} \\ \widetilde{\mathbf{P}}^*_{t|t-1} & \mathbf{P}_{t|t-1} \end{bmatrix}, \tag{6.25}$$

where $\mathbf{P}_{t|t-1}$ and $\widetilde{\mathbf{P}}_{t|t-1}$ are the Hermitian and complementary error covariance respectively:

$$\begin{aligned}
\mathbf{P}_{t|t-1} &= \mathbf{A}_1\mathbf{P}_{t-1|t-1}\mathbf{A}_1^H + \mathbf{A}_2\widetilde{\mathbf{P}}^*_{t-1|t-1}\mathbf{A}_1^H + \mathbf{A}_1\widetilde{\mathbf{P}}_{t-1|t-1}\mathbf{A}_2^H + \mathbf{A}_2\mathbf{P}^*_{t-1|t-1}\mathbf{A}_2^H \\
&\quad + \mathbf{B}_1\mathbf{Q}\mathbf{B}_1^H + \mathbf{B}_2\widetilde{\mathbf{Q}}^*\mathbf{B}_1^H + \mathbf{B}_1\widetilde{\mathbf{Q}}\mathbf{B}_2^H + \mathbf{B}_2\mathbf{Q}^*\mathbf{B}_2^H, \\
\widetilde{\mathbf{P}}_{t|t-1} &= \mathbf{A}_1\mathbf{P}_{t-1|t-1}\mathbf{A}_2^T + \mathbf{A}_2\widetilde{\mathbf{P}}^*_{t-1|t-1}\mathbf{A}_2^T + \mathbf{A}_1\widetilde{\mathbf{P}}_{t-1|t-1}\mathbf{A}_1^T + \mathbf{A}_2\mathbf{P}^*_{t-1|t-1}\mathbf{A}_1^T \\
&\quad + \mathbf{B}_1\mathbf{Q}\mathbf{B}_2^T + \mathbf{B}_2\widetilde{\mathbf{Q}}^*\mathbf{B}_2^T + \mathbf{B}_1\widetilde{\mathbf{Q}}\mathbf{B}_1^T + \mathbf{B}_2\mathbf{Q}^*\mathbf{B}_1^T.
\end{aligned} \tag{6.26}$$

The error covariance matrix $\underline{\mathbf{S}}_{t|t-1}$ for the innovation $\hat{\underline{\mathbf{n}}}_{t|t-1} = \hat{\underline{\mathbf{y}}}_{t|t-1} - \underline{\mathbf{y}}_t$ is

$$\underline{\mathbf{S}}_{t|t-1} = \underline{\mathbf{C}}\underline{\mathbf{P}}_{t|t-1}\underline{\mathbf{C}}^H + \underline{\mathbf{R}} \triangleq \begin{bmatrix} \mathbf{S}_{t|t-1}\widetilde{\mathbf{S}}_{t|t-1} \\ \widetilde{\mathbf{S}}^*_{t|t-1}\mathbf{S}^*_{t|t-1} \end{bmatrix}, \tag{6.27}$$

where $\mathbf{S}_{t|t-1}$ and $\widetilde{\mathbf{S}}_{t|t-1}$ are the Hermitian and complementary innovation covariance respectively:

$$\begin{aligned}
\mathbf{S}_{t|t-1} &= \mathbf{C}_1\mathbf{P}_{t|t-1}\mathbf{C}_1^H + \mathbf{C}_2\widetilde{\mathbf{P}}^*_{t|t-1}\mathbf{C}_1^H + \mathbf{C}_1\widetilde{\mathbf{P}}_{t|t-1}\mathbf{C}_2^H + \mathbf{C}_2\mathbf{P}^*_{t|t-1}\mathbf{C}_2^H + \mathbf{R}, \\
\widetilde{\mathbf{S}}_{t|t-1} &= \mathbf{C}_1\mathbf{P}_{t|t-1}\mathbf{C}_2^T + \mathbf{C}_2\widetilde{\mathbf{P}}^*_{t|t-1}\mathbf{C}_2^T + \mathbf{C}_1\widetilde{\mathbf{P}}_{t|t-1}\mathbf{C}_1^T + \mathbf{C}_2\mathbf{P}^*_{t|t-1}\mathbf{C}_1^T + \widetilde{\mathbf{R}}.
\end{aligned} \tag{6.28}$$

The normal equation for the Kalman gain is

$$\underline{\mathbf{K}}_t\underline{\mathbf{S}}_{t|t-1} = \underline{\mathbf{P}}_{t|t-1}\underline{\mathbf{C}}^H. \tag{6.29}$$

The inverse error covariance matrix $\underline{\mathbf{S}}^{-1}_{t|t-1}$ has the augmented form

$$\underline{\mathbf{S}}^{-1}_{t|t-1} = \begin{bmatrix} \mathbf{P}_{\mathbf{S}}^{-1} & -\mathbf{S}^{-1}_{t|t-1}\widetilde{\mathbf{S}}_{t|t-1}\mathbf{P}_{\mathbf{S}}^{-*} \\ -\mathbf{S}^{-*}_{t|t-1}\widetilde{\mathbf{S}}^*_{t|t-1}\mathbf{P}_{\mathbf{S}}^{-1} & \mathbf{P}_{\mathbf{S}}^{-*} \end{bmatrix}, \tag{6.30}$$

where $\mathbf{P}_{\mathbf{S}} = \mathbf{S}_{t|t-1} - \widetilde{\mathbf{S}}_{t|t-1}\mathbf{S}^{-*}_{t|t-1}\widetilde{\mathbf{S}}^*_{t|t-1}$ is a Schur complement, namely the error covariance for estimating $\hat{\mathbf{n}}_{t|t-1}$ from $\hat{\mathbf{n}}^*_{t|t-1}$. Thus the augmented Kalman gain may be written as

$$\underline{\mathbf{K}}_t = \underline{\mathbf{P}}_{t|t-1}\underline{\mathbf{C}}^H\underline{\mathbf{S}}^{-1}_{t|t-1} \triangleq \begin{bmatrix} \mathbf{K}_t & \widetilde{\mathbf{K}}_t \\ \widetilde{\mathbf{K}}^*_t & \mathbf{K}^*_t \end{bmatrix}, \tag{6.31}$$

where the diagonal and off-diagonal block matrices of the augmented Kalman gain are

$$\begin{aligned}
\mathbf{K}_t &= (\mathbf{P}_{t|t-1}\mathbf{C}_1^H + \widetilde{\mathbf{P}}_{t|t-1}\mathbf{C}_2^H)\mathbf{P}_{\mathbf{S}}^{-1} - (\mathbf{P}_{t|t-1}\mathbf{C}_2^T + \widetilde{\mathbf{P}}_{t|t-1}\mathbf{C}_1^T)\mathbf{S}_{t|t-1}^{-*}\widetilde{\mathbf{S}}_{t|t-1}^*\mathbf{P}_{\mathbf{S}}^{-1}, \\
\widetilde{\mathbf{K}}_t &= (\mathbf{P}_{t|t-1}\mathbf{C}_2^T + \widetilde{\mathbf{P}}_{t|t-1}\mathbf{C}_1^T)\mathbf{P}_{\mathbf{S}}^{-*} - (\mathbf{P}_{t|t-1}\mathbf{C}_1^H + \widetilde{\mathbf{P}}_{t|t-1}\mathbf{C}_2^H)\mathbf{S}_{t|t-1}^{-1}\widetilde{\mathbf{S}}_{t|t-1}\mathbf{P}_{\mathbf{S}}^{-*}.
\end{aligned} \tag{6.32}$$

When complementary covariances $\widetilde{\mathbf{P}}_{t|t-1}$ and $\widetilde{\mathbf{S}}_{t|t-1}$ vanish, and when $\mathbf{C}_2$ is zero, we have $\underline{\mathbf{K}}_t = diag(\mathbf{K}_t, \mathbf{K}_t^*)$, where $\mathbf{K}_t = \mathbf{P}_{t|t-1}\mathbf{C}_1^H\mathbf{S}_{t|t-1}^{-1}$ is the usual KF. Finally, the WLCKF is

$$\underline{\hat{\mathbf{x}}}_{t|t} = \underline{\hat{\mathbf{x}}}_{t|t-1} + \underline{\mathbf{K}}_t\underline{\hat{\mathbf{n}}}_{t|t-1}, \tag{6.33}$$

and the error covariance matrix for $\underline{\hat{\mathbf{e}}}_{t|t} = \underline{\hat{\mathbf{x}}}_{t|t} - \underline{\mathbf{x}}_t$ is

$$\underline{\mathbf{P}}_{t|t} = \left(\underline{\mathbf{I}} - \underline{\mathbf{K}}_t\underline{\mathbf{C}}\right)\underline{\mathbf{P}}_{t|t-1} \triangleq \begin{bmatrix} \mathbf{P}_{t|t} & \widetilde{\mathbf{P}}_{t|t} \\ \widetilde{\mathbf{P}}_{t|t}^* & \mathbf{P}_{t|t}^* \end{bmatrix}. \tag{6.34}$$

and the Hermitian and complementary error covariances are

$$\begin{aligned}
\mathbf{P}_{t|t} &= (\mathbf{I} - \mathbf{K}_t\mathbf{C}_1 - \widetilde{\mathbf{K}}_t\mathbf{C}_2^*)\mathbf{P}_{t|t-1} - (\mathbf{K}_t\mathbf{C}_2 + \widetilde{\mathbf{K}}_t\mathbf{C}_1^*)\widetilde{\mathbf{P}}_{t|t-1}^*, \\
\widetilde{\mathbf{P}}_{t|t} &= (\mathbf{I} - \mathbf{K}_t\mathbf{C}_1 - \widetilde{\mathbf{K}}_t\mathbf{C}_2^*)\widetilde{\mathbf{P}}_{t|t-1} - (\mathbf{K}_t\mathbf{C}_2 + \widetilde{\mathbf{K}}_t\mathbf{C}_1^*)\mathbf{P}_{t|t-1}^*.
\end{aligned} \tag{6.35}$$

Finally, the WLCKF is implemented by initializing $\underline{\hat{\mathbf{x}}}_{0|0} = \underline{\mathbf{0}}$ and $\underline{\mathbf{P}}_{0|0} = \underline{\mathbf{\Pi}}_0$, and recursively running the procedure (6.23)-(6.35). This WLCKF can be implemented in complex arithmetic, or it can be inverted for the real KF of the dual channel real model (6.14)-(6.15) by using real to complex connections (6.3) and (6.13).

Remark 6.2.1. In the state and measurement equations (6.16)-(6.18), the new state $\mathbf{x}_t$ depends on $\mathbf{x}_{t-1}$, $\mathbf{x}_{t-1}^*$, $\mathbf{w}_{t-1}$, and $\mathbf{w}_{t-1}^*$. And measurement $\mathbf{y}_t$ depends on $\mathbf{x}_t$, $\mathbf{x}_t^*$, $\mathbf{n}_t$, and $\mathbf{n}_t^*$. For the state and measurement equations of the WLCKF proposed in [106], the new state $\mathbf{x}_t$ depends only on $\mathbf{x}_{t-1}$ and $\mathbf{w}_{t-1}$, and measurement $\mathbf{y}_t$ depends only on $\mathbf{x}_t$ and $\mathbf{n}_t$. Thus the WLCKF in [106] can be obtained as a special case of the WLCKF considered here by letting matrices $\mathbf{A}_2$, $\mathbf{B}_2$, and $\mathbf{C}_2$ in (6.16)-(6.18) be zero, or equivalently assuming $\mathbf{E}_{11} = \mathbf{E}_{22}$, $\mathbf{E}_{12} = -\mathbf{E}_{21}$, $\mathbf{F}_{11} = \mathbf{F}_{22}$, $\mathbf{F}_{12} = -\mathbf{F}_{21}$, $\mathbf{G}_{11} = \mathbf{G}_{22}$, and $\mathbf{G}_{12} = -\mathbf{G}_{21}$ in the real channel equations (6.14)-(6.15).

6.3 Performance Comparison between WLCKF and CKF

Let's suppose the state and measurement equations for a complex state x_t are

$$x_t = ax_{t-1} + bw_{t-1},\ t = 1, 2, ..., \tag{6.36}$$

and

$$y_t = cx_t + n_t,\ t = 0, 1, ..., \tag{6.37}$$

where $a, b, c \in \mathbb{C}$. The augmented matrices are $\underline{\mathbf{A}} = diag(a, a^*)$, $\underline{\mathbf{B}} = diag(b, b^*)$, and $\underline{\mathbf{C}} = diag(c, c^*)$. Then the recursion for the 2 by 2 augmented covariance matrix $\underline{\mathbf{P}}_{t|t}$ is

$$\begin{aligned}\underline{\mathbf{P}}_{t|t} &= (\underline{\mathbf{P}}_{t|t-1}^{-1} + \underline{\mathbf{C}}^H \underline{\mathbf{R}}^{-1} \underline{\mathbf{C}})^{-1} \\ &= \left[(|a|^2 \underline{\mathbf{P}}_{t-1|t-1} + |b|^2 \underline{\mathbf{Q}})^{-1} + |c|^2 \underline{\mathbf{R}}^{-1}\right]^{-1},\ t = 1, 2, ...\end{aligned} \tag{6.38}$$

Thus the performance of the WLCKF is determined by the impropriety of the initial state x_0 through $\underline{\mathbf{\Pi}}_0$, the driving noise w_t through $\underline{\mathbf{Q}}$, and the measurement noise n_t through $\underline{\mathbf{R}}$. In the following we show that for some special distributions of state and noises, the WLCKF produces smaller MSE than the CKF.

6.3.1 Special Case: x_0 Is Improper, w_t and n_t Are Proper

Suppose $\underline{\mathbf{P}}_{0|0} = \begin{pmatrix} P_{0|0} & \widetilde{P}_{0|0} \\ \widetilde{P}_{0|0}^* & P_{0|0} \end{pmatrix}$, $\underline{\mathbf{Q}} = N_1 \underline{\mathbf{I}}$, and $\underline{\mathbf{R}} = N_2 \underline{\mathbf{I}}$. Assume $\underline{\mathbf{P}}_{0|0}$ has eigenvalues $\{\lambda_1^0, \lambda_2^0\}$. Given the eigenvalues $\{\lambda_1^{t-1}, \lambda_2^{t-1}\}$ of matrix $\underline{\mathbf{P}}_{t-1|t-1}$, the eigenvalues of $\underline{\mathbf{P}}_{t|t}$ are

$$\lambda_i^t = g(\lambda_i^{t-1}), \quad i = 1, 2, \tag{6.39}$$

where the function g is given by

$$g(\lambda) = \frac{N_2(|a|^2\lambda + |b|^2 N_1)}{|c|^2(|a|^2\lambda + |b|^2 N_1) + N_2}, \tag{6.40}$$

Thus the eigenvalues $\{\lambda_1^t, \lambda_2^t\}$ may be conveniently expressed as the function recursion

$$\lambda_i^t = \underbrace{g \circ g \circ \cdots \circ g}_{t \text{ times}}(\lambda_i^0) \triangleq q_t(\lambda_i^0) \tag{6.41}$$

Observe that g is an increasing concave function w.r.t λ. Thus we conclude that q_t is concave for each t. Next we want to compute the widely linear minimum mean squared error (WLMMSE) at the t-th iteration for the WLCKF. This may be written

$$\xi_t^{\mathrm{WL}} = E \parallel \hat{e}_{t|t} \parallel^2 = \frac{1}{2}\mathrm{tr}(\underline{\mathbf{P}}_{t|t}) = \frac{1}{2}(q_t(\lambda_1^0) + q_t(\lambda_2^0)). \tag{6.42}$$

Note the initial *scalar* Hermitian covariance is $P_{0|0}$. Then the t-th LMMSE for the CKF is

$$\xi_t^{\mathrm{L}} = q_t(P_{0|0}). \tag{6.43}$$

To achieve the maximum performance improvement of the WLCKF over the CKF for the special case discussed here, we shall minimize ξ_t^{WL} with fixed $P_{0|0}$ and variable $\widetilde{P}_{0|0}$. It can be seen that at each t, ξ_t^{WL} is a Schur-concave function w.r.t all λ_i^0. Since $\lambda_1^0 + \lambda_2^0 \leq 2P_{0|0}$ [41], the minimum is achieved when

$$[\lambda_1^0 \ \lambda_2^0] = [2P_{0|0} \ 0]. \tag{6.44}$$

Substituting (6.44) into (6.42), we have the minimum ξ_t^{WL}:

$$\min \xi_t^{\mathrm{WL}} = \frac{1}{2}\left(q_t(2P_{0|0}) + q_t(0)\right) \tag{6.45}$$

The ratio of $\min \xi_t^{\mathrm{WL}}$ to ξ_t^{L} is:

$$\theta_t = \frac{\min \xi_t^{\mathrm{WL}}}{\xi_t^{\mathrm{SL}}} = \frac{q_t(2P_{0|0}) + q_t(0)}{2q_t(P_{0|0})}. \tag{6.46}$$

It's obvious that $\frac{1}{2} \leq \theta_t \leq 1$. This is because q_t is concave, and $q_t(2P_{0|0}) + q_t(0) \leq 2q_t(P_{0|0})$ for any $P_{0|0}$. Also $q_t(2P_{0|0}) \geq q_t(P_{0|0})$ for any $P_{0|0}$ and $q_t(0) \geq 0$. Actually the condition for achieving the lower bound is $N_1 \ll N_2 \ll 1$. This coincides with the MMSE analysis in [41].

6.3.2 General Case: w_t and n_t Can Be Improper

In this case we have

$$\underline{\mathbf{Q}} = N_1 \begin{bmatrix} 1 & \rho_w \\ \rho_w^* & 1 \end{bmatrix}, \quad \underline{\mathbf{R}} = N_2 \begin{bmatrix} 1 & \rho_n \\ \rho_n^* & 1 \end{bmatrix}, \tag{6.47}$$

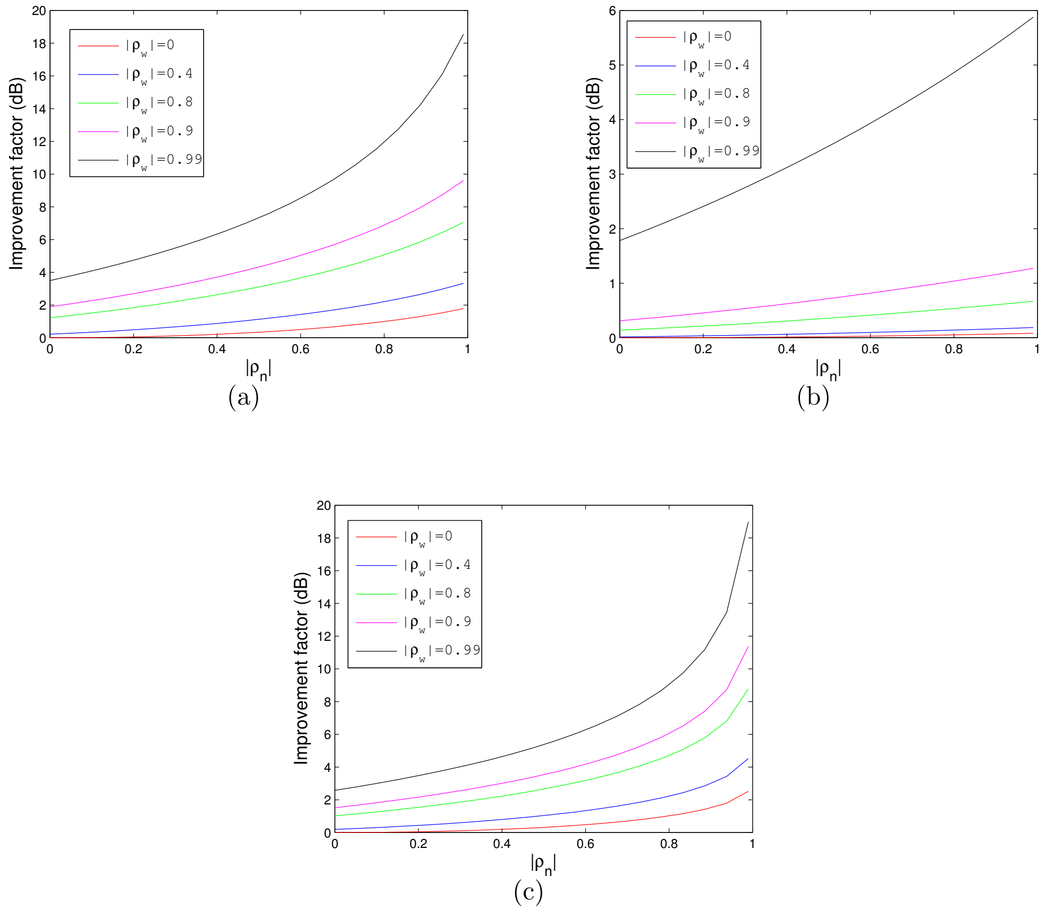

Figure 6.1: MSE performance improvement of the WLCKF over the CKF. (a) $N_1 = -20$dB, $N_2 = -20$dB. (b) $N_1 = -20$dB, $N_2 = -40$dB. (c) $N_1 = -40$dB, $N_2 = -20$dB.

where ρ_w is the *complex correlation coefficient* between w_t and w_t^*, and ρ_n is the complex correlation coefficient between n_t and n_t^*. These determine the level of impropriety. We can show that $0 \leq |\rho_w|, |\rho_n| \leq 1$. Suppose the following matrix properties are satisfied: (1) $(\underline{\mathbf{A}}, \underline{\mathbf{C}})$ is observable, that is, the matrix $[\underline{\mathbf{C}}^T | \underline{\mathbf{A}}^T \underline{\mathbf{C}}^T | \cdots | (\underline{\mathbf{A}}^{m-1})^T \underline{\mathbf{C}}^T]$ is full rank, (2) $(\underline{\mathbf{A}}, \hat{\underline{\mathbf{Q}}})$ is reachable, where $\underline{\mathbf{Q}} = \hat{\underline{\mathbf{Q}}} \hat{\underline{\mathbf{Q}}}^H$, that is, the matrix $[\hat{\underline{\mathbf{Q}}} | \underline{\mathbf{A}} \hat{\underline{\mathbf{Q}}} | \cdots | \underline{\mathbf{A}}^{m-1} \hat{\underline{\mathbf{Q}}}]$ is full rank. Using the argument in [112] we can show that the error covariance matrix $\underline{\mathbf{P}}_{t|t}$ converges to $\underline{\mathbf{P}}$, which is the unique positive semidefinite solution of

$$\underline{\mathbf{P}} = \left[(|a|^2 \underline{\mathbf{P}} + |b|^2 \underline{\mathbf{Q}})^{-1} + |c|^2 \underline{\mathbf{R}}^{-1} \right]^{-1}. \tag{6.48}$$

The above convergence is irrespective of the initial state x_0. Fig. 6.1 plots the performance improvement of the WLCKF over the CKF at different level of impropriety of w_t and n_t. We choose $a = b = c = 1$, and the MSE of the WLCKF converges in this case. From [112] we can also show that the MSE of the CKF converges. The performance improvement is defined by ratio between the convergent MSE of the CKF over that of the WLCKF. As Fig. 6.1 illustrates, the performance improvement is monotone in $|\rho_w|$ for fixed $|\rho_n|$, and monotone in $|\rho_n|$ for fixed $|\rho_w|$.

6.4 Discussion on Extended Widely Linear Complex Kalman Filter

The extended Kalman filters (EKFs) are [45] are initially proposed to address the nonlinear dynamical models for real-valued states and measurements. The essential idea of EKFs is to linearize the nonlinear state update and measurement equations, and hence the approximated posterior mean and covariances can be precise up to the first order in its Taylor expansion. For a dynamical model for complex valued states and measurements, whose model equations are not in the form of widely linear transformations of complex-valued states, we can derive the extended WLCKF (EWLCKF) along the lines of Section 6.2. The derived EWLCKF uses nonlinear model equations to predict states and measurements. And it utilizes the complex Jacobians [113] to modify the Hermitian and complementary covariance matrices and Kalman gain. This treatment is equivalent to the original treatment of Mandic, et al. [106, 114]. Therefore our derivation of EWLCKF shall not be treated as a novelty nor be explicitly presented in the dissertation.

6.5 Unscented Widely Linear Complex Kalman Filter

In this section we consider the following nonlinear model for dual real channel state and measurement evolution:

$$\mathbf{z}_t = [\mathbf{u}_t \quad \mathbf{v}_t]^T = \mathbf{f}_{t-1}(\mathbf{z}_{t-1}, \boldsymbol{\omega}_{t-1}) = \mathbf{f}_{t-1}([\mathbf{u}_{t-1} \quad \mathbf{v}_{t-1}]^T, [\boldsymbol{\mu}_t \quad \boldsymbol{\sigma}_t]^T), t = 1, 2, ..., \tag{6.49}$$

$$\boldsymbol{\psi}_t = [\boldsymbol{\xi}_t \quad \boldsymbol{\kappa}_t]^T = \mathbf{h}_t(\mathbf{z}_t, \boldsymbol{\eta}_t) = \mathbf{h}_t([\mathbf{u}_t \quad \mathbf{v}_t]^T, [\boldsymbol{\rho}_t \quad \boldsymbol{\phi}_t]^T), t = 0, 1, ..., \tag{6.50}$$

where $\mathbf{f}_{t-1}$ and $\mathbf{h}_t$ are time varying nonlinear transformations, and the notation for states and noises is identical with the model equations (6.14)-(6.15). Then the induced complex model equations are

$$\mathbf{x}_t = \widetilde{\mathbf{f}}_{t-1}(\mathbf{x}_{t-1}, \mathbf{w}_{t-1}), \tag{6.51}$$

and

$$\mathbf{y}_t = \widetilde{\mathbf{h}}_t(\mathbf{x}_t, \mathbf{n}_t). \tag{6.52}$$

It can be seen that for all t, $\widetilde{\mathbf{f}}_{t-1}$ and $\widetilde{\mathbf{h}}_t$ are not widely linear transformations. Thus the WLCKF developed in section 6.2 cannot be directly utilized. For such a model, the extended WLCKF is proposed in [106, 114] to exploit the impropriety of complex states and noises. However, the major defect of the EWLCKF is that the posterior means and covariances are accurate only to the first order in a Taylor expansion. A conventional Unscented KF uses the unscented transformation (UT) to generate a fixed set of sigma points to represent the distribution of a random variable [46]. After propagating sigma points through nonlinearities, the estimated posterior mean and covariance are precise at least to second order in a Taylor expansion. Motivated by the power of unscented Kalman filters, in this section we present a novel paradigm for constructing unscented widely linear complex KFs. Our UWLCKFs use *modified* sigma points which preserve the Hermitian *and* complementary covariances of states and noises, while the UWLCKFs proposed in [106] use sigma points which only preserve the Hermitian covariances of states and noises.

Compose complex random states and noises into a complex vector $\mathbf{s}^T = [\mathbf{x}^T \ \mathbf{w}^T \ \mathbf{n}^T]$. Suppose the augmented mean and covariance of $\mathbf{s}$ are

$$\underline{\boldsymbol{\mu}}_s^T = [\boldsymbol{\mu}_s^T \quad \boldsymbol{\mu}_s^H], \ \underline{\mathbf{R}}_{ss} = \begin{bmatrix} \mathbf{R}_{ss} & \widetilde{\mathbf{R}}_{ss} \\ \widetilde{\mathbf{R}}_{ss}^* & \mathbf{R}_{ss}^* \end{bmatrix}. \tag{6.53}$$

In [106] the authors proposed complex sigma points of $\mathbf{s}$ which are constructed from moments $\boldsymbol{\mu}_s$ and $\mathbf{R}_{ss}$. Thus these sigma points only carry $\boldsymbol{\mu}_s$ and $\mathbf{R}_{ss}$, but not $\widetilde{\mathbf{R}}_{ss}$. In fact, there may be multiple ways to generate sigma points for the augmented random vector $\underline{\mathbf{s}}$ which carry both $\underline{\boldsymbol{\mu}}_s$ and $\underline{\mathbf{R}}_{ss}$. But a hidden restriction imposed here is that these sigma points should be augmented vectors. Otherwise they cannot be propagated through the UWLCKF. One approach is to start with sigma points of the corresponding composite real random vector $\boldsymbol{\zeta}^T = [\mathbf{u}^T\ \boldsymbol{\mu}^T\ \boldsymbol{\rho}^T\ \mathbf{v}^T\ \boldsymbol{\sigma}^T\ \boldsymbol{\phi}^T]$. The first and second moments of $\boldsymbol{\zeta}$ are

$$\boldsymbol{\mu}_\zeta = \frac{1}{2}\mathbf{T}^{-1}\underline{\boldsymbol{\mu}}_s,\ \mathbf{R}_{\zeta\zeta} = \frac{1}{4}\mathbf{T}^H\underline{\mathbf{R}}_{ss}\mathbf{T}. \tag{6.54}$$

Using a Cholesky decomposition the composite covariance matrix $\mathbf{R}_{\zeta\zeta}$ may be factored as

$$\mathbf{R}_{\zeta\zeta} = \mathbf{B}\mathbf{B}^T$$

Denote the vector $\mathbf{b}_k$ as the k-th column of matrix $\mathbf{B}$ for $k = 1, 2, ..., 2N$. Then the sigma points $\{\boldsymbol{\mathcal{Z}}_k\}$ of $\boldsymbol{\zeta}$ are [46]

$$\begin{aligned}
&\boldsymbol{\mathcal{Z}}_0 = \boldsymbol{\mu}_\zeta,\ k = 0,\\
&\boldsymbol{\mathcal{Z}}_k = \boldsymbol{\mu}_\zeta + \sqrt{2N+\lambda}\mathbf{b}_k,\ k = 1, ..., 2N,\\
&\boldsymbol{\mathcal{Z}}_k = \boldsymbol{\mu}_\zeta - \sqrt{2N+\lambda}\mathbf{b}_{k-2N},\ k = 2N+1, ..., 4N,
\end{aligned} \tag{6.55}$$

corresponding to the mean weights $\{W_m(k)\}_{k=0}^{4N}$ and covariances weights $\{W_c(k)\}_{k=0}^{4N}$ defined in [46]:

$$\begin{aligned}
&\text{mean weights: } W_m(k) = \begin{cases} \lambda/(2N+\lambda), & k = 0,\\ 1/[2(2N+\lambda)], & k = 1, ..., 4N, \end{cases}\\
&\text{covariance weights: } W_c(k) = \begin{cases} \lambda/(2N+\lambda) + (1-\alpha^2+\beta), & k = 0,\\ W_m(k), & k = 1, ..., 4N, \end{cases}
\end{aligned} \tag{6.56}$$

where $\lambda = \alpha^2(2N+\kappa) - 2N$, and α, β, and κ are parameters controlling the distribution of sigma points. Define a set of augmented vectors $\{\underline{\boldsymbol{\mathcal{X}}}_k\}$ as

$$\underline{\boldsymbol{\mathcal{X}}}_k = \begin{bmatrix} \boldsymbol{\mathcal{X}}_k \\ \boldsymbol{\mathcal{X}}_k^* \end{bmatrix} = \mathbf{T}\boldsymbol{\mathcal{Z}}_k = \begin{cases} \underline{\boldsymbol{\mu}}_s, & k = 0,\\ \underline{\boldsymbol{\mu}}_s + \sqrt{2N+\lambda}\mathbf{T}\mathbf{b}_k, & k = 1, ..., 2N,\\ \underline{\boldsymbol{\mu}}_s - \sqrt{2N+\lambda}\mathbf{T}\mathbf{b}_{k-2N}, & k = 2N+1, ..., 4N. \end{cases} \tag{6.57}$$

We can show that all the $\underline{\boldsymbol{\mathcal{X}}}_k$ compose the sigma points of the augmented vector $\underline{\mathbf{s}}$, since $\underline{\boldsymbol{\mathcal{X}}}_0 = \underline{\boldsymbol{\mu}}_s$ and

$$\begin{aligned}\underline{\mathbf{R}}_{ss} &= \mathbf{T}\mathbf{R}_{\zeta\zeta}\mathbf{T}^H \\ &= \begin{bmatrix}\mathbf{T}\mathbf{b}_1 & \mathbf{T}\mathbf{b}_2 & \cdots & \mathbf{T}\mathbf{b}_{2N}\end{bmatrix}\begin{bmatrix}\mathbf{T}\mathbf{b}_1 & \mathbf{T}\mathbf{b}_2 & \cdots & \mathbf{T}\mathbf{b}_{2N}\end{bmatrix}^H.\end{aligned} \tag{6.58}$$

Equation (6.58) summarizes the Hermitian and complementary identities

$$\mathbf{R}_{ss} = \frac{1}{4n}\sum_{k=1}^{4n}(\boldsymbol{\mathcal{X}}_k - \boldsymbol{\mu}_s)(\boldsymbol{\mathcal{X}}_k - \boldsymbol{\mu}_s)^H \tag{6.59}$$

and

$$\widetilde{\mathbf{R}}_{ss} = \frac{1}{4n}\sum_{k=1}^{4n}(\boldsymbol{\mathcal{X}}_k - \boldsymbol{\mu}_s)(\boldsymbol{\mathcal{X}}_k - \boldsymbol{\mu}_s)^T. \tag{6.60}$$

Therefore we have obtained the sigma points $\{\underline{\boldsymbol{\mathcal{X}}}_k\}$ of $\underline{\mathbf{s}}$ w.r.t weights $\{W_m(k), W_c(k)\}$ from widely linear transformation of the real composite sigma points $\{\boldsymbol{\mathcal{Z}}_k\}$ of $\boldsymbol{\zeta}$ w.r.t weights $\{W_m(k), W_c(k)\}$. Note that each sigma point $\underline{\boldsymbol{\mathcal{X}}}_k$ is an augmented vector. Thus it follows that the complex set $\{\boldsymbol{\mathcal{X}}_k\}$, generated by extracting the top halves of $\{\underline{\boldsymbol{\mathcal{X}}}_k\}$, is sufficient to capture both first and second order statistical information of the augmented random vector $\underline{\mathbf{s}}$. We call $\{\boldsymbol{\mathcal{X}}_k\}$ the *modified* sigma points of $\mathbf{s}$. The impact of these modified sigma points is that $\{\boldsymbol{\mathcal{X}}_k\}$ preserves not only mean $\boldsymbol{\mu}_s$ and Hermitian covariance $\mathbf{R}_{ss}$, but also complementary covariance $\widetilde{\mathbf{R}}_{ss}$.

But what really concerns us is whether the modified sigma points will refine the propagation of mean and covariance through the nonlinearities $\widetilde{\mathbf{f}}$ and $\widetilde{\mathbf{h}}$. Suppose we push each modified sigma point $\boldsymbol{\mathcal{X}}_k$ through any non-linearity $\mathbf{g}$ and acquire $\boldsymbol{\mathcal{Y}}_k = \mathbf{g}(\boldsymbol{\mathcal{X}}_k)$. Compute the following deterministic sample averages:

$$\hat{\boldsymbol{\mu}}_y = \sum_{k=0}^{4N} W_m(k)\boldsymbol{\mathcal{Y}}_k = \sum_{k=0}^{4N} W_m(k)\mathbf{g}(\boldsymbol{\mathcal{X}}_k),$$

$$\mathbf{P}_{yy} = \sum_{k=0}^{4n} W_c(k)(\boldsymbol{\mathcal{Y}}_k - \hat{\boldsymbol{\mu}}_y)(\boldsymbol{\mathcal{Y}}_k - \hat{\boldsymbol{\mu}}_y)^H,$$

$$\widetilde{\mathbf{P}}_{yy} = \sum_{k=0}^{4n} W_c(k)(\boldsymbol{\mathcal{Y}}_k - \hat{\boldsymbol{\mu}}_y)(\boldsymbol{\mathcal{Y}}_k - \hat{\boldsymbol{\mu}}_y)^T.$$

From the argument of [46], it can be verified that the sample averages $\hat{\boldsymbol{\mu}}_y$, and $\mathbf{P}_{yy}$, and $\widetilde{\mathbf{P}}_{yy}$ may be used to approximate the mean $E(\mathbf{g}(\mathbf{s}))$, the Hermitian, and complementary covariance matrices of $\mathbf{g}(\mathbf{s})$. The approximation is precise up to at least second order in a Taylor expansion. The unscented widely linear Kalman filter is described as following, in notation that follows [115]:

(1) Initialize with $\hat{\mathbf{x}}_{0|0} = \mathbf{0}$, $\mathbf{P}_{0|0} = \boldsymbol{\Pi}_0$ and $\widetilde{\mathbf{P}}_{0|0} = \widetilde{\boldsymbol{\Pi}}_0$ as defined in equation (6.21).

(2) At the t-th iteration, $t = 1, 2, \cdots$, Replace $\mathbf{P}_{t-1|t-1}$ with $\mathbf{R}_{xx}$, and $\widetilde{\mathbf{P}}_{t-1|t-1}$ with $\widetilde{\mathbf{R}}_{xx}$, and $\boldsymbol{\mu}^s_{x,t} = [\hat{\mathbf{x}}^T_{t-1|t-1}\ \mathbf{0}\ \mathbf{0}]^T$ with $\boldsymbol{\mu}^s_x$ in (6.53). Construct effective sigma points $\{\mathcal{X}^s_{k,t}\} = \{[(\mathcal{X}^x_{k,t-1})^T\ (\mathcal{X}^w_{k,t-1})^T\ (\mathcal{X}^n_{k,t})^T]^T\}$ by using equations (6.53)-(6.57).

(3) Prediction updates:

$$\boldsymbol{\mathcal{X}}^x_{k,t|t-1} = \widetilde{\mathbf{f}}_{t-1}(\boldsymbol{\mathcal{X}}^x_{k,t-1}, \boldsymbol{\mathcal{X}}^w_{k,t-1})$$

$$\hat{\mathbf{x}}_{t|t-1} = \sum_{k=0}^{4N} W_k^{(m)} \boldsymbol{\mathcal{X}}^x_{k,t|t-1},$$

$$\mathbf{P}_{t|t-1} = \sum_{k=0}^{4N} W_k^{(c)} (\boldsymbol{\mathcal{X}}^x_{k,t|t-1} - \hat{\mathbf{x}}_{t|t-1})(\boldsymbol{\mathcal{X}}^x_{k,t|t-1} - \hat{\mathbf{x}}_{t|t-1})^H,$$

$$\widetilde{\mathbf{P}}_{t|t-1} = \sum_{k=0}^{4N} W_k^{(c)} (\boldsymbol{\mathcal{X}}^x_{k,t|t-1} - \hat{\mathbf{x}}_{t|t-1})(\boldsymbol{\mathcal{X}}^x_{k,t|t-1} - \hat{\mathbf{x}}_{t|t-1})^T,$$

$$\boldsymbol{\mathcal{Y}}_{k,t|t-1} = \widetilde{\mathbf{h}}_t(\boldsymbol{\mathcal{X}}^x_{k,t|t-1}, \boldsymbol{\mathcal{X}}^n_{k,t}),$$

$$\hat{\mathbf{y}}_{t|t-1} = \sum_{k=0}^{4N} W_k^{(m)} \boldsymbol{\mathcal{Y}}_{k,t|t-1}.$$

(4) Measurement updates:

$$\mathbf{S}_{t|t-1} = \sum_{k=0}^{4N} W_k^{(c)} (\boldsymbol{\mathcal{Y}}_{k,t|t-1} - \hat{\mathbf{y}}_{t|t-1})(\boldsymbol{\mathcal{Y}}_{k,t|t-1} - \hat{\mathbf{y}}_{t|t-1})^H,$$

$$\widetilde{\mathbf{S}}_{t|t-1} = \sum_{k=0}^{4N} W_k^{(c)} (\boldsymbol{\mathcal{Y}}_{k,t|t-1} - \hat{\mathbf{y}}_{t|t-1})(\boldsymbol{\mathcal{Y}}_{k,t|t-1} - \hat{\mathbf{y}}_{t|t-1})^T,$$

$$\mathbf{E}_{t|t-1} = \sum_{k=0}^{4N} W_k^{(c)} (\boldsymbol{\mathcal{X}}^x_{k,t|t-1} - \hat{\mathbf{x}}_{t|t-1})(\boldsymbol{\mathcal{Y}}_{k,t|t-1} - \hat{\mathbf{y}}_{t|t-1})^H,$$

$$\widetilde{\mathbf{E}}_{t|t-1} = \sum_{k=0}^{4N} W_k^{(c)} (\boldsymbol{\mathcal{X}}^x_{k,t|t-1} - \hat{\mathbf{x}}_{t|t-1})(\boldsymbol{\mathcal{Y}}_{k,t|t-1} - \hat{\mathbf{y}}_{t|t-1})^T,$$

where the Kalman gains $\mathbf{K}_t$ and $\widetilde{\mathbf{K}}_t$ are

$$\mathbf{K}_t = \mathbf{E}_{t|t-1}\mathbf{P}_S^{-1} - \widetilde{\mathbf{E}}_{t|t-1}\mathbf{S}_{t|t-1}^{-*}\widetilde{\mathbf{S}}_{t|t-1}^{*}\mathbf{P}_S^{-1},$$

$$\widetilde{\mathbf{K}}_t = \widetilde{\mathbf{E}}_{t|t-1}\mathbf{P}_S^{-*} - \mathbf{E}_{t|t-1}\mathbf{S}_{t|t-1}^{-1}\widetilde{\mathbf{S}}_{t|t-1}\mathbf{P}_S^{-*},$$

then update posterior estimates

$$\hat{\mathbf{x}}_{t|t} = \hat{\mathbf{x}}_{t|t-1} + \mathbf{K}_t(\mathbf{y}_t - \hat{\mathbf{y}}_{t|t-1}) + \widetilde{\mathbf{K}}_t(\mathbf{y}_t - \hat{\mathbf{y}}_{t|t-1})^*,$$

$$\mathbf{P}_{t|t} = \mathbf{P}_{t|t-1} - \mathbf{E}_{t|t-1}\mathbf{K}_t^H - \widetilde{\mathbf{E}}_{t|t-1}\widetilde{\mathbf{K}}_t^H,$$

$$\widetilde{\mathbf{P}}_{t|t} = \widetilde{\mathbf{P}}_{t|t-1} - \mathbf{E}_{t|t-1}\widetilde{\mathbf{K}}_t^T - \widetilde{\mathbf{E}}_{t|t-1}\mathbf{K}_t^T.$$

Example 6.5.1. (Phase Demodulation Problem) Consider a scalar real random phase θ_t that is updated as

$$\theta_t = a\theta_{t-1} + bw_{t-1},\ t = 1, 2, ..., \tag{6.61}$$

where w_t is a real driving noise. So, the phase is real, and it evolves or jitters according to a first-order Markov sequence. The measurement in a quadrature demodulator is a noisy complex signal modulated by θ_t:

$$y_t = e^{i\theta_t} + n_t,\ t = 0, 1, ... \tag{6.62}$$

where each n_t is assumed to be a zero mean, scalar *complex* Gaussian random variable [41] with Hermitian variance R and complementary variance $\widetilde{R}$. Suppose $n_t = u_t + jv_t$, where u_t and v_t are correlated with variances R_{uu} and R_{vv}, respectively, and covariance R_{uv}. The complex correlation coefficient between n_t and n_t^* is

$$\rho = \frac{\widetilde{R}}{R} = \frac{R_{uu} - R_{vv} + 2jR_{uv}}{R_{uu} + R_{vv}}, \tag{6.63}$$

which describes the impropriety of n_t. When $|\rho| = 1$, n_t is maximally improper. In the following we let $R_{uu} = R_{vv}$ and set ρ by changing the value of R_{uv}. The signal-to-noise ratio

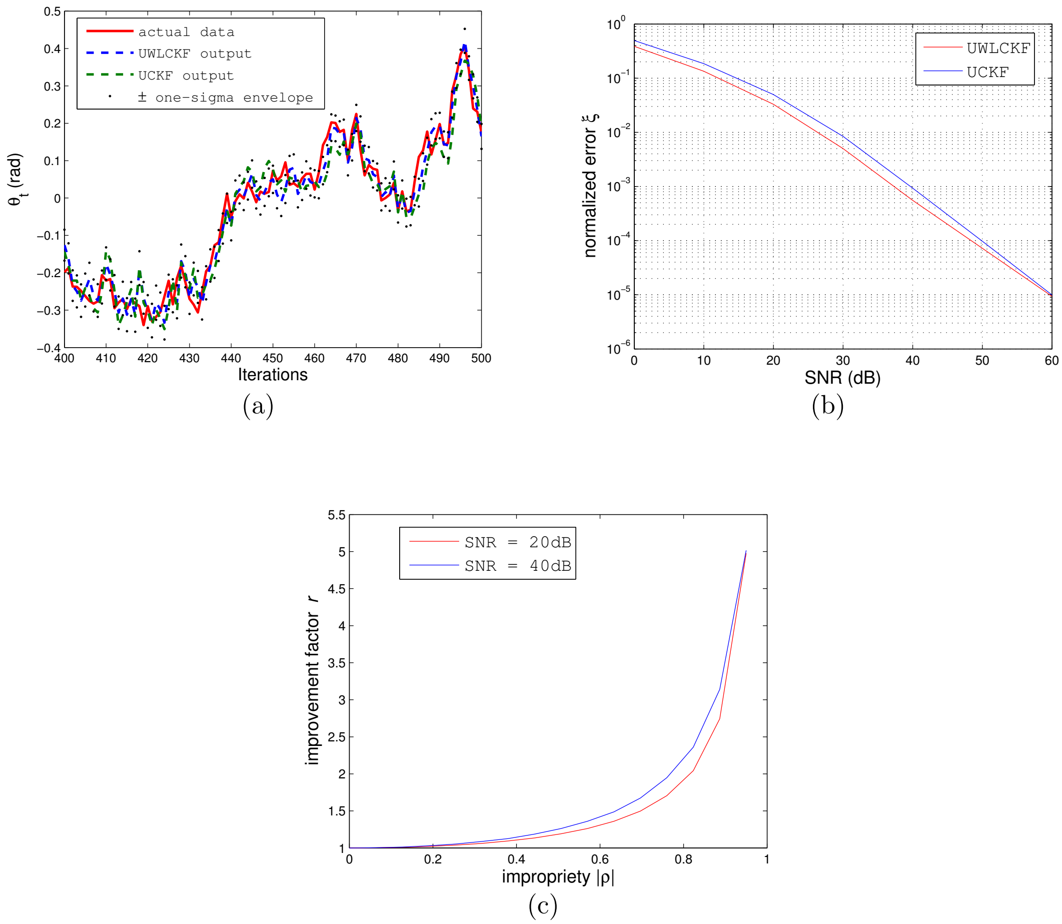

Figure 6.2: Comparison between UWLCKF and UCKF. (a) Phase estimated by UWLCKF at each iteration, SNR = 20dB, $|\rho| = 0.7$. (b) Normalized estimation error ξ of UWLCKF and UCKF vs SNRs, $|\rho| = 0.7$. (c) Performance improvement r of UWLCKF over UCKF vs impropriety of n_t.

at the receiver is $\text{SNR} = R^{-1}$. In simulation we set $a = 0.98$, $b = 0.05$. Each w_t is a standard mean zero and variance one Gaussian real random variable, independent of all others.

Fig. 6.2(a) draws the outputs of the UWLCKF over time at SNR = 20dB and $|\rho| = 0.7$. The widely linear Kalman gain for the UWLCKF is a 2 by 2 matrix and the estimate $\hat{\theta}_{t|t}$ is always real. It can be observed that for most iterations, the estimate $\hat{\theta}_{t|t}$ is close to the phase θ_t. Also the true θ_t is almost confined by the envelope $\hat{\theta}_{t|t} \pm \sqrt{P_{t|t}}$. As a benchmark, we are plotting the estimates of an unscented complex KF that assumes the noise to be proper. Unlike the UWLCKF above, the UCKF estimates θ_t from a real 2 by 1 measurement vector consisting of the real and imaginary part of y_t collected from dual channels. At each iteration the UCKF produces sigma points from the real mean vector $[\hat{\theta}_{t|t}\ \mu_w\ \mu_u\ \mu_v]^T = [\hat{\theta}_{t|t}\ 0\ 0\ 0]^T$ and covariance matrix $\mathbf{M} = diag(P_{t|t}, 1, R_u, R_v)$, and it has a 1 by 2 Kalman gain vector. It can be observed that at most iterations, the UCKF has larger estimation error than the UWLCKF.

Fig. 6.2(b) compares the performances of the UWLCKF and the UCKF. The complex correlation coefficient is $|\rho| = 0.7$. Define the normalized squared error as $\xi = ||\mathbf{e}||_2^2/||\boldsymbol{\theta}||_2^2$, where $\boldsymbol{\theta}$ and $\mathbf{e}$ are vectors consisting of phases and estimation errors in 500 iterations respectively. In the plot each ξ is computed by averaging 1000 Monte-Carlo simulations. It can be seen that in the low-medium SNR regime, UWLCKF requires about 2dB less SNR than the UCKF.

Fig. 6.2(c) shows the performance improvement of the UWLCKF over the UCKF vs the noise impropriety $|\rho|$ at different SNRs. We use the factor $r = \xi_{\text{UCKF}}/\xi_{\text{UWLCKF}}$ to evaluate the advantage of UWLCKF. The normalized squared error ξ_{UCKF} and ξ_{UWLCKF} are defined as above. Each r is computed by averaging 1000 Monte-Carlo simulations. For $|\rho| \geq 0.8$, the gain $r \geq 2$.

6.6 Conclusion

In this chapter we designed widely linear and unscented WL complex Kalman filters for complex noisy dynamical systems with improper states and noises. We show that WLCKFs may significantly improve on the performance of a CKF that ignores corresponding covariance. A simulation for real phase demodulation shows how an UWLCKF produces real estimates from complex baseband measurements and shows the improvement of its performance over an unscented complex KF that assumes proper states and noises.

CHAPTER 7

CONCLUSION

Active sensing is an sensing technology with numerous applications in science and engineering. Advances in sensor technology are providing active sensors that are increasingly agile both in their transmitters and receivers' capabilities. This enable arbitrary waveform illumination of the environment using increased degrees of freedoms, and processing of the scene return to form an image, estimate parameters, or detect targets.

Modern radars are increasingly being equipped with arbitrary waveform generators that enable the transmission of different waveforms across multiple degrees of freedoms: time, frequency, polarization, and aperture. This gives us the opportunity to revisit and extend the classical signal design for radar imaging. We developed a general framework for designing Doppler resilient illuminations through waveform coordination across time, frequency, and aperture. We showed that for a SISO radar, by properly coordinating the waveforms phase coded by complementary sequences, we can annihilate the range sidelobe of ambiguity function inside a modest Doppler interval, and hence bring out the weak targets from the range sidelobe of nearby strong reflectors. We extend such a Doppler resilience waveform design to the MIMO radar case. By properly coordinate the complementary space-time waveform components, the complementarity can be preserved inside a Doppler band around zero Doppler axis.

The advances in optical imaging also promise sophisticated illumination design and receiver design. Vast combinations of structure illumination and receive processing provide us opportunities to investigate the optical imaging methods with faster imaging speed and higher resolution. For optical imaging, we considered an optical imaging with a single-pixel detector. Compared to the 2-D detectors, a single detector can work in a broader band. The imaging approach utilizes a spatial structured illumination generated by an SLM or optical mask. We exploited compressive sensing (CS) as a principle for line-scanned imaging with single-pixel detector. We studied the robustness of CS to the misfocus effect. It turns out the CS design is reliable at moderate demagnification factors. However, at high demagnification factors, the reconstruction performance of CS design becomes highly sensitive even to small misfocus distance.

We exploited the Kalman filter as a powerful signal processing approach to deal with the sensing systems with dynamical state evolution and measurement acquisition. We reasoned that in the presence of impropriety of complex-valued random states or measurements, it is necessary to revisit the theory of conventional Kalman filters. We showed that through incorporating the widely linear processing with the knowledge of complementary covariances, we can develop a class of widely linear complex Kalman filters which better captures the second order statistical information of states/measurements, and hence leads to better performance in estimating the improper complex states.

REFERENCES

[1] P. M. Woodward, *Probability and Information Theory, with Applications to Radar.* McGraw-Hill, New York, 1953.

[2] J. Moyal, "Quantum mechanics as a statistical theory," *Proc. Camb. Phil. Soc.*, vol. 45, pp. 99–124, 1949.

[3] R. C. Heimiller, "Phase shift pulse codes with good periodic correlation properties," *IRE Trans. Inform. Theory*, vol. IT-7, pp. 254–257, Oct. 1961.

[4] R. L. Frank, "Poly-phase codes with good non-periodic correlation properties," *IEEE Trans. Inform. Theory*, p. 43, January 1963.

[5] D. C. Chu, "Polyphase codes with good periodic correlation properties," *IEEE Trans. Inform. Theory*, vol. IT-18, pp. 531–532, Jul. 1972.

[6] R. H. Barker, "Group synchronizing of binary digital sequences," in *Communication Theory* (W. Jackson, ed.), pp. 273–287, London: Butteworth, 1953.

[7] S. W. Golomb and R. A. Scholtz, "Generalized barker sequences," *IEEE Trans. Inform. Theory*, vol. IT-11, pp. 533–537, Oct. 1965.

[8] W. Rummer, "Clutter suppression by complex weighting of coherent pulse trains," *IEEE Trans. Aerosp. Electron. Syst.*, vol. AES-2, pp. 689–699, Nov. 1966.

[9] D. F. Delong and E. M. Hofstetter, "On the design of optimum radar waveforms for clutter rejection," *IEEE Trans. Inform. Theory*, vol. 13, pp. 454–463, Jul. 1967.

[10] D. Cochran, S. Suvorova, S. Howard, and W. Moran, "Waveform libraries: Measures of effectiveness for radar scheduling," *IEEE Signal Processing Magazine*, vol. 26, no. 1, pp. 12–21, 2009.

[11] R. Calderbank, S. D. Howard, and W. Moran, "Waveform diversity in radar signal processing," *IEEE Signal Processing Magazine*, vol. 26, no. 1, pp. 32–41, 2009.

[12] D. Cochran, "Waveform-agile sensing: Opportunities and challenges," in *Proc. IEEE Int. Conf. Acoustics, Speech, and Signal Process., Philadelphia*, Mar. 2005.

[13] S. D. Howard, A. R. Calderbank, and W. Moran, "A simple polarization diversity technique for radar detection," in *Proc. Second Int. Conf. Waveform Diversity and Design*, (Lihue, HI), Jan. 2006.

[14] S. D. Howard, A. R. Calderbank, and W. Moran, "A simple signal processing architecture for instantaneous radar polarimetry," *IEEE Trans. Inform. Theory*, vol. 53, pp. 1282–1289, Apr. 2007.

[15] A. R. Calderbank, S. D. Howard, W. Moran, A. Pezeshki, and M. Zoltowski, "Instantaneous radar polarimetry with multiple dually-polarized antennas," in *Conf. Rec. Fortieth Asilomar Conf. Signals, Syst., Comput.*, (Pacific Grove, CA), pp. 757–761, Oct. 29-Nov. 1 2006.

[16] A. Pezeshki, A. R. Calderbank, W. Moran, and S. D. Howard, "Doppler resilient Golay complementary waveforms," *IEEE Trans. Inform. Theory*, vol. 54, pp. 4254–4266, Sep. 2008.

[17] Y. Chi, A. Pezeshki, and R. Calderbank, "Complementary waveforms for sidelobe suppression and radar polarimetry," in *Principles of Waveform Diversity and Design* (M. Wicks, E. Mokole, S. Blunt, R. Schneible, and V. Amuso, eds.), SciTech Publishing, 2011.

[18] S. J. Searle and S. D. Howard, "A novel polyphase code for sidelobe suppression," in *Proc. Int. Waveform Diversity and Design Conf.*, (Pisa, Italy), June 2007.

[19] S. J. Searle and S. D. Howard, "A novel nonlinear technique for sidelobe suppression in radar," in *Proc. Int. Conf. Radar Systems*, (Edinburgh, UK), Oct. 2007.

[20] S. J. Searle, S. D. Howard, and W. Moran, "On the formation of composite ambiguity functions with frequency separated golay coded pulses," *IEEE Trans. Aeros. and Elctr. Systems*, vol. 45, pp. 1580–1597, Oct. 2009.

[21] J. Li and P. Stoica, *MIMO Radar Signal Processing.* New Jersey: Wiley, 2009.

[22] D. R. Fuhrmann, J. P. Browning, and M. Rangaswamy, "Signaling strategies for the hybrid MIMO phased-array radar," *IEEE Trans. Signal Proc.*, vol. 4, pp. 66–78, Sept. 2010.

[23] B. Friedlander, "Waveform design for MIMO radars," *IEEE Trans. Aeros. and Elctr. Systems*, vol. 43, pp. 1227–1238, Jul. 2007.

[24] A. Leshem, O. Naparstek, and A. Nehorai, "Information theoretic adaptive radar waveform design for multiple extended targets," *IEEE Journal of Selected Topics in Signal Proc.*, vol. 1, pp. 42–55, Jun. 2007.

[25] D. Lovell, "Electro-optic position indicator system," in *U.S. Patent 2,997,699*, Aug. 1961.

[26] J. E. Greivenkamp, "Color dependent optical prefilter for the suppression of aliasing artifacts," *Appl. Opt.*, vol. 29, pp. 676 – 684, Feb. 1990.

[27] E. R. Dowski and W. T. Cathey, "Extended depth of field through wave-front coding," *Appl. Opt.*, vol. 34, pp. 1859 – 1866, Apr. 1995.

[28] M. E. Gehm, S. T. McCain, N. P. Pitsianis, D. J. Brady, P. Potuluri, and M. E. Sullivan, "Static two-dimensional aperture coding for multimodal, multiplex spectroscopy," *Appl. Opt.*, vol. 45, pp. 2965 – 2974, May 2006.

[29] G. Futia, P. Schlup, D. G. Winters, and R. A. Bartels, "Spatially-chirped modulation imaging of absorption and fluorescent objects on single-element optical detector," *Optics Express*, vol. 19, pp. 1626 – 1640, Jan.

[30] R. Willett, R. Marcia, and J. Nichols, "Compressed sensing for practical optical systems: a tutorial," *Opt. Engr.*, vol. 50, no. 7, p. 072601, 2011.

[31] W. Dang, A. Pezeshki, S. D. Howard, W. Moran, and A. R. Calderbank, "Coordinating complementary waveforms for sidelobe suppression," in *Forty-fifth Asilomar Conf. Signals, Syst., Comput,*, (Pacific Grove, CA), Nov 6-9 2011.

[32] W. Dang, A. Pezeshki, S. D. Howard, and W. Moran, "Coordinating complementary waveforms across time and frequency," in *IEEE Statistical Signal Proc. Workshop*, (Ann Arbor, MI), Aug 5-8 2012.

[33] J. S. Sanders, R. G. Driggers, C. E. Halford, and S. T. Griffin, "Imaging with frequency-modulated reticles," *Opt. Eng.*, vol. 30, pp. 1720 – 1724, 1991.

[34] Y. Chi, L. L. Scharf, A. Pezeshki, and A. R. Calderbank, ""sensitivity to basis mismatch in compressed sensing," in *Proc. ICCASP.*, 2010.

[35] J. R. Treichler and B. G. Agee, "A new approach to multipath correction of constant modulus signals," *IEEE Trans. Acoustics, Speech, and Signal Proc.*, vol. ASSP-31, pp. 459–472, Apr. 1983.

[36] Y. Xia, S. C. Douglas, and D. P. Mandic, "Adaptive frequency estimation in smart grid applications," *IEEE Signal Process. Magzine*, pp. 44–54, Sep. 2012.

[37] J. Zhong, J. Dauwels, M. A. Vazquez, and L. Waller, "Sparse acekf for phase reconstruction," *Opt. Express*, vol. 21, pp. 18125–18137, Jul. 2013.

[38] C. Stanciu, J. Benesty, C. Paleologu, T. Gansler, and S. Ciochina, "A widely linear model for stereophonic acoustic echo cancellation," *Signal Process.*, vol. 93, pp. 511–516, Feb. 2013.

[39] B. Picinbono and P. Bondon, "Second-order statistics of complex signals," *IEEE Trans. on Signal Processing*, vol. 45, pp. 411–420, Feb. 1997.

[40] P. J. Schreier and L. L. Scharf, "Second-order analysis of improper complex random vectors and processes," *IEEE Trans. on Signal Processing*, vol. 51, pp. 714–725, Mar. 2003.

[41] P. J. Schreier and L. L. Scharf, *Statistical Signal Processing of Complex-Valued Data: The Theory of Improper and Noncircular Signals.* Cambridge University Press, 2010.

[42] E. Ollila and V. Koivunen, "Generalized complex elliptical distributions," in *Sensor Array and Multichannel Signal Proc. Workshop*, pp. 460–464, Jul. 2004.

[43] B. Picinbono and P. Chevalier, "Widely linear estimation with complex data," *IEEE Trans. on Signal Processing*, vol. 43, pp. 2030–2033, Aug. 1995.

[44] R. E. Kalman, "A new approach to linear filtering and prediction problems," *Trans. of the ASME-Journal of Basic Engineering*, pp. 35–45, Mar. 1960.

[45] F. Daum, "Nonlinear filters: Beyond the Kalman filter," *IEEE Aerospace and Electronics Systems Magazine*, pp. 57–69, 2005.

[46] S. J. Julier and J. K. Uhlmann, "Unscented filtering and nonlinear estimation," *Proc. IEEE*, vol. 92, no. 3, pp. 401–422, 2004.

[47] D. J. Rabideau, "Adaptive MIMO radar waveforms," in *IEEE Radar Conf.*, (Rome, Italy), pp. 1–6, May 2008.

[48] J. Li, L. Xu, P. Stoica, K. W. Forsythe, and D. W. Bliss, "Range compression and waveform optimization for MIMO radar: A Cramer-Rao bound based study," *IEEE Trans. Signal Proc.*, vol. 56, pp. 218–232, Jan. 2008.

[49] T. Higgins, S. D. Blunt, and A. K. Shackelford, "Space-range adaptive processing for waveform-diverse radar imaging," in *IEEE Radar Conf.*, (Washington, DC), pp. 321–326, 2010.

[50] J. Benedetto and J. J. Donatelli, "Ambiguity function and frame-theoretic properties of periodic zero-autocorrelation waveforms," *IEEE Journal of Selected Topics in Signal Proc.*, vol. 1, pp. 6–20, Jun. 2007.

[51] D. R. Fuhrmann and G. S. Antonio, "Transmit beamforming for MIMO radar systems using signal cross-correlation," *IEEE Trans. on Aero. and Elect. Systems*, vol. 44, pp. 171–186, Jan. 2008.

[52] S. P. Sira, A. Papandreou-Suppappola, and D. Morrell, "Dynamic configuration of time-varying waveforms for agile sensing and tracking in clutter," *IEEE Trans. on Signal Proc.*, vol. 55, pp. 3207–3217, Jul. 2007.

[53] R. Niu, P. Willett, and Y. Bar-Shalom, "Tracking considerations in selection of radar waveform for range and range-rate measurements," *IEEE Trans. on Aero. and Elect. Systems*, vol. 38, pp. 467–487, Apr. 2002.

[54] G. Dietl, J. Wang, P.Ding, M. Zoltowski, D. J. Love, and W. Utschick, "Hybrid transmitwaveform design based on beamforming and orthogonal space-time block coding," in *IEEE Int. Conf. on Acoustics, Speech, and Signal Proc.*, May. 2005.

[55] M. I. Skolnik, *Introduction to Radar Systems.* McGraw-Hill, 3rd ed. ed., 2001.

[56] M. R. Bell, "Information theory and radar waveform design," *IEEE Transactions on Information Theory*, vol. 39, pp. 1578–1597, September 1993.

[57] A. O. Hero, C. M. Kreucher, and D. Blatt, "Information theoretic approaches to sensor management," in *Foundations and Applications of Sensor Management* (A. O. Hero, D. C. nón, D. Cochran, and K. Kastella, eds.), Springer-Verlag, 2007.

[58] W. Moran, S. Suvorova, and S. Howard, "Sensor scheduling in radar," in *Foundations and Applications of Sensor Management* (A. O. Hero, D. C. nón, D. Cochran, and K. Kastella, eds.), Springer-Verlag, 2007.

[59] S. Suvorova, S. D. Howard, and W. Moran, "Waveform libraries for radar tracking applications," in *Proc. First Int. Conf. Waveform Diversity and Design*, (Edinburgh, UK), Nov. 2004.

[60] S. Suvorova, S. Howard, and W. Moran, "Multi step ahead beam and waveform scheduling for tracking of manoeuvering targets in clutter," in *Proc. IEEE Int. Conf. Acoustics, Speech, and Signal Process., Philadelphia*, no. 5, pp. 889–892, Mar. 2005.

[61] S. Suvorova, S. Howard, and W. Moran, "Beam and waveform scheduling approach to combined radar surveillance and tracking-the paranoid tracker," in *Proc. 2nd Int. Conf. Waveform Diversity and Design, Kauai, Hawaii*, Jan. 2006.

[62] M. J. E. Golay, "Complementary series," *IRE Trans. Inform. Theory*, vol. 7, pp. 82–87, April 1961.

[63] G. R. Welti, "Quaternary codes for pulsed radar," *IRE Trans. Inform. Theory*, vol. IT-6, pp. 400–408, June 1960.

[64] C. C. Tseng and C. L. Liu, "Complementary sets of sequences," *IEEE Trans. Inform. Theory*, vol. IT-18, pp. 644–652, Sep. 1972.

[65] J. P. Allouche and J. Shallit, "The ubiquitous Prouhet-Thue-Morse sequence," in *Sequences and their applications, Proc. SETA'98* (T. H. C. Ding and H. Niederreiter, eds.), pp. 1–16, Springer Verlag, 1999.

[66] N. Levanon and E. Mozeson, *Radar Signals.* New York: Wiley, 2004.

[67] H. Oruç, "LU factorization of the vandermonde matrix and its applications," *Applied Math. Letters*, vol. 20, pp. 982–987, Feb. 2007.

[68] M. E. A. Mikkawy, "Explicit inverse of a generalized vandermonde matrix," *Applied Math. and Comp.*, vol. 146, pp. 643–651, Dec. 2003.

[69] D. E. Knuth, *The art of computer programming.* Addison-Wesley, 1968.

[70] M. Abramowitz and I. A. Stegun, *Handbook of mathematical functions with formulas, graphs, and mathematical tables.* U.S. Department of Commerce, 1972.

[71] P. Stoica and R. Moses, *Introduction to spectral analysis.* Prentice-Hall, 1997.

[72] H. V. Trees, *Detection, Estimation, and Modulation Theory, Part III.* John Wiley, 1971.

[73] A. Ghosh and E. Ertin, "Waveform agile sensing for tracking with collaborative radar networks," in *IEEE Radar Conf.*, May. 2010.

[74] S. D. Howard, A. R. Calderbank, and W. Moran, "The finite Heisenberg-Weyl groups in radar and communications," *EURASIP Journal on Applied Signal Processing*, Article ID 85685, 2006.

[75] P. P. Vaidyanathan and P. Pal, "Sparse sensing with co-prime samplers and arrays," *IEEE Trans. Signal Proc.*, vol. 59, pp. 573–586, Feb. 2011.

[76] D. Fhurmann and G. S. Antonio, "Transmit beamforming for MIMO radar systems using signal cross-correlation," *IEEE Trans. Aerosp. Electron. Syst.*, vol. 44, pp. 171–186, Jan. 2008.

[77] D. Fhurmann, J. P. Browning, and M. Rangaswamy, "Signaling strategies for the hybrid MIMO phased-array radar," *IEEE J. Select. Topics Signal Proc.*, vol. 4, pp. 66–78, Feb. 2010.

[78] B. M. Keel, J. M. Baden, and T. H. Heath, "A comprehensive review of quasi-orthogonal waveforms," in *Proc. IEEE Radar Conf*, pp. 122–127, Apr. 2007.

[79] X. Song, S. Zhou, and P. Willett, "Reducing the waveform cross correlation of MIMO radar with space-time coding," *IEEE Trans. Signal Proc.*, vol. 8, pp. 4213–4224, Aug. 2010.

[80] C. Y. Chen and P. P. Vaidyanathan, "Mimo radar waveform optimization with prior information of the extended clutter and target," *IEEE Trans. Sig. Proc.*, vol. 57, pp. 3533–3544, Sep. 2009.

[81] T. R. Qureshi, M. D. Zoltowski, A. R. Calderbank, and A. Pezeshki, "Unitary design of radar waveform diversity sets," *Digital Signal Process.*, Oct. 2010.

[82] T. R. Qureshi, M. D. Zoltowski, and A. R. Calderbank, "A novel approach to doppler compensation and estimation for multiple targets in mimo radar with unitary waveform matrix scheduling," in *Proc. IEEE Int. Conf. Acoustics, Speech, and Signal Process., Kyoto, Japan*, pp. 2473–2476, Mar. 2012.

[83] T. R. Qureshi and W. D. Zoltowski, "Adaptive high resolution MIMO radar with unitary waveform matrix scheduling," in *Proc. IEEE Radar Conf., Ottawa, Canada*, pp. 1–5, Apr. 2013.

[84] U. K. Majumder, M. R. Bell, and M. Rangaswamy, "A novel approach for designing diversity radar waveforms that are orthogonal on both transmit and receive," in *Proc. IEEE Radar Conf., Ottawa, Canada*, pp. 1–5, Apr. 2013.

[85] R. Carriles, D. N. Schafer, K. E. Sheetz, J. J. Field, R. Cisek, V. Barzda, A. W. Sylvester, and J. A. Squier, "Invited review article: imaging techniques for harmonic and multiphoton absorption fluorescence microscopy," *Rev. Sci. Instrum.*, vol. 80, p. 081101, 2009.

[86] S. Blonski and T. A. Kowalewski, "Piv analysis of turbulent flow in a micro-channel," *Theor. Appl. Mech.*, vol. 45, p. 489C503, 2007.

[87] R. Heintzmann and P. A. Benedetti, “High-resolution image reconstruction in fluorescence microscopy with patterned excitation,” *Appl. Opt.*, vol. 45, pp. 5037 – 5045, 2006.

[88] J. Romberg, “Imaging via compressive sampling,” *IEEE Signal Process. Mag.*, vol. 25, pp. 14 – 20, Mar. 2008.

[89] J. H. Shapiro, “Computational ghost imaging,” *Phys. Rev. A*, vol. 78, p. 061802, 2008.

[90] J. J. Art and M. B. Goodman, “Rapid-scanning confocal microscopy,” *Methods in Cell Biology*, vol. 38, p. 47C77, 1993.

[91] Y. Barad, H. Eisenberg, M. Horowitz, and Y. Silberberg, “Nonlinear scanning laser microscopy by third harmonic generation,” *Appl. Phys. Lett.*, vol. 70, pp. 922 – 924, 1997.

[92] E. J. Candès and T. Tao, “Decoding by linear programming,” *IEEE Trans. Inform. Theory*, vol. 51, pp. 4203 – 4215, Dec. 2005.

[93] E. J. Candès, J. Romberg, and T. Tao, “Robust uncertainty principles: Exact signal reconstruction from highly incomplete frequency information,” *IEEE Trans. Inform. Theory*, vol. 52, pp. 489 – 509, Feb. 2006.

[94] D. L. Donoho, “Compressed sensing,” *IEEE Trans. Inform. Theory*, vol. 52, no. 4, pp. 1289 – 1306, 2006.

[95] E. J. Candès, “The restricted isometry property and its implications for compressed sensing,” *Acad. des Sci.*, vol. 1, no. 346, pp. 589 – 592, 2008.

[96] Z. Harmany, R. Marcia, and R. Willett, “Sparse poisson intensity reconstruction algorithms,” in *Proc. IEEE Workshop on Statist. Signal Process.*, 2009.

[97] M. Raginsky, R. M. Willett, Z. T. Harmany, and R. F. Marcia, “Compressed sensing performance bounds under poisson noise,” *IEEE Trans. Signal Process.*, vol. 58, pp. 3990 – 4002, Aug. 2010.

[98] M. A. Herman and T. Strohmer, “General deviants: An analysis of perturbations in compressed sensing,” *IEEE J. Sel. Topics in Signal Process.: Special Issue on Compressive Sens*, vol. 4, pp. 342 – 349, Apr. 2010.

[99] Y. Chi, L. L. Scharf, A. Pezeshki, and A. R. Calderbank, “Sensitivity to basis mismatch in compressed sensing,” *IEEE Trans. Signal Process.*, vol. 59, pp. 2182 – 2284, May. 2011.

[100] H. Zhu, G. Leus, and G. B. Giannakis, “Sparsity-cognizant total least-squares for perturbed compressive sampling,” *IEEE Trans. Signal Process.*, vol. 59, pp. 2002 – 2016, May. 2011.

[101] M. Gu, *Advanced Optical Imaging Theory.* Springer-Verlag, 2000.

[102] A. Yariv, *Quantum Electronics*. Wiley, 1989.

[103] Nikon-MicroscopyU, "Depth of field and depth of focus," *Available: http://www.microscopyu.com/articles/formulas/formulasfielddepth.html*.

[104] L. L. Scharf, E. K. P. Chong, A. Pezeshki, and J. Luo, "Compressive sensing and sparse inversion in signal processing: Cautionary notes," in *7th Workshop on Defence Applications of Signal Processing (DASP)*, (Coolum, Queensland, Australia), Jul. 2011.

[105] L. L. Scharf, E. K. P. Chong, A. Pezeshki, and J. Luo, "Sensitivity considerations in compressed sensing," in *Forty-fifth Asilomar Conf. Signals, Syst., Comput.*, (Pacific Grove, CA), Nov. 2011.

[106] D. P. Mandic and S. L. Goh, *Complex Valued Nonlinear Adaptive Filters: Noncircularity, Widely Linear and Neural Models*. Wiley, 2009.

[107] A. S. Aghaei, K. N. Plataniotis, and S. Pasupathy, "Maximum likelihood binary detection in improper complex Gaussian noise," in *Int. Conf. on Acoustics, Speech, and Signal Proc.*, pp. 3209–3212, Mar. 2008.

[108] P. J. Schreier, L. L. Scharf, and C. T. Mullis, "Detection and estimation of improper complex random signals," *IEEE Trans. on Information Theory*, vol. 51, pp. 306–311, Jan. 2005.

[109] W. H. Gerstacker, R. Schober, and A. Lampe, "Equalization with widely linear filtering," in *IEEE ISIT2001*, p. 265, Jun. 2001.

[110] Y. Xia, B. Jelfs, M. V. Hulle, J. C. Prncipe, and D. P. Mandic, "An augmented echo state network for nonlinear adaptive filtering of complex noncircular signals," *IEEE Trans. on Neural networks*, vol. 22, pp. 74–83, Jan. 2011.

[111] T. Kailath, A. H. Sayed, and B. Hassibi, *Linear Estimation*. Prentice Hall, 2000.

[112] J. Walrand, "Ee226a - summary of lecture 13 and 14 Kalman filter: Convergence," *Available: http://robotics.eecs.berkeley.edu/ wlr/226aF05/L13.pdf*.

[113] A. Hjorungnes and D. Gesbert, "Complex-valued matrix differentiation: techniques and key results," *IEEE Trans. on Signal Process.*, vol. 5, pp. 2740–2746, Jun. 2007.

[114] S. L. Goh and D. P. Mandic, "An augmented extended Kalman filter algorithm for complex-valued recurrent neural networks," in *Int. Conf. on Acoustics, Speech and Signal Proc.*, vol. 5, pp. 561–564, May. 2006.

[115] E. A. Wan and R. van der Merwe, "The unscented Kalman filter for nonlinear estimation," in *Adaptive Systems for Signal Proc., Comm., and Control Symp.*, pp. 153–158, Oct. 2000.

[116] T. Høholdt, H. E. Jensen, and J. Justesen, "Aperiodic correlations and the merit factor of a class of binary sequences," *IEEE Trans. Inform. Theory*, vol. IT-31, pp. 549–552, Jul. 1985.

APPENDIX A

PROOF OF THEOREM 2.3.1

Proof: In [116] it has been shown that m_c can be bounded by $L^{0.9}$. At sufficiently small θ, the spectrum $S_{\mathcal{P},\mathcal{Q}}$ can be approximated by

$$\begin{aligned} S_{\mathcal{P},\mathcal{Q}}(\theta) &\approx \frac{S_{\mathcal{P},\mathcal{Q}}^{(M+1)}(0)}{(M+1)!}\theta^{M+1} \\ &= \frac{\sum_{n=0}^{N-1} n^{M+1}(-1)^{p[n]}q[n]}{(M+1)!}\theta^{M+1}. \end{aligned} \tag{A.1}$$

Applying Cauchy-Schwartz inequality, we have

$$\left|\sum_{n=0}^{N-1} n^{M+1}(-1)^{p[n]}q[n]\right|^2 \leq \sum_{n=0}^{N-1} n^{2(M+1)}||\mathbf{q}||_2^2. \tag{A.2}$$

And it's ready to see that

$$\begin{aligned} \sum_{n=0}^{N-1} n^{2(M+1)} &= N^{2M+3}\sum_{n=0}^{N-1}(\frac{n}{N})^{2(M+1)} \cdot \frac{1}{N} \\ &\leq N^{2M+3}\int_0^1 x^{2(M+1)}dx \\ &= \frac{N^{2M+3}}{2M+3}. \end{aligned} \tag{A.3}$$

This yields that

$$\begin{aligned} PPSR_{\mathcal{P},\mathcal{Q}}(\theta) &= (\frac{L}{m_c})^2 \frac{||\mathbf{q}||_1^2}{\left|\frac{S_{\mathcal{P},\mathcal{Q}}^{(M+1)}(0)}{(M+1)!}\theta^{M+1}\right|^2} \\ &\geq L^{0.2}\frac{||\mathbf{q}||_1^2}{||\mathbf{q}||_2^2}\frac{[(M+1)!]^2(2M+3)}{N^{2M+3}}\theta^{-2(M+1)} \\ &\geq L^{0.2}\frac{[(M+1)!]^2(2M+3)}{N^{2M+3}}\theta^{-2(M+1)} \end{aligned} \tag{A.4}$$

APPENDIX B

PROOF OF THEOREM 2.3.3

Proof: (1) For PTM design, the amplitude of $M_{\mathcal{Q}}(\theta)$ can be derived as

$$|M_{\mathcal{Q}}(\theta)| = \Big|\sum_{n=0}^{N-1} e^{jn\theta}\Big| = \left|\frac{\sin\frac{N\theta}{2}}{\sin\frac{\theta}{2}}\right|, \tag{B.1}$$

which stands for the amplitude of Dirichlet kernel. Since $\mathcal{Q}$ is an all 1 sequence, $\beta_{\mathcal{P},\mathcal{Q}} = 1/N$. The spectra $\mathcal{M}_{\mathcal{Q}}(\theta)$ is

$$\mathcal{M}_{\mathcal{Q}}(\theta) = \frac{\sin^2\frac{N\theta}{2}}{\sin^2\frac{\theta}{2}}, \tag{B.2}$$

whose zero-crossings nearest $\theta = 0$ are $\theta = \pm\frac{2\pi}{N}$. Thus for large N the value of $\gamma_{\mathcal{P},\mathcal{Q}}/2$ shall be very small such that $\sin(\gamma_{\mathcal{P},\mathcal{Q}}/2) \approx \gamma_{\mathcal{P},\mathcal{Q}}/2$. Note $M_{\mathcal{Q}}(0) = N^2$. Let $\mathcal{M}_{\mathcal{Q}}(\theta) = \frac{1}{2}\mathcal{M}_{\mathcal{Q}}(0)$, then it follows that

$$\sin\frac{N\theta}{2} \approx \frac{N\theta}{2\sqrt{2}}. \tag{B.3}$$

Thus $N\theta/2\sqrt{2}$ can be approximated by the fixed point of function $\sin(\sqrt{2}x)$, say θ_0. This yields $\gamma_{\mathcal{P},\mathcal{Q}} = \sqrt{2}\theta_0/N$. One can readily check that the envolope of $\mathcal{M}_{\mathcal{Q}}(\theta)$ is $\csc^2(\theta/2)$. And

$$\begin{aligned} SL_{\mathcal{P},\mathcal{Q}} &= \frac{1}{\mathcal{M}_{\mathcal{Q}}(0)}\frac{d}{d\theta}\csc^2(\theta/2)\Big|_{\theta=\gamma_{\mathcal{P},\mathcal{Q}}/2} \\ &= -\frac{2}{N^2}\csc^2(\gamma_{\mathcal{P},\mathcal{Q}}/4)\cot(\gamma_{\mathcal{P},\mathcal{Q}}/4) \\ &\approx -\frac{128}{N^2\gamma_{\mathcal{P},\mathcal{Q}}^3} \\ &= -\frac{32\sqrt{2}N}{\theta_0^3}. \end{aligned} \tag{B.4}$$

(2) For Binomial design, $|M_{\mathcal{Q}}(\theta)|$ is

$$\begin{aligned} |M_{\mathcal{Q}}(\theta)| &= \left|\sum_{n=0}^{N-1}\binom{N-1}{n}e^{jn\theta}\right| \\ &= |(1+e^{j\theta})^{N-1}| \\ &= 2^{N-1}\Big|\cos\frac{\theta}{2}\Big|^{N-1}, \end{aligned} \tag{B.5}$$

Since $q[n] = \binom{N-1}{n}$ for $n = 0, 1, ..., N-1$, we have

$$\sum_{n=0}^{N-1} q[n] = \sum_{n=0}^{N-1}\binom{N-1}{n} = 2^{N-1}, \tag{B.6}$$

and

$$\sum_{n=0}^{N-1} q[n]^2 = \sum_{n=0}^{N-1} \binom{N-1}{n}^2 = \binom{2(N-1)}{N-1} \approx \frac{4^{N-1}}{\sqrt{\pi(N-1)}} \tag{B.7}$$

for large N. Therefore $\beta_{\mathcal{P},\mathcal{Q}} = \mathcal{O}(N^{-1/2})$. The spectrum $\mathcal{M}_{\mathcal{Q}}(\theta)$ is

$$\mathcal{M}_{\mathcal{Q}}(\theta) = 4^{N-1} \cos^{2(N-1)}(\theta/2). \tag{B.8}$$

Let $\mathcal{M}_{\mathcal{Q}}(\theta) = \frac{1}{2}\mathcal{M}_{\mathcal{Q}}(0)$, then it follows that $\cos(\gamma_{\mathcal{P},\mathcal{Q}}/4) = (1/2)^{\frac{1}{2(N-1)}}$. For large N we have

$$\sin(\gamma_{\mathcal{P},\mathcal{Q}}/4) = \sqrt{1 - (1/4)^{\frac{1}{2(N-1)}}} \approx \sqrt{2}\sqrt{1 - (1/2)^{\frac{1}{2(N-1)}}}, \tag{B.9}$$

thus

$$\gamma_{\mathcal{P},\mathcal{Q}} \approx 4\sqrt{2}\sqrt{1 - (1/2)^{\frac{1}{2(N-1)}}}. \tag{B.10}$$

For small θ, the Taylor expansion shows that $(1/2)^{\theta} \approx 1 - \ln 2 \cdot \theta$. Therefore $\gamma_{\mathcal{P},\mathcal{Q}}$ can be approximated as

$$\gamma_{\mathcal{P},\mathcal{Q}} \approx 4\sqrt{\ln 2}\sqrt{\frac{1}{N-1}}. \tag{B.11}$$

Since the envolope of $\mathcal{M}_{\mathcal{Q}}(\theta)$ is itself, we have

$$\begin{aligned} SL_{\mathcal{P},\mathcal{Q}} &= \frac{d}{d\theta} \cos^{2(N-1)}(\theta/2)\bigg|_{\theta=\gamma_{\mathcal{P},\mathcal{Q}}/2} \\ &= -2(N-1)\sin(\gamma_{\mathcal{P},\mathcal{Q}}/4)\cos^{(2N-3)}(\gamma_{\mathcal{P},\mathcal{Q}}/4) \\ &\approx -2(N-1) \cdot \frac{\gamma_{\mathcal{P},\mathcal{Q}}}{4} \cdot \big(\frac{1}{4}\big)^{\frac{2N-3}{2N-2}} \\ &\approx -\frac{\sqrt{\ln 2}}{2}\sqrt{N-1}. \end{aligned} \tag{B.12}$$

APPENDIX C

PROOF OF THEOREM 2.4.1

Proof: This Theorem can be proved by inclusion. It is obvious that the Theorem is true for $m = 1$ ($D = 2$) by earlier discussion. Now suppose for $D = 2^{m-1}$, $m \geq 2$, the length-N^{m-1} sequences $\widetilde{\mathcal{P}}_0$ and $\widetilde{\mathcal{Q}}$ achieve M-th order nulls of the spectrum $S_{\widetilde{\mathcal{P}}_0,\widetilde{\mathcal{Q}},1}(\theta), \ldots, S_{\widetilde{\mathcal{P}}_0,\widetilde{\mathcal{Q}},2^{m-1}}(\theta)$. When $D = 2^m$, for even r between 0 and $2^m - 1$, we have $\omega^{r2^{m-1}} = 1$. Then by construction of the length-N^m sequences $\mathcal{P}$ and $\mathcal{Q}$, $S_{\mathcal{P},\mathcal{Q},r}(\theta)$ can be written by

$$\begin{aligned}
S_{\mathcal{P},\mathcal{Q},r}(\theta) &= \sum_{k=0}^{N-1}\Bigg(\sum_{\substack{n=0 \\ p'_k=0}}^{N^{m-1}-1} \omega^{r\widetilde{p}_{0,n}} q'_k \widetilde{q}_n e^{j(n+kN^{m-1})\theta} + \sum_{\substack{n=0 \\ p'_k=1}}^{N^{m-1}-1} \omega^{r(\widetilde{p}_{0,n}+2^{m-1})} q'_k \widetilde{q}_n e^{jn+kN^{m-1}\theta} \Bigg) \\
&= \sum_{k=0}^{N-1} q'_k e^{jkN^{m-1}\theta} \sum_{n=0}^{N^{t-1}-1} (\omega^2)^{r\widetilde{p}_{0,n}/2} \widetilde{q}_n e^{jn\theta} \\
&= \sum_{k=0}^{N-1} q'_k e^{jkN^{m-1}\theta} S_{\widetilde{\mathcal{P}}_0,\widetilde{\mathcal{Q}},\frac{r}{2}}(\theta).
\end{aligned} \tag{C.1}$$

Since $\frac{r}{2}$ goes through 1 to $2^{m-1} - 1$, each $S_{\widetilde{\mathcal{P}}_0,\widetilde{\mathcal{Q}},\frac{r}{2}}(\theta)$ has a M-th order null at $\theta = 0$ and hence so does $S_{\mathcal{P},\mathcal{Q},r}(\theta)$.

For odd r, note $\omega^{r2^{m-1}} = -1$. Thus $S_{\mathcal{P},\mathcal{Q},r}(\theta)$ can be written by

$$\begin{aligned}
S_{\mathcal{P},\mathcal{Q},r}(\theta) &= \sum_{k=0}^{N-1}\Bigg(\sum_{\substack{n=0 \\ p'_k=0}}^{N^{m-1}-1} \omega^{r\widetilde{p}_{0,n}} q'_k \widetilde{q}_n e^{j(n+kN^{m-1})\theta} + \sum_{\substack{n=0 \\ p'_k=1}}^{N^{m-1}-1} \omega^{r(\widetilde{p}_{0,n}+2^{m-1})} q'_k \widetilde{q}_n e^{jn+kN^{m-1}\theta} \Bigg) \\
&= \sum_{n=0}^{N^{m-1}-1} \omega^{r\widetilde{p}_{0,n}} \widetilde{q}_n e^{jn\theta} \sum_{k=0}^{N-1} (-1)^{p'_k} q'_k e^{jkN^{m-1}\theta} \\
&= \sum_{n=0}^{N^{m-1}-1} \omega^{r\widetilde{p}_{0,n}} \widetilde{q}_n e^{jn\theta} S_{\mathcal{P}',\mathcal{Q}'}(N^{m-1}\theta),
\end{aligned} \tag{C.2}$$

therefore each $S_{\mathcal{P},\mathcal{Q},r}(\theta)$ has a M-th order null at $\theta = 0$.

APPENDIX D

PROOF OF LEMMA 4.6.1

Proof: At $K = 1$, matrices $\mathbf{C}_{2,0}[k]$ and $\mathbf{C}_{2,1}[k]$ are

$$\mathbf{C}_{2,0}[k] = \begin{bmatrix} C_{xx}[k] & C_{xy}[k] \\ C_{yx}[k] & C_{yy}[k] \end{bmatrix}, \ \mathbf{C}_{2,1}[k] = \begin{bmatrix} C_{yy}[k] & -C_{xy}[k] \\ -C_{yx}[k] & C_{xx}[k] \end{bmatrix}.$$

Thus $a_0\mathbf{C}_{2,0}[k]+a_1\mathbf{C}_{2,1}[k] = \mathbf{0}$, $\forall k$, requires that $a_0+a_1 = 0$ and $a_0-a_1 = 0$, i.e., $a_0 = a_1 = 0$.

Now suppose at $K = p$, we have that

$$\sum_{d=0}^{2^p-1} a_d \mathbf{C}_{2^p,d}[k] = \mathbf{0}, \ \forall 1 - L \leq k \leq L - 1$$

only if $a_d = 0$, $d = 0, ..., 2^p - 1$. At $K = p + 1$, the matrices $\mathbf{C}_{2^{p+1},d}[k]$ are

$$\mathbf{C}_{2^{p+1},d}[k] = I_{0\leq d\leq 2^p-1} \cdot \begin{bmatrix} 1 & 1 \\ 1 & 1 \end{bmatrix} \otimes \mathbf{C}_{2^p,d}[k] + I_{2^p\leq d\leq 2^{p+1}-1} \cdot \begin{bmatrix} 1 & -1 \\ -1 & 1 \end{bmatrix} \otimes \mathbf{C}_{2^p,d}[k],$$

where $I.$ is the indicator function. Clearly, the sufficient and necessary condition of

$$\sum_{d=0}^{2^{p+1}-1} a_d \mathbf{C}_{2^{p+1},d}[k] = \mathbf{0}, \ \forall 1 - L \leq k \leq L - 1$$

is that

$$\sum_{d=0}^{2^p-1} a_d \mathbf{C}_{2^p,d}[k] = \sum_{d=0}^{2^p-1} a_{d+2^p} \mathbf{C}_{2^p,d}[k] = \mathbf{0} \ \forall 1 - L \leq k \leq L - 1.$$

This is true only if $a_d = 0$ for $0 \leq d \leq 2^p - 1$ and $2^p \leq d \leq 2^{p+1} - 1$, or equivalently $a_d = 0$ for $0 \leq d \leq 2^{p+1} - 1$.

APPENDIX E

PROOF OF THEOREM 4.6.2

Proof: Note that the first M Taylor moments of all entries in $\mathbf{\Delta}_{2^K}(k,\theta)$ around $\theta = 0$ are zero if only if the first M Taylor moments of all entries in $e^{j\theta}\mathbf{\Delta}_{2^K}(k,\theta)$ around $\theta = 0$ are zero. Write $e^{j\theta}\mathbf{\Delta}_{2^K}(k,\theta)$ as

$$\begin{aligned}
e^{j\theta}\mathbf{\Delta}_{2^K}(k,\theta) &= \frac{1}{2^K}\sum_{r=1}^{2^K-1} e^{j\theta} S_{\mathcal{P},\mathcal{Q},r}(\theta)\mathbf{\Delta}_{2^K,r}[k] \\
&= \frac{1}{2^K}\sum_{r=1}^{2^K-1}\sum_{n=0}^{N-1}\sum_{m=0}^{\infty} \omega_{2^K}^{rp_n} q[n]\frac{(n+1)^m}{m!}\theta^m \mathbf{\Delta}_{2^K,r}[k] \\
&= \frac{1}{2^K}\sum_{m=0}^{\infty}\frac{\theta^m}{m!}\sum_{r=1}^{2^K-1}\sum_{n=0}^{N-1} \omega_{2^K}^{rp_n} q[n](n+1)^m \mathbf{\Delta}_{2^K,r}[k]
\end{aligned}$$

If we have

$$\sum_{n=0}^{N-1} \omega_{2^K}^{rp_n} q[n](n+1)^m = 0,\ r = 1, ..., 2^K-1, m = 0, ..., M,$$

or equivalently

$$\begin{bmatrix} 1 & 1 & \cdots & 1 \\ 1 & 2 & \cdots & N \\ \vdots & \vdots & \ddots & \vdots \\ 1^M & 2^M & \cdots & N^M \end{bmatrix} \begin{bmatrix} \omega_{2^K}^{rp_0} q_0 \\ \omega_{2^K}^{rp_1} q_1 \\ \vdots \\ \omega_{2^K}^{rp_{N-1}} q_{N-1} \end{bmatrix} = \mathbf{0},\ r = 1, ..., 2^K - 1,$$

then the first M Taylor moments of all entries in $e^{j\theta}\mathbf{\Delta}_{2^K}(k,\theta)$ around $\theta = 0$ are zero for all k.

Conversely, denote $a_{m,r} = \sum_{n=0}^{N-1} \omega_{2^K}^{rp_n} q[n](n+1)^m$. Substitute (4.37) into (E), we have

$$e^{j\theta}\mathbf{\Delta}_{2^K}(k,\theta) = \frac{1}{2^K}\sum_{m=0}^{\infty}\sum_{d=0}^{2^K-1}\sum_{r=1}^{2^K-1} \omega_{2^K}^{-rd} a_{m,r}\mathbf{\Delta}_{2^K,d}[k]$$

Zero forcing the first M-th Taylor moments of all entries in $e^{j\theta}\mathbf{\Delta}_{2^K}(k,\theta)$ around $\theta = 0$ are zero for all k requires

$$\sum_{d=0}^{2^K-1} a_{m,d}\mathbf{\Delta}_{2^K,d}[k] = \mathbf{0},\ m = 0, ..., M,$$

where $a_{m,d} = \sum_{r=1}^{2^K-1} \omega_{2^K}^{-rd} a_{m,r}$. Using the result in Lemma 4.4.1, we can show that $a_{m,d} = 0$, $d = 0, ..., 2^K - 1$, $m = 0, ..., M$. This yields the discrete Fourier transformation

$$\begin{bmatrix} 1 & 1 & 1 & \cdots & 1 \\ 1 & \omega_{2^K}^{-1} & \omega_{2^K}^{-2} & \cdots & \omega_{2^K}^{-(2^K-1)} \\ 1 & \vdots & \vdots & \ddots & \vdots \\ 1 & \omega_{2^K}^{-(2^K-1)} & \omega_{2^K}^{-2(2^K-1)} & \cdots & \omega_{2^K}^{-(2^K-1)^2} \end{bmatrix} \begin{bmatrix} 0 \\ a_{m,1} \\ \vdots \\ a_{m,2^K-1} \end{bmatrix} = \mathbf{0}, m = 0, ..., M.$$

The Parseval's theorem indicates that $a_{m,r} = 0$, $r = 1, ..., 2^K - 1$, $m = 0, ..., M$.

APPENDIX F

PROOF OF THEOREM 4.7.1

Proof: for arbitrary two integers $0 \le d, d' \le D_1D_2 - 1$, write $d = D_2d_1 + d_2$, and $d' = D_2d'_1 + d'_2$. From the construction of $(\mathbf{p}, \mathbf{q})$ we have

$$\begin{aligned}\sum_{\substack{n=0\\p_n=d}}^{N-1} q_n n^m &= \sum_{\substack{n_1=0\\p_{1,n_1}=d_1}}^{N_1-1} \sum_{\substack{n_2=0\\p_{2,n_2}=d_2}}^{N_2-1} q_{1,n_1} q_{2,n_2} (n_1R_1 + n_2R_2)^m \\ &= \sum_{\ell=0}^{m} \binom{m}{\ell} R_1^\ell R_2^{m-\ell} \sum_{\substack{n_1=0\\p_{1,n_1}=d_1}}^{N_1-1} q_{1,n_1} n_1^\ell \cdot \sum_{\substack{n_2=0\\p_{2,n_2}=d_2}}^{N_2-1} q_{2,n_2} n_2^{m-\ell}.\end{aligned}$$

and

$$\sum_{\substack{n=0\\p_n=d'}}^{N-1} q_n n^m = \sum_{\ell=0}^{m} \binom{m}{\ell} R_1^\ell R_2^{m-\ell} \sum_{\substack{n_1=0\\p_{1,n_1}=d'_1}}^{N_1-1} q_{1,n_1} n_1^\ell \cdot \sum_{\substack{n_2=0\\p_{2,n_2}=d'_2}}^{N_2-1} q_{2,n_2} n_2^{m-\ell}$$

Since $(\mathbf{p}_1, \mathbf{q}_1) \in \mathcal{N}_{D_1}(N_1, M)$, and $(\mathbf{p}_2, \mathbf{q}_2) \in \mathcal{N}_{D_2}(N_2, M)$, we have

$$\sum_{\substack{n=0\\p_{i,n}=d_i}}^{N_i-1} q_{i,n} n^m = \sum_{\substack{n=0\\p_{i,n}=d'_i}}^{N_i-1} q_{i,n} n^m,\ m = 0, \dots, M,\ \forall 0 \le d_i, d'_i \le D_i - 1,\ i = 1, 2,$$

Thus we have

$$\sum_{\substack{n=0\\p_n=d}}^{N-1} q_n n^m = \sum_{\substack{n=0\\p_n=d'}}^{N-1} q_n n^m,\ \forall 0 \le d, d' \le D_1D_2 - 1,\ m = 0, \dots, M. \tag{F.1}$$

APPENDIX G

PROOF OF THEOREM 4.7.3

Proof: Decompose the residue matrix as

$$\mathbf{\Delta}_{2^K}(k,\theta)\mathbf{\Delta}_{2^K,\text{odd}}(k,\theta)+\mathbf{\Delta}_{2^K,\text{even}}(k,\theta),$$

where $\mathbf{\Delta}_{2^K,\text{odd}}(k,\theta)$ is defined as

$$\begin{aligned}
\mathbf{\Delta}_{2^K,\text{odd}}(k,\theta) &= \frac{1}{2^K}\sum_{\substack{r=1\\ r\text{ is odd}}}^{2^K-1} S_{\mathbf{p}_K,\mathbf{q}_K,r}(\theta)\mathbf{\Delta}_{2^K,r}[k] \\
&= \frac{1}{2^K}\sum_{\substack{r=1\\ r\text{ is odd}}}^{2^K}\sum_{n=0}^{N^{K-1}-1}\omega_{2^K}^{rp_{K-1,n}}q_{K-1,n}e^{jn\theta}S_{\mathbf{p}_1,\mathbf{q}_1}(N^{K-1}\theta)\sum_{d=0}^{2^K-1}\omega_{2^K}^{-rd}\mathbf{C}_{2^K,d}[k] \\
&= \frac{1}{2^K}S_{\mathbf{p}_1,\mathbf{q}_1}(N^{K-1}\theta)\sum_{n=0}^{N^{K-1}-1}\left(\sum_{d=0}^{2^K-1}\sum_{\substack{r=1\\ r\text{ is odd}}}^{2^K}\omega_{2^K}^{r(p_{K-1,n}-d)}\mathbf{C}_{2^K,d}[k]\right)q_{K-1,n}e^{jn\theta},
\end{aligned}$$

Using the fact that

$$\sum_{\substack{r=1\\ r\text{ is odd}}}^{2^K-1}\omega_{2^K}^{rp}=\begin{cases}2^{K-1}, & p=0,2^{K-1}\\ 0, & \text{otherwise}\end{cases},$$

for $p=0,\dots,2^K-1$, we can be further write $\mathbf{\Delta}_{2^K,\text{odd}}(k,\theta)$ as

$$\begin{aligned}
\mathbf{\Delta}_{2^K,\text{odd}}(k,\theta) &= \frac{1}{2}S_{\mathbf{p}_1,\mathbf{q}_1}(N^{K-1}\theta)\sum_{n=0}^{N^{K-1}-1}(\mathbf{C}_{2^K,p_{K-1,n}}[k]-\mathbf{C}_{2^K,p_{K-1,n}+2^{K-1}}[k])q_{K-1,n}e^{jn\theta} \\
&= S_{\mathbf{p}_1,\mathbf{q}_1}(N^{K-1}\theta)\sum_{n=0}^{N^{K-1}-1}\mathbf{J}_2\otimes\mathbf{C}_{2^{K-1},p_{K-1,n}}[k]q_{K-1,n}e^{jn\theta} \\
&= S_{\mathbf{p}_1,\mathbf{q}_1}(N^{K-1}\theta)\mathbf{J}_2\otimes\boldsymbol{\chi}_{\mathbf{p}_{K-1},\mathbf{q}_{K-1}}(k,\theta) \\
&= S_{\mathbf{p}_1,\mathbf{q}_1}(N^{K-1}\theta)\mathbf{J}_2\otimes\left[S_{\mathbf{q}_{K-1}}(\theta)\delta[k]\mathbf{I}_{2^{K-1}}+\mathbf{\Delta}_{2^{K-1}}(k,\theta)\right],
\end{aligned}$$

where $\mathbf{J}_2$ is the 2×2 anti-diagonal matrix whose anti-diagonal entries are all 1.

The term $\mathbf{\Delta}_{2^K,\text{even}}(k,\theta)$ is defined as

$$\begin{aligned}
\mathbf{\Delta}_{2^K,\text{even}}(k,\theta) &= \frac{1}{2^K}\sum_{\substack{r=1\\ r\text{ is even}}}^{2^K-1} S_{\mathbf{p}_K,\mathbf{q}_K,r}(\theta)\mathbf{\Delta}_{2^K,r}[k] \\
&= \frac{1}{2^K}\sum_{\substack{r=1\\ r\text{ is even}}}^{2^K-1} S_{\mathbf{p}_{K-1},\mathbf{q}_{K-1},\frac{r}{2}}(\theta)S_{\mathbf{q}_1}(N^{K-1}\theta)\sum_{d=0}^{2^K-1}\omega_{2^K}^{-rd}\mathbf{C}_{2^K,d}[k] \\
&= \frac{1}{2^K}\sum_{\substack{r=1\\ r\text{ is even}}}^{2^K-1} S_{\mathbf{p}_{K-1},\mathbf{q}_{K-1},\frac{r}{2}}(\theta)S_{\mathbf{q}_1}(N^{K-1}\theta)\sum_{d=0}^{2^{K-1}-1}\omega_{2^{K-1}}^{-\frac{r}{2}d}\left(\mathbf{C}_{2^K,d}[k]+\mathbf{C}_{2^K,d+2^{K-1}}[k]\right) \\
&= \frac{1}{2^{K-1}}S_{\mathbf{q}_1}(N^{K-1}\theta)\sum_{r=1}^{2^{K-1}-1} S_{\mathbf{p}_{K-1},\mathbf{q}_{K-1},r}(\theta)\sum_{d=0}^{2^{K-1}-1}\omega_{2^{K-1}}^{-rd}\mathbf{I}_2\otimes\mathbf{C}_{2^{K-1},d}[k] \\
&= S_{\mathbf{q}_1}(N^{K-1}\theta)\cdot\mathbf{I}_2\otimes\mathbf{\Delta}_{2^{K-1}}(k,\theta).
\end{aligned}$$

Therefore we have

$$\begin{aligned}
&\mathbf{\Delta}_{2^K}(k,\theta) \\
&= \mathbf{\Delta}_{2^K,\text{odd}}(k,\theta)+\mathbf{\Delta}_{2^K,\text{even}}(k,\theta) \\
&= S_{\mathbf{p}_1,\mathbf{q}_1}(N^{K-1}\theta)\mathbf{J}_2\otimes\left[S_{\mathbf{q}_{K-1}}(\theta)\delta[k]\mathbf{I}_{2^{K-1}}+\mathbf{\Delta}_{2^{K-1}}(k,\theta)\right]+S_{\mathbf{q}_1}(N^{K-1}\theta)\mathbf{I}_2\otimes\mathbf{\Delta}_{2^{K-1}}(k,\theta) \\
&= \left[S_{\mathbf{q}_1}(N^{K-1}\theta)\mathbf{I}_2+S_{\mathbf{p}_1,\mathbf{q}_1}(N^{K-1}\theta)\mathbf{J}_2\right]\otimes\mathbf{\Delta}_{2^{K-1}}(k,\theta)+S_{\mathbf{p}_1,\mathbf{q}_1}(N^{K-1}\theta)S_{\mathbf{q}_{K-1}}(\theta)\delta[k]\mathbf{J}_2\otimes\mathbf{I}_{2^{K-1}}.
\end{aligned}$$

APPENDIX H

PROOF OF THEOREM 4.7.8

Proof: From previous definition of $\mathbf{\Delta}_{2^K,\text{odd}}(k,\theta)$ and $\mathbf{\Delta}_{2^K,\text{even}}(k,\theta)$, we have

$$\begin{aligned}
\mathbf{\Delta}_{2^K,\text{odd}}(k,\theta) &= \frac{1}{2^K}\sum_{\substack{r=1\\ r \text{ is odd}}}^{2^K-1} S_{\mathbf{q}}(\theta+\frac{r2\pi}{2^K})\sum_{d=0}^{2^K-1}\omega_{2^K}^{-rd}\mathbf{C}_{2^K,d}[k]\\
&= \frac{1}{2^{K-1}}\sum_{\substack{r=1\\ r \text{ is odd}}}^{2^K-1} S_{\mathbf{q}}(\theta+\frac{r2\pi}{2^K})\sum_{d=0}^{2^{K-1}-1}\omega_{2^K}^{-rd}\mathbf{J}_2\otimes\mathbf{C}_{2^{K-1},d}[k]\\
&= \frac{1}{2^{K-1}}\mathbf{J}_2\otimes\left(\sum_{\substack{r=1\\ r \text{ is odd}}}^{2^K-1} S_{\mathbf{q}}(\theta+\frac{r2\pi}{2^K})\sum_{d=0}^{2^{K-1}-1}\omega_{2^K}^{-rd}\mathbf{C}_{2^{K-1},d}[k]\right),
\end{aligned}$$

$$\begin{aligned}
\mathbf{\Delta}_{2^K,\text{even}}(k,\theta) &= \frac{1}{2^K}\sum_{\substack{r=1\\ r \text{ is even}}}^{2^K-1} S_{\mathbf{q}}(\theta+\frac{r2\pi}{2^K})\sum_{d=0}^{2^K-1}\omega_{2^K}^{-rd}\mathbf{C}_{2^K,d}[k]\\
&= \frac{1}{2^{K-1}}\sum_{\substack{r=1\\ r \text{ is even}}}^{2^K-1} S_{\mathbf{q}}(\theta+\frac{r2\pi}{2^K})\sum_{d=0}^{2^{K-1}-1}\omega_{2^{K-1}}^{-\frac{r}{2}d}\mathbf{I}_2\otimes\mathbf{C}_{2^{K-1},d}[k]\\
&= \frac{1}{2^{K-1}}\mathbf{I}_2\otimes\left(\sum_{\substack{r=1\\ r \text{ is even}}}^{2^K-1} S_{\mathbf{q}}(\theta+\frac{r2\pi}{2^K})\mathbf{\Delta}_{2^{K-1},\frac{r}{2}}[k]\right).
\end{aligned}$$

APPENDIX I

PROOF OF THEOREM 4.8.1

Proof: Given $(\mathbf{p}, \mathbf{q}) \in \mathcal{N}^{2^K}(N, M)$ and an arbitrary permutation π_{2^K}, denote $\mathbf{p}' = \mathcal{A}(\pi_{2^K})\mathbf{p}$, and write $P_n(\mathbf{p}', \mathbf{q}, \phi)$ by

$$P_n(\mathbf{p}', \mathbf{q}, \phi) = \sum_{d=0}^{2^K-1} \left(\sum_{\substack{n=0 \\ p'[n]=d}}^{N-1} |q[n]|^2 \right) \mathbf{a}_{2^K}(\phi)^T \cdot \mathbf{C}_{2^K,d}[0] \cdot \mathbf{a}_{2^K}(\phi)^*.$$

For $2 \leq k \leq K$, we have

$$\begin{aligned}
&\sum_{d=0}^{2^k-1} \left(\sum_{\substack{n=0 \\ p'[n]=d}}^{N-1} |q[n]|^2 \right) \mathbf{a}_{2^k}(\phi)^T \cdot \mathbf{C}_{2^k,d}[0] \cdot \mathbf{a}_{2^k}(\phi)^* \\
&= 2 \sum_{d=0}^{2^{k-1}-1} \left[(1 + \cos(2^{k-1}\phi)) \sum_{\substack{n=0 \\ p'[n]=d}}^{N-1} |q[n]|^2 + \right. \\
&\qquad \left. (1 - \cos(2^{k-1}\phi)) \sum_{\substack{n=0 \\ p'[n]=d+2^{k-1}}}^{N-1} |q[n]|^2 \right] \mathbf{a}_{2^{k-1}}(\phi)^T \cdot \mathbf{C}_{2^{k-1},d}[0] \cdot \mathbf{a}_{2^{k-1}}(\phi)^* \\
&\leq 4 \sum_{d=0}^{2^{k-1}-1} \left(\max_{i \in \{0,1\}} \sum_{\substack{n=0 \\ p'[n]=d+i2^{k-1}}}^{N-1} |q[n]|^2 \right) \mathbf{a}_{2^{k-1}}(\phi)^T \cdot \mathbf{C}_{2^{k-1},d}[0] \cdot \mathbf{a}_{2^{k-1}}(\phi)^*,
\end{aligned}$$

where the last equality holds at $\phi = 0$. Since

$$\begin{aligned}
&\sum_{d=0}^{1} \left(\sum_{\substack{n=0 \\ p'[n]=d}}^{N-1} |q[n]|^2 \right) \mathbf{a}_2(\phi)^T \cdot \mathbf{C}_{2,d}[0] \cdot \mathbf{a}_2(\phi)^* \\
&= 2 \left(\sum_{\substack{n=0 \\ p'[n]=0}}^{N-1} |q[n]|^2 + \sum_{\substack{n=0 \\ p'[n]=0}}^{N-1} |q[n]|^2 + C_{xy}[0] \cos\phi \cdot \left(\sum_{\substack{n=0 \\ p'[n]=0}}^{N-1} |q[n]|^2 - \sum_{\substack{n=0 \\ p'[n]=0}}^{N-1} |q[n]|^2 \right) \right) \\
&\leq 2 \left(\sum_{\substack{n=0 \\ p'[n]=0}}^{N-1} |q[n]|^2 + \sum_{\substack{n=0 \\ p'[n]=0}}^{N-1} |q[n]|^2 + |C_{xy}[0]| \cdot \left| \sum_{\substack{n=0 \\ p'[n]=0}}^{N-1} |q[n]|^2 - \sum_{\substack{n=0 \\ p'[n]=0}}^{N-1} |q[n]|^2 \right| \right),
\end{aligned}$$

where the last equality holds if $\phi = 0$. Thus the noise power $P_n(\mathbf{p}', \mathbf{q}, \phi)$ when (1) $\sum_{p'[n]=d} |q[n]|^2 \geq \sum_{p'[n]=d+2^{k-1}} |q[n]|^2$, $0 \leq d \leq 2^{k-1} - 1$ for each $2 \leq k \leq K$; (2)

$\sum_{p'[n]=0} |q[n]|^2 \geq \sum_{p'[n]=1} |q[n]|^2$ if $C_{xy}[0] \geq 0$ or $\sum_{p'[n]=0} |q[n]|^2 \leq \sum_{p'[n]=1} |q[n]|^2$ if $C_{xy}[0] < 0$; (3) $\phi = 0$. By substituting the above condition into the expression of $P_n(\mathbf{p'}, \mathbf{q}, \phi)$, we get the result in theorem 4.8.1.

APPENDIX J

PROOF OF THEOREM 5.5.2

Proof: For notation simplicity, we write x and z instead of x_3 and z_3 respectively. Use triangle inequality we obtain

$$\begin{aligned} I(z)|e_{m,\ell}(z)| \leq & \left|\int_{-\Delta/M}^{0} \Big|\sum_{p\neq 0} a_{m,\ell+p}\mathcal{G}(x+p\Delta/M,z)\Big|^2 dx\right| \\ & + 2\left|\mathrm{Re}\left\{a_{m,\ell}\sum_{p\neq 0} a_{m,\ell+p}\int_{-\Delta/M}^{0}\mathcal{G}(x,z)\mathcal{G}(x+p\Delta/M,z)dx\right\}\right| \\ & \leq \int_{-\Delta/M}^{0}\Big(\sum_{p\neq 0} a_{m,\ell+p}\big|\mathcal{G}(x+p\Delta/M)\big|\Big)^2 dx \\ & + 2a_{m,l}\sum_{p\neq 0} a_{m,\ell+p}\int_{-\Delta/M}^{0}|\mathcal{G}(x,z)||\mathcal{G}(x+p\Delta/M,z)|dx. \end{aligned} \tag{J.1}$$

From Cauchy-Schwartz inequality we have

$$\begin{aligned} |\mathcal{G}(x+p\Delta/M,z)| &= \left|\int_{x+p\Delta/M}^{x+(p+1)\Delta/M} e^{-(\frac{y}{w(z)})^2} e^{-i\frac{ky^2}{2R(z)}}dy\right| \\ &\leq \left(\int_{x+p\Delta/M}^{x+(p+1)\Delta/M} e^{-(\frac{y}{w(z)})^2}dy\right)^{1/2}\left(\int_{x+p\Delta/M}^{x+(p+1)\Delta/M} dy\right)^{1/2} \\ &= \sqrt{\Delta/M}\left(\int_{x+p\Delta/M}^{x+(p+1)\Delta/M} e^{-(\frac{y}{w(z)})^2}dy\right)^{1/2}. \end{aligned} \tag{J.2}$$

It easy to show that for $x \in [-\Delta/M, 0]$, the integral

$$\int_{x+p\Delta/M}^{x+(p+1)\Delta/M} e^{-(\frac{y}{w(z)})^2}dy \leq \begin{cases} \Delta/M\exp\big(-(\frac{x+p\Delta/M}{w(z)})^2\big), & p>0 \\ \Delta/M, & p=0\ . \\ \Delta/M\exp\big(-(\frac{x+(p+1)\Delta/M}{w(z)})^2\big), & p<0 \end{cases} \tag{J.3}$$

Thus we have

$$
\begin{aligned}
&\int_{-\Delta/M}^{0}\big(\sum_{p\neq 0} a_{m,\ell+p}\big|\mathcal{G}(x+p\Delta/M,z)\big|\big)^2dx\\
&\le 2\int_{-\Delta/M}^{0}\big(\sum_{p<0} a_{m,\ell+p}\big|\mathcal{G}(x+p\Delta/M,z)\big|\big)^2dx+2\int_{-\Delta/M}^{0}\big(\sum_{p>0} a_{m,\ell+p}\big|\mathcal{G}(x+p\Delta/M,z)\big|\big)^2dx\\
&\le 2(\Delta/M)^2\int_{-\Delta/M}^{0}\big[\sum_{p=-\ell}^{-1} e^{-\frac{(x+(p+1)\Delta/M)^2}{2w^2(z)}}\big]^2dx+2(\Delta/M)^2\int_{-\Delta/M}^{0}\big[\sum_{p=1}^{N-\ell-1} e^{-\frac{(x+p\Delta/M)^2}{2w^2(z)}}\big]^2dx\\
&= 2(\Delta/M)^2\int_{0}^{\Delta/M}\big[\sum_{p=-\ell}^{-1} e^{-\frac{(x+p\Delta/M)^2}{2w^2(z)}}\big]^2dx+2(\Delta/M)^2\int_{0}^{\Delta/M}\big[\sum_{p=1}^{N-\ell-1} e^{-\frac{(x-p\Delta/M)^2}{2w^2(z)}}\big]^2dx\\
&= 2(\Delta/M)^2\bigg(\int_{0}^{\Delta/M}\big[\sum_{p=1}^{\ell} e^{-\frac{(x-p\Delta/M)^2}{2w^2(z)}}\big]^2dx+\int_{0}^{\Delta/M}\big[\sum_{p=1}^{N-\ell-1} e^{-\frac{(x-p\Delta/M)^2}{2w^2(z)}}\big]^2dx\bigg)
\end{aligned}
\tag{J.4}
$$

For $p>0$, we have

$$
\begin{aligned}
(x-p\Delta/M)^2 &= x^2-2px\Delta/M+p^2(\Delta/M)^2\\
&\ge x^2-2p(\Delta/M)^2+p^2(\Delta/M)^2,\quad x\in[0,\Delta/M],
\end{aligned}
\tag{J.5}
$$

Thus it follows that

$$
\begin{aligned}
e^{-\frac{(x-p\Delta/M)^2}{2w^2(z)}} &\le e^{-\frac{x^2-2p(\Delta/M)^2+p^2(\Delta/M)^2}{2w^2(z)}}\\
&= e^{\frac{(\Delta/M)^2}{2w^2(z)}}e^{-\frac{x^2}{2w^2(z)}}e^{-\frac{(p-1)^2(\Delta/M)^2}{2w^2(z)}},\ x\in[0,\Delta/M],
\end{aligned}
\tag{J.6}
$$

and

$$
\begin{aligned}
\int_{0}^{\Delta/M}\big[\sum_{p=1}^{\ell} e^{-\frac{(x-p\Delta/M)^2}{2w^2(z)}}\big]^2dx &\le e^{\frac{(\Delta/M)^2}{w^2(z)}}\int_{0}^{\Delta/M}\big[\sum_{p=1}^{\ell} e^{-\frac{x^2}{2w^2(z)}}e^{-\frac{(p-1)^2(\Delta/M)^2}{2w^2(z)}}\big]^2dx\\
&\le e^{\frac{(\Delta/M)^2}{w^2(z)}}S_\ell^2\int_{0}^{\Delta/M} e^{-\frac{x^2}{w^2(z)}}dx,
\end{aligned}
\tag{J.7}
$$

where the finite sum S_ℓ is

$$
S_\ell=\sum_{p=0}^{\ell-1} e^{-\frac{p^2(\Delta/M)^2}{2w^2(z)}}. \tag{J.8}
$$

Similarly we have

$$
\int_{0}^{\Delta/M}\big[\sum_{p=1}^{N-\ell-1} e^{-\frac{(x-p\Delta/M)^2}{2w^2(z)}}\big]^2\le e^{\frac{(\Delta/M)^2}{w^2(z)}}S_{N-\ell-1}^2\int_{0}^{\Delta/M} e^{-\frac{x^2}{w^2(z)}}dx. \tag{J.9}
$$

Therefore from eq (J.4) we have

$$\int_0^{\Delta/M} \Big(\sum_{p\neq 0} a_{m,\ell+p}\big|\mathcal{G}(x+p\Delta/M,z)\big|\Big)^2 dx \leq 2(\Delta/M)^2 e^{\frac{(\Delta/M)^2}{w^2(z)}}(S_\ell^2+S_{N-\ell-1}^2)\int_0^{\Delta/M} e^{-\frac{x^2}{w^2(z)}}dx \tag{J.10}$$

The second term on the right hand side of (J.1) can be bounded as

$$\begin{aligned}
&a_{m,\ell}\sum_{p\neq 0} a_{m,\ell+p}\int_{-\Delta/M}^{0} |\mathcal{G}(x,z)||\mathcal{G}(x+p\Delta/M,z)|dx \\
&\leq a_{m,\ell}(\Delta/M)^2\Big\{\sum_{p=-\ell}^{-1} a_{m,\ell+p}\int_{-\Delta/M}^{0} e^{-\frac{(x+(p+1)\Delta/M)^2}{2w^2(z)}}dx + \sum_{p=1}^{N-\ell-1} a_{m,\ell+p}\int_{-\Delta/M}^{0} e^{-\frac{(x+p\Delta/M)^2}{2w^2(z)}}dx\Big\} \\
&\leq a_{m,\ell}(\Delta/M)^2\Big\{\sum_{p=1}^{\ell}\int_0^{\Delta/M} e^{-\frac{(x-p\Delta/M)^2}{2w^2(z)}}dx + \sum_{p=1}^{N-\ell-1}\int_0^{\Delta/M} e^{-\frac{(x-p\Delta/M)^2}{2w^2(z)}}dx\Big\} \\
&\leq a_{m,\ell}(\Delta/M)^2 e^{\frac{(\Delta/M)^2}{2w^2(z)}}(S_\ell+S_{N-\ell})\int_0^{\Delta/M} e^{-\frac{x^2}{2w^2(z)}}dx.
\end{aligned} \tag{J.11}$$

In summary, the amplitude of $I(z)e_{m,\ell}(z)$ can be bounded as

$$\begin{aligned}
I(z)|e_{m,\ell}(z)| \leq &\int_{-\Delta/M}^{0}\Big(\sum_{p\neq 0} a_{m,\ell+p}\big|\mathcal{G}(x+p\Delta/M)\big|\Big)^2 dx \\
&+ 2a_{m,l}\sum_{p\neq 0} a_{m,\ell+p}\int_{-\Delta/M}^{0}|\mathcal{G}(x,z)||\mathcal{G}(x+p\Delta/M,z)|dx \\
\leq\ & 2(\Delta/M)^2\Big[e^{\frac{(\Delta/M)^2}{2w^2(z)}}(S_\ell+S_{N-\ell-1})\int_0^{\Delta/M} e^{-\frac{x^2}{2w^2(z)}}dx \\
&+ e^{\frac{(\Delta/M)^2}{w^2(z)}}(S_\ell^2+S_{N-\ell-1}^2)\int_0^{\Delta/M} e^{-\frac{x^2}{w^2(z)}}dx\Big]
\end{aligned} \tag{J.12}$$

It is obvious that for each ℓ we have $S_\ell + S_{N-\ell-1} \leq 2S_N$, and $S_\ell^2 + S_{N-\ell-1}^2 < 2S_N^2$. Therefore we have

$$I(z)|e_{m,\ell}(z)| \leq 4(\Delta/M)^2\Big[e^{\frac{(\Delta/M)^2}{2w^2(z)}} S_N\int_0^{\Delta/M} e^{-\frac{x^2}{2w^2(z)}}dx + e^{\frac{(\Delta/M)^2}{w^2(z)}} S_N^2\int_0^{\Delta/M} e^{-\frac{x^2}{w^2(z)}}dx\Big] \tag{J.13}$$

Note that

$$
\begin{aligned}
S_N &= 1 + \sum_{k=1}^{N-1} e^{-\frac{k^2(\Delta/M)^2}{2w^2(z)}} \\
&\le 1 + \frac{1}{\Delta/M} \sum_{k=1}^{N-1} \int_{(k-1)\Delta/M}^{k\Delta/M} e^{-\frac{x^2}{2w^2(z)}}\,dx \\
&\le 1 + \frac{1}{\Delta/M} \int_0^{(N-1)\Delta/M} e^{-\frac{x^2}{2w^2(z)}}\,dx \\
&= 1 + \sqrt{\frac{\pi}{2}} \frac{Mw(z)}{\Delta} \operatorname{erf}\left(\frac{(N-1)\Delta}{\sqrt{2}Mw(z)} \right),
\end{aligned} \tag{J.14}
$$

where the error function is defined as $\operatorname{erf}(x) = \frac{2}{\sqrt{\pi}} \int_0^x e^{-t^2} dt$. Denote $r(z) = \frac{\Delta}{\sqrt{2}Mw(z)}$ and the above result can be expressed as

$$
S_N \le 1 + \frac{\sqrt{\pi}}{2} r^{-1}(z) \operatorname{erf}\big((N-1)r(z)\big). \tag{J.15}
$$

Also note that the integrals are

$$
\int_0^{\Delta/M} e^{-\frac{x^2}{2w^2(z)}}\,dx = \sqrt{2}w(z)\operatorname{erf}\big(r(z)\big), \tag{J.16}
$$

and

$$
\int_0^{\Delta/M} e^{-\frac{x^2}{w^2(z)}}\,dx = w(z)\operatorname{erf}\big(\sqrt{2}r(z)\big). \tag{J.17}
$$

Finally, we have the bound

$$
\begin{aligned}
I(z)|e_{m,\ell}(z)| &\le 4(\Delta/M)^2 \left[e^{\frac{(\Delta/M)^2}{2w^2(z)}} S_N \int_0^{\Delta/M} e^{-\frac{x^2}{2w^2(z)}}\,dx + e^{\frac{(\Delta/M)^2}{w^2(z)}} S_N^2 \int_0^{\Delta/M} e^{-\frac{x^2}{w^2(z)}}\,dx \right] \\
&\le 4(\Delta/M)^2 w(z) \Bigg[\sqrt{2} \left(1 + \frac{\sqrt{\pi}}{2} r^{-1}(z) \operatorname{erf}\big((N-1)r(z)\big) \right) \operatorname{erf}\big(r(z)\big) e^{r^2(z)} \\
&\quad + \left(1 + \frac{\sqrt{\pi}}{2} r^{-1}(z) \operatorname{erf}\big((N-1)r(z)\big) \right)^2 \operatorname{erf}\big(\sqrt{2}r(z)\big) e^{2r^2(z)} \Bigg].
\end{aligned} \tag{J.18}
$$